Monte Carlo Simulation of Solid Rocket Exhaust Plumes at High Altitude

by

Jonathan Matthew Burt

A dissertation submitted in partial fulfillment
of the requirements for the degree of
Doctor of Philosophy
(Aerospace Engineering)
in The University of Michigan
2006

Doctoral Committee:

Professor Iain D. Boyd, Co-Chair
Professor Wei Shyy, Co-Chair
Professor Philip L. Roe
Research Professor Michael R. Combi

To my parents, and to Alissa.

Acknowledgements

I'd first like to thank my advisor, Prof. Iain Boyd, for continual guidance and encouragement over the last four years. Much of my work, knowledge and interest in rarefied gas dynamics is a result of your teaching and oversight, and I am grateful for the opportunity you have given me to pursue this as a career path. I'd also like to acknowledge my committee members, Profs. Shyy, Roe and Combi, and all of the other faculty members who have provided suggestions, answered questions, and in many other ways made my graduate school experience more productive and enjoyable.

A number of other people have provided important input for the research presented in this thesis. While there are far too many to name here, I'd like to acknowledge a few people who have been particularly helpful, and without whom I would not have been able to perform much of my dissertation research. First, I'd like to thank Tom Smith, Dean Wadsworth and Jay Levine at the Air Force Research Laboratory for overseeing my research and for providing the generous financial support that enabled me to perform this work. Ingrid Wysong, Sergey Gimelshein and Matt Braunstein have also been enormously helpful over the past several years, through their many suggestions and comments, and through the discussions and e-mail exchanges we have had on the progress and direction of my research.

My experience at the University of Michigan would have been far less enjoyable had it not been for the many students I have met and friends I have gained while here. Again I cannot name everyone, but in particular I'd like to thank Anish, Yoshi, Matt, Anton, Michael M., John Y., Jose, Kooj, Jerry, Tom, Allen, Andy, Andrew, Javier P., Javier D., Quanhua, Leo, Dave and Chunpei. You have helped me to grow and mature as a student, a researcher and an individual.

I'd also like to thank my family, and particularly my parents, for your unconditional support and encouragement, and for providing me with the self confidence and motivation that has allowed me to become the person that I am today. Lastly, I'd like to thank Alissa, for your comfort and support during my time spent writing this thesis, and for the happiness you have brought to me.

Table of Contents

List of Figures

Figure

List of Tables

Table

List of Appendices

Appendix

Chapter I

Introduction and Background

1.1 Applications of solid rocket plume analysis

Propulsion of aircraft and spacecraft through the combustion of solid fuels has both an extensive history and a wide range of applications. For reasons of production cost, low maintenance, simplicity, scalability and safety, solid propellant motors have for the past several decades been a popular alternative to liquid-based chemical rocket propulsion systems. Solid rocket motors (SRMs) have found wide use as a means of satellite orbit insertion and orbit transfer, as well as in ballistic missile defense systems and similar applications where the lack of throttle control or reignition capabilities are outweighed by cost savings or safety advantages over liquid propellant rocket engines.

While most liquid propellant engines consist of a large number of components, including fuel and oxidizer pumps, temperature control systems, storage tanks and a separate combustion chamber, a typical SRM has a relatively simple structure consisting of a large enclosure where the propellant grain is both stored and combusted, and a convergent-divergent (De Laval) nozzle where combustion products are accelerated to provide thrust. The simple construction and lack of moving parts allow an SRM to be constructed for considerably less expense than a liquid rocket engine with the same thrust

and propellant mass. At the same time, the solid propellant tends to require far less long term maintenance and generally presents fewer safety hazards than liquid fuels, making SRM systems preferred for applications involving storage on ships or submarines. SRM boosters are commonly used to augment the thrust from primary propulsion systems on satellite launch vehicles, and reusable solid rocket boosters on the space shuttle provide much of the thrust required for orbit insertion.

While the overall structure of an SRM is relatively simple, a large amount of detailed analysis and testing may be needed in the design optimization for high efficiency, low weight, reliability, and other factors specific to the mission requirements. SRM design presents several difficulties not faced in the development of liquid rocket engines. In particular, the SRM designer must consider challenges associated with the presence of small alumina (Al_2O_3) particles in the exhaust flow. These particles result from the use of aluminum in the propellant grain to dampen combustion instabilities and increase specific impulse. [*Dupays* (2002)] A typical grain consists of an ammonium perchlorate oxidizer with a hydrocarbon binder, and a 10-20% mass fraction of aluminum powder. Through a complicated process of combustion, agglomeration, droplet breakup and nonequilibrium crystallization, the presence of aluminum results in the formation of micron-size alumina particles within the exhaust flow through the nozzle and plume. These particles commonly account for about 15-30% of the total mass flow through the nozzle exit plane, and contribute significantly to a number of exhaust flow properties of interest to the SRM designer. [*Geisler* (2002)]

One such potentially important property is rocket or spacecraft base heating. At high altitudes where the flow through the nozzle is typically highly underexpanded and shocks

due to plume-atmosphere interaction are suppressed, the alumina particles tend to develop large temperature lags relative to the surrounding gas. Particle emission may dominate the radiative energy balance throughout the plume, and contribute greatly to radiative heating of rocket or spacecraft components within the plume line of sight. The surface temperatures of these components may increase by several hundred degrees due to radiative heat transfer from the particles, so an understanding and accurate estimation of this effect may be crucial in designing for acceptable thermal loading.

Another unwanted characteristic of alumina particles in the plume is the potential for impingement and contamination on the rocket or spacecraft surface. One common application of SRMs is as secondary thrusters for stage separation, orbit stabilization or small trajectory corrections. As particles are forced outward from the nozzle centerline by the rapidly expanding gas in a high altitude side thruster plume, there is some possibility that particles ejected from the thruster will collide with downstream spacecraft surfaces. This presents problems of systems operation and reliability, and must be addressed as part of the design process.

The presence of alumina particles also creates challenges in SRM design for low observable signatures. These particles tend to dominate plume radiative emission in much of the IR through near-UV range (wavelengths of 0.2 to 5 μm) and may dramatically alter the optical thickness and scattering properties of the plume as well. [*Simmons* (2000)] In the development of SRM propulsion and control systems for ballistic missile applications, accurate determination of particle radiation characteristics may therefore be required.

Radiation analysis for solid rocket plumes plays another important role in the missile defense community. Ballistic missile defense systems require a database of emission characteristics for existing SRM designs, so that observed threats may be quickly and accurately identified. In addition, the kill vehicle must be able to distinguish the hard body (i.e. the rocket or reentry vehicle) from the plume, and needs to quickly identify the target location based on IR emission characteristics.

Ideally, the required performance, contamination and radiation analysis could be carried out through experiments involving full-scale SRM exhaust flows in low density test chambers. Due however to the extensive time, cost, and general impracticality of this approach, numerical simulations are a far more popular means of determining plume properties of interest, and historically much of the effort involved in SRM plume analysis has been devoted to the development and application of detailed numerical models.

1.2 The physics of high altitude SRM exhaust flows

While the computational analysis of high altitude solid rocket plume flows presents several major advantages over experimental measurement, significant disadvantages do exist in the numerical approach. A number of complex or poorly understood physical phenomena within the combustion chamber, nozzle and plume can make accurate simulation extremely difficult or expensive. Several potentially important physical processes have generally been overlooked in the interest of reducing computational expense or code complexity, and the coupling between some flowfield characteristics has been neglected in even the most ambitious numerical studies. A number of processes involving the alumina particles are particularly challenging to include in simulations, but

may need to be modeled for accurate determination of various flowfield and radiation properties. To provide a general sense of the physical phenomena related to alumina particle formation, size distribution, phase composition, and interaction with the surrounding gas, a brief outline of relevant processes in SRM exhaust flows is presented here.

1.2.1 Particle formation inside the motor

During the burning process in an SRM, aluminum particles embedded within the propellant grain are continually exposed to the advancing surface on which most of the combustion takes place. These exposed particles tend to rapidly melt and coalesce into larger agglomerates, with a diameter typically on the order of 100 μm, which immediately begin a process of surface oxidation. Some of the aluminum content on the agglomerate surface may vaporize and react with oxygen in the surrounding gas to form a detached flame front, while heterogeneous combustion on the particle surface creates a liquid Al_2O_3 shell.

As the particle is accelerated into the intensely turbulent stream of hot exhaust gases flowing toward the nozzle entrance, surface pressure and shear stresses tend to break off portions of the material into smaller droplets, exposing additional unburned aluminum and further promoting the oxidation process. A large number of micron-size liquid droplets, termed “smoke” particles, may be sheared off the agglomerate surface during this stage. At the nozzle entrance, the particle phase is typically made up of a bimodal distribution of agglomerate and smoke particles, both in liquid form. [*Simmons* (2000), *Geisler* (2002)]

Within the subsonic convergent nozzle region, the particle size distribution is further modified due to breakup and agglomeration processes. As the gas rapidly expands and accelerates in a transition from thermal to bulk kinetic energy, the agglomerate particles develop large velocity lags relative to the surrounding gas. This increases the surface forces on a particle, and further promotes breakup.

Due to the size dependence in the ratio of surface forces to particle mass, the velocity lag on a particle is a strong function of its size. Within the convergent nozzle region, the smallest particles tend to move along gas streamlines at roughly the local gas bulk velocity. Larger particles are more gradually accelerated, and may move along trajectories which diverge significantly from the gas streamlines. The difference in speed and direction between particles of different sizes tends to promote collisions between these particles. Some fraction of the collisions result in agglomeration, and the newly created agglomerate particles then rotate according to the dynamics of off-center coalescing collisions. This rotation in turn may trigger an additional breakup mode, where the agglomerate breaks into smaller droplets because centrifugal forces outweigh the restoring influence of surface tension. Ultimately, the combination of breakup and agglomeration processes tends to produce a polydisperse particle size distribution within the nozzle, with particles ranging in diameter from about 0.1 to 10 μm.

1.2.2 Particle phase change

As the gas and particles are accelerated through the nozzle throat, the gas temperature quickly drops to well below the melting temperature of the particle material (about 2325 K) and particle phase change processes may begin. As with velocity lags, temperature

lags depend strongly on particle size due to the size dependence in the ratio of surface heat transfer to heat capacity. While larger particles tend to retain a relatively constant temperature (to within a few hundred K) during their course through the nozzle, smaller sub-micron scale particles experience rapid temperature changes as a result of convective heat transfer with the cooler surrounding gas. As a result, the smallest particles are the first to experience phase change within the nozzle.

While the mechanics of alumina particle crystallization are extremely complicated and not fully understood, the general processes may be summarized as follows: First, when a liquid droplet has supercooled to some temperature well below its melting temperature, homogeneous nucleation occurs at locations at or near the surface. (Due to convective cooling, the surface temperature is slightly lower than the temperature at points closer to the particle center.) Heterogeneous crystallization fronts then quickly progress from these nucleation points to cover the surface of the particle, after which a single unified crystallization front moves inward from the fully solidified surface. Heat released during the phase change process tends to increase the particle temperature, which in turn reduces the speed of the crystallization front and slows the overall rate of phase change.

The polycrystalline lattice structure behind the front may be that of several different metastable solid phases, collectively termed the γ phase. A further process of phase transition immediately begins in the region behind the front, where γ phase structures are converted to a stable α phase and some additional heat is released. [*Rodionov et al.* (1998)] As this secondary phase change process is suppressed when particles are cooled at a sufficiently fast rate, the smallest particles – those experiencing the most rapid

cooling – may retain a large γ phase mass fraction throughout the divergent nozzle region and plume.

For larger particles, the crystallization process may begin well downstream of the nozzle exit, and will continue at a significantly slower rate. This slower rate results from the fact that convective heat transfer is reduced as the gas density decreases with downstream distance, so the heat released during the phase change process is opposed by a smaller heat transfer to the gas than occurs further upstream. Thus, during crystallization the temperature of these larger particles increases to just below the melting temperature. At this increased temperature the velocity of the crystallization front approaches zero, and the heat release associated with phase change balances the heat lost to convective and radiative cooling. As a result, the particle temperature may for some time remain nearly constant. [*Plastinin et al.* (1998)] Another phenomenon observed in the larger particles (greater than 2 μm in diameter) is the creation of gas bubbles thought to contain water vapor which is exposed during the crystallization process. Scanning electron microscope (SEM) images of alumina particles collected from an SRM exhaust flow have been found to include hollow shells, and the measured material density for these particles was well below that expected for solid alumina. [*Gosse et al.* (2003)]

One important characteristic of SRM exhaust flows is the strong dependence of the particle size distribution on nozzle size. For a given set of chamber and atmospheric conditions, a larger nozzle results in a more gradual acceleration of the gas. With a greater residence time in the nozzle, large agglomerate particles may develop significantly lower velocity lags, which inhibits breakup due to surface forces and skews the particle size distribution at the nozzle exit in favor of larger particles. Agglomeration

processes within the nozzle are also affected, as particles are more likely to experience coalescing collisions when the nozzle residence time increases. As with velocity lags, particle temperature lags are also lower in a larger nozzle. This tends to delay the onset of crystallization, and results in a greater mass fraction of the stable α phase further downstream in the plume.

1.2.3 Gas properties in the plume

Due to the large mass fraction of alumina particles through much of the flowfield, bulk properties of the exhaust gas may be significantly influenced by the presence of these particles. Velocity lags, particularly among the larger particles, can result in two phase flow losses, where momentum transfer between the particles and gas pushes the sonic line at the throat somewhat further downstream and reduces the gas velocity through much of the nozzle and plume. At the same time, interphase energy transfer may account for an increase in gas temperatures. Heat addition to the particles through heterogeneous combustion and crystallization results in an increase in temperature lags between particles and the surrounding gas, while energy exchange during interphase collisions can reduce temperature lags through an increase in gas temperatures. The effect of the particles on the gas depends on the local particle mass fraction, which in turn is a strong function of both location in the flowfield and aluminum content in the propellant grain.

A typical SRM exhaust flow at high altitudes (above 100 km) is highly underexpanded, so that the gas experiences a rapid pressure drop just downstream of the nozzle exit. While a diffuse shock may form within the plume-atmosphere interaction

region far from the plume centerline, the repeating pattern of barrel shocks, shock reflections and Mach discs found in lower altitude exhaust flows is typically absent. [*Simmons* (2000)] Streamlines may curve by over 90° around the nozzle lip, so that a backflow region forms upstream of the nozzle exit plane. In the rapid expansion occurring within this region, the gas velocity distribution begins to diverge significantly from the Maxwellian distribution expected at equilibrium, and thermal energy is increasingly distributed nonuniformly among the various translational and internal degrees of freedom. Along streamlines far from the central axis in a single-nozzle axisymmetric exhaust flow, the gas may experience considerable thermal nonequilibrium within a short distance of the nozzle exit. Rotational freezing can occur as a result of the low collision frequency in this region, and flow characteristics may approach the free molecular limit where quantities such as the scalar pressure lose their physical significance. Similar features may be found further downstream near the plume centerline.

1.2.4 The farfield plume region

In the rapid expansion process around the nozzle exit, both velocity and temperature lags for the alumina particles may jump significantly, and the rate of change in particle temperatures may fall due to the reduction in heat transfer rates associated with a drop-off in gas density beyond the nozzle exit. As within the nozzle, velocity and temperature lags are strong functions of particle size, so that smaller particles will be more rapidly accelerated in both radial and axial directions following the local gas bulk velocity. As a result, the smallest particles will experience the largest curvature in trajectories within the

nearfield plume region around the nozzle lip, and far downstream in the plume these particles will have a greater maximum divergence angle than particles of larger size.

As the gas density continues to decrease with downstream distance, heat and momentum transfer between particles and the surrounding gas becomes negligible. Particles far downstream of the nozzle tend to move along straight trajectories at constant velocity, and the particle energy balance within these farfield plume regions is dominated by radiative heat transfer. Depending on the motor size and grain composition, these regions will likely have some intermediate optical thickness, so that long-range radiative energy exchange may significantly influence particle temperatures.

1.3 A short history of high altitude SRM exhaust flow modeling efforts

Published numerical and analytical studies of solid rocket exhaust flows may be divided into two broad categories: those that focus on flow properties within the motor, and those that primarily consider properties of the plume. To accurately simulate an SRM plume flow, some detailed knowledge of gas and particle phase characteristics within the nozzle is generally required. Studies in the second category therefore tend to rely on results from those in the first. A brief historical outline for both types is presented here, with an emphasis on numerical investigations of SRM exhaust flows under the typical conditions, as described above, encountered in space or at very high altitudes. Note that this description is not intended as a comprehensive review, but as a general overview of historical modeling efforts with brief summaries of illustrative work over the past several decades.

To clarify the following discussion of various simulation methods for SRM exhaust flows, brief lists of methods appropriate for nozzle and plume flow simulation are provided in Tables (1.1) and (1.2). References for a number of nozzle simulation approaches are shown in Table (1.1), along with a short description of some advantages and disadvantes for each approach. Table (1.2) contains similar information for the simulation of high altitude SRM plume flows.

Method	Examples	Advantages	Disadvantages
Quasi-1D	*Bailey et al*. (1961), *Hunter et al.* (1981)	▪ Very inexpensive ▪ May easily add physics models, 2-way coupling	▪ Inaccurate particle radial distribution ▪ No boundary layers, wall interaction
Method of characteristics	*Kliegel and Nickerson* (1961)	▪ Inexpensive ▪ Accounts for 2D gas effects	▪ Limited to divergent nozzle region ▪ Assumes inviscid gas
2 phase CFD: Eulerian tracking	*Chang* (1980)	▪ Low memory requirements ▪ Simple 2-way coupling	▪ Numerical diffusion ▪ Poorly suited for range of particle sizes
2 phase CFD: Lagrangian tracking	*Hwang and Chang* (1988), *Najjar et al*. (2003)	▪ No unphysical particle diffusion ▪ Allows direct particle physics models	▪ High memory requirements ▪ Expensive ▪ Potential for scatter

Table 1.1. Approaches for SRM nozzle simulation.

Method	Examples	Advantages	Disadvantages
Method of characteristics	*Clark et al.* (1981), *Rattenni* (2000)	▪ Inexpensive ▪ May apply to large expansion angles	▪ Assumes inviscid gas ▪ Neglects rarefaction effects
Navier Stokes	*Candler et al.* (1992), *Vitkin et al.* (1997)	▪ Robust, efficient ▪ May easily integrate with nozzle flow simulation	▪ Requires empirical correlations for gas-particle interaction ▪ Valid only for low Kn
DSMC	*Hueser et al.* (1984)	▪ Accurate at high Kn ▪ Unconditionally stable ▪ Allows direct molecular-level physics models	▪ Very expensive ▪ Large memory requirements

Table 1.2. Approaches for high altitude SRM plume simulation.

1.3.1 Nozzle flow simulations

Much of the early numerical work on SRM exhaust flows focused on gas and particle properties in the nozzle, with an emphasis on nozzle design, efficiency and thrust prediction. Some of these early studies are described in a review paper of *Hoglund* (1962), which discusses computational and analytical treatments of two phase nozzle flows within a few distinct categories.

The first of these categories is the quasi-one dimensional flow, where nozzle dimensions are used to prescribe gas properties at a number of points along the length of the nozzle, and the flow is generally assumed isentropic and chemically frozen. Particle drag and heat transfer correlations are employed to plot the variation of velocity and temperature through the nozzle for a given particle size. The resulting particle velocity and temperature lags may then be used to roughly determine overall efficiency and performance characteristics, and particle loss terms can be brought into the governing equations for the gas to account for two phase flow losses. In one of the most ambitious

of these early studies, *Bailey et al*. (1961) compute the quasi-one dimensional nozzle flow solution for a reacting gas, and use a post-processing approach to determine the two dimensional trajectories and temperatures for particles of various sizes through the nozzle.

In a more complicated treatment, the method of characteristics (MOC) is employed to model a supersonic inviscid gas flow through the divergent portion of the nozzle, and representative particles are tracked through the resulting flowfield using a Lagrangian scheme. This allows the inherently two dimensional nature of the gas flowfield solution to influence particle properties, and provides a somewhat more realistic approximation of the nozzle flow problem. *Kliegel and Nickerson* (1961) apply this technique with a modification for two-way coupling, where bulk gas properties downstream of the nozzle throat are affected by the presence of the particle phase.

With advances in both computer power and numerical schemes, later efforts at SRM nozzle simulation have involved progressively greater complexity and physical modeling capabilities. Around two decades after the first quasi-one dimensional studies appear in the literature, *Chang* (1980) presents results from a series of geometrically complex two phase flows through the transonic portion of the nozzle. A finite difference Eulerian formulation is used to compute properties for both the gas and particles, and source terms in the governing equations for each phase allow for potentially strong two way interphase coupling of momentum and energy. While the gas is assumed chemically frozen and inviscid (with the exception of viscous characteristics in gas-particle interaction) the model does incorporate effects such as particle radiative heat loss and variable particle velocity and temperature lags through regions of subsonic as well as supersonic flow.

Hunter et al. (1981) describe a one-dimensional nozzle flow simulation procedure which includes a large number of additional effects, such as evaporation, sublimation, nonequilibrium phase change, and radiative heat transfer. The gas is modeled as an inviscid mixture of a number of different species, and an Eulerian approach is used to calculate the variation in particle properties with downstream distance. A Weber number criterion is employed for the determination of droplet breakup.

A paper of *Hwang and Chang* (1988) written several years later incorporates a more computationally efficient Lagrangian tracking scheme for particles of several different sizes, and uses a simple eddy viscosity model to account for turbulent diffusion effects. As in previous studies, source terms in the gas equations allow for two-way coupling between the particles and gas. The "diffusive" component of particle velocity – that due to turbulence in the gas – is shown to be several orders of magnitude lower than the convective velocity component associated with bulk gas motion, and the presence of particles is found to significantly increase gas temperatures through the divergent portion of the nozzle.

One of the most ambitious recent efforts in simulating the flow within an SRM is that of *Najjar et al*. (2003). In a large project involving a number of researchers, detailed multiphase three dimensional computational fluid dynamics (CFD) codes have been developed for application to the flow of gas and condensed phase particles through the propellant grain and nozzle. The gas is modeled using the compressible unsteady Navier Stokes (NS) equations, and large eddy simulation (LES) techniques are employed to account for the influence of large scale turbulent structures. Agglomerate particles are treated using a Lagrangian tracking scheme, and models are provided for a number of

physical processes including droplet evaporation and breakup, crystallization, and surface oxidation. Smaller smoke particles are included through a simplified Eulerian approach, where the mean temperature and velocity of these particles are approximated as small perturbations from the temperature and velocity of the surrounding gas.

A number of theoretical and numerical studies have focused on the size distribution and acoustic damping properties of alumina particles within the combustion chamber and nozzle. In one early study, *Fein* (1966) uses a simplified theory for particle growth in the chamber to derive a series of expressions for the particle size distribution, and shows that this distribution should be relatively independent of motor size if breakup and agglomeration processes in the nozzle are neglected. *Jenkins and Hoglund* (1969) provide a more detailed treatment of processes which influence the particle size distribution through the combustion chamber and nozzle. Models are included for particle growth due to the condensation of gaseous aluminum in the chamber, as well as coalescing collisions associated with either acoustic waves or the variation in velocity lag between particles of different sizes.

Several theoretical models for the determination of particle size in the chamber and nozzle are reviewed by *Hermsen* (1981) and are found to generally exhibit poor agreement with each other and with available experimental data. In a more recent theoretical study, *Kovalev* (2002) derives an expression for the limiting agglomerate diameter at the nozzle throat, based on simplified models for particle formation at the grain surface and breakup due to gas-dynamic forces. Another recent study by Dupays (2002) considers the tendency of alumina particles to dampen combustion instabilities within the chamber. Detailed reactive two phase CFD simulations are run for internal

SRM exhaust flows, and a correlation is found between aluminum combustion and unsteady flow properties in the gas.

1.3.2 Continuum approaches for simulating high altitude plume flows

While a number of computational studies have focused on the characteristics of low altitude plume flows from solid propellant rockets (see, for example, *Dash et al.* (1985)) the two phase simulation of high altitude SRM plumes has a comparatively recent and sparse history. In what may be one of the first such numerical studies, *Clark, Fisher and French* (1981) consider the distribution of alumina particles in the plume back-flow region for an SRM exhausting into a vacuum. An uncoupled method of characteristics (MOC) approach is used to determine gas properties in the plume, and corrections are made for boundary layer growth along the inner wall of the nozzle. Representative particles are then tracked through the plume using a predictor-corrector technique. Forces on these particles are determined through a rough empirical correlation for the particle drag coefficient.

A similar simulation procedure has been used more recently by *Rattenni* (2000) to calculate convective and radiative surface heat transfer rates from a spacecraft-mounted SRM used for orbit insertion. A quasi-one dimensional method is employed to determine gas properties and species concentrations within the nozzle, with an equilibrium chemistry model in the convergent nozzle region and a model for turbulent boundary layer growth along the nozzle wall. A MOC technique is used to model both the gas and particles within the plume, where the particle phase consists of five discrete sizes and some modeling capabilities are included for droplet crystallization. Particle radiative heat

transfer is then computed through a post-processing approach, following assumptions that gas phase IR emission is negligible and the plume is optically thin.

In the early 1990s a series of two phase CFD calculations were performed to simulate the SRM plume flow from a high altitude flight experiment [*Erdman et al.* (1992)] involving UV radiation measurements from a set of onboard sensors. *Candler et al.* (1992) present results from axisymmetric simulations at altitudes between about 105 and 120 km, where gas properties are computed using the steady state compressible NS equations and an Eulerian approach is used for particle phase calculations. Spectral radiance is measured through a line-of-sight procedure which assumes that the gas is transparent and the particle phase is optically thin. There is reasonable agreement in the shape of the UV radiance profile between the calculations and experimental data, although particle phase enthalpies at the nozzle exit must be modified by a nonphysical scaling factor for quantitative agreement.

As discussed by these authors, the NS equations are likely invalid under the highly rarefied conditions expected through much of the flowfield, so a continuum-based CFD approach can at best give only rough approximations of flowfield properties through the plume. Slightly better agreement with experimental radiance values is found through a similar set of two phase CFD simulations by *Anfimov et al.* (1993) where particle emissive properties are determined by a complicated system of absorption index correlations for four different mechanisms of intrinsic radiation from liquid or solid phase alumina.

In a comprehensive numerical study on plume radiation by *Vitkin et al.* (1997) a simulation is performed for a two phase axisymmetric SRM plume expanding into a

vacuum. An Eulerian description is used for the alumina particles, and the governing equations are adjusted to flow-aligned coordinates to more accurately characterize the large curvature of streamlines around the nozzle lip. While no experimental data is used for comparison, a detailed evaluation is made on the relative influence of gas thermal, chemiluminescent, and particle radiation mechanisms on the total plume radiation intensity. Continuum particle radiation is found to dominate over nearly all of the visible through IR wavelengths considered, while a CO_2 vibrational band creates a sharp spike within the IR range.

1.3.3 The direct simulation Monte Carlo method

Some generalized NS-based CFD codes have more recently been applied to two phase highly underexpanded SRM plume flows, including plumes expanding into a vacuum. (See for example *York et al*. (2001).) While a number of physical models are included and the codes may include impressive capabilities for the simulation of geometrical complex unsteady flows, the governing NS equations may break down under conditions expected through much of the flowfield at very high altitudes. This creates uncertainty in the overall accuracy of the results, and leads to interest in alternate simulation methods which remain valid for more rarefied flow regimes.

One such method is the direct simulation Monte Carlo (DSMC) method of *Bird* (1994), which has over several decades gained acceptance as an accurate, robust and broadly applicable technique for modeling gas flows under nonequilibrium conditions. DSMC falls into the more general category of Monte Carlo methods, which involve the use of quasi-random number generators to find approximate solutions to mathematical

problems. While these methods tend to suffer from effects of statistical scatter and can require long run times depending on the desired level of precision in output values, they may offer significant advantages over deterministic methods (efficiency, stability, ease of implementation) particularly when the problem is geometrically complex or involves a large number of degrees of freedom.

The DSMC method approximates a numerical solution to the Boltzmann equation – the governing equation for dilute gas flows based on a statistical representation of molecular velocities – by decoupling in time the advection and collision terms in the equation. These terms are shown on the left and right sides, respectively, of Eq. (1.1).

$$\frac{\partial}{\partial t}\left(n_g f\right) + u_i \frac{\partial}{\partial x_i}\left(n_g f\right) + \frac{\partial}{\partial u_i}\left(F_i n_g f\right) = G(f) \tag{1.1}$$

Here f is the gas velocity distribution function; u_i is a point in velocity space (given in index notation); x_i is a point in physical space; F_i is the net body force per unit mass, n_g is the local number density; and $G(f)$ is a nonlinear integral term which accounts for the production and removal of gas particles at each point in velocity space through collisions. A derivation of Eq. (1.1) and a detailed evaluation of the collision term are given by *Vincenti and Kruger* (1986).

In DSMC a large number of particles, each representing a large number of atoms or molecules, are tracked through a computational grid, and are sorted into cells according to their location. (Note that the term "particle" is used here by convention, and does not refer to condensed phase particles as described above.) During each time step, some fraction of the particles in a cell collide with each other, and probabilistic techniques are used for calculations of individual collisions. All particles are then moved through the grid according to assigned velocities, and particles are created or removed at inflow and

outflow boundaries. Finally, macroscopic quantities are sampled by averaging various particle properties in each cell, and the process is then repeated at the next time step.

As no assumptions are made about the shape of the gas velocity distribution, the DSMC method retains validity for all flow regimes between free molecular and continuum, so long as binary collisions are the dominant type of molecular interaction. The equilibrating effect of these collisions may be characterized by the Knudsen number (Kn), which is defined as the ratio of the gas mean free path to a macroscopic length scale based on boundary dimensions, flow structures or gradients in bulk gas properties. While some CFD methods can give accurate solutions up to Knudsen numbers around 0.1, higher Knudsen number flows (in the transitional through free molecular regimes) typically require alternate methods based on approximate solutions to the Boltzmann equation. DSMC is the most mature of these alternate methods, and has the most extensive history of application to engineering problems.

Although several studies in the literature involve the DSMC simulation of freely expanding or highly rarefied plumes (see for example *Boyd et al.* (1992) and *Nyakutake and Yamamoto* (2003)) few published DSMC simulation results exist for high altitude SRM plume flows. Among these SRM plume flow studies is a paper of *Hueser et al.* (1984). Here a MOC/DSMC hybrid approach is used to model axisymmetric SRM plumes expanding into a vacuum or near-vacuum, and the influence of alumina particles is neglected. A continuum breakdown parameter based on gas density gradients is used to prescribe a handoff surface between MOC and DSMC simulation domains, where DSMC is used only in regions of significant nonequilibrium. An iterative procedure is employed so that a DSMC solution for the flow around the nozzle lip provides information for

MOC calculations in the near-equilibrium region downstream of the nozzle exit. While these simulations likely provide very accurate results for gas density and species concentrations far from the plume centerline, other flow properties which may be of interest – particularly plume radiation characteristics – cannot be accurately determined without inclusion of the particle phase.

The scarcity of published SRM flow results is likely due to some combination of three factors: First, DSMC is in general far more computationally expensive than continuum CFD methods for the simulation of a given flow. As a result, DSMC has only recently gained widespread acceptance as a solution method for large scale flow problems, following increases in processor speed and dramatic reductions in the price of memory. Second, a large fraction of applications requiring SRM plume simulations are related to missile defense or other military technology development programs, so many simulation efforts have not been published in the open literature. Lastly, at the inception of the research project described in this thesis, no DSMC codes included general capabilities for modeling a condensed particle phase in a manner appropriate for SRM plume simulations. As alumina particles may contribute significantly to a number of plume flow properties, the accurate simulation of these flows generally requires consideration of particle-gas interactions.

1.4 Outline of the thesis

The work described in this thesis has been performed with the goal of extending the applicability of DSMC as a tool for simulating high altitude SRM exhaust flows. A series of physical models and numerical methods are developed to improve the accuracy and

efficiency of SRM plume simulations, and the influence of various physical phenomena on flowfield and radiation properties is gauged for a representative flow. Particular emphasis is placed on modeling particle-gas interactions, particle radiation, and gas characteristics in flows where the local Knudsen number will vary by several orders of magnitude between different flowfield regions.

In Chapter 2, a series of numerical procedures is presented for the inclusion of small solid particles in the DSMC simulation of a nonequilibrium gas flow. As a test case, these procedures are applied to a particle beam flow through a convergent nozzle into a vacuum. Simulation results are compared with experimental data through an analysis of the relation between the source pressure and the shape of the particle beam. Following an assumption of locally free molecular flow, equations for momentum and energy transfer between a particle and the surrounding gas are generalized to include conditions where the particle has a nonspherical shape, or where the particle is rotating. A formula for the moment on a rotating particle is derived as well, and closed form solutions are presented for the heat transfer and moment on a rotating particle under near-equilibrium conditions.

Chapter 3 covers the extension of the two phase DSMC procedures to flows for which interphase momentum and energy exchange may significantly influence properties of the gas. A two-way coupling model is developed so that gas molecule velocities and internal energies may be influenced by the presence of the particle phase, and a simple test case is used to show that the two-way coupling method allows for momentum and energy conservation in a time-averaged sense. Calculation procedures are then extended to cover two-way coupled flows involving rotating particles.

In Chapter 4, additional models are presented for physical processes which are potentially important in the SRM plume flows of interest. First, a series of nondimensional parameters is derived to evaluate the influence of interphase momentum and energy coupling on properties of both the particles and gas. These parameters are used to automatically disable certain calculation procedures during a two phase DSMC simulation. A representative plume flow simulation is employed to determine appropriate parameter cutoff values, and to demonstrate the potential reduction in simulation time associated with the selective disabling of coupling calculations. A model is also introduced for nonequilibrium crystallization of liquid Al_2O_3 droplets. Emphasis is placed on the heat release associated with crystallization, which may have a significant effect on particle and gas temperatures throughout the plume.

In Chapter 5, a modification to DSMC gas collision procedures is presented for efficiently simulating regions of near-equilibrium flow. The model described here is based on the ellipsoidal statistical Bhatnagar-Gross-Krook (ES-BGK) equation of *Holway* (1966), which is a simplified approximation of the Boltzmann equation, and which is most appropriate for Knudsen number regimes between those for which DSMC and continuum NS methods are generally applied. Due to the large gas densities in the nearfield plume region just downstream of the nozzle exit, the DSMC method becomes extremely expensive in this region. A relatively simple hybrid scheme is therefore proposed to increase overall simulation efficiency. In this scheme, calculations based on the ES-BGK equation replace DSMC collision procedures in high density near-equilibrium regions, and standard DSMC techniques are used through the rest of the simulation domain.

With the ES-BGK equation as a starting point, a particle method is developed to include effects of rotational nonequilibrium, and to enforce exact conservation of momentum and energy. A homogeneous rotational relaxation problem is employed to demonstrate that the proposed scheme is consistent with both DSMC and theoretical results for the rate of relaxation toward equilibrium. The method is then applied to the simulation of a rarefied nozzle expansion flow involving a diatomic gas, and relatively good agreement is found with DSMC results and experimental measurements.

A detailed model for particle radiation is presented in Chapter 6. Procedures are described for incorporating a Monte Carlo ray trace (MCRT) radiation model into a two phase DSMC code, to generate information on plume emission signatures and to account for the potentially strong coupling between flowfield properties and particle radiation characteristics. The model allows for spectrally resolved radiative transport calculations in an emitting, absorbing and scattering medium of arbitrary optical thickness, and is built on a series of correlations and approximations which are particularly appropriate for consideration of Al_2O_3 particles. Modifications to the model are described so that soot particles may be included in the simulation, and procedures are discussed for the inclusion of continuum emission from within the nozzle.

In Chapter 7, numerical procedures and models described in Chapters 2 through 6 are used to simulate the flow around a single-nozzle solid propellant rocket at very high altitude (114 km). A number of flowfield properties are presented, and plume spectral radiance values are calculated for comparison with previous numerical results and measured data from a flight experiment. Results are generally encouraging, and show that the proposed calculation procedures allow for a relatively high degree of overall

accuracy. As the level of accuracy is subject to a range of simplifying approximations and assumptions, a series of parametric studies is performed to determine the effects of various models and input values on flowfield and radiation properties of interest.

Three categories of model parameters are independently considered. For the first category, results are compared among simulations for which interphase momentum and energy transfer procedures are modified. The second category involves particle radiation modeling. Here elements of coupling between the radiative transfer calculations and the flowfield simulation are disabled, and input parameters are altered for various particle radiation properties. Finally, the potential influence of soot particles on plume radiation is considered. Results from these parametric studies demonstrate the complex interaction between several different effects, and should help to clarify the influence of a number of physical phenomena on flowfield and radiation characteristics.

Chapter 8 contains concluding remarks, including a summary of current progress in the simulation of rarefied SRM plume flows. Modeling difficulties are discussed, and several areas of future work are proposed.

Chapter II

The Simulation of Small Particles in a Rarefied Gas

2.1 The two phase DSMC approach

The Direct Simulation Monte Carlo (DSMC) method has in recent years become a standard tool for analyzing rarefied gas flows, and allows relatively efficient modeling of flows for which continuum CFD techniques are generally invalid. One such flow is the free expansion of a gas into a near-vacuum, as occurs in high-altitude rocket exhaust plumes. The DSMC method is therefore an ideal foundation for the simulation of the two phase plume flows of interest. In a recent paper by *Gallis et al.* (2001), equations are derived for the average force and heat transfer rates to a small spherical solid particle moving through a gas with a delta-function incident velocity distribution. These equations can be used as the basis for the inclusion of solid particles in a DSMC code, and therefore as a starting point for a general method of simulating two phase rarefied flows.

Through the use of these equations, the DSMC code MONACO [*Dietrich and Boyd* (1996)] has been modified to allow for the creation, tracking, and cell-averaged property calculations of a solid particle phase within a two dimensional planar or axisymmetric gas flow simulation. The particles are assumed to be chemically inert, spherical, and

small enough so that each particle is only influenced by gas molecules located in the same grid cell as the particle center. (For simplicity, the term "molecule" is used here to signify molecules in a diatomic or polyatomic gas as well as individual atoms for a monatomic gas species.) In addition, heat is assumed to travel far more efficiently within the particle than between the particle and gas (i.e. the thermal conductivity of the particle material is assumed to be much higher than the product of the particle diameter and the gas convective heat transfer coefficient) so that a low Biot number approximation [*Incropera and DeWitt* (1996)] is used and the temperature is assumed to be spatially uniform within each particle. Particle-particle collisions and interphase mass transfer are not considered, and an initial assumption is made of one-way coupled flow: The gas phase momentum and energy flux are assumed to be much greater than the momentum and energy transfer rates respectively from the particles to the gas, so that the two latter processes can be neglected.

A Lagrangian particle representation is used, where each computational particle tracked through the grid represents a large number of solid particles in the actual flow being modeled. Standard DSMC techniques are employed for tracking particle center locations through an arbitrary unstructured grid, and particle movement – as with gas molecule movement – is decoupled from the momentum and energy transfer to the particles during each time step. As is the case in SRM plume flows and nearly all two phase flows involving condensed phase particles within a carrier gas, the particle mass is assumed to be much greater than the mass of the gas molecules, so that Brownian motion of the particles can be ignored without much loss of accuracy.

As described by *Gallis et al.* (2001), the average rates of momentum and energy transfer to a solid particle from a computational gas molecule within the same grid cell can be calculated by considering the computational gas molecule as a large spatially homogeneous collection of individual gas molecules, which move through the cell at a uniform incident velocity. A fraction of these molecules will collide with the particle during a given time step, and those that do collide will be deflected off the particle surface in one of three ways: either by specular reflection, by isothermal diffuse reflection with full accommodation to the particle temperature, or by adiabatic diffuse reflection where the molecule speed relative to the particle is unchanged in the collision. Previous analysis of experimental data (see for example *Epstein* (1924)) has shown that gas-solid interactions in rarefied flow can generally be modeled with a high degree of accuracy as involving only the first two types of reflection, and most DSMC simulations in the literature involving gas-solid interactions have included only specular and isothermal diffuse reflection. Adiabatic diffuse reflection is therefore not considered in the current implementation of the method. While these equations are intended for use in a DSMC simulation involving a monatomic gas, modifications have been made for consideration of diatomic gases by assuming that in a gas-solid collision involving isothermal diffuse reflection, the translational, rotational and vibrational energy modes of the gas molecule are all fully accommodated to the particle temperature.

Given the above assumptions, the heat transfer rate to a solid particle from a DSMC gas molecule within the same grid cell is calculated using the following expression:

$$\dot{Q}_p = \frac{\pi R_p^2 \tau \, W_g c_r}{V_c}\left(\frac{1}{2}mc_r^2 + e_{int} - (2+\sigma)\ k_B T_p - \frac{k_B \theta_v \sigma}{\exp(\ \theta_v/T_p) - 1}\right) \tag{2.1}$$

Here R_p is the radius of the solid particle, V_c is the cell volume, τ is the thermal accommodation coefficient for the particle, W_g is the gas molecule relative weight (the number of real molecules represented by each computational gas molecule), c_r is the relative speed of the computational molecule with respect to the particle, m is the mass of an individual gas molecule, and e_{int} is the total internal energy (including rotational and vibrational modes) of the computational molecule. Additionally, k_B is Boltzmann's constant, T_p is the particle temperature, θ_v is the characteristic temperature of vibration for the gas species, and σ is a dimensionless parameter set to equal one for a diatomic gas or zero for a monatomic gas. Under the assumption that the vast majority of the energy lost by a gas molecule during the collision process is transferred to the particle as thermal energy, Eq. (2.1) can be used to compute the rate of heat transfer to the particle. The corresponding force on the particle can be given as

$$\mathbf{F}_p = \frac{\pi R_p^2 \, W_g}{V_c}\left(m c_r + \frac{\tau}{3}\sqrt{2\pi \, m \, k_B T_p} \right) \mathbf{u}_r \tag{2.2}$$

where $\mathbf{u}_r$ is the relative velocity of the gas molecule with respect to the particle.

Note that the thermal accommodation coefficient τ is equal to the fraction of interphase collisions which involve diffuse reflection, and that the remaining fraction (1-τ) of collisions involves specular reflection. Also note that no consideration is made for the effect of collisions between reflected molecules and incident molecules surrounding the particle, so that the gas is assumed to be locally free-molecular for the calculation of gas-particle interactions. As a result, this method neglects the potentially significant variation in the gas velocity distribution over the particle surface expected when the

particle Knudsen number – the ratio of the freestream mean free path to the particle diameter – is of order one or smaller.

As implemented in the code, the temperature and velocity of a particle are updated during each time step by summing over the force and heat transfer contributions of every computational gas molecule within the same grid cell, using Eqs. (2.1) and (2.2). The resulting change in particle temperature is then calculated as the total heat transfer rate multiplied by a factor $\Delta t/(m_p c_s)$, where Δt is the size of the time step, m_p is the particle mass, and c_s is the specific heat of the particle. Likewise, the change in particle velocity is equal to the total force multiplied by $\Delta t/m_p$. Particle positions are then varied during each time step by the vector product of Δt and the average of initial and final velocities.

2.2 Application to a free expansion flow

To evaluate the overall accuracy of the numerical procedures described above, and to ensure proper implementation in MONACO, a series of simulations are performed for comparison with the results of an experimental study by *Israel and Friedlander* (1967) which examines the aerodynamic focusing of aerosol beams through a vacuum. As described by the authors, a particle-air mixture is ejected through a convergent nozzle into a near-vacuum, with a small plate oriented normal to the nozzle axis placed some distance downstream. In the nearfield free expansion region just beyond the nozzle exit, the gas and particles interact in such a way that the particle trajectories, and therefore the size of the particle beam, will depend on the source pressure p_o of the gas. The solid angle δ of the beam is determined by measuring the area of the particle deposition on the plate.

2.2.1 Evaluation of the two phase simulation method

As discovered by *Israel and Friedlande*r, there is a particular source pressure, or range of pressures, for which the value of δ is minimized. This is explained by the following logic: As the gas freely expands in the region just beyond the nozzle exit, a force is exerted on the particles in the outward radial direction, following the streamlines of the gas. This outward force counters the initially inward-directed momentum of the particles as they tend, due to inertia, to follow straight trajectories after exiting through the convergent nozzle. At relatively high values of p_o, the influence of the gas outweighs the influence of particle inertia, so that the particles are redirected by the gas into outward radial trajectories, and the particle-gas interaction acts to increase the value of δ. Likewise, at very low source pressures, the gas exerts little influence on the particles in the near-field expansion region, and the particles tend to follow relatively straight trajectories that pass through the central axis, then continue in radially outward directions further downstream. Thus, at some intermediate p_o value, the countering influences of drag and particle inertia will cancel each other out. Particle trajectories will then be nearly parallel to the nozzle axis in the far-field plume region, and the size of the particle beam will be minimized.

Experiments were conducted by *Israel and Friedlander* over a wide range of source pressures, using three different sizes of spherical latex particles. As the largest particles were found to have Knudsen numbers too small for accurate modeling using the equations discussed above, and as particle depositions corresponding to the smallest particle size were found in the experiment to show a less conclusive trend, only the

medium-sized particles – of diameter 0.365 μm – are considered in the simulations used for comparison with experimental results. While these experiments only allow for direct validation of the Gallis momentum transfer formulation as implemented in the current code, the existence of a source pressure for which the beam size is minimized – as well as agreement in the value of this pressure – can provide convincing evidence of the overall accuracy and functionality of the code.

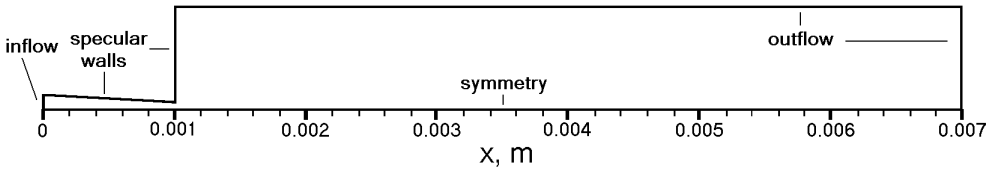

Figure 2.1. Grid geometry and boundary conditions.

Due to both the enormous computational expense of DSMC simulations involving regions of relatively high density gas, and the fact that the DSMC method often requires massive computation time to produce accurate flow rates in simulations involving very low Mach numbers, the grid domain in all simulations described here includes only the comparatively high Mach number ($M \geq 0.2$), low density section of the nozzle within 1 mm of the throat. Following the description of nozzle geometry in the experimental paper, the inflow boundary then corresponds to a local nozzle radius of 0.2352 mm, with a specularly reflecting wall converging at a constant angle of 3.25 degrees toward a throat of radius 0.0785 mm. Additional boundary conditions imposed in the simulations include a specularly reflecting wall along the plane of the nozzle exit, outflow boundaries parallel and normal to the central axis which runs through the nozzle, and a symmetry boundary along this axis. Grid dimensions and boundary types are shown in Fig. (2.1).

Although gas properties within the nozzle could, in theory, be more accurately modeled through the use of diffusely reflecting – rather than specular – wall boundaries, the resulting boundary layer along the nozzle wall would be very thin relative to the size of the grid. As large gas property gradients are expected within this boundary layer, accurate simulation would require a reduction in cell size along the nozzle wall, and the computational expense of each simulation would increase considerably. Moreover, it can be assumed that the existence of a thin boundary layer along the nozzle wall would have little if any influence on particle properties in the farfield plume region.

Not counting the region within the nozzle, the grid used in all simulations extends an axial distance of 6mm and a radial distance of 0.8 mm, comprising a total of about 31,600 cells. As described in the experimental paper, a skimmer is used to aid in evacuating the gas in the region just beyond the nozzle exit, while not interfering with particle trajectories in the beam. Because insufficient details are given of the skimmer geometry, it is neglected in the boundary conditions of the simulations described here. Moreover, the skimmer is used in the experiments only to better facilitate the desired far-field vacuum condition, so it should not in principle need to be considered in simulations where this condition can be prescribed through the use of DSMC outflow boundaries.

The gas here is a mixture of N_2 and O_2, with mass fractions of 0.79 and 0.21 respectively. For all cases considered, the source temperature is 298 K, and assumptions of one-dimensional isentropic flow within the nozzle give an inflow Mach number of 0.20, with a corresponding gas static temperature of 295.63 K and axial gas velocity of 69.176 m/s. Note that all of these values are independent of the source pressure. The inflow static pressure is determined using the isentropic relation between the inflow and

source temperatures and pressures. The gas number density along the inflow boundary is then calculated from the inflow temperature and pressure, using the ideal gas law.

For simplicity, and with likely little influence on the simulation results, the radial component of the inflow gas velocity is set to zero. Following an assumption that the particles experience very little temperature variation through the low Mach number section of the nozzle not included in the grid domain, the inflow particle temperature is set to equal the source temperature of 298 K. Further, the axial component of the inflow particle velocity is assumed to equal that of the gas, and the corresponding particle radial velocity is calculated so that, within the plane of symmetry defined by the grid, all particle velocity vectors along the inflow boundary are parallel to the wall.

This last approximation, while greatly oversimplifying the particle trajectories at the inflow boundary, can be assumed to allow for accurate representation of the particle properties within the plume. As evidence of the validity of this assumption, consider the following two cases: First, when the source pressure is relatively high, the particles tend to follow the gas streamlines throughout the nozzle, so that any significant difference between the local gas and particle radial velocity components at the inflow boundary will quickly disappear a short distance downstream. Second, if the source pressure is very low, then the particles will not follow the streamlines within the nozzle, and particles will tend to impact the walls and pass through the central axis in a manner that seems physically consistent with the inflow condition described here. For comparison, a few simulations are repeated using values of the particle inflow radial velocity component that scale with distance from the central axis, such that particle trajectories along the inflow boundary are parallel to the nozzle wall only at the point where the inflow and

wall boundaries meet. As described below, these simulations result in very small beam sizes for low source pressures, as the lack of particle-wall collisions allows for a very small "focal point" of the beam, some distance downstream of the nozzle, where the beam diameter approaches zero as the source pressure is reduced. While focal points were observed in the experiments involving the largest particle size (which is not considered here) the lack of particle-wall collisions, and the assumption that particles follow the gas streamlines even for very low source pressures, does not reflect the expected physical characteristics of the flow, and the results from these simulations can be considered less valid than those for which the inflow particle velocity is constant.

Axisymmetric simulations are performed over a range of source pressures p_o from 14.8 mmHg to 96 mmHg, each corresponding to a p_o value used in the experiment. The gas molecule relative weight W_g varies from 3×10^8 to 6×10^8 depending on the source pressure, so that approximately 200,000 computational gas molecules are simultaneously tracked through the grid. For all cases considered, the analogous relative weight W_p of the particle phase is set to equal one, and the inflow particle mass flux m_p is 0.12 kg/m^{2}s. This corresponds to a particle number density of about 6.1×10^{13} particles/m^3 along the inflow boundary, and a total of between 10,000 and 15,000 particles simultaneously within the grid domain. Following experimentally determined properties for latex or similar materials, all particles are given a specific heat of 2180 J/kg K, a material density of 1120 kg/m^3, and a thermal accommodation coefficient of 0.89.

Note that collisions between particles, as well as the effect of interphase collisions on the gas, are not considered, so that the magnitude of m_p will have no influence on any flow properties other than particle phase fluxes and bulk densities. Of the properties

which are affected, all trends (for example, the shape of iso-contour lines) will still be independent of the value of m_p. As no values for particle flux or flow rate are given by *Israel and Friedlander*, the value of 0.12 kg/m^{2}s used here is chosen only so that the number of particles tracked through the grid is large enough to allow for relatively low statistical scatter, but not so large that excessive computational expense is required for convergence to steady state.

Flow properties in each cell are averaged over approximately 300,000 time steps following convergence. Figure (2.2) is included here for clarification of basic flowfield characteristics, and shows the Mach number of the gas at an intermediate source pressure of 34.5 mmHg. For all simulations, the particle number flux along the planar outflow boundary is plotted in Fig. (2.3) as a function of distance r from the axis.

Ideally, the profiles shown in Fig. (2.3) would have relatively flat regions near the central axis, followed in each case by a sharp drop-off to zero at a radial value r_o that could be interpreted as the "edge" of the particle beam. The corresponding beam solid angle could then be calculated as $\delta = \pi r_o^2/L^2$ where L = 6 mm. Unfortunately, as displayed in the figure, the radial decay in the number flux is approximately exponential, particularly for the lower source pressures considered. While the edge of a particle beam could therefore be defined as the r value for which the number flux drops below some given value, the resulting δ values would then be highly dependent on both the cutoff value chosen and the assumption that, in all experiments for which the simulation results are to be compared, the particle deposition was collected over approximately the same time interval.

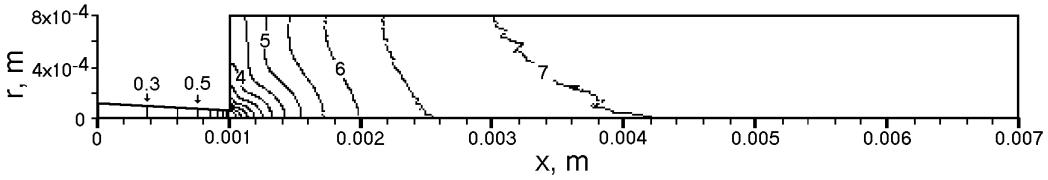

Figure 2.2. Contours of gas Mach number for a source pressure of 34.5 mmHg.

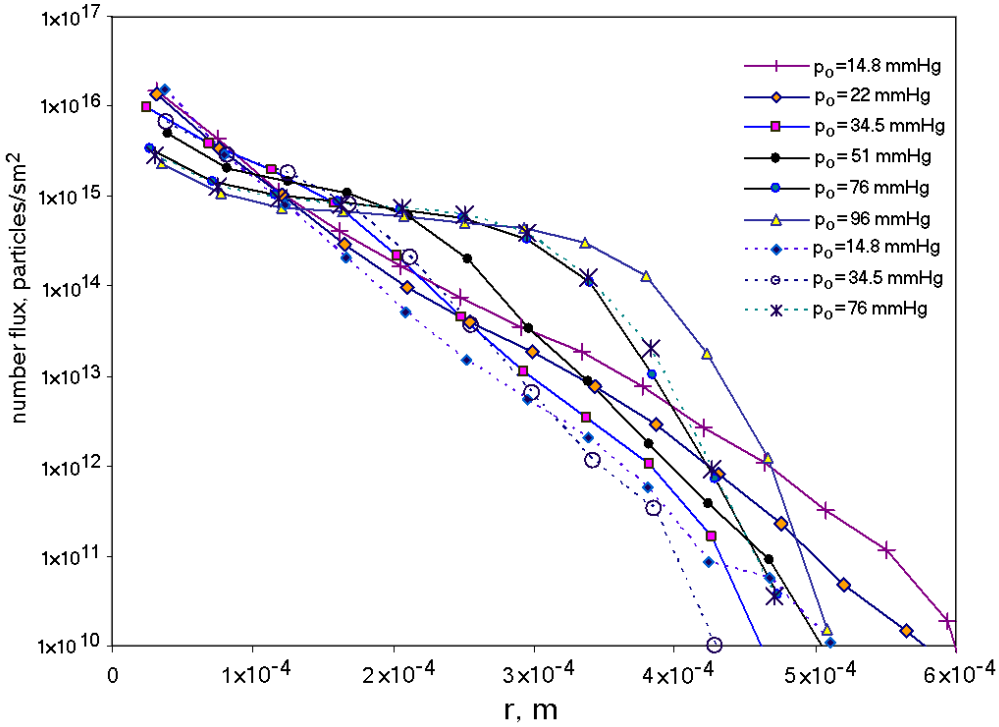

Figure 2.3. Particle number flux profiles along outflow boundary. Dotted lines correspond to simulations where inflow particle velocity varies with distance from the axis.

A more characteristic value to use for the radial length scale – if not the beam radius itself – would be one that describes the size of the highest flux region near the axis, as well as the dependence of the observed deposition size on the time interval over which the deposition was collected. A smaller length scale, and therefore a smaller δ value, would then correspond to a weaker dependence of the deposition size on the time

interval, so that running the experiment for longer would do little to increase the deposition size. Based on the observation that the outflow particle number flux scales roughly exponentially with r for most source pressures considered, the following radial length scale is used: For each set value of the source pressure p_o, $f(r) = B \exp(-Ar)$ is the exponential trend line for the outflow particle number flux profile, where A and B are constants determined from a least-squares fit. A larger value of A then corresponds to a number flux distribution more closely concentrated toward the central axis. Thus, by dimensional reasoning, the particle deposition radius r_o should scale roughly with 1/A, which can then be used as the relevant length. Finally, as the solid angle δ is proportional to r_o^2, it follows that δ should scale with $1/A^2$. The simulation results shown in Fig. (2.3) are used to obtain A values corresponding to each source pressure p_o considered, so that the variation of δ with p_o can be approximated from the simulations and compared to analogous experimental results.

Note that, in addition to the simplifying assumptions used to define boundary conditions and other simulation parameters, a major potential problem with this validation method is that values of A will depend on the radial distance over which the least-squares trend line fit is performed, as well as the distribution of grid points along the outflow boundary. This dependence is particularly large at higher source pressures, where the outflow number flux distribution is shown in Fig. (2.3) to vary significantly from an exponential shape. For consistency, all A values are calculated using exponential trend lines that extend over the entire radial distance for which the outflow particle number flux is nonzero. It can be argued that equally valid but very different values of A could be found by performing each least-squares fit over a different set of grid points, or by

neglecting the points where the particle number flux is nearly zero. Subject to these inherent problems and simplifications, it is still expected that, if the simulations accurately model the flows considered in the experiments, the plot of p_o against $1/A^2$ from the simulation results will have the same general shape as a plot of p_o against δ from the experiments.

Figures (2.4) and (2.5) show, respectively, the dependence of $1/A^2$ on p_o from the simulations, and experimental values of δ as a function of p_o. A comparison of the trends on the two plots reveals some major differences: The sharp increase in beam size at very low source pressures, as found in the experiment, is far less pronounced in the numerical results. The range of p_o values for which the beam size varies little with p_o is much smaller in Fig. (2.4) than in Fig. (2.5), where this range extends from p_o = 34.5 mmHg through 96 mmHg, the largest source pressure considered in the simulations.

Two very important trends are however found in both sets of results. First, in both Figs. (2.4) and (2.5), there is a reduction in beam size as p_o is increased from the lowest value (14.8 mmHg), with a consistently positive curvature that leads to a minimum beam size, followed by an increase in beam size with source pressure as p_o is further increased. Second, the p_o value for which the beam size is minimized is the same (34.5 mmHg) in both figures. Furthermore, the comparatively rapid increase in beam size with p_o observed on the right side of Fig. (2.4) can be attributed to the fact that, for the corresponding simulations, the outflow number flux profiles are not very well correlated with the exponential trend lines used to define the beam size.

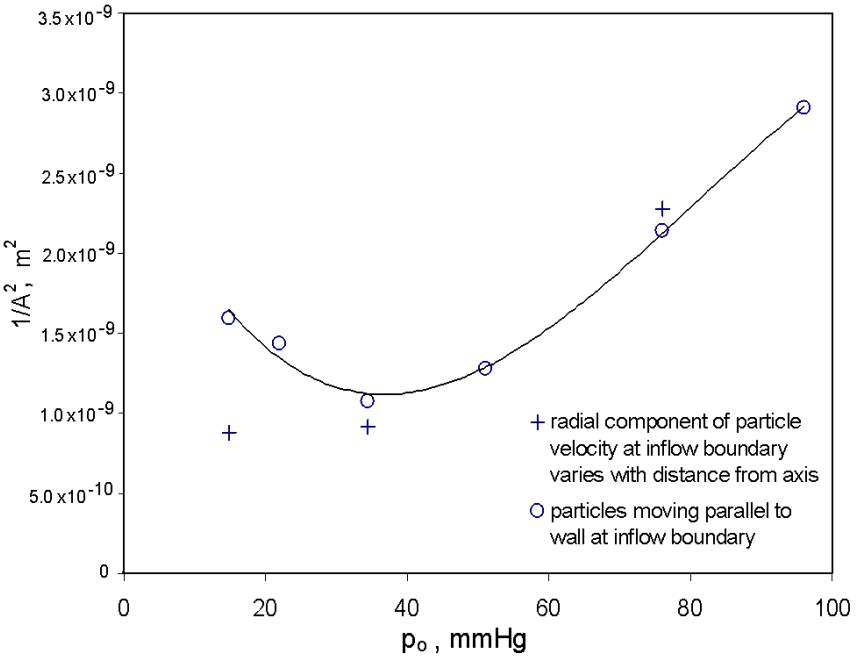

Figure 2.4. Values of $1/A^2$ as a function of source pressure, based on the numerical results.

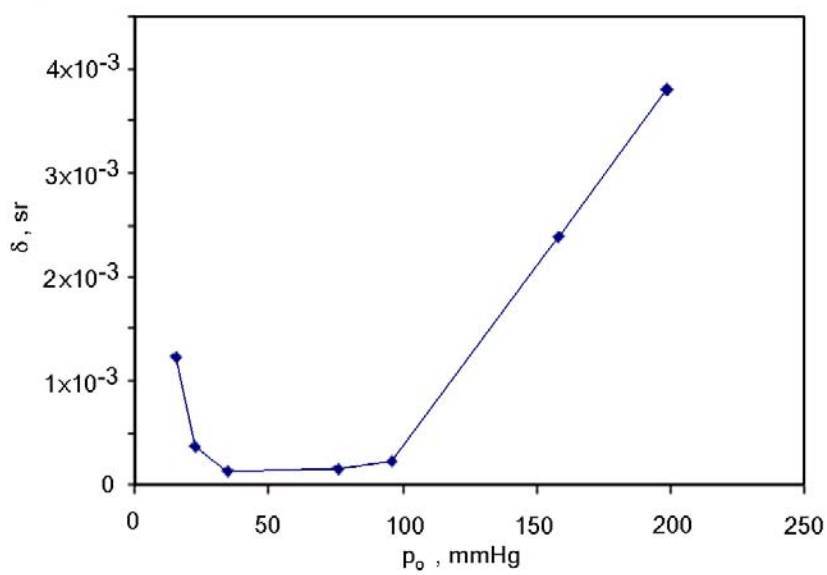

Figure 2.5. Source pressure vs. experimental values of δ.

Note the data points in Fig. (2.4) marked with "+" symbols, which correspond to the simulations for which the radial component of particle velocity along the inflow boundary is set to vary with distance from the axis. As discussed above, these simulations should under-predict the beam size for lower source pressures, so that the trend observed in Fig. (2.4) of a monotonic increase in beam size with p_o should not be thought to reflect the overall accuracy of the simulation method.

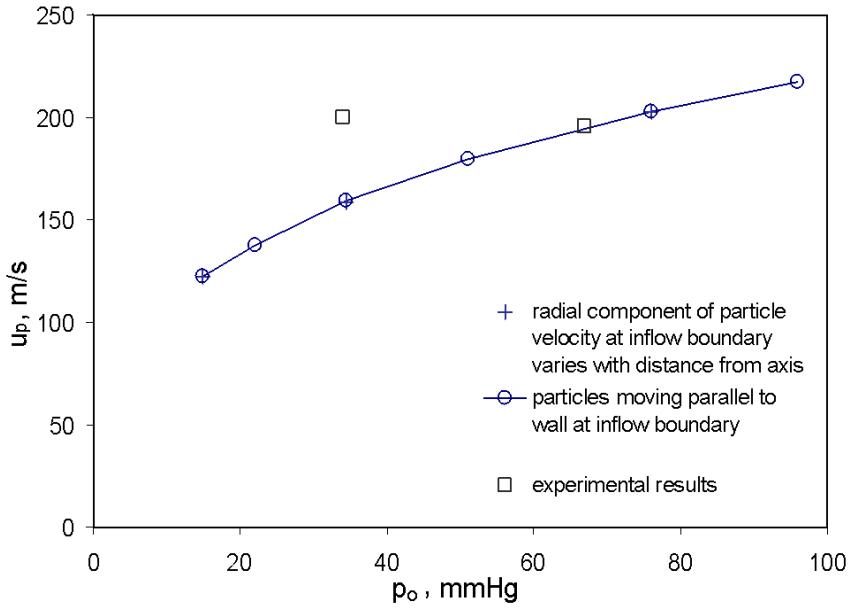

Figure 2.6. Variation with source pressure of terminal particle velocity along the central axis.

Figure (2.6) shows the dependence on p_o of the average terminal particle velocity $u_{p\infty}$ along the central axis, as measured from the simulation results at the outflow boundary 6 mm downstream from the nozzle exit plane. Because a denser gas exerts greater force on the particles as it expands within and beyond the nozzle, the trend of increasing $u_{p\infty}$ with p_o observed in Fig. (2.6) is very much expected. Experimental measurements of $u_{p\infty}$ give values of roughly 200 m/s for source pressures of both 34.5 mmHg and 65 mmHg,

subject to errors of approximately 10 m/s. While the difference in trends between experimental and simulation results is significant here, it should be noted that the terminal bulk gas velocity along the axis is found numerically to exceed 700 m/s, so that, as a fraction of the terminal gas speed, the differences in particle speed are relatively small. Also note that the discrepancy observed in Fig. (2.6) involves only one of the two experimental data points, and that as discussed by *Israel and Friedlander* (1967), the experimental method for measuring $u_{p\infty}$ is inherently imprecise and prone to potentially large errors.

Subject to the assumptions and simplifications described above, the simulation results agree well with data from the experiments. In general then, it can be assumed that both the two phase DSMC method of *Gallis et al.* (2001) and the current implementation of this method do function as expected, and allow for relatively accurate simulation of two phase rarefied flows. Note however that only dilute particle concentrations have been considered, as the *Gallis* procedures only allow for simulations of one-way coupled flow where the influence of the particle phase on the gas can be neglected. While not explicitly stated by *Israel and Friedlander*, it is assumed that particle concentrations in the experiments are small enough that the rate of momentum transfer from the gas to the particles is consistently much lower than the gas momentum flux, so that two-way coupling effects are negligible and the *Gallis* method is appropriate for the simulation of these flows. However, the assumption of one-way coupling is not always valid for the SRM plume flows of interest, where the particle phase mass fraction is relatively high and interphase momentum and energy transfer may significantly alter the properties of the gas. A detailed numerical model for two-way coupling is therefore necessary for more

general simulations of rarefied particle-gas flows. One such model is introduced in Chapter 3.

2.2.2 Additional results

Additional simulation results are provided here for the particle beam flows described in the previous section. These results, although not usable for comparison with the experiments, demonstrate the utility of the method while allowing for a deeper understanding of the physical characteristics of the flows considered here.

Figure (2.7) shows the variation in the relative Mach number M_p of the particles with respect to the surrounding gas. M_p is defined as the magnitude of the vector difference between the particle and the gas bulk velocities, divided by the local sonic speed of the gas. Values of M_p are plotted along the central axis for simulations at source pressures of 14.8, 34.5 and 96 mmHg. The first and last of these pressures are, respectively, the lowest and highest p_o values considered in this study. The inclusion of results from these three simulations should therefore allow for an understanding of the full range of flow conditions. Note that points with x-coordinate values between 0 and 0.001 m are located within the nozzle, and all other points are in the plume.

Neglecting effects of statistical scatter in the far-field plume region, the relative Mach number is found in all three simulations to continuously increase with downstream distance. This follows from the fact that throughout both the nozzle and plume, the gas velocity is increasing and the gas temperature is decreasing, while the particle velocity varies far less rapidly. To reinforce this last point, a corresponding plot of average particle speed along the central axis is included here as Fig. (2.8).

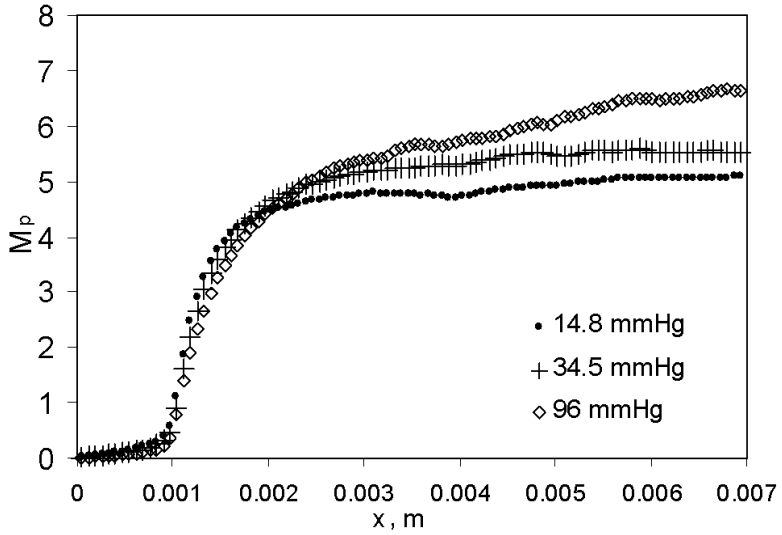

Figure 2.7. Comparison of relative particle Mach numbers along the central axis for simulations at three different source pressures.

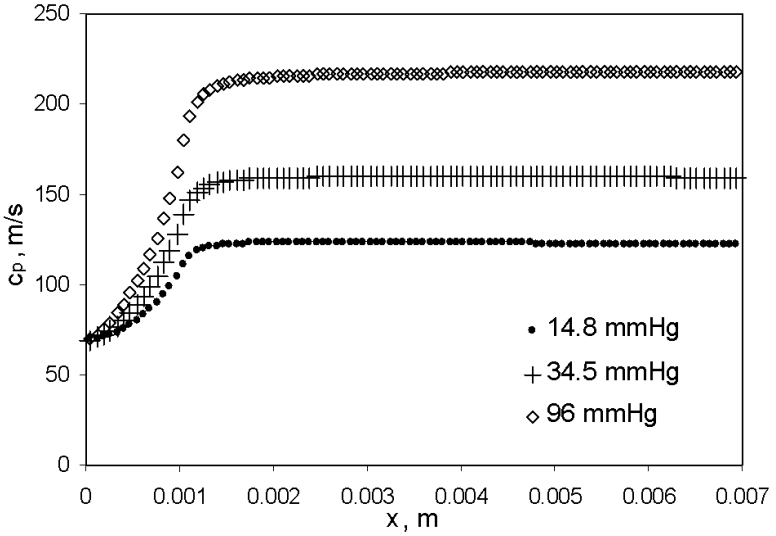

Figure 2.8. Particle speed along the central axis.

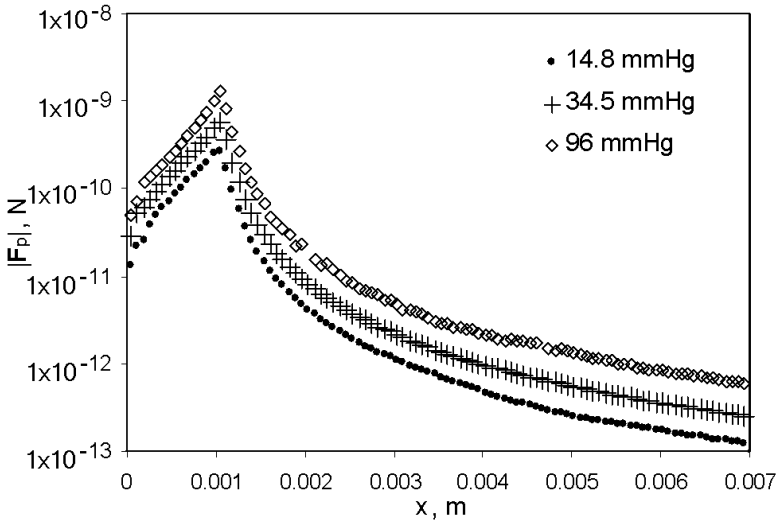

Figure 2.9. Drag force on particles along the central axis.

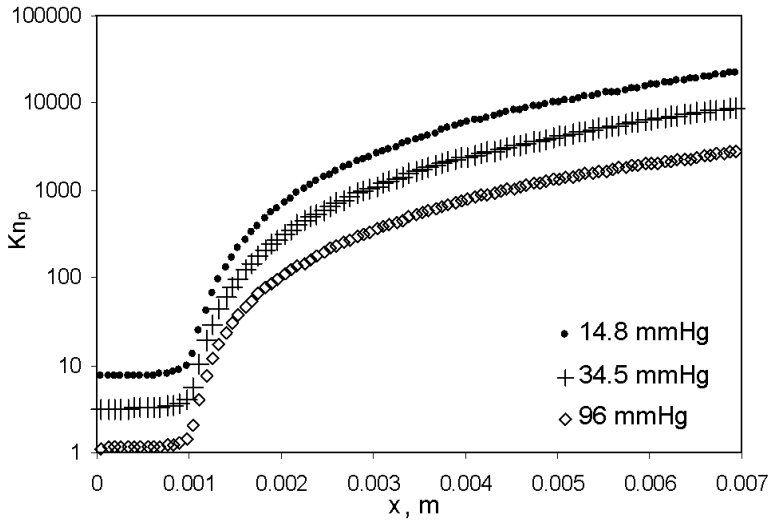

Figure 2.10. Particle Knudsen number along the central axis.

As discussed above in the comparison with experimental results, the particles are shown in Fig. (2.8) to reach a near-terminal velocity within a short distance of the nozzle exit, and the magnitude of this terminal velocity increases with the source pressure p_o. An interesting trend observed in Fig. (2.8) is that the size of the near-field region of the plume where particle acceleration is significant has little, if any, dependence on the value of p_o.

Figure (2.9) shows the magnitude of the average drag force $\mathbf{F}_p$ on the particles along the axis. Under steady state conditions, this force is equal to the dot product of the particle velocity with the velocity gradient tensor, multiplied by the particle mass. Thus, $|\mathbf{F}_p|$ can be thought to scale roughly with the slope of the particle speed curves plotted in Fig. (2.9). A comparison with Fig. (2.9) then explains the general trends observed in Fig. (2.8), most notably that the lack of variation in far-field particle velocity corresponds to a sharp drop-off in the force exerted on the particles by the expanding gas.

Another prominent trend in Fig. (2.9) is that for all three simulations considered, the values of $|\mathbf{F}_p|$ are far greatest around the nozzle exit, with a global maximum at the exit plane. This can be explained by the following logic: At the inflow boundary, the average particle and gas velocities are approximately equal. Thus, even though the gas density is greatest at this boundary, the drag force should be relatively small. (The thermophoretic force due to the gas temperature gradient may be significant here, and accounts in part for the fact that $\mathbf{F}_p$ is still much greater at the inflow boundary than in the far-field region of the plume.) As the gas expands and accelerates through the nozzle, the particle velocity lag dramatically increases, so that $|\mathbf{F}_p|$ values increase greatly with downstream distance through the nozzle. The particle velocity lag continues to grow as the gas expands beyond

the nozzle exit, but there is a rapid reduction in gas density that offsets the increasing relative velocity of the gas. As a result, values of $|\mathbf{F}_p|$ will decrease throughout the plume. The force exerted on the particles therefore reaches a maximum value at the nozzle exit, beyond which the slope of the $|\mathbf{F}_p|$ profile changes sign. Furthermore, the requirement that $|\mathbf{F}_p|$ values be relatively small within a short distance both upstream and downstream of the nozzle exit gives rise to a sharp spike in the force profile at the exit plane, as shown in the figure.

The variation in particle Knudsen number along the central axis is displayed in Fig. (2.10). For all three simulations, the particles are found to be in the transition regime within and just beyond the nozzle, and well within the free molecule regime further downstream. Note the distinction between the particle Knudsen number, which characterizes the effect of collisions in creating local variation in the gas properties near the particle surface, and the Knudsen number of the flow, which characterizes the overall influence of collisions on average properties in the gas.

All simulations used for comparison with experimental results are characterized by a lack of significant energy transfer between the particles and gas. This is reflected in the fact that particle temperatures are found to be nearly uniform throughout the grid domain. In order to consider the effects of interphase energy transfer, the simulation boundary conditions must then be changed in ways that do not reflect the flow characteristics in the experiments. As particle temperatures are almost universally greater than the local gas temperature in the two phase SRM plume flows of interest, a simple and desirable way to evaluate the heat transfer formulation is to perform simulations where the particle temperature at the inflow boundary is much greater than the local temperature of the gas,

and where all other parameters are unchanged from the simulations described above. Thus, the simulations corresponding to source pressures of 14.8, 34.5, and 96 mmHg are repeated with the inflow particle temperature increased by 100 K to 398 K.

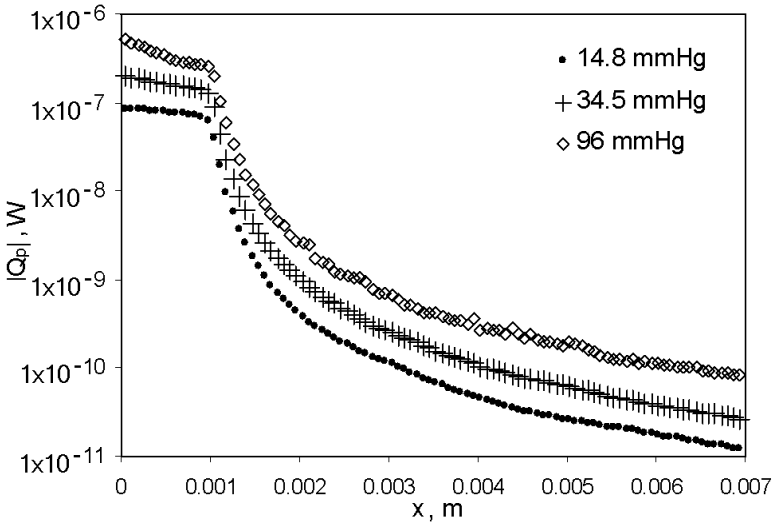

Figure 2.11. Magnitude of the average particle heat transfer rate along the axis.

Figure (2.11) shows the variation in the magnitude of the interphase energy transfer rate along the central axis, for all three of these simulations. While the temperature difference between the gas and particles is found to increase continuously with downstream distance in both the nozzle and plume, the heat transfer rate from the particles to the gas is shown in the figure to continuously decrease. This trend can be attributed to the reduction in gas density through the nozzle, and the far more rapid reduction in gas density within the plume. This density effect outweighs the influence of the growing temperature lag, so that even as the average energy transferred per interphase collision increases with downstream distance, the decline in collision frequency results in an overall reduction in the heat transfer rate as particles move downstream. Because the drop-off in gas density is most prominent in the near-field region of the plume, the

decrease in the heat transfer rate should be greatest in this region just beyond the nozzle exit, as is shown in Fig. (2.11).

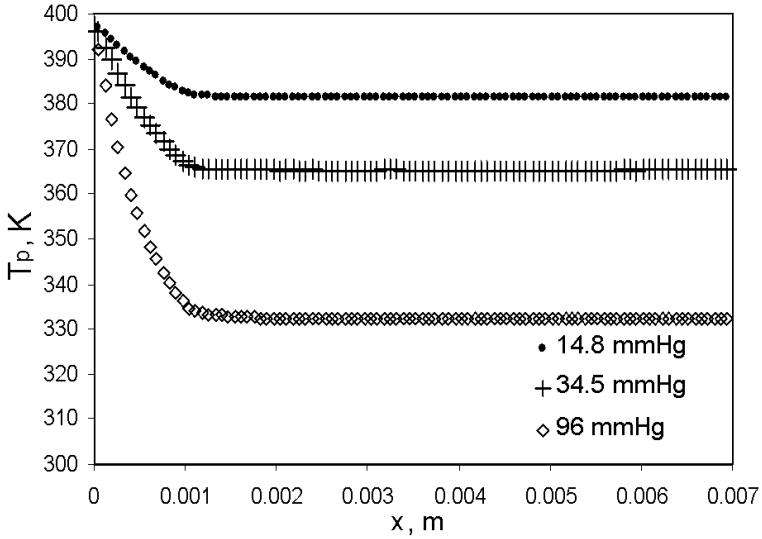

Figure 2.12. Variation along the axis in average particle temperatures.

The average heat transfer rate to an individual particle can be expressed as $\dot{Q}_p = m_p c_s \mathbf{u}_p \cdot \nabla T_p$, where m_p is the particle mass, c_s is the specific heat of the particle material, $\mathbf{u}_p$ is the mean particle velocity, and T_p is the average particle temperature. The gradient of T_p should then scale roughly with the magnitude of the heat transfer rate. This trend is observed for all three simulations through a comparison of Fig. (2.11) with Fig. (2.12), which shows the variation of average particle temperature with distance along the axis. As displayed in Fig. (2.12), the particle temperature varies significantly through the nozzle and the near-field plume region, then reaches a nearly constant value within a short distance of the nozzle exit. This final value is found to be highly dependent on the gas source pressure. Note that analogous trends for the particle speed are observed in Fig. (2.11).

As shown in Eq. (2.2), the force exerted on a particle by a colliding gas molecule will depend on the temperature of the particle. It follows that a change in particle temperature must alter the magnitude of the average force on the particles, so that the distribution of particle speed will also change. Figure (2.13) shows the ratio of the cell-averaged particle speed c_p in all three simulations to a corresponding particle speed c_p^o in simulations where the inflow particle temperature is set to the original value of 298 K. This ratio (c_p/c_p^o) is plotted over 100 points along the central axis.

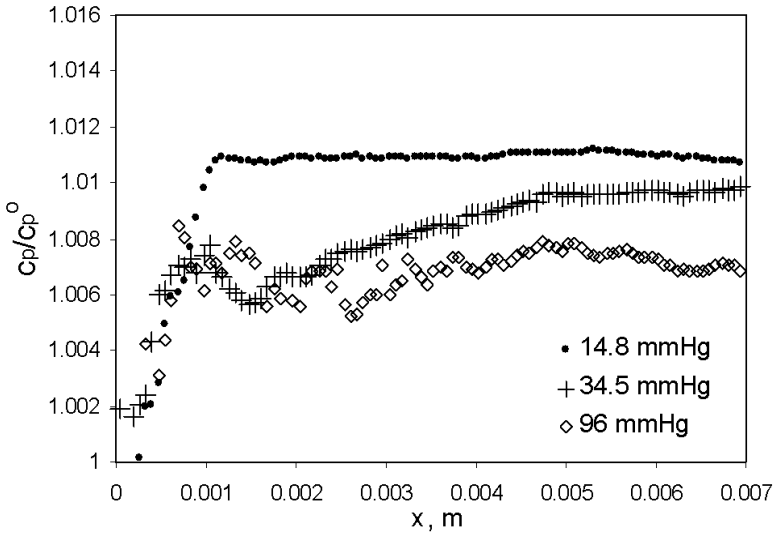

Figure 2.13. Fractional change in average particle speed associated with an increase in particle temperature.

From Eq. (2.2), it is expected that an increase in particle temperature will result in a greater force exerted on the particles by the accelerating gas. As T_p increases, values of c_p should then increase, and the ratio (c_p/c_p^o) should be greater than one. This is observed in Fig. (2.13), where (with the exception of a very few points near the inflow boundary which are not shown, and where c_p/c_p^o is just slightly below unity) the ratio of particle speeds is found to be consistently greater than one. In addition, the values of (c_p/c_p^o) tend

to rise with downstream distance, because the force – and therefore the spatial gradient in the particle speed – will increase with particle temperature. The considerable statistical scatter observed in Fig. (2.13) is a consequence of the fact that even though the particle speed is influenced by the value of T_p, this influence is relatively small, and the ratio (c_p/c_p^o) is consistently very close to unity.

2.3 Simulation of nonspherical particles

While experimental studies have shown that alumina (Al_2O_3) particles in solid rocket exhaust flows tend to be nearly spherical, surface forces on a solidifying alumina droplet may result in particle shapes which differ noticeably from a perfect sphere. [*Reed and Calia* (1993), *Gosse et al.* (2003)] Nonspherical particles are also prominent in similar flows involving a two phase free expansion, including liquid propellant rocket plume flows and spacecraft fuel venting flows. In particular, ice particles from condensed water vapor in rocket exhausts, and soot particles associated with heterogeneous combustion in both solid and liquid propellant rockets, may have highly nonspherical shapes. [*Kassal* (1974), *Simmons* (2000)]

Following the assumptions discussed in Section 2.1 on which the method of *Gallis et al.* (2001) is based, these nonspherical particles can also be considered through the following analysis. First, a few additional assumptions must be made for any nonspherical particle: The particle is assumed to have a convex shape, which is defined here as a shape bounded by a surface through which no straight line can pass more than twice. In addition, the particle is assumed to move through the gas with an isotropic distribution of orientations relative to any fixed coordinate system, so that no one

orientation is more likely than any other. While this implies that a nonspherical particle must be rotating, it is further assumed that any rotation effects – particle angular momentum, the side force due to an asymmetric surface pressure distribution, rotation-induced time variation in interphase momentum and heat transfer, etc. – are relatively small and can be neglected. These assumptions are expected to be valid over most relevant flow regimes for a variety of particle types. Note however that particle rotation effects will be considered in more detail in Section 2.4, where some of these assumptions are relaxed.

Subject to the above assumptions, the convective heat transfer rate between a solid particle and the surrounding gas will depend on the particle shape only through the value of the average collision cross section for interphase collisions, given here as σ. Furthermore, the average momentum transfer rate will depend on the particle shape only through the value of σ and through the distribution function of the collision angle θ. Here θ is defined as the angle between the relative velocity $\mathbf{u}_r = \mathbf{u}_m - \mathbf{u}_p$ of an incident gas molecule and the inward normal vector at the collision point on the particle surface, where $\mathbf{u}_m$ and $\mathbf{u}_p$ are the velocities of the gas molecule and particle, respectively, in a fixed reference frame. Thus, if the particle shape dependence for σ and the distribution function $f(\theta)$ can be found, then subject to the assumptions described above, the influence of particle shape on the rates of interphase momentum and energy transfer can be determined.

2.3.1 Collision angle distribution function

First consider the dependence of $f(\theta)$ on the particle shape. For an arbitrary convex particle, let the particle surface be divided into a large number N of flat surface elements, each of area ∂A. Now assume that a gas molecule collides with the particle on a particular surface element i. If all orientations of the particle for which this collision may occur are equally likely, then the relative velocity vector of the incident molecule has an isotropic distribution over $\theta \in [0,\pi/2]$. This vector will be contained within a solid angle element of size $\sin\theta d\theta d\phi$, where ϕ is the azimuthal angle relative to some reference direction in the plane of the surface element. Therefore $f(\theta)$ must be proportional to the size of the solid angle, so that $f(\theta) \propto \sin\theta$.

Now, if we remove the requirement that the collision occurs on the surface element i, and only assume that a collision does occur somewhere on the particle surface, then the probability that the collision point will be located on element i must be proportional to the projected area of this element in the direction of the relative velocity vector $\mathbf{u}_r$. Thus $f(\theta)$ is proportional to this projected area $\partial A\cos\theta$, so that $f(\theta) \propto \cos\theta$. By the above arguments, $f(\theta)$ must then be proportional to $\sin\theta\cos\theta$. Applying a trigonometric identity and the normalization condition $\int_0^{\pi/2} f(\theta) d\theta = 1$, we find that

$$f(\theta) = \sin 2\theta. \tag{2.3}$$

As this distribution function is valid for any surface element, it must also be valid for the particle as a whole. Note that $f(\theta)$ will have no dependence on the particle shape, so long as the above assumptions are valid.

2.3.2 Average collision cross section

Next consider the particle shape dependence of the average collision cross section σ. As above, assume that the particle surface is made up of a large number N of flat surface elements, each with area ∂A. Now define θ_i as the angle between the inward normal vector on a given element i and the relative velocity vector $\mathbf{u}_r$ of an incident gas molecule. Under the assumption that the gas molecule is much smaller than the particle, the instantaneous collision cross section σ' will be the sum of the projected areas of all exposed faces:

$$\sigma' = \sum_{i=1}^{N} \partial A \max\{\cos\theta_i, 0\} \tag{2.4}$$

The average collision cross section σ can then be approximated as the average of a large number M of σ' values, each of which corresponds to a randomly chosen particle orientation relative to $\mathbf{u}_r$. If θ_{ij} is the value of θ on surface element i for the jth realization of σ', then σ can be given by

$$\begin{aligned}
\sigma &= \lim_{M\to\infty} \frac{1}{M} \sum_{j=1}^{M} \sum_{i=1}^{N} \partial A \max\{\cos\theta_{ij}, 0\} \\
&= \sum_{i=1}^{N} \left(\partial A \lim_{M\to\infty} \frac{1}{M} \sum_{j=1}^{M} \max\{\cos\theta_{ij}, 0\} \right) \\
&= \sum_{i=1}^{N} \left(\partial A \int_0^{\pi} g(\theta_i) \max\{\cos\theta_i, 0\} d\theta_i \right)
\end{aligned} \tag{2.5}$$

Here $g(\theta_i)$ is the distribution function of θ_i for a collision which may occur anywhere on the particle surface. From the solid angle argument used in the derivation of Eq. (2.3), it can be shown that $g(\theta_i) \propto \sin\theta_i$ if the particle has no preferred orientation relative to $\mathbf{u}_r$.

Applying the normalization condition $\int_0^{\pi} g(\theta_i) d\theta_i = 1$, we find that $g(\theta_i) = \frac{1}{2} \sin\theta_i$ for $\theta_i \in [0,\pi]$, so $\int_0^{\pi} g(\theta_i) \max\{\cos\theta_i, 0\} d\theta_i = \frac{1}{4}$. If the total surface area of the particle is $A_s = \sum_{i=1}^{N} \partial A$ then substitution into Eq. (2.5) gives the final result that $\sigma = \frac{1}{4} A_s$. Thus, for a convex particle of arbitrary shape, the average collision cross section will be one fourth of the particle surface area.

2.3.3 Effective particle size and density

As $f(\theta)$ has no particle shape dependence and σ depends only on the particle surface area, then subject to the assumptions discussed above, any convex particle can be modeled as a spherical particle of the same surface area for calculations of interphase momentum and energy transfer. Following a standard convention [*Crowe et al.* (1998)] let the particle shape be characterized by a shape factor $\psi \equiv A_o/A_s$, where A_o is the surface area of a sphere with the same volume as the particle. Define R_o as the radius of this same sphere, which for most particle shapes will be comparable to one-half of some characteristic average particle length. The effective particle radius R_p, for use in momentum and energy transfer calculations, can then be determined from known values of ψ and R_o through the following relation:

$$R_p = R_o \psi^{-1/2} \tag{2.6}$$

As $R_p \geq R_o$ it follows that a convex nonspherical particle in locally free-molecular flow will behave like a spherical particle of equal mass but greater volume. Thus, the larger effective radius for a nonspherical particle will be accompanied by a reduction in

the effective particle density. If the particle mass m_p is calculated as $m_p=4/3\pi\rho_p R_p^3$ then the effective particle density ρ_p can be found through the relation $\rho_p = \rho_o \psi^{3/2}$, where ρ_o is the actual density of the particle material.

Through this analysis, the solid particle model of *Gallis et al*. (2001), as well as a two-way coupling method discussed in the following section, can be extended and applied to a variety of nonspherical particles. While the analysis is not strictly valid for particles with highly complicated non-convex shapes, such as soot agglomerates, it is thought that this can provide at least a first-order approximation for the properties of such particles when included in a simulation.

2.4 Extension to rotating particles

The procedures described in Section 2.1 may be further extended for consideration of rotating particles in a locally free-molecular nonequilibrium gas. Following a discussion on the relevance of particle rotation to the plume flows of interest, a series of equations are derived to compute the net force, heat transfer, and moment on a rotating sphere for an arbitrary gas velocity distribution. Procedures are then presented for these equations to be used as part of a numerical scheme for the simulation of two phase rarefied flows.

2.4.1 The potential importance of particle rotation

Despite the long history of SRM plume modeling efforts described in Chapter 1, little study has been devoted to the effects of Al_2O_3 particle rotation in the flow regimes common to rocket exhaust plumes, and rotation has generally been neglected in plume modeling and analysis. In order to understand and quantify the influence of particle

rotation on various flow properties, the mechanisms by which particles in the plume develop angular momentum must first be considered.

As discussed in Section 1.2, liquid Al_2O_3 droplets are continually formed during the combustion process inside an SRM, with a bimodal size distribution concentrated around diameters of roughly 1 μm and 100 μm. [*Salita* (1991)] The droplets are then accelerated through the rocket nozzle, where they may encounter several different phenomena that tend to contribute angular momentum. First, smaller droplets are accelerated by the expanding gas far more rapidly than the larger droplets, so that droplets of different sizes develop widely varying velocities. The high number density and considerable relative velocities between droplets of different sizes allow for a large number of collisions, which results in the coalescence of droplets into larger agglomerates. These agglomerates in turn tend to rotate due to the off-center nature of most coalescing collisions. [*Vasenin et al.* (1995)] At the same time, larger droplets tend to break apart within the nozzle due to collisions or surface stresses imposed by the accelerating gas, and these breakup processes may impose significant angular momentum on the resulting droplet products.

Within the subsonic converging nozzle region, larger droplets may diverge considerably from gas streamlines and accumulate in the boundary layers along the nozzle wall, where large transverse gradients in the bulk gas velocity can also induce rotation. [*Crowe et al*. (1998)] As the droplets cool and solidify into solid particles, inelastic collisions between particles may contribute to rotation as well. Turbulent and acoustic fluctuations in the gas can intensify many of these rotation mechanisms.

As particles exiting the nozzle in an SRM exhaust flow may have large angular velocities, a question arises regarding how rotation affects particle properties within the

plume. Due to the potentially nonequilibrium velocity distribution and locally free-molecular nature of the gas surrounding these particles, existing continuum-based correlations for the force and moment on a rotating sphere are not generally valid. The accurate simulation of high altitude SRM plume flows involving rotating particles may therefore require the use of a gas kinetics-based approach.

Over the past several decades, a number of authors have studied various properties associated with the rotation of solid bodies within a free-molecular equilibrium gas. *Epstein* (1924) derived the moment imparted on a rotating sphere, subject to several constraints including a lack of translational motion. *Wang* (1972) determined the drag and lift coefficients for a rotating sphere, and showed that the direction of the transverse "lift" force is opposite that of the Magnus force for continuum flow. *Ivanov and Yanshin* (1980) derived force and moment equations for various bodies of revolution. While all of these authors have developed closed form solutions which are applicable to the general flow regimes of interest, the formulas they provide are limited by the assumption of Maxwellian gas velocity distribution, and none have considered the effect of rotation on interphase heat transfer. In addition, these formulas tend to be very complicated and poorly suited for evaluation within a larger numerical scheme for the simulation of high-altitude plume flows. A more appropriate set of formulas may be derived as an extension to the force and heat transfer equations of *Gallis et al.* (2001) presented in Section 2.1.

2.4.2 The Green's function approach

Equations (2.1) and (2.2) are based on Green's functions derived by *Gallis et al.* for momentum and energy transfer rates to a nonrotating solid sphere in a free-molecular

nonequilibrium gas. As described by these authors, the net force $\mathbf{F}_{p,net}$ and convective heat transfer rate $\dot{Q}_{p,net}$ on the sphere may be calculated as

$$\mathbf{F}_{p,net} = \int \mathbf{F}_p(\mathbf{u}_r) f(\mathbf{u}_r) d\mathbf{u}_r \tag{2.7}$$

$$\dot{Q}_{p,net} = \int \dot{Q}_p(\mathbf{u}_r) f(\mathbf{u}_r) d\mathbf{u}_r \tag{2.8}$$

where $\mathbf{u}_r$ is the gas velocity in a particle-centered coordinate system, $f(\mathbf{u}_r)$ is the gas velocity distribution function (neglecting the influence of gas molecules reflected off the body surface), the integration in Eqs. (2.7) and (2.8) is carried out over all velocity space, and the symbols $\mathbf{F}_p$ and $\dot{Q}_p$ represent Green's functions for the force and heat transfer rates respectively. Following the assumptions in Section 2.1, and an additional assumption that all nonrotational modes of internal energy are unexcited, these Green functions can be given as follows:

$$\mathbf{F}_p(\mathbf{u}_r) = \pi R_p^2 n_g \left(mc_r + \frac{\tau}{3}\sqrt{2\pi\, m\, k_B T_p} \right) \mathbf{u}_r \tag{2.9}$$

$$\dot{Q}_p(\mathbf{u}_r) = \pi R_p^2 \tau\, n_g c_r \left(\frac{1}{2} mc_r^2 + e_r - (2 + \frac{1}{2}\zeta_r) k_B T_p \right) \tag{2.10}$$

Here $c_r = |\mathbf{u}_r|$, ζ_r is the number of rotational degrees of freedom for the gas, e_r is the mean rotational energy per gas molecule, n_g is the gas number density, and all other symbols are as described in Section 2.1. (Note that Eqs. (2.9) and (2.10) are not true Green's functions in a strict mathematical sense. The term "Green's function" is however used here for consistency with the analysis of *Gallis et al*.)

2.4.3 Force on a rotating particle

In considering the Green's function $\mathbf{F}_p(\mathbf{u}_r)$ for the force imparted by the gas on a rotating spherical particle, first note that $\mathbf{F}_p$ is equal to the product of the interphase collision frequency $\pi R_p^2 n_g c_r$ and the average momentum transferred to the particle per collision. The average momentum transfer can be divided into a term due to the momentum of incident gas molecules, a term which accounts for the average momentum exchange during specular reflection, and a corresponding term for diffuse reflection. It can be shown that the first term is equal to $m\mathbf{u}_r$, the second is zero, and only the third term may be affected by the particle angular velocity.

Next, using the velocity superposition principle, the momentum transfer due to diffuse reflection is separated into a component independent of rotation and a component which depends on the particle angular velocity $\boldsymbol{\omega}_p$ but is independent of T_p . This latter component is the only contributor in a time-averaged sense to the force Green's function $\mathbf{F}_{rot}$ due to rotation, and allows the Green's function for the total force on the particle to be computed as $\mathbf{F}_p = \mathbf{F}_{nr} + \mathbf{F}_{rot}$ where the nonrotational force component $\mathbf{F}_{nr}$ is found using Eq. (2.9).

Following the above logic, the rotational force term $\mathbf{F}_{rot}$ is equal to the product of the collision frequency for diffusely reflecting collisions and the rotational component of the average momentum transferred during diffuse reflection. Hence

$$\mathbf{F}_{rot}(\mathbf{u}_r) = -\pi R_p^2 n_g \tau c_r \, m\langle \mathbf{u}_t \rangle \tag{2.11}$$

where $\mathbf{u}_t$ is the tangential velocity of the particle surface at the collision point in a particle-centered reference frame. In order to evaluate $\langle \mathbf{u}_t \rangle$ we first define two Cartesian coordinate systems (x_1, y_1, z_1) and (x_2, y_2, z_2). In both coordinate systems the origin is at

the particle center, the z_1 and z_2 axes are located along a line normal to the plane containing the vectors $\mathbf{u}_r$ and $\boldsymbol{\omega}_p$, and the y_1 and y_2 axes are oriented in the directions of $-\mathbf{u}_r$ and $\boldsymbol{\omega}_p$ respectively. Unit vectors along the axes can be given as

$$\hat{\mathbf{j}}_1 = -\frac{\mathbf{u}_r}{c_r} \qquad \hat{\mathbf{k}}_1 = \frac{\boldsymbol{\omega}_p \times \mathbf{u}_r}{c_r \omega_p \sin\phi} \qquad \hat{\mathbf{i}}_1 = \hat{\mathbf{j}}_1 \times \hat{\mathbf{k}}_1$$

$$\hat{\mathbf{j}}_2 = \frac{\boldsymbol{\omega}_p}{\omega_p} \qquad \hat{\mathbf{k}}_2 = \hat{\mathbf{k}}_1 \qquad \hat{\mathbf{i}}_2 = \hat{\mathbf{j}}_2 \times \hat{\mathbf{k}}_2 \tag{2.12}$$

where $\omega_p = |\boldsymbol{\omega}_p|$, and ϕ is the angle between the x_1 and x_2 axes as well as between the y_1 and y_2 axes. Two additional angles must also be used here: θ is defined as the angle between the outward normal vector at the collision point $\mathbf{n}_c$ and the y_1 axis, and ε is the angle between the x_1 axis and the projection of $\mathbf{n}_c$ onto the x_1-z_1 plane. All angles are shown in relation to relevant vectors in Fig. (2.14).

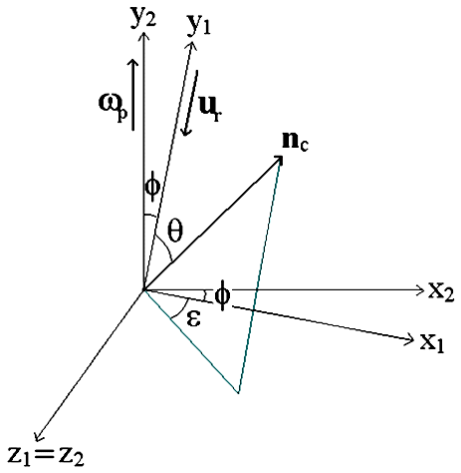

Figure 2.14. Angles used to determine the mean tangential velocity $\langle \mathbf{u}_t \rangle$.

Based on the above definitions, the tangential particle surface velocity $\mathbf{u}_t$ can be determined through the following procedure. First, we express the unit vector $\mathbf{n}_c$ in the (x_1, y_1, z_1) coordinate system and relate the two coordinate systems to each other:

$$\mathbf{n}_c = \sin\theta\cos\varepsilon\,\hat{\mathbf{i}}_1 + \cos\theta\,\hat{\mathbf{j}}_1 + \sin\theta\sin\varepsilon\,\hat{\mathbf{k}}_1 \tag{2.13}$$

$$\begin{bmatrix} \hat{\mathbf{i}}_1 \\ \hat{\mathbf{j}}_1 \\ \hat{\mathbf{k}}_1 \end{bmatrix} = \begin{bmatrix} \cos\phi & -\sin\phi & 0 \\ \sin\phi & \cos\phi & 0 \\ 0 & 0 & 1 \end{bmatrix} \begin{bmatrix} \hat{\mathbf{i}}_2 \\ \hat{\mathbf{j}}_2 \\ \hat{\mathbf{k}}_2 \end{bmatrix} \tag{2.14}$$

Substitution then gives

$$\mathbf{n}_c = \begin{bmatrix} \sin\theta\cos\varepsilon\cos\phi + \cos\theta\sin\phi \\ \cos\theta\cos\phi - \sin\theta\cos\varepsilon\sin\phi \\ \sin\theta\sin\varepsilon \end{bmatrix}^T \begin{bmatrix} \hat{\mathbf{i}}_2 \\ \hat{\mathbf{j}}_2 \\ \hat{\mathbf{k}}_2 \end{bmatrix}. \tag{2.15}$$

From Eqs. (2.12) and (2.15) and the relation $\mathbf{u}_t = \boldsymbol{\omega}_p \times (R_p\mathbf{n}_c)$, we find a formula for $\mathbf{u}_t$ in the (x_2, y_2, z_2) coordinate system.

$$\mathbf{u}_t = \omega_p R_p \left[\sin\theta\sin\varepsilon\,\hat{\mathbf{i}}_2 - \left(\sin\theta\cos\varepsilon\cos\phi + \cos\theta\sin\phi\right)\hat{\mathbf{k}}_2 \right] \tag{2.16}$$

Next, viewing angle arguments are used to derive the following joint distribution function for the angles θ and ε:

$$f(\theta,\varepsilon) = \frac{1}{\pi}\cos\theta \tag{2.17}$$

where $\theta \in [0, \pi/2]$ and $\varepsilon \in [0, 2\pi]$. Finally, to determine $\langle \mathbf{u}_t \rangle$ we integrate over all solid angle elements $d\Omega = \sin\theta d\theta d\varepsilon$ corresponding to possible directions of $\mathbf{n}_c$. From Eqs. (2.12), (2.16) and (2.17) we find:

$$\langle \mathbf{u}_t \rangle = \int_0^{2\pi}\int_0^{\pi/2} \mathbf{u}_t f(\theta,\varepsilon)\sin\theta d\theta d\varepsilon = -\frac{2}{3}\frac{R_p}{c_r}\boldsymbol{\omega}_p \times \mathbf{u}_r \tag{2.18}$$

Substitution into Eq. (2.11) gives the Green's function for the rotational component of the force imparted by a locally free-molecular gas on a rotating spherical particle.

$$\mathbf{F}_{rot}(\mathbf{u}_r) = \frac{2\pi}{3} R_p^3 m n_g \tau \, \boldsymbol{\omega}_p \times \mathbf{u}_t \tag{2.19}$$

By substituting the sum of the Eqs. (2.9) and (2.19) into Eq. (2.7), the total force on the particle can then be determined.

2.4.4 Moment due to particle rotation

Absent any additional forces which are not associated with interphase collisions, the rotating particle will experience a damping moment about the particle center which will tend over time to reduce the magnitude of the angular velocity $\boldsymbol{\omega}_p$. Depending on the angle between the vector $\boldsymbol{\omega}_p$ and the gas bulk velocity relative to the particle, the moment may also have a component orthogonal to $\boldsymbol{\omega}_p$ which tends to change the axis about which the particle rotates. This moment can be determined using the same Green's function approach as above. Again, incident and specularly reflected gas molecules do not contribute to the moment, and the average moment contribution during diffuse reflection can be shown to depend only on the tangential velocity of the particle surface. The Green's function $\mathbf{M}_p(\mathbf{u}_r)$ for this moment can then be expressed as the product of the collision frequency for diffuse reflection and the negative average angular momentum about the particle center imparted on diffusely reflected gas molecules:

$$\mathbf{M}_p(\mathbf{u}_r) = -\pi R_p^2 n_g \tau c_r \, m \langle R_p \mathbf{n}_c \times \mathbf{u}_t \rangle \tag{2.20}$$

The term $\langle R_p \mathbf{n}_c \times \mathbf{u}_t \rangle$ is evaluated using Eqs. (2.15), (2.16) and (2.17), by integrating over θ and ε.

$$<R_p \mathbf{n}_c \times \mathbf{u}_t> = \int_0^{2\pi}\int_0^{\pi/2} R_p \mathbf{n}_c \times \mathbf{u}_t f(\theta,\varepsilon)\sin\theta d\theta d\varepsilon$$

$$= \frac{1}{4}\omega_p R_p^2 \left[-\cos\phi \sin\phi \,\hat{\mathbf{i}}_2 + (3-\cos^2\phi)\,\hat{\mathbf{j}}_2 \right] \tag{2.21}$$

From Eqs. (2.12) and the relation $\cos\phi = -\frac{1}{c_r \omega_p}\mathbf{u}_r \cdot \boldsymbol{\omega}_p$, the bracketed terms in Eq. (2.21) can be rewritten in terms of $\mathbf{u}_r$ and $\boldsymbol{\omega}_p$. Substitution into Eq. (2.20) then gives an explicit formula for the particle moment Green's function:

$$\mathbf{M}_p(\mathbf{u}_r) = \frac{1}{4}\pi R_p^4 m n_g \tau c_r \left(\frac{\mathbf{u}_r \cdot \boldsymbol{\omega}_p}{c_r^2}\mathbf{u}_r - 3\,\boldsymbol{\omega}_p \right) \tag{2.22}$$

The total moment imposed on a rotating particle in a locally free-molecular gas flow can be determined by multiplying Eq. (2.22) by the gas velocity distribution function $f(\mathbf{u}_r)$ then integrating over all velocity space.

2.4.5 Heat transfer rate

As discussed in Section 2.1, it is assumed that the translational and rotational energy modes of a diffusely reflected gas molecule are fully accommodated to the particle temperature. As neither energy mode will be affected during a specularly reflecting collision, the heat transfer Green's function must be proportional to the frequency of diffusely reflecting collisions. For a nonrotating particle, this function will include a term which accounts for the lost kinetic energy of an incident gas molecule, a term for the kinetic energy gained by this molecule as it is diffusely reflected off the particle surface, and a term for the corresponding change in the average rotational energy of the molecule. For clarity, Eq. (2.10) may be rewritten as

$$\dot{Q}_p(\mathbf{u}_r) = \pi R_p^2 n_g \tau c_r \left[\frac{1}{2} m c_r^2 - \langle e_{kin}^* \rangle + \left(e_r - \frac{1}{2} \zeta_r k_B T_p \right) \right] \tag{2.23}$$

where the three terms described above are expressed separately within the brackets, and where $\langle e_{kin}^* \rangle = 2k_B T_p$ is the average kinetic energy of diffusely reflected gas molecules in a particle-fixed coordinate frame.

In the case of a rotating particle, two additional considerations must be made. First, the average post-collision kinetic energy term $\langle e_{kin}^* \rangle$ will be greater than $2k_B T_p$, and will depend on the local tangential velocity of the particle surface. Second, the total rate of energy transfer from the gas to the particle is equal to the sum of the heat transfer rate and a work term associated with the force and moment on the particle. It can be shown through asymptotic analysis that the total energy transfer rate becomes independent of the force if the particle is much more massive than the gas molecules, but this is not true for the moment. Thus, in determining the heat transfer Green's function $\dot{Q}_p(\mathbf{u}_r)$ for a rotating particle, a term $\mathbf{M}_p(\mathbf{u}_r) \cdot \boldsymbol{\omega}_p$ must be subtracted from the total energy transfer rate to account for the rate at which work is performed on the particle by the gas.

To determine the average kinetic energy of a gas molecule diffusely reflected off the rotating particle, consider a single particle surface element with outward normal unit vector $\mathbf{n}_c$ which moves at a tangential velocity $\mathbf{u}_t$. In a particle-centered reference frame, the average kinetic energy of a gas molecule diffusely reflected off this element is found to be

$$e_{kin}^* = 2 k_B T_p + \frac{1}{2} m \mathbf{u}_t \cdot \mathbf{u}_t \,. \tag{2.24}$$

The average kinetic energy of molecules diffusely reflected off any point on the particle surface can then be determined by integrating over all surface elements where a collision may occur. From Eqs. (2.16), (2.17) and (2.24):

$$<e_{kin}^{*}>=\int_0^{2\pi}\int_0^{\pi/2} e_{kin}^{*} f(\theta,\varepsilon)\sin\theta d\theta d\varepsilon = 2k_B T_p + \frac{1}{8} m\omega_p^2 R_p^2\left[3-\cos^2\phi\right] \tag{2.25}$$

By substituting this result into Eq. (2.23) then subtracting $\mathbf{M}_p(\mathbf{u}_r)\cdot\boldsymbol{\omega}_p$, we find the heat transfer Green's function for a rotating particle:

$$\dot{Q}_p(\mathbf{u}_r) = \pi R_p^2 n_g \tau c_r\left[\frac{1}{2}mc_r^2 - \left(2+\frac{1}{2}\zeta_r\right)k_B T_p + e_r + \frac{1}{8}m\omega_p^2 R_p^2\left(3-\frac{(\mathbf{u}_r\cdot\boldsymbol{\omega}_p)^2}{c_r^2\omega_p^2}\right)\right] \tag{2.26}$$

Note from Eq. (2.26) that the rotational component of the heat transfer rate scales with the square of the particle angular velocity, so that a greater value of ω_p corresponds to an increase in heat transfer from the gas to the particle. This property can be justified physically by considering a single surface element in a coordinate frame which is fixed to the local tangential surface velocity. In this coordinate frame the average kinetic energy of diffusely reflected gas molecules will be independent of ω_p, while the average kinetic energy of incident gas molecules tends to increase as ω_p^2. Thus, the only effect of particle rotation here is to increase the interphase energy transfer associated with the kinetic energy of incident gas molecules which are involved in diffusely reflecting collisions.

In the special case where a particle which moves at the bulk velocity of a Maxwellian simple gas, Eq. (2.8) may be integrated analytically to provide a closed form solution for the net heat transfer rate. The gas velocity distribution function here can be written as

$$f(\mathbf{u}_r)d\mathbf{u}_r = \pi^{-3/2}\,\beta^3\exp\left[-\beta^2\mathbf{u}_r^2\right]d\mathbf{u}_r \tag{2.27}$$

where $\beta=\sqrt{m/(2k_B T_g)}$ is the inverse of the gas thermal speed scale and T_g is the equilibrium gas temperature. By integrating the product of Eqs. (2.26) and (2.27) over all $\mathbf{u}_r \in \mathbb{R}^3$, we find

$$\dot{Q}_{p,net} = \sqrt{\pi} R_p^2 n_g \tau \beta^{-1} \left[(4+\zeta_r) k_B (T_g - T_p) + \frac{2}{3} m \omega_p^2 R_p^2 \right] . \tag{2.28}$$

From Eq. (2.22), the corresponding moment imparted on the particle by the surrounding gas is found to be

$$\mathbf{M}_{p,net} = -\frac{4}{3} \sqrt{\pi} R_p^4 \rho_g \tau \beta^{-1} \boldsymbol{\omega}_p . \tag{2.29}$$

It follows from Eqs. (2.28) and (2.29) that the component of $\dot{Q}_{p,net}$ associated with particle rotation is equal in magnitude to one-half the rate $\mathbf{M}_{p,net} \cdot \boldsymbol{\omega}_p$ at which rotational work is performed on the particle. Thus, half of the particle rotational energy lost through the moment $\mathbf{M}_{p,net}$ is transformed into thermal energy within the particle, and the remainder of the lost rotational energy is transferred to the gas. Also note from Eq. (2.28) that $\dot{Q}_{p,net}$ increases with ω_p independent of the relation between the particle temperature and that of the surrounding gas. Thus, in the typical case where $T_p > T_g$, the two bracketed terms in Eq. (2.28) are of opposite sign. Assuming the first of these terms is greater in magnitude than the second, we find that particle rotation tends to reduce the magnitude of the net heat transfer rate $\dot{Q}_{p,net}$.

2.4.6 DSMC Implementation

The proposed scheme for inclusion of rotating particles in a DSMC simulation is similar to that described in Section 2.1. Representative solid particles are tracked along with DSMC gas molecules through a computational grid, and during each time step the total force, moment, and heat transfer rate for each particle are determined by adding contributions from all gas molecules which are assigned to the same cell.

The force, moment and heat transfer contributions to a particle from a single DSMC gas molecule are computed by evaluating Eqs. (2.9), (2.19), (2.22) and (2.26) with the number density n_g replaced by the ratio of the gas numerical weight W_g to the cell volume. Once all N_g molecules in the cell have been considered, the particle velocity, angular velocity and temperature are altered according to the relations

$$\Delta \mathbf{u}_p = \frac{\Delta t}{m_p} \sum_{i=1}^{N_g} (\mathbf{F}_p)_i \qquad \Delta \boldsymbol{\omega}_p = \frac{\Delta t}{2/5\, \mu\, m_p R_p^2} \sum_{i=1}^{N_g} (\mathbf{M}_p)_i \qquad \Delta T_p = \frac{\Delta t}{m_p c_s} \sum_{i=1}^{N_g} (\dot{Q}_p)_i \tag{2.30}$$

where the subscript "i" denotes the contribution from a single DSMC gas molecule, and μ is the ratio of the particle moment of inertia to that of a uniform density sphere with the same size and mass. The particle position is then updated by the product of Δt with the average of initial and final velocities, following an assumption that the particle experiences uniform acceleration over the time interval Δt.

Chapter III

Numerical Procedures for Two-Way Coupled Flows

3.1 Derivation of a model for two-way coupling

As discussed in Chapter 1, high altitude SRM plume flows are often characterized by a considerable transfer of momentum and energy between the gas and solid particles, such that the properties of each phase are significantly affected by the presence of the other. Under these conditions, the assumption of one-way coupling in the model of *Gallis et al.* (2001) is invalid, and the influence of particles on the surrounding gas must be considered. While the procedure outlined in Section 2.1 may still be used to model the time-variation of particle properties, additional steps must be included in the calculations to account for potentially significant two-way coupling effects. The following analysis provides a physical model for the effect of an interphase collision on a gas molecule, and allows for a numerical procedure through which two-way coupling may be considered.

First, note that all assumptions discussed in Section 2.1 for the method of *Gallis et al.* (2001) are again used for consideration of momentum and energy transfer from a particle to the surrounding gas. Most importantly, the particle is assumed to be in a locally free molecular flow, so that any influence of reflected gas molecules on an incident molecule can be neglected during the collision process. The characteristics of the collision will

therefore depend only on the properties of the particle and the single gas molecule involved in the collision. Further, all interphase collisions must involve either specular reflection or diffuse reflection with full thermal accommodation.

3.1.1 Specular reflection

Consider the collision process between an individual gas molecule and a spherical solid particle. As shown in Section 2.3, the collision angle θ between the initial relative velocity vector $\mathbf{u}_r$ and the local particle surface normal at the collision point will have a range of $[0,\pi/2]$ and a distribution function given by Eq. (2.3). Let δ represent the deflection angle in the collision, defined as the angle between $-\mathbf{u}_r$ and the post-collision relative velocity vector $\mathbf{u}_r^* = \mathbf{u}_m^* - \mathbf{u}_p^*$, where $\mathbf{u}_m^*$ and $\mathbf{u}_p^*$ are the absolute velocity vectors of the gas molecule and the particle respectively following the collision. (The superscript "$*$" is used here to denote any post-collision value.) Thus, a δ value of zero is equivalent to the relation $\mathbf{u}_r^* = -\mathbf{u}_r$. For a collision involving specular reflection, any given θ will correspond to a δ value of 2θ. The distribution functions for θ and δ can then be related by $f(\delta)d\delta = f(\theta)d\theta$, so that, from Eq. (2.3), the deflection angle for a specularly reflecting collision will have the following distribution:

$$f(\delta) = \tfrac{1}{2}\sin\delta \quad \text{for } \delta \in [0,\pi] \tag{3.1}$$

Note that the azimuthal angle ε of the vector $\mathbf{u}_r^*$, relative to a fixed direction in the plane normal to $\mathbf{u}_r$, must have a uniform distribution over $[0,2\pi]$. From comparison with the distribution function $g(\theta_i)$ discussed in Section 2.3, it can then be shown that Eq. (3.1) corresponds to a total lack of directional dependence in $\mathbf{u}_r^*$. Thus, following a specularly

reflecting collision, the relative velocity of the gas molecule will have a magnitude of $c_r=|\mathbf{u}_r|$ and may be oriented with equal probability in any direction.

3.1.2 Diffuse reflection

If the collision instead involves diffuse reflection, then the collision dynamics are far more complicated, and a more involved procedure must be used to efficiently sample the deflection angle δ from the correct distribution function $f(\delta)$. In order to determine the shape of $f(\delta)$, two coordinate systems must now be used: First, let a coordinate system (x,y,z) be defined so that the origin is at the particle center, the y-axis is parallel to the initial relative velocity vector $\mathbf{u}_r$, and the collision point is located on the x-y plane. For the second coordinate system (x',y',z'), the origin is at the collision point, the y'-axis is along the local surface normal, and the particle center is on the x'-y' plane. Both coordinate systems are shown in Fig. (3.1), as are the relevant angles described below.

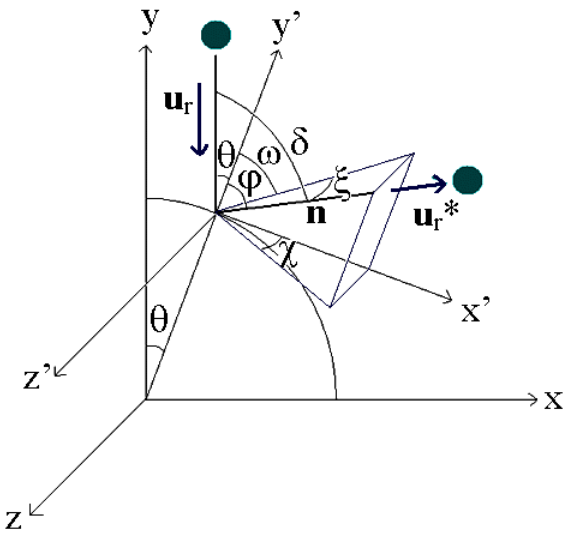

Figure 3.1. Coordinate systems and angles used in the evaluation of $f(\delta)$ for diffuse reflection.

Next, let φ denote the angle between the post-collision relative velocity vector $\mathbf{u}_r^*$ and the y'-axis, and designate as χ the azimuthal angle between the x'-axis and the projection of $\mathbf{u}_r^*$ onto the x'-z' plane. While specular reflection requires that φ = θ and χ = 0, in the case of diffuse reflection φ will have a continuous distribution over $[0,\pi/2]$ and χ will be uniformly distributed over $[-\pi,\pi]$. Through further analysis, it can be shown that the probability that the post-collision trajectory of a diffusely reflecting molecule will be contained within the differential solid angle dχdφsinφ centered at (φ,χ) must be proportional to both cosφ and the size of the solid angle. By imposing the normalization condition and a trigonometric identity, we find the following form for the distribution function of φ:

$$f(\varphi) = \sin(2\varphi) \quad \text{for } \varphi \in [0,\pi/2] \tag{3.2}$$

The angles θ, φ, and χ can then be related to the total deflection angle δ by

$$\cos\delta = (\cos\theta - \sin\theta\tan\varphi\cos\chi)\left[\frac{1-(\sin\varphi\sin\chi)^2}{1+(\tan\varphi\cos\chi)^2}\right]^{1/2}. \tag{3.3}$$

A derivation of Eq. (3.3) is provided in Appendix B.

A Monte Carlo integration method may be employed to determine the shape of the distribution function for δ. First, a value of θ is generated by applying the inverse cumulative distribution function method [*Bird* (1994)] to Eq. (2.3). Here a random number *R* in [0,1] is related to the desired θ value by

$$R = \int_0^\theta \sin(2\theta')\,d\theta' = 2\int_0^\theta \sin\theta'\cos\theta'\,d\theta' = \sin^2\theta \tag{3.4}$$

Applying the same technique to Eq. (3.2), a value for φ is found by setting a second random number equal to $\sin^2\varphi$. The azimuthal angle χ is then randomly generated with

uniform probability over the range [$-\pi,\pi$]. Once θ, φ, and χ are known, Eq. (3.3) is used to calculate the corresponding value of δ. This procedure is repeated a large number of times, and δ values are sorted into bins of finite width $\Delta\delta$. The frequency that δ values fall within each bin is then recorded to produce a histogram that approximates the shape of the distribution function for δ over [$0,\pi$]. The resulting shape is found to be closely approximated by the following sixth-order polynomial:

$$f(\delta) = 0.02042\delta^6 - 0.2515\delta^5 + 1.104\delta^4 - 1.903\delta^3 + 0.4938\delta^2 + 1.248\delta \qquad (3.5)$$

As an alternate procedure, an analogy with radiation transport may be used to find an exact closed-form solution for $f(\delta)$. *Siegel and Howell* (1981) derive an expression for the scattering phase function $\Phi(\beta)$ for the angle β between incident and scattered radiation from a diffusely reflecting sphere with dimensions much larger than the wavelengths of interest. They find

$$\Phi(\beta) = \frac{8}{3\pi}\sin\beta - \beta\cos\beta\,. \qquad (3.6)$$

A comparison of the above analysis with the derivation of Eq. (3.6) shows that β is analogous to ($\pi - \delta$) and $f(\delta)$ is proportional to $\sin\delta\cdot\Phi(\pi - \delta)$. From Eq. (3.6) and the normalization condition $\int_0^\pi f(\delta)d\delta = 1$ it follows that

$$f(\delta) = \frac{4}{3\pi}\sin\delta\,\left(\sin\delta + (\pi - \delta)\cos\delta\right). \qquad (3.7)$$

It can be shown that the deflection angle δ and post-collision relative speed c_r^* are statistically independent in a diffusely reflecting collision, hence Eqs. (3.5) and (3.7) are valid for any molecule-particle collision pair for which diffuse reflection is involved. Note that a spherical particle has been used here for simplicity, but the analysis in Section

2.3 allows Eqs. (3.5) and (3.7) to be extended to a range of nonspherical particles. Both the numerical solution and the polynomial approximation are shown in Fig. (3.2), along with the equivalent distribution function for specular reflection given as Eq. (3.1). Note that a plot of Eq. (3.7), which is not shown in the figure, is nearly identical to that of Eq. (3.5).

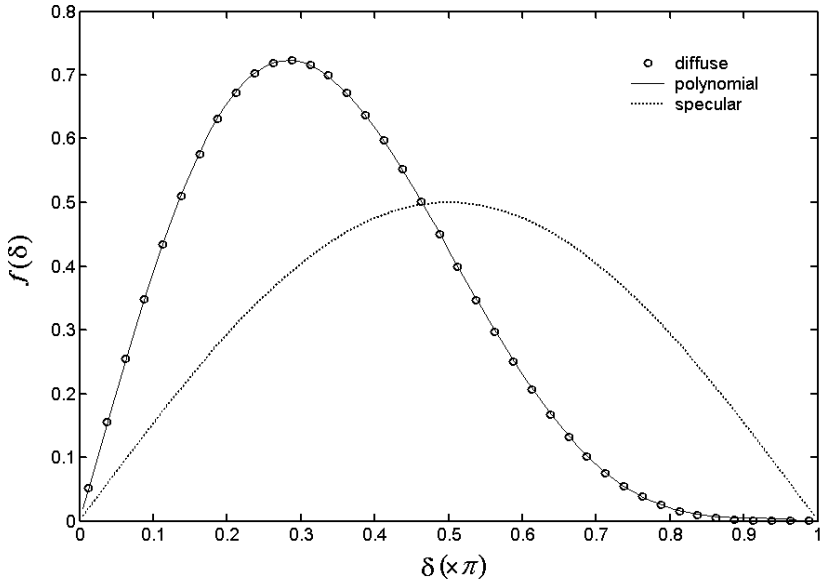

Figure 3.2. Comparison of distribution functions for the deflection angle δ.

3.1.3 Two-way coupling in DSMC

The above distributions are utilized in the following procedure, which allows a solid particle in a two phase DSMC simulation to influence the surrounding gas. We first determine which, if any, computational gas molecules will collide with the particle during each time step. A modification of the no time counter (NTC) method of *Bird* (1994) is used to find the number N_s of computational gas molecules that are selected as potential collision partners for the particle. The value of n_s is given by

$$N_s = \text{floor}(W_p N_g \pi R_p^2 (c_r)_{max} \Delta t / V_c + R) \tag{3.8}$$

where the operator "floor" rounds to the nearest smaller integer; R is a random number in [0,1]; W_p is the particle numerical weight (i.e. the number of actual solid particles represented by each computation particle); N_g is the number of computational gas molecules assigned to the same grid cell as the particle; R_p is the particle radius; Δt is the time step; V_c is the cell volume; and $(c_r)_{max}$ is the maximum pre-collision relative speed, over a large number of time steps, for any molecule-particle pair in this cell. Once N_s randomly selected molecules have been chosen as potential collision partners, those that do collide are selected with probability $c_r/(c_r)_{max}$. It can be shown that this selection scheme corresponds to a probability

$$P_{coll} = \pi W_p R_p^2 c_r \Delta t / V_c \tag{3.9}$$

that the particle will collide with a given molecule in the cell. Due to time step limitations inherent in DSMC, it has been found that P_{coll} values are almost universally several orders of magnitude smaller than one, so that the number of collisions per particle per time step is usually zero and is rarely greater than one.

If a given computational gas molecule is found to collide with the particle, then the collision is determined to involve either isothermal diffuse reflection, with a probability equal to the particle thermal accommodation coefficient τ, or specular reflection, with probability $1-\tau$. If a specularly reflecting collision takes place, then the relative speed c_r is unchanged in the collision, and the post-collision relative velocity $\mathbf{u}_r^*$ is found by multiplying c_r by a unit vector $\mathbf{n}$ which is sampled from an isotropic distribution. (An efficient algorithm for calculating $\mathbf{n}$ is discussed by *Bird* (1994).) If diffuse reflection occurs, then a value of δ is found by applying Eq. (3.3) to values of θ, φ, and χ

determined using the sampling techniques described above. Depending on the efficiency of the random number generator, it may instead be more efficient to sample δ values directly by applying the acceptance-rejection method to Eq. (3.7). In this procedure, a value of δ is randomly generated with uniform probability in the interval $[0,\pi]$, and a second random number R is generated between zero and the maximum of the function $f(\delta)$ over $[0,\pi]$. If $f(\delta)>R$ then this δ value is accepted and used in subsequent calculations. Otherwise the δ value is rejected, and the procedure is repeated.

Next, the azimuthal angle ε of the post-collision relative velocity $\mathbf{u}_r^*$ around the initial relative velocity vector $\mathbf{u}_r$ is randomly generated from a uniform distribution over $[0,2\pi]$. As kinetic energy is not conserved in diffusely reflecting collisions, the post-collision relative speed c_r^* cannot be assumed to equal the initial relative speed c_r . Instead, a value of c_r^* must be determined by applying the acceptance-rejection method to the distribution function

$$f(c_r^*) = 2\beta^4 c_r^{*3} \exp(-\beta^2 c_r^{*2}) \tag{3.10}$$

where $\beta = [m/(2k_B T_p)]^{1/2}$ is the inverse of the most probable thermal speed for an equilibrium gas at the particle temperature T_p, m is the gas molecule mass, and k_B is Boltzmann's constant. For the case of a diffusely reflected polyatomic gas molecule, the post-collision value of the rotational energy e_r must also be altered. As shown by *Bird* (1994), the rotational energy of a diffusely reflected diatomic molecule can be calculated as

$$e_r = -\ln(R) k_B T_P \tag{3.11}$$

where R is a randomly generated number in (0,1]. Note that vibrational activation is assumed here to be negligible for all flows of interest, so that the vibrational term in Eq.

(2.2) can be neglected and conservation of energy requires that the gas molecule vibrational energy not be altered during an interphase collision.

Now let u_r, v_r, and w_r be the components of $\mathbf{u}_r$ in the global coordinate system used in the simulation. The corresponding components of $\mathbf{u}_r^*$ can be computed from the values of u_r, v_r, and w_r, the pre- and post-collision relative speeds c_r and c_r^*, and the angles δ and ε using equations similar to those derived by *Bird* (1994) for binary elastic collisions. We first define three unit vectors $\mathbf{n}$, $\mathbf{t}_1$ and $\mathbf{t}_2$ such that

$$\mathbf{n} = -\mathbf{u}_r / c_r \qquad \mathbf{t}_1 = \frac{\mathbf{n} \times \hat{\mathbf{i}}}{|\mathbf{n} \times \hat{\mathbf{i}}|} \qquad \mathbf{t}_2 = \mathbf{t}_1 \times \mathbf{n} \tag{3.12}$$

where $\hat{\mathbf{i}}$ is the unit vector along the x-axis in the global coordinate system. Next, $\mathbf{u}_r^*$ may be given in terms of the above unit vectors as

$$\mathbf{u}_r^* = c_r^* \left(\mathbf{n} \cos\delta + \mathbf{t}_1 \sin\delta \cos\varepsilon + \mathbf{t}_2 \sin\delta \sin\varepsilon \right) \tag{3.13}$$

Substitution of Eqs. (3.12) into Eq. (3.13) gives the following expressions for the components of $\mathbf{u}_r^*$:

$$\begin{aligned}
u_r^* &= \frac{c_r^*}{c_r}\left[-u_r \cos\delta + \sin\delta \sin\varepsilon (v_r^2 + w_r^2)^{1/2} \right] \\
v_r^* &= \frac{c_r^*}{c_r}\left[-v_r \cos\delta - \frac{\sin\delta (c_r w_r \cos\varepsilon + u_r v_r \sin\varepsilon)}{(v_r^2 + w_r^2)^{1/2}} \right] \\
w_r^* &= \frac{c_r^*}{c_r}\left[-w_r \cos\delta + \frac{\sin\delta (c_r v_r \cos\varepsilon - u_r w_r \sin\varepsilon)}{(v_r^2 + w_r^2)^{1/2}} \right]
\end{aligned} \tag{3.14}$$

Eqs. (3.14) are evaluated to find $\mathbf{u}_r^*$ if the collision involves diffuse reflection. Once the components of $\mathbf{u}_r^*$ have been calculated for either type of collision, the absolute gas molecule velocity is updated to a final value of $\mathbf{u}_m^* = \mathbf{u}_r^* + \mathbf{u}_p$, where $\mathbf{u}_p$ is the velocity assigned to the solid particle. Note that the collision-induced velocity difference for the

particle is assumed much smaller than that of the molecule. This follows from the previous assumption that the particle is much more massive than the particle, and allows the true post-collision particle velocity $\mathbf{u}_p^*$ to be replaced by $\mathbf{u}_p$ for the calculation of $\mathbf{u}_m^*$.

This procedure is repeated for each representative solid particle during every time step. It can be shown, by multiplying collision energy and momentum transfer expressions by Eqs. (3.1), (3.7), and (3.10) then integrating over the intervals $\delta \in [0,\pi]$ and $c_r^* \in [0,\infty)$, that the average momentum and energy imparted on a gas molecule through a collision are equal in magnitude, respectively, to the average momentum and energy transfer rates to the solid particle (given by Eqs. (2.1) and (2.2)) multiplied by the ratio of the time step Δt to the collision probability P_{coll}. This property has been verified for both specular and diffuse reflection, and confirms that the method described here is consistent with the force and heat transfer equations of *Gallis et al*. (2001) In addition, and in contrast to the one-way coupled method described in Section 2.1, the two-way coupling procedure allows the total momentum and energy of the flow to be conserved in a time-averaged sense.

3.2 Demonstration of momentum and energy conservation

In order to demonstrate the consistency of the two-way coupling method with the one-way coupling procedures discussed in Section 2.1, a sample simulation is performed. All flow properties are based on those expected along the axis and just beyond the nozzle exit plane in the exhaust flow of a small solid propellant rocket. The simulation geometry is simplified in order to isolate the effects of gas-particle interaction, and only a small domain is considered to limit the computational expense. The simulation is performed on

a rectangular two-dimensional grid, consisting of 0.1 mm long uniform inflow and outflow boundaries, separated on either end by 20 mm long specularly reflecting walls. The grid geometry is shown in Fig. (3.3). As no energy or longitudinal momentum may be transferred through the walls, it can be expected that, if the new two-way coupling method is physically consistent, the total momentum and energy flux will be the same over any transverse plane which passes through the grid.

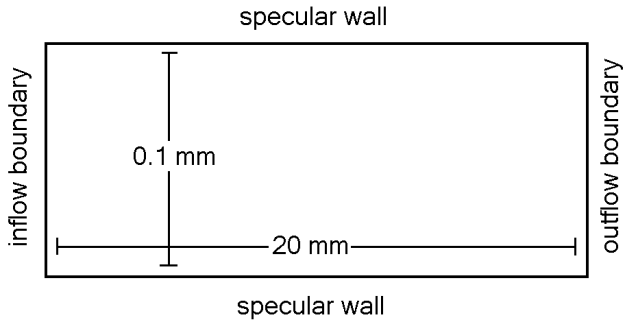

Figure 3.3. Grid dimensions and boundary types.

3.2.1 Simulation parameters

The gas in this simulation is a mixture of H_2, CO and N_2, with inflow number densities of $2\times10^{23}m^{-3}$, 1×10^{23} m^{-3} and 1×10^{23} m^{-3} respectively. At the inflow boundary the gas is assigned a bulk speed of 2000 m/s and a temperature of 1000K. The solid phase consists of spherical alumina particles, of diameter 3×10^{-6} m and 6×10^{-6} m, with a mass flow fraction of 40% divided equally between particles of either size. All particles have a velocity of 1200 m/s and a temperature of 2200 K at the inflow boundary, with a total particle mass flux of 13.33 kg/s-m^2.

The grid is divided into 5000 square cells of length 2×10^{-5} m, or approximately two mean free paths. Collisions within the gas phase are considered using the variable hard

sphere (VHS) model, with reference molecular diameters given by *Bird* (1994). The time step size is 1.5×10^{-9} s and the relative weights W_g and W_p are set so that, at steady state, about 270,000 computational gas molecules and 10,000 solid particles are contained within the grid. This corresponds to roughly 54 computational gas molecules and 2 solid particles per cell. Once steady state has been reached, various gas and particle properties are evaluated, and averaging is performed over approximately 200,000 time steps.

3.2.2 Results and discussion

Simulation results are shown in Figs. (3.4), (3.5) and (3.6), based on values extracted along a line between the centers of the inflow and outflow boundaries. Due to the relatively small changes in the characteristics of either phase expected over the limited grid domain, the interphase transfer of momentum and energy should be nearly constant with downstream distance, so that most flow properties will vary linearly through the grid. The expected linear variation is observed in Fig. (3.4), where average gas and particle speeds are plotted against longitudinal distance from the inflow boundary. The slower particle phase is found to accelerate at a nearly constant rate, while the faster gas decelerates as momentum is transferred to the particles.

Figure (3.5) shows the corresponding trends in the gas and particle number densities. Neglecting the significant statistical scatter, the particle number density is found to decrease approximately linearly and the gas number density is found to increase linearly, as is expected from comparison with Fig. (3.4) and considerations of mass conservation. In Fig. (3.6) the longitudinal variations in the average particle temperature and gas translational temperature are shown. The gas and particle temperatures are found to

increase and decrease respectively with downstream distance, as energy is transferred to the gas from the higher temperature particles.

As noted in Section 3.1, the accuracy and consistency of the two-way coupling method can be determined by verifying that momentum and energy are transferred between the two phases at equal rates, so that the total momentum or energy transfer rate will be the same through any transverse plane which intersects the grid domain. In order to show this, momentum and energy transfer rates of each phase are calculated along nine equally spaced planes. While approximations for these rates could be easily found through algebraic manipulations of the cell-averaged velocities, densities, and temperatures, the small size of the grid and the extreme sensitivity of flux values to statistical scatter require that a more direct approach be used.

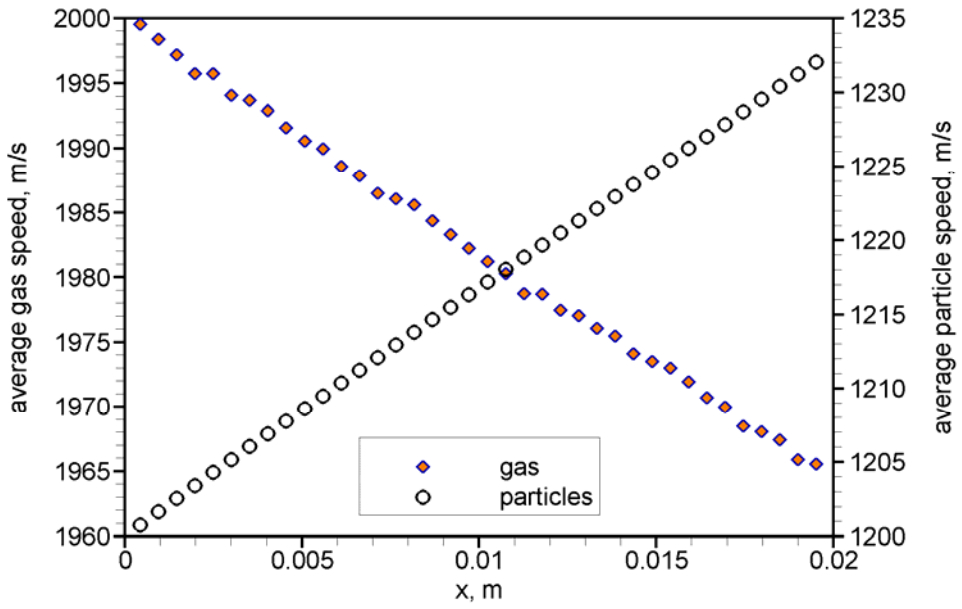

Figure 3.4. Longitudinal variation in average gas and particle speeds.

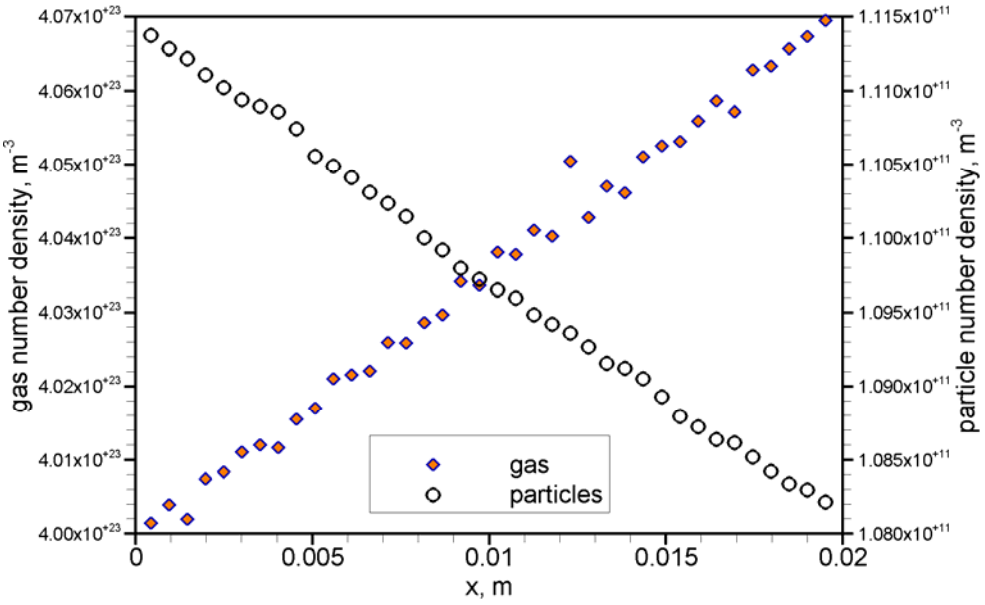

Figure 3.5. Gas and particle number densities.

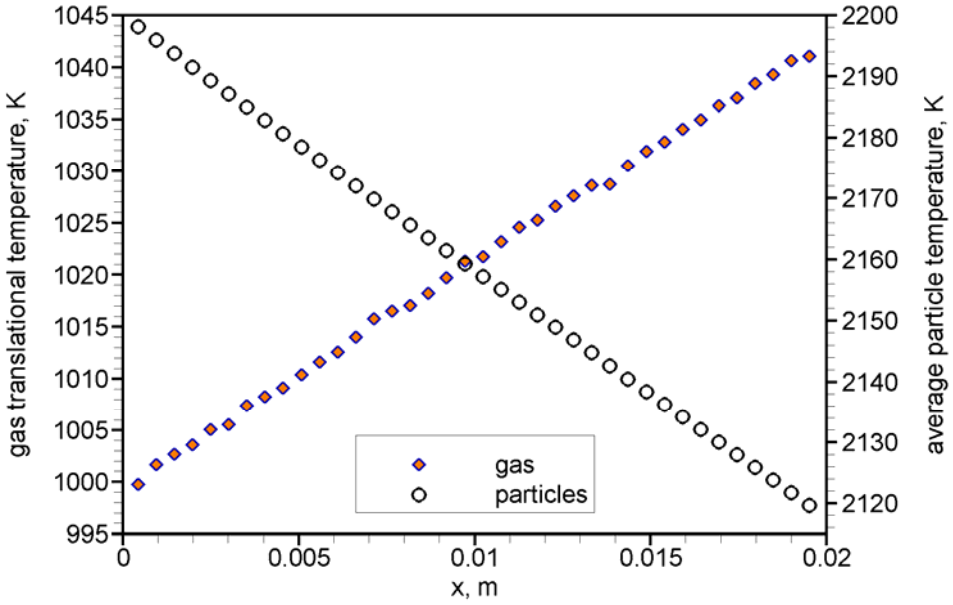

Figure 3.6. Variation in gas and particle temperatures.

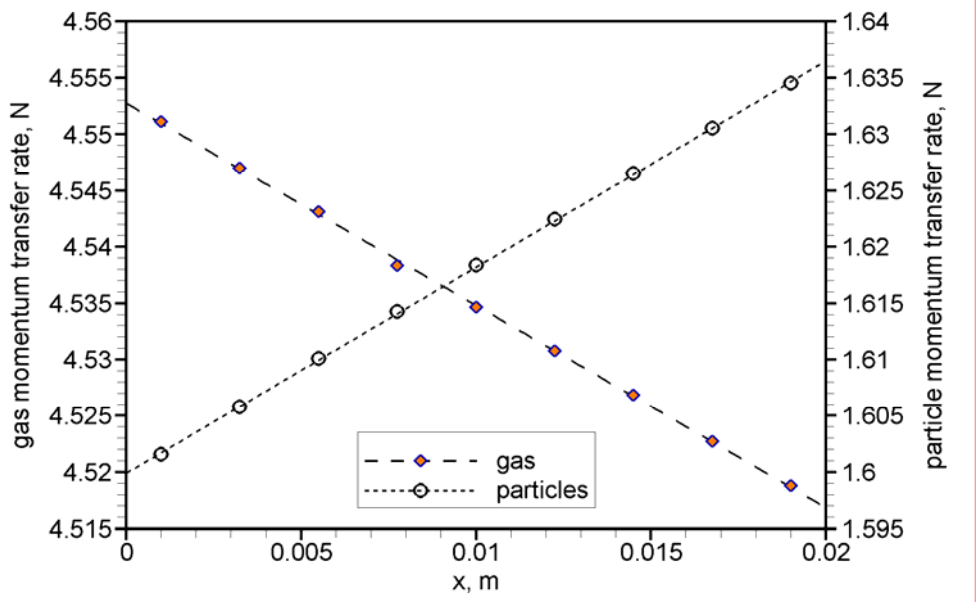

Figure 3.7. Variation in longitudinal momentum transfer rates with downstream distance.

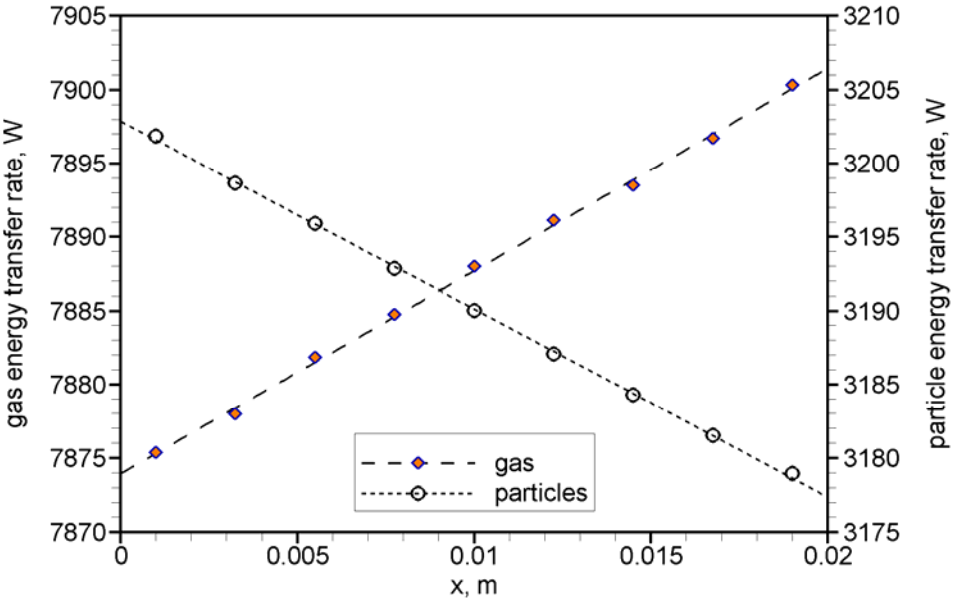

Figure 3.8. Energy transfer rates for gas and particles.

The procedure used here for calculating fluxes is as follows: During every time step for which sampling is performed, additional calculations are carried out to determine which computational gas molecules or solid particles pass through each of the nine planes. Values are recorded for the mass, momentum, and energy transferred through each plane, to which the mass, longitudinal momentum, kinetic energy, and internal energy of each of these objects is either added or subtracted, depending on the direction in which the object passes through the plane. Resulting values are then divided by the time step size Δt, and averaging is performed over all sampling time steps. Each time-averaged momentum and energy transfer value is then divided by the ratio of the corresponding mass transfer rate to the average mass transfer rate assigned at the inflow boundary (equal to 0.002 kg/s for the gas and 0.001333 kg/s for the particles).

Note that the last step is required to account for statistical fluctuations in the number of objects which pass through the selected planes. This is also necessary to correct for a slight reduction in the gas number flux with downstream distance, due to the fact that computational gas molecules may exit the grid through the inflow boundary. The correction is only on the order of 0.1%, but is found to significantly improve the accuracy of results, as the values of interest will vary only slightly through the length of the grid.

The variation in longitudinal momentum transfer rates is shown in Fig. (3.7). While different scales are used for the particles and gas, the ranges of both scales are equal, so that trends in the two profiles can be easily compared. As expected, momentum is found to be removed from the gas at nearly the exact rate that momentum is added to the particle phase. Both data sets are closely approximated by linear least-squares trend lines,

with slopes that differ in magnitude by less than 2%. Similar trends can be found in Fig. (3.8), which shows the variation in energy transfer rates with downstream distance. Again, the magnitudes of linear trend lines are nearly equal, and energy is observed to be removed from the particles at approximately the same rate that energy is added to the gas.

The small discrepancies which are observed in Figs. (3.7) and (3.8), and the local variation in the total momentum and energy transfer rates which these discrepancies imply, can be explained by a number of factors. First, some error may be due to the collision selection scheme given by Eq. (3.8), as gas molecules most likely to collide with a given particle may not be chosen as potential collision partners. This may slightly reduce the interphase collision frequency, and is a problem inherent in the NTC method of *Bird* (1994) on which the collision selection scheme is based.

A more likely error source is the fact that momentum and energy are conserved only in a time-averaged sense, as the instantaneous momentum and energy transfer arising from a single interphase collision is not modeled in the same manner for calculations used to alter properties of the two different phases. This difference in collision modeling arises from the wide disparity expected in number density between solid particles and gas molecules, so that the interphase collision frequency for a single solid particle is likely several orders of magnitude larger than that of a gas molecule. (For the simulation described here, these two collision frequencies differ by a factor of about 4×10^{12}.)

The lack of exact momentum and energy conservation should give rise to random walk errors, which are magnified in the results of Figs. (3.7) and (3.8) due to the extreme numerical sensitivity of the observed trends. However, these errors are shown to be relatively small, and are expected to further decrease when the sampling period is

lengthened. As the DSMC method generally requires time (or ensemble) averaging over a large number of time steps, instantaneous momentum and energy conservation should not be required to achieve levels of accuracy in the simulation results within the expected statistical scatter. It can therefore be assumed that Figs. (3.7) and (3.8) do adequately demonstrate the conservation of momentum and energy, so that the two-way coupling method is physically consistent with the procedures for momentum and energy exchange described in Section 2.1. The initial one-way coupling method is shown in Chapter 2 to exhibit a relatively high degree of overall accuracy, so it follows from the above arguments that the new method should be reasonably accurate as well.

3.3 Two-way coupling procedures for rotating particles

For the DSMC simulation of two-way coupled two phase flows involving rotating solid particles, the two-way coupling scheme must be consistent with the Green's function approach outlined in Section 2.4. In this case the net momentum exchange between a particle and the surrounding gas will include a transverse "lift" term associated with particle rotation, and the moment, rotational work and rotation-induced heat transfer on the particle must be included in procedures for two-way coupling.

As discussed in Section 2.4, particle rotation will have no effect on interphase collisions involving specular reflection, and the interphase collision frequency will be unaffected by particle rotation as well. Two-way coupling procedures involving rotating particles will therefore be similar to those described in Section 3.1.3: First, a number N_s of randomly selected potential collision partners are chosen for each representative particle during each time step, where the value of N_s is calculated using Eq. (3.8). Some

of the selected DSMC gas molecules are then determined to collide with the particle using a statistical sampling technique described in Section 3.1.3. A fraction (1-τ) of these collisions will involve specular reflection, and are again handled through the same techniques used for nonrotating particles. All other interphase collisions result in diffuse reflection with full thermal accommodation, and must be considered through a set of procedures which are different from those described above.

As stated in Section 3.1.2, for a diffusely reflecting collision involving a nonrotating particle, the magnitude and direction of the post-collision relative velocity will be statistically independent. This is not true however for a rotating particle, so in this case Eqs. (3.5) and (3.7) are not valid and an alternate numerical procedure must be used. The post-collision relative velocity $\mathbf{u}_r^*$ is found here by separately determining nonrotational $\mathbf{u}_{nr}^*$ and rotational $\mathbf{u}_{rot}^*$ components, then adding the two together. As a first step, the acceptance-rejection method is used with Eq. (3.10) to find the magnitude c_{nr}^* of $\mathbf{u}_{nr}^*$. The angle θ between the negative initial relative velocity vector $-\mathbf{u}_r$ and the outward normal unit vector $\mathbf{n}_c$ at the collision point on the particle surface is then calculated using Eq. (3.4). A corresponding azimuthal angle α_1 is sampled from a uniform distribution over $[0,2\pi]$.

Following expressions derived in Section 3.1.3, the outward normal unit vector $\mathbf{n}_c$ at the collision point may be given in terms of θ and α_1 as

$$\mathbf{n}_c = \mathbf{n}'\cos\theta + \mathbf{t}'_1 \sin\theta\cos\alpha_1 + \mathbf{t}'_2 \sin\theta\sin\alpha_1 \tag{3.15}$$

where the orthonormal vectors $\mathbf{n}'$, $\mathbf{t}'_1$ and $\mathbf{t}'_2$ are defined by

$$\mathbf{n}' = -\mathbf{u}_r / c_r \qquad \mathbf{t}'_1 = \frac{\mathbf{n}'\times\hat{\mathbf{i}}}{|\mathbf{n}'\times\hat{\mathbf{i}}|} \qquad \mathbf{t}'_2 = \mathbf{t}'_1\times\mathbf{n}' \tag{3.16}$$

and $\hat{\mathbf{i}}$ is the unit vector along the x-axis in the global coordinate system. Substitution of Eqs. (3.16) into Eq. (3.15) gives expressions for the three components of $\mathbf{n}_c$.

$$n_{c,x} = \frac{1}{c_r}\left[-u_r\cos\theta + \sin\theta\sin\alpha_1 (v_r^2 + w_r^2)^{1/2}\right]$$

$$n_{c,y} = \frac{1}{c_r}\left[-v_r\cos\theta - \frac{\sin\theta\,(c_r w_r \cos\alpha_1 + u_r v_r \sin\alpha_1)}{(v_r^2 + w_r^2)^{1/2}}\right] \tag{3.17}$$

$$n_{c,z} = \frac{1}{c_r}\left[-w_r\cos\theta + \frac{\sin\theta(c_r v_r \cos\alpha_1 - u_r w_r \sin\alpha_1)}{(v_r^2 + w_r^2)^{1/2}}\right]$$

Next, we find the angle φ between the vectors $\mathbf{n}_c$ and $\mathbf{u}_{nr}^*$ as in Section 3.1.2 by sampling $\sin^2\varphi$ from a uniform distribution over [0,1]. An azimuthal angle α_2 relative to a plane normal to the x-axis is sampled from a uniform distribution over $[0,2\pi]$. Once the normal vector $\mathbf{n}_c$ is known and values have been selected for φ, α_2 and c_{nr}^*, the nonrotational component $\mathbf{u}_{nr}^*$ of the post-collision relative velocity is determined. This velocity can be expressed as

$$\mathbf{u}_{nr}^* = c_{nr}^*\left(\mathbf{n}_c\cos\varphi + \mathbf{t}''_1\sin\varphi\cos\alpha_2 + \mathbf{t}''_2\sin\varphi\sin\alpha_2\right) \tag{3.18}$$

where the unit vectors $\mathbf{t}''_1$ and $\mathbf{t}''_2$ are defined by

$$\mathbf{t}''_1 = \frac{\mathbf{n}_c \times \hat{\mathbf{i}}}{|\mathbf{n}_c \times \hat{\mathbf{i}}|} \qquad \mathbf{t}''_2 = \mathbf{t}''_1 \times \mathbf{n}_c \tag{3.19}$$

The following expressions may be derived from Eqs. (3.18) and (3.19) to find the components of $\mathbf{u}_{nr}^*$:

$$u_{nr}^* = c_{nr}^*\left[n_{c,x}\cos\varphi + \sin\varphi\sin\alpha_2 (1 - n_{c,x}^2)^{1/2}\right]$$

$$v_{nr}^* = c_{nr}^*\left[n_{c,y}\cos\varphi + \frac{\sin\varphi(n_{c,z}\cos\alpha_2 - n_{c,x}n_{c,y}\sin\alpha_2)}{(1 - n_{c,x}^2)^{1/2}}\right] \tag{3.20}$$

$$w_{nr}^{*} = c_{nr}^{*}\left[n_{c,z}\cos\varphi - \frac{\sin\varphi\,(n_{c,y}\cos\alpha_2 + n_{c,x}n_{c,z}\sin\alpha_2)}{(1-n_{c,x}^2)^{1/2}} \right]$$

Finally, the rotational component of $\mathbf{u}_r^*$ is computed as $\mathbf{u}_{rot}^* = R_p\,\boldsymbol{\omega}_p \times \mathbf{n}_c$ where R_p and $\boldsymbol{\omega}_p$ are the particle radius and angular velocity respectively, and the gas molecule velocity is reassigned to the post-collision value $\mathbf{u}_p + \mathbf{u}_{nr}^* + \mathbf{u}_{rot}^*$. For a diffusely reflecting collision involving a diatomic gas molecule, the rotational energy of the molecule must also be resampled from an equilibrium distribution at the particle temperature, as given by Eq. (3.11).

Chapter IV

Additional Models for SRM Plume Simulation

4.1 Overview

While the DSMC method allows for a high degree of accuracy in the simulation of rarefied gas flows, excessive computational cost is often cited as a major drawback. The same is true for the two-phase model described in Chapters 2 and 3; calculations are generally very expensive, such that any improvement in efficiency will help extend the applicability of the method to larger-scale flows. With this in mind, a series of coupling parameters are developed to quantitatively evaluate the importance of interphase momentum and energy exchange for both the particles and gas. If coupling in a particular direction and location is determined to have a negligible effect on bulk flow characteristics, corresponding calculations for momentum or energy exchange can then be avoided, and the overall numerical efficiency will increase.

In the current implementation, four different nondimensional parameters are periodically evaluated in each cell within the computational grid, and time-averaged parameter values are compared to set cutoff values to assess the significance of interphase coupling in either direction. Derivations are provided for all parameters, and a time-averaging scheme used to reduce memory requirements is described.

As discussed in Chapter 1, phase change processes involving liquid Al_2O_3 may have a significant impact on a variety of SRM plume flow properties, so that the accurate simulation of high altitude plume flows generally requires inclusion of a model for Al_2O_3 particle phase change. Propulsive efficiency, particle radiation, particle size distributions and other flow characteristics are strongly dependent on the phase composition of particles within the nozzle and plume. [*Reed and Calia* (1993)]

At the nozzle exit plane, the smallest particles are typically made up of some combination of stable α and metastable γ solid phases, while the largest particles consist entirely of liquid Al_2O_3. Particles of intermediate size may exist as multiphase "slush balls" within the plume nearfield region, where finite-rate crystallization kinetics and steam release allow for combinations of liquid, multiple solid phases, and trapped water vapor within a single particle. [*Gosse et al.* (2003)] Phase composition and phase change processes will have direct and significant effects on the refractive index and the temperature distribution for the particles, as well as other flow characteristics which may be of interest. Accurate plume simulation therefore requires the consideration of particle phase change, particularly the initial crystallization process for liquid Al_2O_3.

A nonequilibrium particle phase change model is presented here, following procedures of *Henderson* (1977), *Hunter et al.* (1981) and *Plastinin et al.* (1998) In this model, it is assumed that homogeneous crystallization begins on the surface of a liquid droplet, at a nucleation temperature well below that required for equilibrium melting. A heterogeneous crystallization front then progresses toward the particle center, at a velocity which varies as a function of the particle temperature. During this process, the particle temperature may either increase or decrease, depending on the balance between

convective heat transfer and heat release during crystallization. A simple model for particle melting is also implemented to account for any phase change effects associated with particle-shock interactions. [*Hunter et al.* (1981)] Following a detailed description of the phase change model, results from a series of subscale plume flow simulations are used to indicate the potential importance of particle phase change, and to find appropriate cutoff values for the determination of regions with significant interphase coupling.

4.2 Interphase coupling parameters

To reduce the computational cost of two-phase DSMC plume flow simulations, calculations for momentum and energy exchange between the gas and particles should ideally be made only where the flow is locally determined to involve significant interphase coupling. A series of coupling parameters are proposed so that this determination may be made automatically during a simulation. Coupling parameters are periodically evaluated in each grid cell during two-phase DSMC calculations, and regions of interphase coupling are identified through a comparison between time-averaged parameter values and predetermined cutoff values.

Four separate coupling parameters are used here. The first parameter P_{1m} quantifies the importance of momentum coupling from the gas to the particles; a smaller value of P_{1m} indicates that the gas has less influence on the particle phase momentum flux. A second parameter P_{1e} relates to energy coupling from the gas to the particles, while parameters P_{2m} and P_{2e} indicate the significance of momentum and energy coupling, respectively, from the particles to the gas. These parameters are formulated with the goal

of minimizing the cost of parameter evaluations, while allowing for reasonable accuracy over a wide range of flow regimes.

4.2.1 Gas-to-particle momentum coupling

The gas-to-particle momentum coupling parameter P_{1m} is defined here to scale with the fractional change in average particle speed, due to interphase momentum transfer, over the mean time required for particles to move a streamwise distance L. The variable L here represents some global characteristic length scale; for a plume flow we set L to equal the nozzle exit diameter. Neglecting spatial variation in the particle speed gradient ∇c_p, it follows that

$$P_{1m} \propto \frac{1}{c_p}\left(L\frac{\mathbf{u}_p}{c_p}\right)\bullet\nabla c_p = \frac{\partial c_p}{\partial t}\frac{L}{c_p^{\,2}} \tag{4.1}$$

where $\mathbf{u}_p$ and c_p are the local bulk velocity and speed of the particle phase, respectively.

To evaluate the $\frac{\partial c_p}{\partial t}$ term, we use the fact that $m_p\frac{\partial c_p}{\partial t}$ is roughly equal to the product of the average interphase collision frequency f_p for a single particle and the magnitude of the average momentum transferred per collision. (In the special case where every particle in the cell has the same mass and velocity, it can be shown that $m_p\frac{\partial c_p}{\partial t}$ is equal to the dot product of this average momentum transfer and $f_p\mathbf{u}_p/c_p$.) If all particles are much larger than gas molecules and the thermal speed of the particle phase is small, then the collision frequency may be approximated as

$$f_p = \tfrac{1}{4}\,\pi n_g c_{r2} D_p^{\,2} \tag{4.2}$$

where n_g is the gas number density, D_p is the average particle diameter, and c_{r2} is the average gas molecule speed relative to $\mathbf{u}_p$. If there are N_g DSMC gas molecules in the computational cell of interest, each with some velocity $\mathbf{u}_{m,i}$, then the quantity c_{r2} can be given by

$$c_{r2} = \frac{1}{N_g} \sum_{i=1}^{N_g} |\mathbf{u}_{m,i} - \mathbf{u}_p| . \tag{4.3}$$

In determining the average momentum transfer per collision, we assume that all particles are much more massive than gas molecules, and that following an interphase collision the gas molecule velocity is on average equal to that of the particle. As shown in Section 3.1, the latter assumption is exact for specularly reflecting collisions, and is a reasonably good approximation for diffusely reflecting collisions. Under these assumptions, the average momentum transfer magnitude is roughly equal to mc_{r1}, where m is the mass per gas molecule, and c_{r1} is the magnitude of the difference between $\mathbf{u}_p$ and the gas bulk velocity $\mathbf{u}_g$. The magnitude of the average force exerted by the gas on a single particle can then be given as

$$m_p \frac{\partial c_p}{\partial t} = f_p \, m \, c_{r1} = \tfrac{1}{4} \pi \rho_g \, c_{r2} \, D_p^{\,2} \, c_{r1} \, . \tag{4.4}$$

where $\rho_g = m n_g$ is the mass density of the gas. Next, Eq. (4.4) is rearranged and substituted into Eq.(4.1), and the average particle mass m_p is approximated as $\frac{\pi}{6} \rho_p D_p^{\,3}$. Ignoring a multiplicative constant of order one, we then have the final formulation for the momentum coupling parameter P_{1m}:

$$P_{1m} = \frac{\rho_g}{\rho_p} \frac{c_{r1} c_{r2}}{c_p^{\,2}} \frac{L}{D_p} \tag{4.5}$$

4.2.2 Particle-to-gas momentum coupling

An expression for the parameter P_{2m}, which characterizes momentum coupling from the particles to the gas, is derived in a similar manner as that of P_{1m} above. Following *Crowe et al*. (1998), P_{2m} is proportional to the magnitude of the total drag force on the particle phase per unit volume, divided by the streamwise gas momentum flux and nondimensionalized through multiplication by the length scale L. The streamwise gas momentum flux is approximated here as $\rho_g c_{g1}^2$, and from Eq. (4.4) the magnitude of the force per unit volume is $\frac{1}{4}\pi \rho_g c_{r2} D_p^2 c_{r1} n_p$ where n_p is the particle number density and c_{g1} is the bulk gas speed. Neglecting a constant of order one, the parameter P_{2m} may then be defined by

$$P_{2m} = n_p D_p^2 L \frac{c_{r1} c_{r2}}{c_{g1}^2} . \tag{4.6}$$

In comparing Eqs. (4.5) and (4.6), note that an identical formulation for P_{1m} could be found by substituting an approximate particle momentum flux $m_p n_p c_p^2$ for the gas momentum flux in the derivation of P_{2m}. The above derivation for Eq. (4.5) is used only to show the physical significance of this parameter.

4.2.3 Gas-to-particle energy coupling

The definition of the parameter P_{1e} for energy coupling from the gas to the particles is analogous to that of P_{1m}: Here P_{1e} scales with the fractional change in average particle temperature T_p over the time required for particles to travel a streamwise distance L.

$$P_{1e} \propto \frac{1}{T_p}\left(L \frac{\mathbf{u}_p}{c_p} \right) \bullet \nabla T_p = \frac{\partial T_p}{\partial t} \frac{L}{c_p T_p} \tag{4.7}$$

The time-derivative of T_p is related to the average heat transfer rate $\dot{Q}_p$ per particle by $\dot{Q}_p = c_s m_p \frac{\partial T_p}{\partial t}$ where c_s is the particle specific heat. Approximating m_p as $\frac{\pi}{6}\rho_p D_p^3$, we then have

$$P_{1e} \propto \left(\frac{6}{\pi} \frac{\dot{Q}_p}{\rho_p D_p^3 c_s} \right) \frac{L}{c_p T_p} \ . \tag{4.8}$$

Note that $\dot{Q}_p$ is equal to the product of the interphase collision frequency f_p and the average heat transfer per collision. To evaluate the latter term, a few initial assumptions are used: First, we assume that the interphase heat transfer process is dominated by the exchange of gas translational energy. It is also assumed that the ratio of $|\mathbf{u}_p - \mathbf{u}_g|$ to the local sonic speed of the gas (the average particle Mach number) is much less than one. Under such conditions the mean translational energy of a colliding gas molecule in a particle-centered coordinate system can be approximated as $\frac{2}{3} m\, c_{r3}^2$ The variable c_{r3} is defined here as the root-mean-squared gas molecule speed relative to the bulk particle velocity $\mathbf{u}_p$, and may be calculated as

$$c_{r3} = \left(\frac{1}{N_g} \sum_{i=1}^{N_g} |\mathbf{u}_{mi} - \mathbf{u}_p|^2 \right)^{1/2} \tag{4.9}$$

If the collision involves diffuse reflection with full thermal accommodation to the particle temperature, then the average post-collision translational energy will be $2k_B T_p$. Otherwise specular reflection is assumed, and the gas molecule will retain its initial translational energy relative to the particle. From the above approximations, it follows that

$$\dot{Q}_p = \frac{\pi}{6} n_g c_{r2} D_p^2 \tau \left(m c_{r3}^2 - 3 k_B T_p \right). \tag{4.10}$$

By definition, all coupling parameters here must be greater than or equal to zero, so the absolute value of $\dot{Q}_p$ is used in the equation for P_{1e}. Substitution into Eq. (4.8) then gives the following result:

$$P_{1e} = \frac{L}{D_p} \frac{c_{r2}}{c_p} \frac{\rho_g}{\rho_p} \frac{\tau}{c_s T_p} \left| c_{r3}^2 - \frac{3 k_B T_p}{m} \right| \tag{4.11}$$

While Eq. (4.11) has been derived for a flow in which the average particle Mach number is low and gas internal energy transfer is negligible during interphase collisions, this parameter should be able to accurately characterize energy coupling over a very wide range of flow regimes. If, for example, the parameter were derived under the assumption that the particles move hypersonically with respect to the gas, the coefficient 3 in Eq. (4.11) would be replaced by 4, and all other terms would be identical. Moreover, this last term becomes negligible in comparison with c_{r3}^2 as the relative Mach number increases, so that Eq. (4.11) should be equally valid at the high and low Mach number limits.

4.2.4 Particle-to-gas energy coupling

The final coupling parameter P_{2e}, which determines the importance of energy coupling from the particle phase to the gas, has a similar definition to that of P_{2m}. Again following *Crowe et al.* (1998), P_{2e} is proportional to the interphase energy transfer rate $\dot{E}$ per unit volume, and inversely proportional to the streamwise energy flux of the gas Φ_g. In determining the energy transfer rate, we neglect particle rotation effects and assume that all particles are much more massive than gas molecules. It follows from these

assumptions that $\dot{E} = \dot{Q}_p n_p$, so nondimensionalization by the length scale L gives the relation $P_{2e} \propto \dot{Q}_p n_p L/\Phi_g$.

Next, $\dot{Q}_p$ is given by Eq.(4.10), and the energy flux Φ_g is approximated as the product of the streamwise gas number flux and the average energy per molecule. For simplicity we consider the special case of a monatomic simple gas, where the latter term will equal $\frac{1}{2} m_g c_{g2}^2$ and $\Phi_g \approx \frac{1}{2} \rho_g c_{g1} c_{g2}^2$. Here the variable c_{g2} represents the root-mean-squared gas molecule velocity, and may be calculated as

$$c_{g2} = \left(\frac{1}{N_g} \sum_{i=1}^{N_g} \mathbf{u}_{m,i} \cdot \mathbf{u}_{m,i} \right)^{1/2} . \tag{4.12}$$

Neglecting a coefficient of order one, substitution into the above relation for P_{2e} gives the formula

$$P_{2e} = n_p L \, D_p^2 \frac{c_{r2}}{c_{g1}} \frac{\tau}{c_{g2}^2} \left| c_{r3}^2 - \frac{3 k_B T_p}{m_g} \right| . \tag{4.13}$$

4.2.5 Implementation in DSMC

As implemented in the DSMC code MONACO for two-phase flow simulations, all four coupling parameters are periodically evaluated at each cell within the computational grid. For the local determination of interphase coupling, a few additional symbols are required: Let C_1 represent a user-defined cutoff value for momentum and energy coupling from the gas to the particle phase, and define C_2 as the equivalent value for coupling from the particles to the gas. If $\max\{P_{1m}, P_{1e}\} \geq C_1$ then a parameter Ψ_1 is set to equal one; otherwise Ψ_1 will equal zero. A similar parameter Ψ_2 will be one if $\max\{P_{2m}, P_{2e}\} \geq C_2$ or

zero if $\max\{P_{2m},P_{2e}\}<C_2$. Next, define $<\Psi_1>$ and $<\Psi_2>$ as the average of a large number of evaluations of Ψ_1 and Ψ_2, respectively, in a given cell. In the case of a steady flow simulation, these averages are taken over all Ψ_1 and Ψ_2 values calculated for the cell following the attainment of steady state conditions.

The values of $<\Psi_1>$ and $<\Psi_2>$ are then used to determine the importance of coupling. At any given cell, interphase momentum and energy transfer are assumed to significantly affect particle properties only if $<\Psi_1> \geq ½$. (This is equivalent to the condition that $\max\{P_{1m},P_{1e}\}\geq C_1$ is satisfied at least 50% of the time.) Various properties of particles in the cell are therefore altered due to particle-gas interaction only if this condition is met. Otherwise all related calculations are avoided, and numerical efficiency is improved through a reduction in the total number of operations. Similarly, calculations described in Chapter 3 for use in modifying local gas phase properties are performed only if $<\Psi_2> \geq ½$.

The procedure described here is expected to significantly reduce the overall computational cost of a variety of two-phase DSMC simulations. This is particularly true for the high altitude SRM plume flows of interest, where interphase coupling in either direction may be important only within a small fraction of the flowfield under consideration. The reduction in total simulation time associated with this procedure will be considered for a representative plume flow in Section 4.4.

4.3 Particle phase change

As discussed in Chapter 1, the phase composition of an individual particle within an SRM plume flow is typically a strong function of particle size, position in the plume, nozzle geometry and several other factors. Phase change processes will in turn influence

the particle temperature, as well as that of the surrounding gas, and may greatly affect radiative properties throughout the plume. Several previous studies involving SRM exhaust flow simulations have included consideration of the nonequilibrium phase change processes typical to such flows. [*Reed and Calia* (1993), *Henderson* (1977)] However, little effort has been devoted to the detailed characterization of particle phase composition in high altitude plume flows, where the flow around an individual particle is locally free-molecular and gas-particle interactions must be considered through a kinetic theory based approach.

Following the model of *Hunter et al.* (1981) we consider only the dominant crystallization process involving formation of the metastable γ phase, and neglect the γ-to-α transition which typically occurs among smaller particles in the nearfield plume region. The omission of a secondary phase change model is justified by both a lack of experimental data and an assumption that the γ-to-α transition has a relatively small effect on most flowfield properties of interest. However, any reduction in simulation accuracy associated with this omission is corrected in part by the fact that the value used here for the latent heat of fusion ($h_f = 1.07\times10^6$ J/kg) accounts for the full transition of particle material from liquid alumina to the stable α phase.

The standard model for crystallization kinetics in Al_2O_3 particles involves an assumption that the phase change process is initiated only after a spherical liquid droplet has supercooled to a nucleation temperature T_f significantly below the equilibrium melting temperature T_m. Once this occurs, nucleation takes place uniformly over the outer surface of the particle, and a heterogeneous crystallization front then progresses

toward the particle center at a rate given by

$$\frac{dr_l}{dt} = -\frac{A_c}{R_p}(T_m - T_p)^{n_c} \tag{4.14}$$

where T_p and R_p are the particle temperature and radius respectively, r_l is the ratio of the crystallization front radius to R_p, and A_c and n_c are constants with $A_c = 2.7\times10^{-6}$ $ms^{-1}K^{-1.8}$ and $n_c = 1.8$ as given by *Plastinin et al.* (1996) This variation in r_l in turn affects the particle temperature through the energy balance equation

$$c_s\, m_p \frac{dT_p}{dt} = \dot{Q}_p - 3\, h_f m_p\, r_l^2 \frac{dr_l}{dt}. \tag{4.15}$$

As currently implemented, the relation between the interphase heat transfer rate $\dot{Q}_p$ and the temporal variation in particle temperature is divided into three separate cases: solidification, melting, and constant-phase heating or cooling. First, if $T_p < T_f$ and $r_l = 1$, or if $T_p < T_m$ and $r_l \in (0,1)$, then the particle is determined to be in the process of solidification, and r_l is updated according to Eq. (4.14). The temperature change ΔT_p is then given by

$$\Delta T_p = \frac{\dot{Q}_p\, \Delta t}{c_s\, m_p} - \frac{h_f}{c_s}\Delta\left(r_l^3\right) \tag{4.16}$$

where $\Delta(r_l^3)$ is the variation in r_l^3 during the time step of length Δt. This case must be considered for all particles throughout the grid domain, even in regions where gas-to-particle coupling is neglected.

The relatively large local Δt values which can be encountered for solidifying particles within uncoupled regions may produce significant discretization errors in ΔT_p, such that T_p can exceed the melting temperature T_m during the crystallization process. To avoid this possibility, a variable N_s is set to equal the smallest integer for which $N_s >$

$50\times\Delta T_p/T_m$. If $N_s > 1$ then the initial values of T_p and r_l are reassigned to the particle, the time step is divided into N_s intervals of length $\Delta t/ N_s$, and the above procedure is iteratively repeated N_s times to find the final values of T_p and r_l.

If $T_p \geq T_m$, $r_l < 1$ and $\dot{Q}_p > 0$, then the particle is in the process of melting. In this case we assume that T_p is held constant and all thermal energy transferred to the particle is used in the phase transition. Note that for a melting particle, the normalized crystallization front radius r_l does not physically represent a phase transition surface, but is used instead to record the cube-root of the liquid volume fraction. The current implementation enforces energy conservation by allowing for the special case when, in a single time step, the last solid material in the particle melts and the remaining collision energy is used to increase the particle temperature. Following *Hunter et al.* (1981) the normalized front radius is first updated according to Eq.(4.16), where ΔT_p is set equal to zero. If the resulting r_l value is greater than one, then the particle temperature is increased by

$$\Delta T_p = \frac{h_f}{c_s}\left(r_l^3 - 1\right) \tag{4.17}$$

after which r_l is set to equal one. In the last case, where the particle is neither solidifying nor melting, the temperature is varied as

$$\Delta T_p = \frac{\dot{Q}_p \, \Delta t}{c_s \, m_p} \tag{4.18}$$

following the standard procedure for Lagrangian tracking of single-phase particles.

4.4 Application to a representative plume flow

In order to evaluate the above models, demonstrate capabilities of the code, and determine appropriate coupling parameter cutoff values, simulations are performed for a subscale SRM exhausting into a vacuum. Inflow conditions along the nozzle exit plane are based on values provided by *Anfimov et al.* (1993) for a Star 27 SRM used in the Bow Shock Ultraviolet 2 test flight discussed in Chapter 1, with dimensions reduced by a factor of 10 for a nozzle exit inner diameter of 7.85 cm. While the reduction in scale should ideally be accompanied by increases in particle velocity and temperature lags, the goal here is to determine general characteristics of a representative plume flow, so this error source can be tolerated with the understanding that the precise modeling of an actual flow is not desired here. The scale reduction allows for a dramatic decrease, by about two orders of magnitude, in overall computational cost.

4.4.1 Simulation parameters

The gas is a mixture of N_2, H_2 and CO, and the variable hard sphere (VHS) collision model [*Bird* (1994)] is used for collisions within the gas phase. At the nozzle exit, the gas is assigned a bulk speed of 3113 m/s, a temperature of 1433 K and a density of 0.011 kg/m^3, with mole fractions of 0.38 for H_2 and 0.31 for both N_2 and CO. The particle mass loading at the nozzle exit is approximately 30%, and particles are divided into a discrete size distribution with seven diameter values ranging from 0.3 to 6 μm. Due to a lack of available flowfield information at the nozzle exit, most particle properties given by *Anfimov et al.* (1993) are assumed uniform over the exit plane. The one exception is in the initial particle directions; for both particles and gas, bulk velocities along the nozzle

exit plane are set to scale linearly with distance from the axis. Particle trajectories and gas streamlines at the nozzle exit will have no radial component along the axis, and will reach a maximum off-axis angle of 17.2° (equal to the nozzle divergence angle) at the nozzle lip.

A rough estimate of the initial solid mass fraction for each particle size is found by taking the difference between the nucleation temperature (T_f = 1930 K) for homogeneous crystallization of Al_2O_3 and the assigned particle temperature, then multiplying this by the ratio of the specific heat to the latent heat of fusion for liquid Al_2O_3. Based on this procedure and the initial particle temperatures given by *Anfimov et al.*, at the nozzle exit the largest particles are in a completely liquid state and the smallest particles have a liquid mass fraction of 58%. Particle properties at the nozzle exit are given in Table (4.1).

Diameter, μm	Mass flux, kg/m^2s	Temperature, K	Speed, m/s	Liquid mass fraction
0.3	0.0443	1562	2992	0.579
0.4	0.0367	1634	3051	0.661
0.6	0.133	1834	3023	0.89
1	0.592	2293	2973	1
2	2.29	1920	2855	0.989
4	7.53	2178	2674	1
6	1.84	2407	2472	1

Table 4.1 Particle properties at the nozzle exit.

The thermal accommodation coefficient on the particle surface is set to 0.9, so that 90% of interphase collisions involve diffuse reflection with full accommodation to the particle temperature while the remaining 10% involve specular reflection. Interphase momentum and energy transfer is computed using the two-way coupling approach

described in Chapters 2 and 3, and the crystallization of liquid Al_2O_3 droplets is considered using the phase change model outlined in Section 4.3.

An axisymmetric simulation is performed on an unstructured rectangular grid extending from the nozzle exit plane 100 m downstream and 40 m outward from the central axis. The simulation is repeated for several different coupling parameter cutoff values, where values for both gas-to-particle and particle-to-gas coupling are equal and range from 0 to 0.1. Each case requires about 200 CPU hours on four 1.4 GHz AMD Opteron processors.

4.4.2 Variation in calculated flow properties with cutoff values

Figure (4.1) shows the variation in the maximum downstream distance for interphase coupling in either direction as a function of the cutoff values. Except for the largest cutoff values considered, the length of the coupling domain is found to vary as roughly the inverse square-root of the corresponding cutoff value. It follows that, as expected, smaller cutoff values result in greater residence time for either particles or gas molecules within the region where they may be influenced by interphase momentum or energy transfer.

In Fig. (4.2), the axial velocity component for the smallest particle size is plotted as a function of the cutoff value for gas-to-particle coupling, at two different points located 50 m downstream from the nozzle exit plane and distances of 3.5 m and 14 m from the central axis. Corresponding plots are given as Figs. (4.3) and (4.4) for particles of intermediate size (1 μm diameter) and for the largest particles, respectively. As shown on all three plots, farfield particle velocity varies significantly with the cutoff value C_1 for $C_1 > 10^{-4}$, while a relatively weak dependence is found for $C_1 \leq 10^{-4}$.

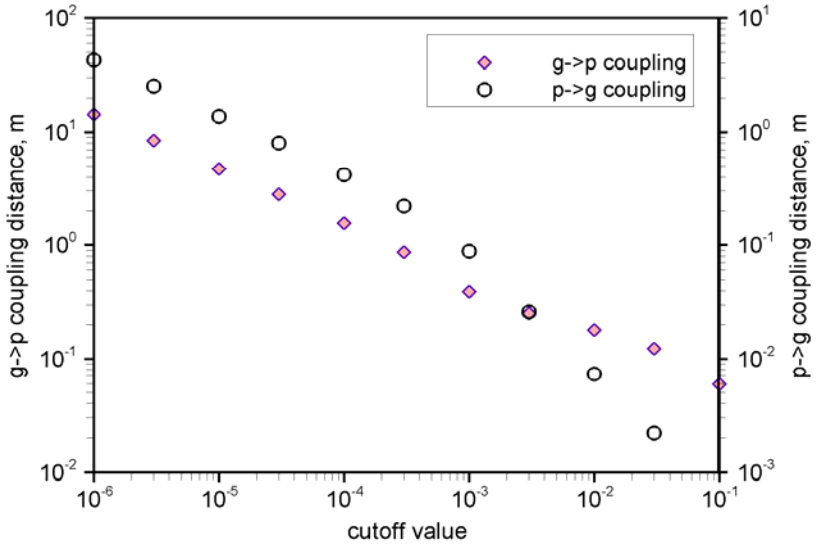

Figure 4.1. Maximum downstream distance for interphase coupling.

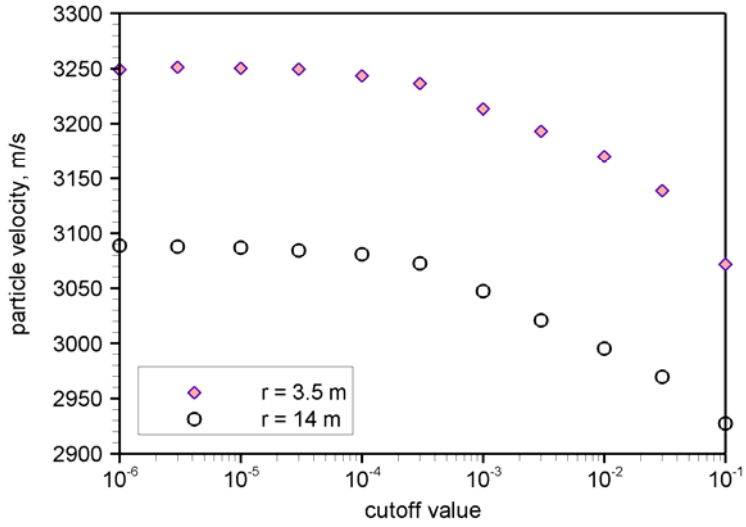

Figure 4.2. Axial velocity component for 0.3 μm diameter particles as a function of cutoff value C_1 for gas-to-particle coupling.

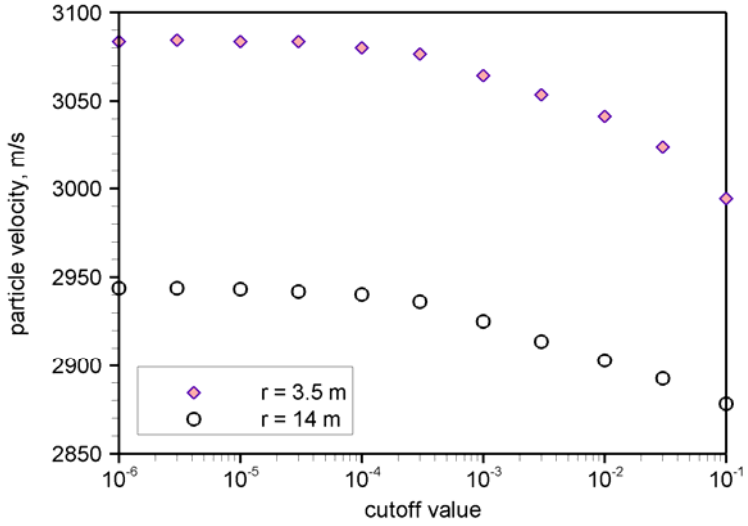

Figure 4.3. Axial velocity component for 1 μm particles as a function of cutoff value.

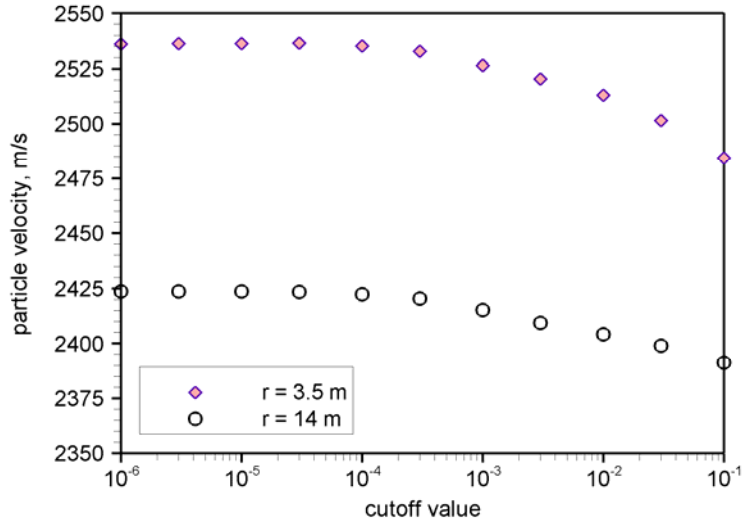

Figure 4.4. Axial velocity component for 6 μm particles as a function of cutoff value.

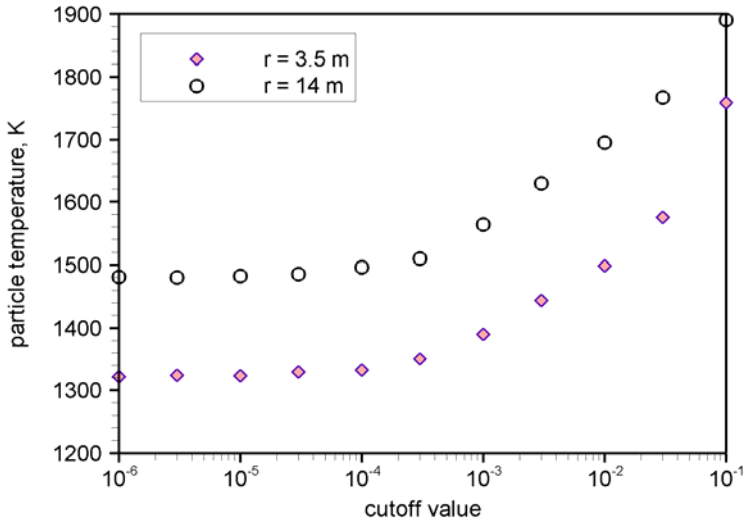

Figure 4.5. Temperature of 0.3 μm particles as a function of cutoff value.

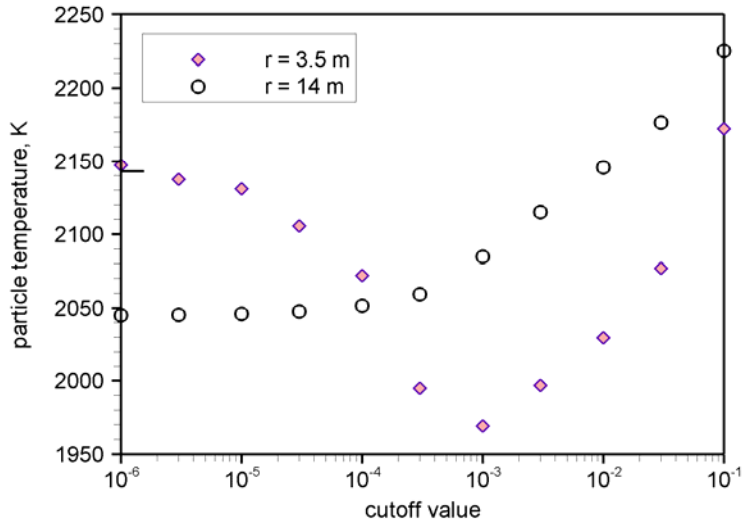

Figure 4.6. Temperature of 1 μm particles as a function of cutoff value.

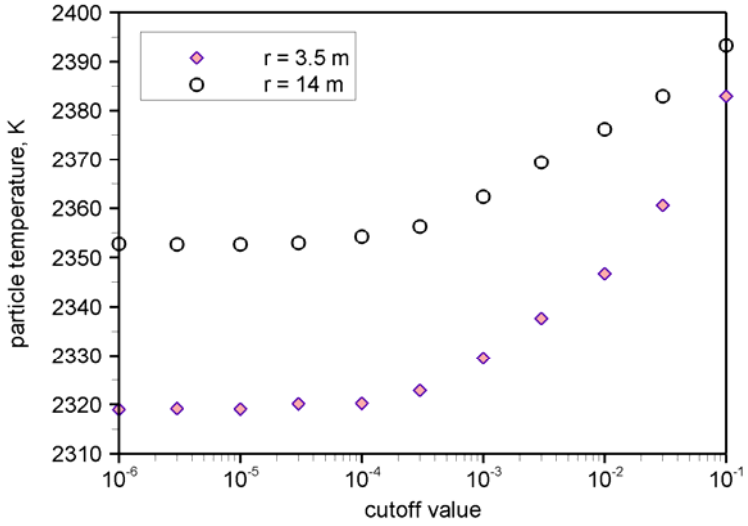

Figure 4.7. Temperature of 6 μm particles as a function of cutoff value.

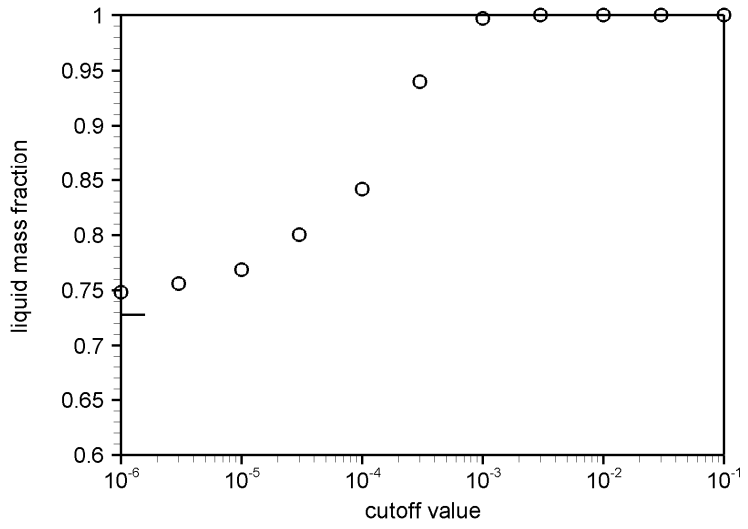

Figure 4.8. Variation in liquid mass fraction for 1 μm particles.

A similar trend is observed in Figs. (4.5) through (4.7), which show the variation with C_1 in particle temperature for the same three particle sizes and at the same two locations. Again particle temperature is generally found to be a strong function of the cutoff value only for $C_1 > 10^{-4}$. The one exception to this trend is found in Fig. (4.6), for 1 μm diameter particles at the point (50,3.5). In this case, the average particle temperature initially decreases as C_1 is reduced from the maximum value of 0.1, due to the corresponding increase in particle residence time within the gas-to-particle coupling region where heat is transferred from particles to the colder surrounding gas. However, for $C_1 < 10^{-3}$ the average particle temperature increases as C_1 is further reduced. This is explained by the fact that for this particular case, the residence time of 1 μm particles within the gas-to-particle coupling region is great enough for a fraction of the initially liquid particles to cool below the homogeneous crystallization temperature $T_f = 1930$ K. Once the temperature of a liquid particle reaches T_f, the solidification process immediately begins and the particle temperature increases following the energy balance of Eq. (4.15). The fraction of 1 μm particles for which this process takes place will increase for smaller values of C_1, so the average temperature of these particles will increase as a result.

This trend is further illustrated by Fig. (4.8), which shows the variation in liquid mass fraction with C_1 for the same particle size and location. For $C_1 > 10^{-3}$ all 1 μm particles at this point are found to be entirely liquid, while the liquid mass fraction decreases for smaller C_1 to a value of 0.728 at $C_1 = 0$. In both Figs. (4.6) and (4.8) the data point for $C_1 = 0$ is represented by a horizontal line through the vertical axis. Note that all other data sets in Figs. (4.5) to (4.7) show monotonic trends through the full C_1 range, as the phase

composition for these cases does not vary as a function of C_1. At both locations and for the full range of C_1 values considered here, all 0.3 μm particles have completely solidified, and all 6 μm particles are entirely liquid. In addition, 1 μm particles are entirely liquid at the point (50,14) due to the reduced interphase heat transfer which results from the relatively low gas number density far from the axis.

Various gas properties were examined at the same two flowfield locations, to determine any dependence on the cutoff value C_2 for particle-to-gas coupling. Of the properties considered, only a weak dependence could be found for the gas translational temperature, while the variation in all other properties was within statistical scatter. The lack of C_2 dependence can be attributed to the very small domains for particle-to-gas coupling, as well as the dominance of the expansion process over interaction with the particle phase in determining bulk gas properties far from the nozzle.

4.4.3 Relation between cutoff values and simulation efficiency

Figure (4.9) shows the variation with cutoff values ($C_1 = C_2$) in overall simulation efficiency. The vertical axis here gives the total cpu time per time step at steady state, normalized by the corresponding value when both cutoff values are set to zero. As expected, simulation time is shown to decrease monotonically as cutoff values are increased. For a given level of precision in simulation results, the use of coupling parameters allows for a roughly 20% reduction in calculation time when cutoff values are set to 10^{-6}, or a 65% reduction when these values are set to 0.1.

Based on a comparison of Fig. (4.9) with the results discussed above, a cutoff value of 10^{-4} is recommended for both C_1 and C_2 in order to balance overall numerical efficiency

and accuracy in computed flow characteristics for both the particles and gas. As shown in Fig. (4.9), the utilization of coupling parameters to identifying regions of negligible interphase coupling results in a 30% reduction in simulation time when this cutoff value is used. While no universal cutoff value can be found to optimize this balance under all flow conditions, particularly when particle phase change is important, a value of 10^{-4} can in general be expected to provide both reasonably good accuracy and efficiency.

Note however that the increase in efficiency associated with the use of these coupling parameters does correspond to an unavoidable reduction in overall accuracy. While a roughly 30% savings may not be considered sufficiently large to warrant implementation of the method described here, the efficiency increase may under certain conditions be much greater, particularly when the grid is extended to include the full domain of interest for plume radiation signature analysis.

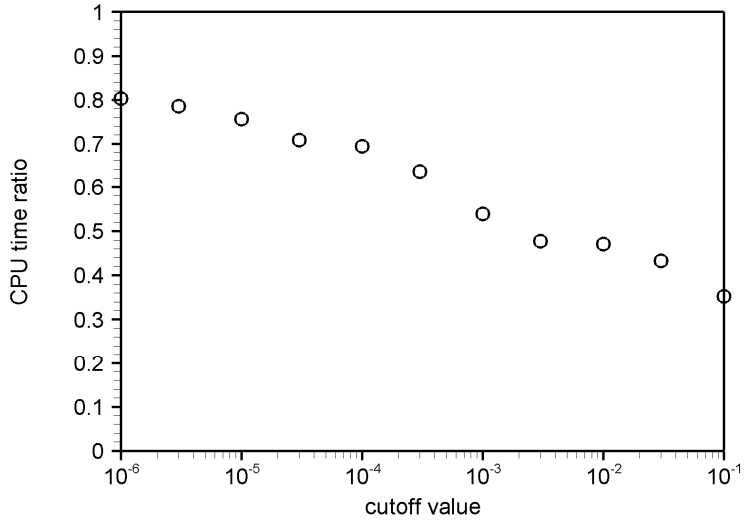

Figure 4.9. Total cpu time per time step at steady state, normalized by CPU time for the zero cutoff values case.

4.4.4 Additional results

Selected results for the case where $C_1 = C_2 = 10^{-4}$ are displayed in Figs. (4.10) and (4.11). Figure (4.10) shows the contours of mass-averaged particle temperature and gas translational temperature. As expected, particle temperatures are uniformly higher than that of the surrounding gas, with the lowest particle temperatures occurring far from the central axis where the smaller particles are concentrated. A slight reduction in average particle temperature is found close to the axis, as a result of the increased heat transfer toward the center of the plume nearfield region where the gas number density is greatest.

Contours of the Sauter mean particle diameter are shown in Fig. (4.11), along with the overall liquid mass fraction for the particles. (The Sauter mean diameter is the diameter of a particle with a volume-to-surface area ratio equal to that of the particle phase as a whole, and is calculated as the ratio of mean-cubed to mean-squared particle diameters in each cell.) The concentration of larger particles toward the axis is found to result in a greater content of liquid alumina within this region, as the reduced surface area-to-volume ratio among larger particles allows for a more gradual process of cooling and solidification. Note that no streamwise variation is visible among any particle properties shown in Figs. (4.10) or (4.11), due to the large difference in scale between the simulation domain and the regions of significant interphase momentum and energy exchange.

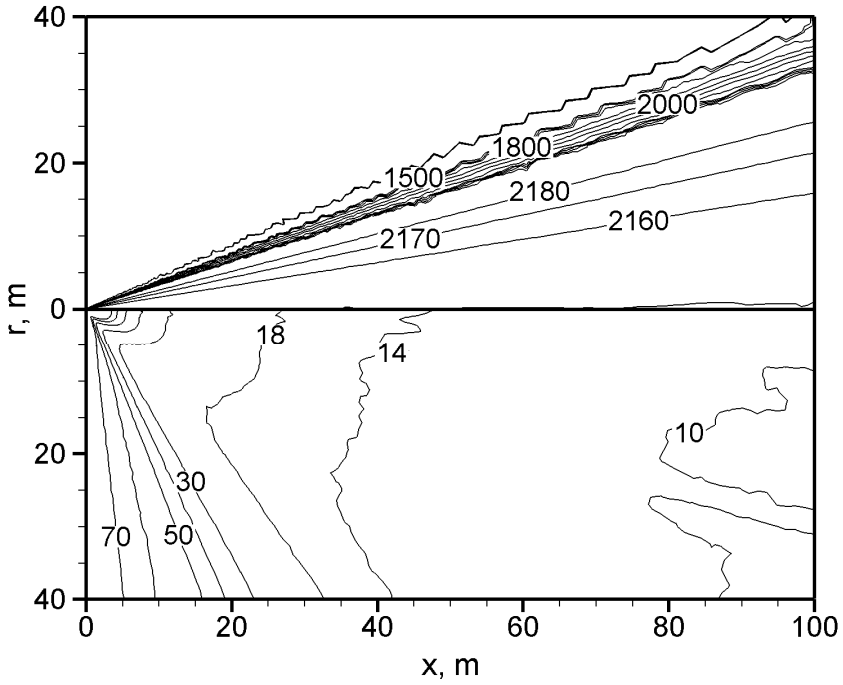

Figure 4.10. Contours of mass-averaged particle temperature (top) and gas translational temperature. All values are in SI units.

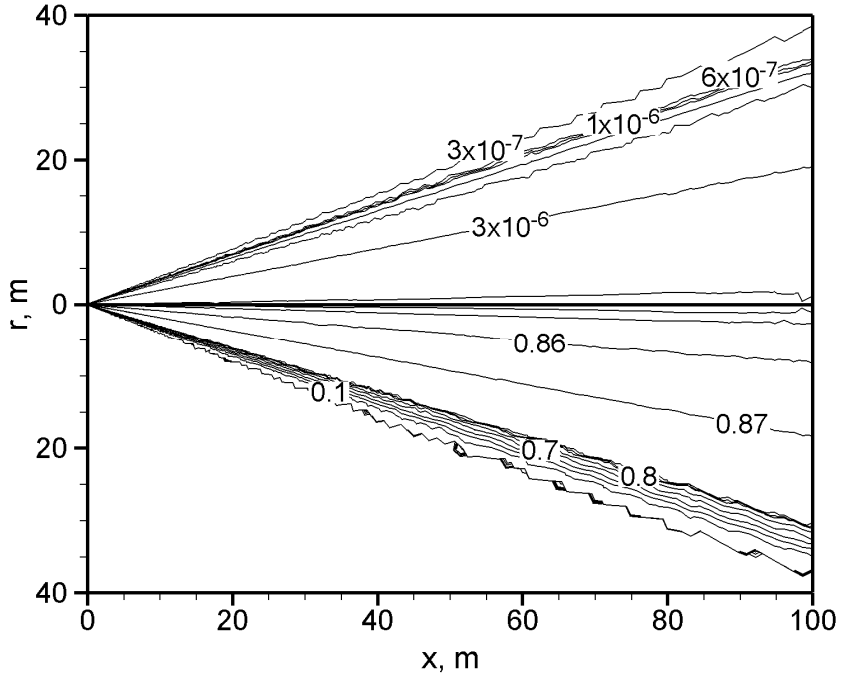

Figure 4.11. Sauter mean particle diameter (top) and liquid mass fraction of particles.

Chapter V

An Alternate Approach for Gas Simulation in Near-Equilibrium Regions

5.1 Overview and motivation

In this chapter a particle method is presented for the numerical simulation of rarefied gas flows, based on the ellipsoidal statistical Bhatnagar-Gross-Krook (ES-BGK) model of the Boltzmann equation. [*Holway* (1966)] The simulation procedure includes consideration of rotational nonequilibrium, and enforces exact momentum and energy conservation for a mixture involving monatomic and diatomic species. This method is applied to the simulation of a rarefied nozzle expansion flow, and flowfield characteristics are compared with experimental data as well as results from DSMC and Navier-Stokes simulations of the same flow.

The ES-BGK method is shown from this comparison to allow for a relatively high degree of accuracy in transitional flow regimes, while avoiding the intermolecular collision calculations which typically make the DSMC simulation of low Knudsen number flows prohibitively expensive. The procedures described here are intended for implementation in a hybrid scheme along with traditional DSMC, to be used only in high

density flowfield regions where DSMC is particularly inefficient. Results from a series of SRM plume simulations using this hybrid scheme are presented in Chapter 7.

5.1.1 Problems inherent in the DSMC simulation of SRM plume flows

As described in Chapter 1, the gas phase in a high altitude SRM exhaust plume typically experiences a high degree of thermal nonequilibrium through much of the flowfield. During the rapid expansion process just beyond the nozzle exit, the gas velocity distribution begins to diverge significantly from the equilibrium limit, and thermal energy is increasingly distributed non-uniformly among the translational and internal degrees of freedom. Further downstream, these nonequilibrium effects continue to increase as the gas rapidly expands and thermal energy is converted into energy associated with bulk motion of the exhaust flow. Geometric effects lead to an imbalance in the distribution of translational energy, where the translational temperature tends to be higher in the streamwise direction than along transverse directions. [*Boyd* (2003)] Rotational freezing occurs due to the combination of large gradients and low collision frequency, and the flow ultimately approaches a near-free molecular regime where the influence of collisional processes becomes negligible.

In engineering practice, the simulation of such highly rarefied flows is most often performed using the DSMC method as discussed in Chapter 1. The DSMC method has been shown to provide accurate solutions for highly rarefied nozzle and plume flows (see for example *Boyd et al.* (1992)) and retains validity through the full range of possible Knudsen numbers for a dilute gas. In theory then, DSMC may be applied to the entire flowfield for a high altitude SRM exhaust plume.

The main obstacle, however, to DSMC calculations for this type of flow is the enormous computational cost of simulating the higher density gas through much of the plume nearfield region. There are three major factors which tend to make DSMC prohibitively expensive, even on large parallel machines, for the simulation of relatively high-density flows: First, for accurate simulation the cell size should ideally be much smaller than any characteristic length scale for gradients in macroscopic flow quantities, and nonphysical diffusion effects become increasingly significant as the cell size increases. [*Bird* (1994), *Breuer et al*. (1995)] This generally limits cell dimensions to roughly one mean free path, so that a very large number of cells may be required for the simulation of even small-scale flows when the gas density is high. Second, the temporal decoupling of collision and advection processes is in general a valid approximation only if the time step is no larger than the local mean collision time. This means that for a high density or low Knudsen number flow, a very large number of time steps may be required to reach steady state conditions.

The above two requirements may be relaxed somewhat when macroscopic gradient length scales are very large compared to the mean free path, so that the flow approaches a near-homogeneous state. However, a third limiting factor for high density flows cannot be relaxed under near-homogeneous conditions: The collisional process driving a flow toward equilibrium is modeled in DSMC through the probabilistic calculation of individual collisions between pairs of representative particles. (By convention, the term "particle" is used throughout this chapter to designate a computational gas molecule which represents a large number of actual molecules or atoms.) The collision frequency increases with the gas density, so that for a fixed set of simulation parameters, a higher

density flow corresponds to an increase in the average number of collisions experienced per particle during each time step. Under conditions typical in the plume nearfield region of a high altitude SRM exhaust plume, this last requirement can make DSMC simulation of such flows prohibitively expensive on all but the largest parallel machines.

5.1.2 The NS-DSMC hybrid approach

In practice, these plume flow simulations may be performed using a finite volume representation of the Navier-Stokes (NS) equations in the high density regions where the continuum and quasi-equilibrium assumptions underlying these equations are considered valid. The DSMC method is then used only in the lower density regions where these assumptions break down, and where a DSMC flowfield calculation is feasible using available computational resources. The interface between NS and DSMC regions is modeled either through an uncoupled matching of boundary conditions for two independent simulations, or using a single hybrid code where the interface location may be varied dynamically during the simulation through the evaluation of one or more continuum breakdown parameters.

For either approach, the accurate determination of the boundary beyond which the NS solution is invalid may be difficult and expensive. As a result, there is generally some significant tradeoff between overall simulation accuracy and efficiency. Increased accuracy results from a more precise or conservative determination of the proper boundary for the NS domain. This in turn requires a greater computational load, either through an iterative procedure to evaluate the boundary then update the overall flowfield

solution, or through an extension of the DSMC domain into regions which may be accurately handled by the NS solver.

5.1.3 An all-particle hybrid scheme

This tradeoff between accuracy and efficiency may to some extent be avoided if an alternate simulation approach is used in flowfield regions where the validity of the NS equations is questionable, but the application of DSMC is particularly expensive. This alternate method should be more efficient than DSMC in modeling relatively high density flows, able to account for nonequilibrium phenomena which characterize a transition Knudsen number regime out of range of NS solutions, and in good quantitative agreement with both NS and DSMC for near-equilibrium flows. One such method is presented here, using a particle-based probabilistic solution to the ellipsoidal statistical Bhatnagar-Gross-Krook (ES-BGK) model of the Boltzmann equation.

In recent years, several authors have developed particle methods in which standard DSMC collision operations are replaced by alternate procedures that account for the collisional drive toward equilibrium, while avoiding the calculation of individual collisions. [*Montanero et al.* (1998), *Gallis and Torczynski* (2000), *Macrossan* (2001), *Bruno, Longo, and Capitelli* (2002), *Bruno and Longo* (2002)] In place of collision calculations on pairs of representative particles, some fraction of particles is randomly selected during each time step, and these particles are assigned new velocities according to predetermined distribution functions.

In several of these methods, the collision process in each cell within the computational grid is based on the homogeneous form of the Bhatnagar-Gross-Krook

(BGK) equation. [*Bhatnagar, Gross, and Krook* (1954)]

$$d(\mathrm{n_g} f)/dt = \nu \mathrm{n_g}(f_\mathrm{e} - f) \tag{5.1}$$

Here f is the velocity distribution function for a simple monatomic gas, f_e is a Maxwellian distribution with the same average and variance as f, $\mathrm{n_g}$ is the number density, and ν is a characteristic relaxation rate. This is a simplified linear model of the highly nonlinear Boltzmann equation, valid under spatially homogeneous conditions. (See Chapter 1 for a discussion of the Boltzmann equation, given as Eq. (1.1).) The detailed physics of the collision term in the Boltzmann equation is ignored here in favor of a Maxwell-type molecular model in which the entire distribution function f decays toward equilibrium at a velocity-independent rate.

As proposed by *Macrossan* (2001) and independently implemented by *Gallis and Torczynski* (2000) and *Andries et al.* (2000), the method may be modified for better quantitative agreement with the Boltzmann equation as a solution to

$$d(\mathrm{n_g} f)/dt = \nu \mathrm{n_g}(f_\mathrm{G} - f) \tag{5.2}$$

where f_G is an anisotropic Gaussian distribution function. This modification to the BGK equation was proposed by *Holway* (1966) to correct for the nonphysical constraint in the BGK model of unity Prandtl number, and has recently been shown to satisfy Boltzmann's H-theorem for entropy production. [*Andries and Perthame* (2001)] Following *Cercignani* (1988), this is referred to here as the ellipsoidal statistical BGK (ES-BGK) model.

In addition to potential advantages in efficiency and accuracy over a NS/DSMC hybrid scheme, an important advantage should be noted for the simulation of SRM plume flows using a hybrid scheme involving DSMC and a particle method based on Eq. (5.2). As described in previous chapters, the accurate simulation of these plume flows requires

implementation of a variety of models for the inclusion of solid and liquid particles, including capabilities for strong two-way coupling between gas and condensed phase properties. The hybrid NS/DSMC simulation of such multiphase flows may require a large number of physical models to be independently implemented in the continuum NS solver, in a manner which is consistent and easily integrated with corresponding models in the DSMC code. By contrast, in an ES-BGK/DSMC hybrid scheme, only collision calculations on gas phase particles are altered in high density regions, and all other calculation procedures are left unchanged through the entire computational domain. As no additional physical models are required in regions of near-equilibrium flow, ES-BGK particle methods offer a significant advantage over NS solvers in ease of implementation for the hybrid simulation of high altitude SRM plume flows.

In the remainder of this chapter, particle methods of *Macrossan* (2001) and *Gallis and Torczynski* (2000) based on Eqs. (5.1) and (5.2) are extended for consideration of a gas mixture involving monatomic and diatomic species, and a procedure is described to enforce exact momentum and energy conservation in a flow involving rotational nonequilibrium. A simple homogeneous test case is then used to verify the accuracy of the proposed rotational relaxation model. Next, the method is applied to a nozzle flow test case involving a small cold-gas thruster with N_2 propellant exhausting into a vacuum, and results are compared with DSMC, NS, and experimental data for the same flowfield. Relatively good agreement is found between ES-BGK, DSMC and experimental results, particularly in higher density regions near the nozzle throat. It is also shown that the ES-BGK flowfield solution incorporates some nonequilibrium effects which are captured as well by DSMC but neglected in the NS calculation.

5.2 Numerical procedure

As discussed in the previous section, all procedures unrelated to intermolecular collisions in the ES-BGK particle method are identical to those in DSMC. However, the process of calculating individual representative collisions is replaced by a procedure which involves the resampling of particle properties from predetermined distributions. All steps in these resampling calculations are described in this section, with a particular emphasis on operations related to rotational nonequilibrium effects. The ES-BGK method presented here is the first to allow for consideration of translational-rotational energy exchange while enforcing exact conservation of momentum and energy.

5.2.1 Reassignment of particle velocities

Consider the ES-BGK collision procedure in a cell containing N_g particles, where each particle may be assigned to one of several different monatomic or diatomic gas species. We assume vibrational and electronic energy modes are unexcited, and the variable hard sphere (VHS) collision model [*Bird* (1994)] is used to approximate the variation of dynamic viscosity μ with translational temperature T_t. As a first step in the method, T_t is calculated as a function of the average momentum and translational energy of all particles in the cell:

$$T_t = \frac{1}{3k_B}\frac{N_g}{(N_g - 1)}\left(\left\langle m\,\mathbf{u}^2\right\rangle_a - \left\langle m\,\mathbf{u}\right\rangle_a^2 / \left\langle m\right\rangle_a\right) \tag{5.3}$$

Here m and **u** are the mass and velocity respectively of an individual particle, k_B is Boltzmann's constant, the operator $\langle\ \rangle_a$ designates an average over all particles in the

cell, and the notation $\mathbf{x}^2$ for any vector $\mathbf{x}$ is used to represent $\mathbf{x}\cdot\mathbf{x}$. The coefficient $N_g/(N_g-1)$ in Eq. (5.3) corrects for a statistical error which appears when the traditional formula for T_t based on the velocity distribution is applied to a discrete set of particle velocities. [*Sun and Boyd* (2005)]

Using a first order Chapman-Enskog expansion of the ES-BGK equation, it can be shown that the correct relations for heat flux and shear stress are recovered in a near-equilibrium flow if the relaxation rate is given by

$$\nu = \Pr \cdot \frac{p}{\mu} \tag{5.4}$$

where Pr is the Prandtl number and p is the pressure. [*Mieussens and Struchtrup* (2004)] From the ideal gas equation of state and the VHS approximation that μ scales with temperature to some constant power ω, Eq. (5.4) may be rewritten as

$$\nu = \Pr \cdot n_g k_B \left(\frac{T_{ref}^{\omega}}{\mu_{ref}} \right) T_t^{1-\omega} \tag{5.5}$$

where T_{ref} is a reference temperature and μ_{ref} is the dynamic viscosity at T_{ref}. For a simple VHS gas, this viscosity can be calculated as a function of ω and the molecular collision diameter d_{ref} at the reference temperature:

$$\mu_{ref} = \frac{30(mk_B T_{ref}/\pi)^{1/2}}{4(5-2\omega)(7-2\omega)d_{ref}^2} \tag{5.6}$$

Note that in most cases the value of d_{ref} is itself determined from experimental measurements of μ_{ref}. Eq. (5.6) is useful however in a hybrid code (discussed in Section 5.1) involving both DSMC and the method proposed here, as reference collision diameters are among the required input parameters for DSMC collision calculations. A simple approximate extension of Eq. (5.6) to a gas mixture may be obtained by summing

the product of μ_{ref} and the time-averaged species mass fraction in the cell over all gas species.

Once a relaxation rate ν has been determined, Eq. (5.2) may be integrated to give the distribution function f after some finite time step Δt as a linear combination of the initial distribution $f(0)$ and a corresponding anisotropic Gaussian distribution f_G.

$$f(\Delta t) = f(0)\exp(-\nu\Delta t) + f_G\left(1 - \exp(-\nu\Delta t)\right) \tag{5.7}$$

From Eq. (5.7), we determine the number of particles N_v selected for reassignment of velocity components as

$$N_v = \text{floor}\left[N_g\left(1 - \exp(-\nu\Delta t)\right) + R\right] \tag{5.8}$$

where ν is evaluated using Eq. (5.5), R is a random number in [0,1] and the operator "floor" rounds to the nearest smaller integer. Note that a time-averaged value of the number density n_g should be used in Eq. (5.5) to avoid an error associated with statistical fluxuations in the calculated relaxation rate. Once N_v is known, this number of unique particles is then randomly selected and assigned to a list for velocity resampling. (In order to reduce calls to the random number generator, if $N_v > \frac{1}{2}N_g$ then $N_g - N_v$ randomly chosen particles are removed from a list which initially includes all particles in the cell, and the remaining particles are used for resampling.) In the special case where $N_v = 1$, momentum conservation requires that the velocity of the selected particle remains constant, so that N_v values of zero and one are equivalent during the resampling procedure. To correct for the resulting error, if N_v is calculated as one through Eq. (5.8) then an additional random number is generated and N_v is set with equal probability to either zero or two.

After N_v particles have been selected, all velocity components of these particles are

resampled from a normalized Maxwellian distribution. Each velocity component is set to either

$$u_i^* = \cos(2\pi R_1)\sqrt{-\ln(R_2)/m} \quad \text{or} \quad u_i^* = \sin(2\pi R_1)\sqrt{-\ln(R_2)/m} \tag{5.9}$$

where the subscript i denotes the direction, m is the particle mass, and R_1 and R_2 are random numbers between 0 and 1. Two statistically independent values of u_i^* may be obtained if Eqs. (5.9) are evaluated for the same values of R_1 and R_2, so that only a single random number must be generated per velocity component. Following *Gallis and Torczynski* (2000), all resampled velocities are then modified to give new values $c_i^{(1)}$ which conform to an anisotropic Gaussian distribution:

$$u_i^{(1)} = S_{ij} u_j^* \tag{5.10}$$

where

$$S_{ij} = \delta_{ij} - \frac{1-\Pr}{2\Pr}\left[\frac{1}{k_B T_t}\frac{N_g}{N_g - 1}\left(\left\langle m u_i u_j \right\rangle_a - \left\langle m u_i \right\rangle_a \left\langle m u_j \right\rangle_a / \left\langle m \right\rangle_a\right) - \delta_{ij}\right] \tag{5.11}$$

Here δ_{ij} is the Kronecker delta, u_i and u_j are particle velocity components before resampling, T_t is evaluated using Eq. (5.3), and the superscript (1) indicates a newly reassigned value.

5.2.2 Rotational energy resampling

To account for the effect of collisions on the rotational energy distribution among diatomic gas species, we define a rotational relaxation rate ν_r such that, in a homogeneous gas, the instantaneous cell-averaged rotational temperature T_r will vary as

$$dT_r / dt = -\nu_r (T_r - T_{eq}) \tag{5.12}$$

Here T_{eq} is the equilibrium temperature to which both T_r and T_t converge after a long

period of time, and T_r is given by

$$T_r = \frac{2}{k_B} \langle E_r \rangle_a / \langle \zeta_r \rangle_a \tag{5.13}$$

The above symbols E_r and ζ_r denote rotational energy and rotational degrees of freedom, respectively, for an individual particle. Substitution of Eq. (5.13) into Eq. (5.12) gives the familiar equation of *Jeans* (1916) for the relaxation of internal energy modes.

The equilibrium temperature T_{eq} can be expressed as a weighted sum of the rotational and translational temperatures

$$\zeta_{t,eff} T_t + \langle \zeta_r \rangle_a T_r = \left(\zeta_{t,eff} + \langle \zeta_r \rangle_a \right) T_{eq} \tag{5.14}$$

where $\zeta_{t,eff}$ is the effective number of translational degrees of freedom for all particles in the cell. If all N_g particles are together considered as an isolated system, then it follows from Eqs. (5.3) and (5.13) and energy conservation arguments that

$$\frac{d}{dt}\left[\langle m\mathbf{u} \rangle_a^2 / \langle m \rangle_a + 3\left(\frac{N_g\text{-}1}{N_g} \right) k_B T_t + \langle \zeta_r \rangle_a k_B T_r \right] = 0 \tag{5.15}$$

while momentum and mass conservation require that the first term within the brackets be constant in time as well. By comparing Eqs. (5.14) and (5.15) and noting that T_{eq} is a time invariant quantity, it can be shown that there are effectively $3(N_g\text{-}1)/N_g$ translational degrees of freedom in the cell, so that the equilibrium temperature may be given from Eq. (5.14) as

$$T_{eq} = \frac{3\left((N_g\text{-}1)/N_g \right) T_t + \langle \zeta_r \rangle_a T_r}{3(N_g\text{-}1)/N_g + \langle \zeta_r \rangle_a} \tag{5.16}$$

Note that the arguments used to derive Eq. (5.16) make no assumptions regarding how the translational and rotational temperatures relax toward the equilibrium state, so that this equation should also be valid for DSMC and other methods for which a discrete

set of particle velocities is used to describe the velocity distribution of a gas in rotational nonequilibrium. As there are exactly three translational degrees of freedom for any real gas under consideration here, this derivation reveals the existence of a deterministic error which scales as $(N_g\text{-}1)/N_g$ and may significantly influence calculated bulk flow properties when the average number of particles per cell is very small. While it appears that no previous references to this error source exist in the literature, the upper bound of the resulting error should be relatively small (less than 5%) when particle numerical weights are set such that over 20 particles are assigned to each cell, as is standard practice in DSMC.

The rotational relaxation rate ν_r shown in Eq. (5.12) is defined here as the frequency of inelastic collisions, given as the ratio of the collision frequency F_{coll} to the rotational collision number Z_r. To determine F_{coll}, consider a cell containing particles of N_{spec} different species, each with a mass m_i, VHS reference collision diameter $d_{ref,i}$ and number density n_i averaged over a large number of time steps. Assuming a near-equilibrium flow, we can efficiently calculate the collision frequency as

$$F_{coll} = \frac{4}{n_g}\sqrt{\frac{k_B T_{ref}}{2\pi}}\left(\frac{T_t}{T_{ref}}\right)^{1-\omega}\sum_{i=1}^{N_{spec}}\sum_{j=1}^{i} n_i n_j A_{ij}(2-\delta_{ij}) \tag{5.17}$$

where

$$A_{ij} = \frac{\pi}{4}\left(d_{ref,i}+d_{ref,j}\right)^2\sqrt{\frac{m_i+m_j}{m_i m_j}}$$

and n_g is the sum of n_i values over all N_{spec} species. Note that no implied summations are used in the index notation of Eq. (5.17).

The rotational collision number Z_r is calculated using a modified form of a formula given by *Parker* (1959).

$$Z_r = \frac{3/5\ Z_r^{\infty}}{1 + (\pi^{1/2}/2)(T^*/T_{eq})^{1/2} + (\pi + \pi^2/4)(T^*/T_{eq})} \tag{5.18}$$

The above constants Z_r^{∞} and T^* are determined for N_2 as Z_r^{∞}=23.0 and T^*=91.5 K. [*Bird* (1994)] As a modification to Parker's formula, the equilibrium temperature T_{eq} is used here in place of T_t following observations of *Boyd* (1990) that, for a single intermolecular collision, Z_r tends to vary as a function of both the translational and rotational collision energies. The 3/5 factor in the numerator, also not in Parker's original formula, accounts for the fact that Z_r is defined here to characterize the rate at which T_r relaxes toward T_{eq}, not toward T_t as used by Parker and others. [*Bird* (1994)]

By analogy with Eq. (5.8), Eq. (5.12) can be integrated in time to give an initial estimate of the number of particles N_r for which to resample rotational energy as

$$N_r \approx N_g \left(1 - \exp\left(-\frac{F_{coll}}{Z_r}\Delta t\right)\right) \tag{5.19}$$

where F_{coll} and Z_r are evaluated using Eqs. (5.17) and (5.18) respectively. (The exact determination of N_r requires a more involved procedure, and is discussed in detail below.) In the implementation proposed here, N_r particles are randomly selected from the list of N_v particles which have already been tagged for velocity resampling, and the rotational energy E_r of each selected diatomic particle is reassigned to a normalized value

$$E_r^{(1)} = -\ln(R) \tag{5.20}$$

where a unique random number $R \in (0,1]$ is used for each particle.

5.2.3 Momentum and energy conservation

To avoid random walk errors and permit overall accuracy for a near-equilibrium flow comparable to that of either DSMC or NS simulations, we desire for both momentum and

energy to be exactly conserved during the resampling procedures. It follows that all reassigned velocities $\mathbf{u}^{(1)}$ and rotational energies $E_r^{(1)}$ must be modified to final values $\mathbf{u}^{(2)}$ and $E_r^{(2)}$ such that

$$\left\langle \mathrm{m}\mathbf{u}^{(2)} \right\rangle_{\mathrm{v}} = \left\langle \mathrm{m}\mathbf{u}^{(0)} \right\rangle_{\mathrm{v}} \tag{5.21}$$

and

$$\frac{1}{2}\mathrm{N_v}\left\langle \mathrm{m}(\mathbf{u}^{(2)})^2 \right\rangle_{\mathrm{v}} + \mathrm{N_r}\left\langle E_{\mathrm{r}}^{(2)} \right\rangle_{\mathrm{r}} = \frac{1}{2}\mathrm{N_v}\left\langle \mathrm{m}(\mathbf{u}^{(0)})^2 \right\rangle_{\mathrm{v}} + \mathrm{N_r}\left\langle E_{\mathrm{r}}^{(0)} \right\rangle_{\mathrm{r}} \tag{5.22}$$

where the operators $\langle\ \rangle_{\mathrm{v}}$ and $\langle\ \rangle_{\mathrm{r}}$ denote averages over all particles used in the resampling of velocity and rotational energy respectively. Further, to satisfy energy equipartition at the equilibrium limit, translational and rotational temperatures based on reassigned values must be equal. This condition can be written as

$$\frac{1}{3\mathrm{k_B}}\frac{\mathrm{N_v}}{(\mathrm{N_v}-1)}\left(\left\langle \mathrm{m}(\mathbf{u}^{(2)})^2 \right\rangle_{\mathrm{v}} - \left\langle \mathrm{m}\mathbf{u}^{(2)} \right\rangle_{\mathrm{v}}^2 / \langle \mathrm{m} \rangle_{\mathrm{v}}\right) = \frac{2}{\mathrm{k_B}}\left\langle E_{\mathrm{r}}^{(2)} \right\rangle_{\mathrm{r}} / \langle \zeta_{\mathrm{r}} \rangle_{\mathrm{r}} \tag{5.23}$$

where ζ_r is the number of rotational degrees of freedom for an individual particle. For each of the N_v particles selected for velocity resampling, the final velocity is calculated as

$$\mathbf{u}^{(2)} = \boldsymbol{B} + C\left(\mathbf{u}^{(1)} - \left\langle \mathrm{m}\mathbf{u}^{(1)} \right\rangle_{\mathrm{v}} / \langle \mathrm{m} \rangle_{\mathrm{v}}\right) \tag{5.24}$$

while each of the N_r particles with resampled rotational energies is given a final value of

$$E_{\mathrm{r}}^{(2)} = D\,E_{\mathrm{r}}^{(1)}. \tag{5.25}$$

By algebraic manipulation of Eqs. (5.21) through (5.25), it can be shown that momentum conservation, energy conservation and energy equipartition are all satisfied if the vector $\boldsymbol{B}$ and scalar constants C and D are chosen as follows:

$$\boldsymbol{B} = \left\langle \mathrm{m}\mathbf{u}^{(0)} \right\rangle_{\mathrm{v}} / \langle \mathrm{m} \rangle_{\mathrm{v}} \tag{5.26}$$

$$C = \left[\left(\frac{3(\mathrm{N_v} - 1)}{3(\mathrm{N_v} - 1) + \mathrm{N_r} \langle \zeta_\mathrm{r} \rangle_\mathrm{r}} \right) \left(\frac{\left\langle \mathrm{m}(\mathbf{u}^{(0)})^2 \right\rangle_\mathrm{v} - \left\langle \mathrm{m}\mathbf{u}^{(0)} \right\rangle_\mathrm{v}^2 / \langle \mathrm{m} \rangle_\mathrm{v} + 2(\mathrm{N_r}/\mathrm{N_v}) \left\langle E_\mathrm{r}^{(0)} \right\rangle_\mathrm{r}}{\left\langle \mathrm{m}(\mathbf{u}^{(1)})^2 \right\rangle_\mathrm{v} - \left\langle \mathrm{m}\mathbf{u}^{(1)} \right\rangle_\mathrm{v}^2 / \langle \mathrm{m} \rangle_\mathrm{v}} \right) \right]^{1/2} \quad (5.27)$$

$$D = \left(\frac{\mathrm{N_v} \langle \zeta \rangle_\mathrm{r}}{3(\mathrm{N_v} - 1) + \mathrm{N_r} \langle \zeta_\mathrm{r} \rangle_\mathrm{r}} \right) \left(\frac{\left\langle \mathrm{m}(\mathbf{u}^{(0)})^2 \right\rangle_\mathrm{v} - \left\langle \mathrm{m}\mathbf{u}^{(0)} \right\rangle_\mathrm{v}^2 / \langle \mathrm{m} \rangle_\mathrm{v} + 2(\mathrm{N_r}/\mathrm{N_v}) \left\langle E_\mathrm{r}^{(0)} \right\rangle_\mathrm{r}}{2 \left\langle E_\mathrm{r}^{(1)} \right\rangle_\mathrm{r}} \right) \quad (5.28)$$

5.2.4 A correction factor for the rotational relaxation rate

From the definition of rotational temperature indicated by Eq. (5.13), the right hand side of Eq. (5.28) may be expressed as a ratio of temperatures: The denominator gives the rotational temperature based on values of $E_\mathrm{r}^{(1)}$, while the numerator gives the temperature corresponding to the conditions of Eq. (5.23). Thus, Eq. (5.28) may be used to show that the temperature $\mathrm{T}^{(2)}$ based on resampled and renormalized values of either particle velocity $\mathbf{u}^{(2)}$ or rotational energy $E_\mathrm{r}^{(2)}$ can be given as

$$\mathrm{T}^{(2)} = \left(\frac{\mathrm{N_v} / \mathrm{k_B}}{3(\mathrm{N_v} - 1) + \mathrm{N_r} \langle \zeta_\mathrm{r} \rangle_\mathrm{r}} \right) \left(\left\langle \mathrm{m}(\mathbf{u}^{(0)})^2 \right\rangle_\mathrm{v} - \left\langle \mathrm{m}\mathbf{u}^{(0)} \right\rangle_\mathrm{v}^2 / \langle \mathrm{m} \rangle_\mathrm{v} + 2 \left(\frac{\mathrm{N_r}}{\mathrm{N_v}} \right) \left\langle E_\mathrm{r}^{(0)} \right\rangle_\mathrm{r} \right). \quad (5.29)$$

As particles are randomly chosen for velocity or rotational energy resampling, the averaged quantities in Eq. (5.29) will, on average, equal the corresponding quantities averaged over all N particles in the cell. If we denote the equivalent temperature based on cell-averaged values as $\mathrm{T_a}^{(2)}$, then it follows from substitution of Eqs. (5.3) and (5.13) into Eq. (5.29) that

$$\mathrm{T_a}^{(2)} = \frac{3((\mathrm{N_v}\text{-}1)/\mathrm{N_r})\mathrm{T_t} + \langle \zeta_\mathrm{r} \rangle_\mathrm{a} \mathrm{T_r}}{3(\mathrm{N_v}\text{-}1)/\mathrm{N_r} + \langle \zeta_\mathrm{r} \rangle_\mathrm{a}}. \quad (5.30)$$

As the temperature $\mathrm{T_a}^{(2)}$ is generally not equal to the equilibrium temperature $\mathrm{T_{eq}}$ determined from Eq. (5.16), the procedure used to calculate $\mathrm{N_r}$ must be based on a relaxation rate other than the true characteristic rate for rotational relaxation $\nu_\mathrm{r} = F_\mathrm{coll}/ \mathrm{Z_r}$.

A correction factor β is therefore introduced as the ratio of this required relaxation rate to ν_r, so that in a homogeneous adiabatic flow,

$$dT_r / dt = -\beta \nu_r (T_r - T_a^{(2)}) . \tag{5.31}$$

From a comparison of Eqs. (5.12) and (5.31), it follows that

$$\beta = (T_r - T_{eq}) \big/ (T_r - T_a^{(2)}) . \tag{5.32}$$

Substituting Eqs. (5.16) and (5.30) into Eq. (5.32), we find

$$\beta = \frac{3 + \langle \zeta_r \rangle_a N_r^* / (N_v\text{-}1)}{3 + \langle \zeta_r \rangle_a N_g / (N_g\text{-}1)} \tag{5.33}$$

where N_r^* is an approximation to the integer value N_r based on an exact solution to Eq. (5.31). If Eq. (5.31) is integrated over the time step interval Δt, then the same reasoning used to find N_v by Eq. (5.8) may be used to calculate N_r^* as

$$N_r^* = N_g \left(1 - \exp\left(-\beta \frac{F_{coll}}{Z_r} \Delta t \right) \right). \tag{5.34}$$

Note from Eqs. (5.33) and (5.34) that β and N_r^* cannot be independently determined, but must instead be calculated simultaneously using an iterative method. In the implementation proposed here, β is initially set to one and N_r^* is found by Eq. (5.34), after which β and N_r^* are updated using Eqs. (5.33) and (5.34) respectively. This procedure is repeated four additional times, after which the number of particles to select for rotational energy resampling is computed as $N_r = \text{floor}[N_r^* + R]$ where R is a random number in [0,1]. This simple "brute force" approach is found to give a reasonable balance of accuracy and efficiency over a wide range of conditions, and more complicated iterative schemes with faster convergence should not generally be required due to the insignificant contribution of this procedure to the total computational expense.

5.3 Homogeneous rotational relaxation

To verify the accuracy of the scheme for rotational relaxation, all procedures described in the previous section are implemented in a modified version of the DSMC code MONACO [*Dietrich and Boyd* (1996)] and applied to a zero-dimensional test case based on simulations of *Bird* (1994). An isolated control volume of N_2 gas is given initial conditions involving translational equilibrium at 500 K and a rotational temperature of 0 K. The simulation domain consists of a single cell with specularly reflecting walls and 10,000 particles, and the time step is set to 1/2 of the initial mean collision time. The rotational collision number is found from Eqs. (5.16) and (5.18) to hold a constant value of $Z_r = 4.31$, so that the rotational and translational temperatures will vary in time according to analytical expressions similar to those derived by *Bird* (1994).

$$T_r = 300\left(1 - \exp\left(-\frac{t}{4.31\,\tau_{coll}}\right)\right), \quad T_t = 300 + 200\exp\left(-\frac{t}{4.31\,\tau_{coll}}\right) \tag{5.35}$$

Here both temperatures T_t and T_r are given in K, t is the total elapsed time and τ_{coll} is a characteristic mean collision time. The variable τ_{coll} may be defined in terms of the instantaneous mean collision frequency F_{coll} as

$$\tau_{coll} = t\left[\int_0^t F_{coll}(t')\,dt'\right]^{-1} \tag{5.36}$$

where F_{coll} is calculated for a VHS gas using Eq. (5.17).

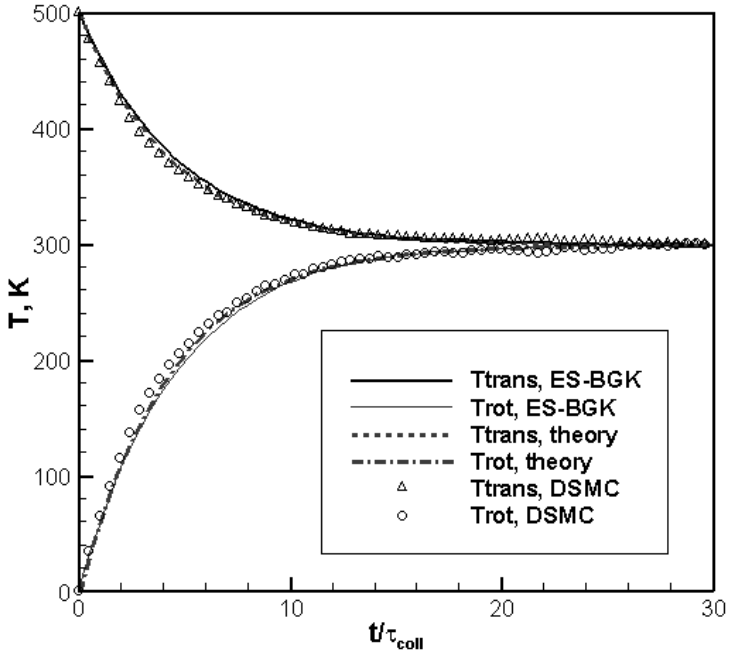

Figure 5.1. Time variation in temperatures for rotational relaxation.

Figure (5.1) shows the variation in both T_r and T_t as functions of the normalized time t/τ_{coll}. Results from the ES-BGK simulation are presented along with results from a DSMC simulation under identical conditions, and theoretical curves based on Eqs. (5.35) are also shown for comparison. For consistency, a constant rotational collision number of 4.31 is used in the DSMC simulation. The ES-BGK data points are found to be in close agreement with both theory and DSMC, while a slight underprediction is observed in the relaxation rate from the ES-BGK simulation. This discrepancy can be traced to the fact that only a fraction of particles are chosen for velocity resampling during each time step. If the artificial condition $N_v=N_g$ is imposed, then nearly perfect agreement is found between the ES-BGK and theoretical curves of Fig. (5.1).

As discussed by *Bird* (1994), even DSMC results for homogeneous rotational relaxation with constant Z_r can only be approximated by an analytical solution, and the

scale of the disagreement between DSMC and theoretical curves is comparable to that between theory and ES-BGK. Both DSMC and ES-BGK results have some dependence on the VHS temperature exponent ω, so by comparison with DSMC we can conclude that rotational relaxation is modeled with acceptable accuracy by the method proposed here.

5.4 Nozzle flow simulation

Relatively little published experimental data may be considered appropriate for evaluation of the proposed ES-BGK method under conditions similar to those expected in the SRM plume flows of interest. The most detailed set of flowfield property measurements for a suitable rarefied expansion flow is likely that of *Rothe* (1971), where an electron beam technique is used to measure density and rotational temperature for the flow of N_2 through a very small nozzle into a vacuum chamber.

Both NS and DSMC simulations of the internal nozzle flow have been performed by *Chung et al*. (1995) In the DSMC simulation by these authors, the computational domain is restricted to the lower density regions beyond the nozzle throat, with inflow conditions at the throat based on a NS simulation of the flow within the convergent section of the nozzle. Generally good agreement is found between DSMC results and experimental data, while a NS simulation of the entire nozzle flow gives relatively poor agreement with the experiment in areas downstream of the throat where nonequilibrium effects become significant.

5.4.1 Simulation setup and boundary conditions

To evaluate the accuracy of the ES-BGK approach presented here, ES-BGK and DSMC simulations are performed for the divergent nozzle and nearfield plume flow investigated by *Rothe* (1971). Identical grids, boundary conditions and numerical weights are used for the two simulations, with the same grid geometry and inflow conditions at the nozzle throat employed in the DSMC simulation of *Chung et al*. (1995) As the ES-BGK particle method is based on assumptions of near-equilibrium flow, we can investigate the applicability of the method to higher Knudsen number regimes by comparing ES-BGK results with both DSMC and experimental data.

Following *Chung et al.* we use a VHS temperature exponent (ω) of 0.24 and assume fully diffuse reflection for particle collisions with the nozzle wall. These authors investigated a number of different models for translational energy transfer during particle-wall collisions, and found best agreement with experimental data when all collisions are assumed diffuse, with a 10% probability of thermal accommodation to the wall temperature of 300 K. Energy exchange between translational and rotational modes was calculated using a detailed model which allows the exchange probability to vary as a function of the total incident energy of the colliding particle.

As noted by *Chung et al.*, a lack of experimental measurements on the interaction of N_2 gas with solid graphite (the nozzle wall material) leaves some doubt as to the validity of this energy exchange model. A more commonly accepted procedure for modeling rotational energy transfer during particle-wall collisions in DSMC involves an assumption that particle rotational energy is resampled from an equilibrium distribution at the wall temperature with some uniform probability. Therefore, as a simplification to

the procedure described by Chung et al., it is assumed here that 10% of particle-wall collisions involve full accommodation of both translational and rotational energy to the wall temperature, and the remaining 90% of these collisions involve adiabatic diffuse reflection. In the latter type of collision, the post-collision direction of the particle trajectory is randomly assigned according to the equilibrium velocity distribution for particles which pass through a plane, while the incident values of both translational and rotational energy are retained.

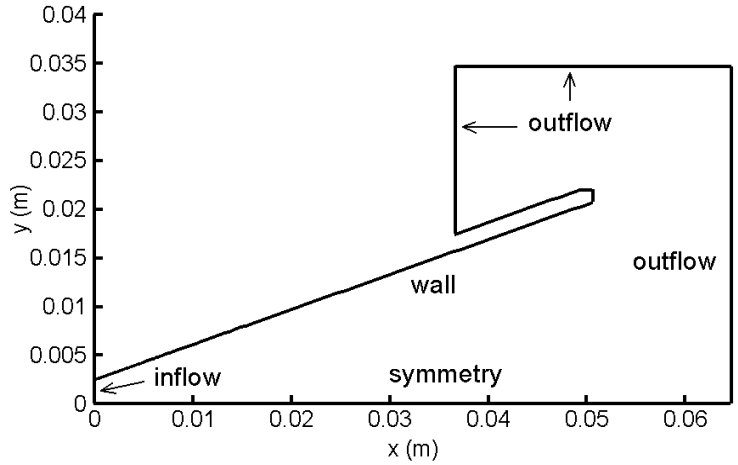

Figure 5.2. Grid geometry for ES-BGK and DSMC simulations.

Axisymmetric ES-BGK and DSMC simulations are performed on a 1.4 GHz AMD Athlon cluster, with static domain decomposition among eight separate tasks. Each calculation is run for 24 hours, with roughly 15 million particles at steady state and an unstructured grid of about 41,000 triangular cells scaled according to the local mean free path. The grid geometry is shown in Fig. (5.2) following that used by *Chung et al.* Not visible in the figure is the wall curvature at the throat, where the radius of curvature is one half the throat radius of 2.55 mm. The nozzle divergence angle is 20°, the exit-to-throat area ratio is 66, and the simulation domain extends 14 mm downstream of the exit

plane. To avoid unphysical flow characteristics beyond the exit plane due to the small domain size, we neglect the effect of ambient pressure in the vacuum chamber and use outflow boundaries within the plume region.

5.4.2 Comparison of flowfield property contours

Mach number contours for both ES-BGK and DSMC simulations are shown in Fig. (5.3), where the top half and bottom half of the figure give ES-BGK and DSMC results respectively. Excellent agreement between the two methods is found in the area around the nozzle throat. In both simulations, a significant reduction in Mach number is found toward the centerline in this region, as results from a weak compression wave due to the curvature of streamlines at the throat. [*Chung et al*. (1995)] Mach number contours along the nozzle wall are also nearly identical, and both results show a termination of the sonic line at the nozzle lip due to the rapid acceleration expected at the lip in any highly underexpanded nozzle flow.

In contrast, prominent differences between the two results appear along the centerline beyond a point about 1 cm downstream of the throat. As the degree of rarefaction increases with downstream distance, the centerline Mach number gradient in the DSMC simulation becomes significantly greater than in the ES-BGK simulation, so that the intersection of the Mach 4 contour line with the axis occurs roughly 2.6 cm further upstream in DSMC than in ES-BGK results. This difference in Mach number is likely a result of the unphysical lack of velocity dependence in the collisional relaxation rate of Eq. (5.2), which should correspond to some reduction in the streamwise temperature gradient within areas of low collision frequency. The difference between the results is

however largely restricted to a narrow region along the axis, and very good agreement between the two sets of contours is still found well downstream of the throat at points further from the centerline. Note that no contour lines are shown within the plume backflow region beyond the nozzle lip, due to the small sample size in this very low density region.

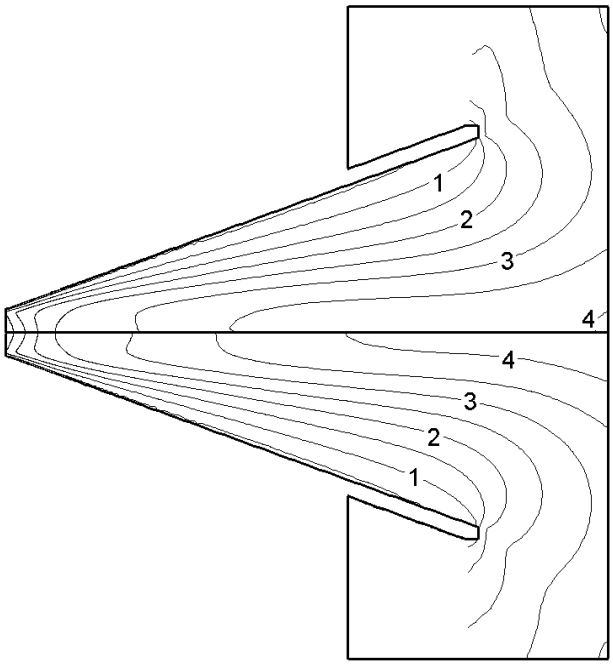

Figure 5.3. Mach number contours for ES-BGK (top) and DSMC (bottom).

Contours of density are shown in Fig. (5.4), again with ES-BGK results in the top half and DSMC results in the bottom half of the figure. All values are normalized by the stagnation density $\rho_o = 5.323\times10^{-3}$ kg/m^3. As in Fig. (5.3) we find excellent agreement around the nozzle throat and further downstream in regions far from the centerline. Both results show an off-axis local maximum in the density profile just downstream of the throat, which is consistent with a weak compression wave described by *Chung et al*. (1995) and mentioned above in the discussion of Mach number contours. As above, the

greatest difference between the two results is found along the axis at points far from the throat. Here there is a noticeable increase in the ES-BGK expansion rate relative to that of DSMC, so that at a given point on the axis the density is lower in the ES-BGK results.

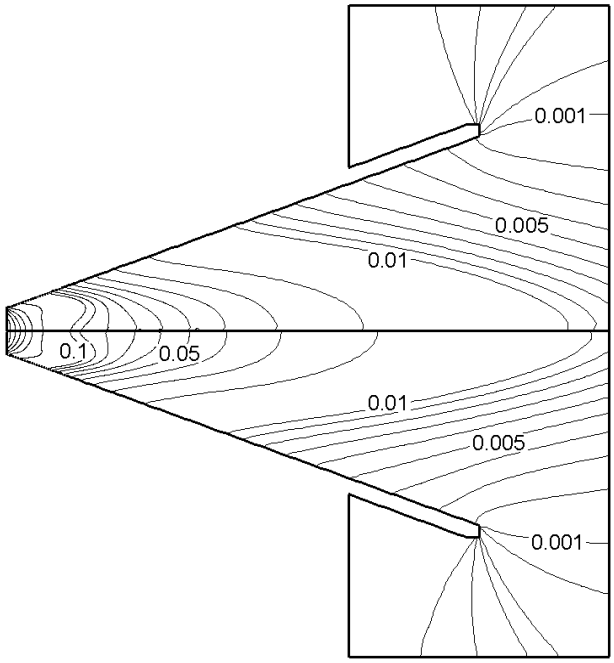

Figure 5.4. Density contours for ES-BGK (top) and DSMC (bottom). Values are normalized by the stagnation density.

5.4.3 Centerline property variation

This difference in expansion rates is also found in Fig. (5.5), which shows the normalized density variation along the centerline. The axial coordinate x in the plot is normalized by the throat radius R_t = 2.55 mm, and a dotted vertical line gives the location of the nozzle exit plane. Here results for the ES-BGK and DSMC simulations are plotted against those for DSMC and NS simulations of *Chung et al*. (1995) and the experimental data points of *Rothe* (1971).

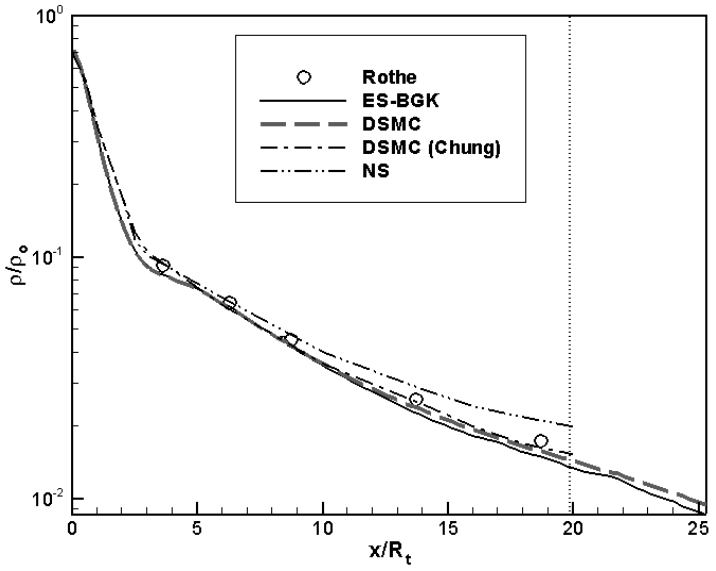

Figure 5.5. Density variation along the nozzle centerline.

For $x/R_t < 10$ very similar centerline density profiles are found for the two simulations presented here, and a slight difference is observed between these and the DSMC and NS contours given by *Chung et al.* The reason for this discrepancy is not clear, but two likely possibilities are some difference in grid resolution within this region between the two sets of simulations, or a discretization of flow conditions at the nozzle throat from the use of a finite number of uniform inflow boundaries. In general, the ES-BGK result agrees very well with both DSMC density profiles and the experimental values. A significantly higher level of overall accuracy is found in the ES-BGK results than in those from the NS simulation, particularly far downstream of the throat where density is slightly underpredicted by ES-BGK but greatly overpredicted by the NS approach.

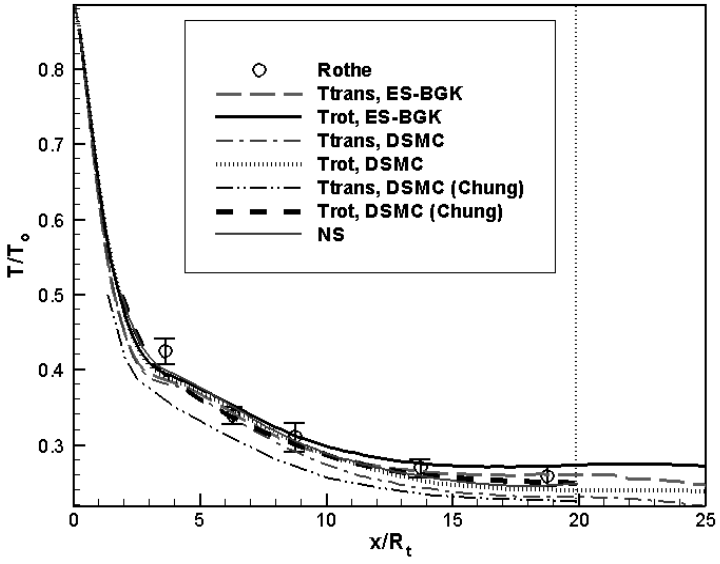

Figure 5.6. Variation of rotational and translational temperature along the centerline.

Figure (5.6) shows the variation in translational and rotational temperature along the nozzle centerline for ES-BGK and both DSMC simulations, along with the NS centerline temperature and rotational temperature values of *Rothe* (1971). All temperatures here are normalized by the stagnation temperature T_o = 300 K. In comparing the two temperature profiles from the ES-BGK simulation, note that the rotational temperature is uniformly higher than the translational temperature, and that the difference between the two values increases with downstream distance. This trend is also observed in both sets of DSMC results, and demonstrates the rotational energy lag expected in rarefied expansion flows due to a finite rotational relaxation time. The quantitative level of agreement between the experimental measurements and ES-BGK results is in general comparable to that between the experiment and DSMC, although the ES-BGK rotational temperature near the nozzle exit is significantly higher than that found using the other methods.

5.4.4 Comparison of results along a radial plane

Density profiles across a radial plane near the nozzle exit are shown in Fig. (5.7). This plane is defined by the axial location $x/R_t = 18.7$, and radial coordinates y are normalized by the local nozzle radius R_w. As discussed above, the correlation between ES-BGK and DSMC results in this region decreases significantly toward the nozzle centerline, where the ES-BGK density is about 7% lower than that found for either DSMC simulation. Further from the centerline, the agreement between ES-BGK and DSMC results increases considerably, with nearly identical values found at points close to the nozzle wall. At all points along this plane, ES-BGK density values are uniformly lower than those found experimentally, while the density values extracted from the NS solution are significantly greater than the experimental values. Except for a small region roughly half way between the axis and nozzle wall, the ES-BGK density values are found to more closely approximate measured values than do results from the NS simulation.

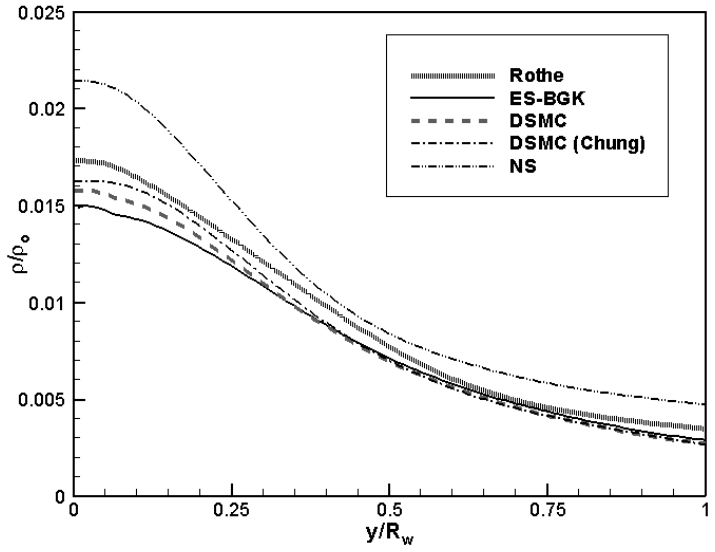

Figure 5.7. Density variation along a radial plane at x/R_t=18.7.

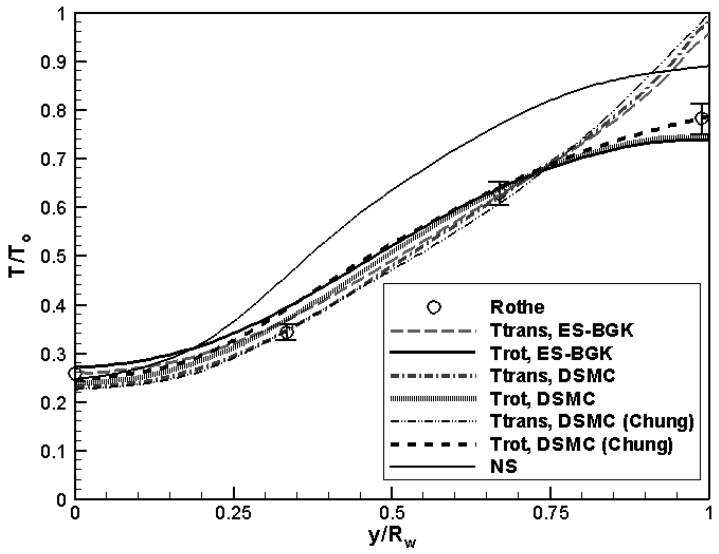

Figure 5.8. Temperature variation along a radial plane at x/R_t=18.7.

Profiles of rotational and translational temperature along the same radial plane are shown in Fig. (5.8). In comparing the ES-BGK rotational temperature profile with that from the DSMC simulation performed here, we find an overestimate of about 13% in the ES-BGK values near the axis, and a slight underestimate (less than 1%) at the nozzle wall. The same general pattern is also observed in a comparison of translational temperature profiles, although the translational temperature is underpredicted in the ES-BGK simulation by roughly 3% at the wall. While some of these discrepancies are significant, the general trends shown in the DSMC results are qualitatively reproduced very well by the ES-BGK method: The rotational temperature is slightly higher than the translational temperature for $y/R_w < 0.7$, with a sign reversal in the temperature difference beyond this point. At the nozzle wall, the translational temperature is almost fully

accommodated to the wall temperature, while the rotational temperature is considerably lower.

The difference between translational and rotational temperatures at the wall in both the ES-BGK and DSMC results may be attributed to the wall collision model. All particle-wall collisions are diffuse, so that the translational component of average thermal energy for reflected particles corresponds to either the wall temperature or the local stagnation temperature as measured by the velocity of incident particles. As the wall and stagnation temperatures are nearly equal, we expect a very small difference between the wall surface temperature and the gas translational temperature at the wall. In contrast, the average post-collision rotational energy of particles involved in adiabatic diffuse reflection corresponds to the rotational component of the gas static temperature, not the stagnation temperature. Rotational energy accommodation occurs for only a small fraction of wall collisions, so there should be relatively little difference in the average rotational energy between incident and reflected particles.

In low density regions where the rotational relaxation time is large compared to other characteristic time scales for the flow, a significant lag may develop between rotational and translational temperatures. As the region under consideration has both a large rotational relaxation time and a boundary condition which tends to disproportionately increase the translational temperature, the trends observed at the wall in Fig. (5.8) seem physically justified.

Note that the NS simulation does not account for rotational nonequilibrium, so only a single temperature for this simulation is shown in the figure. The NS temperature profile shows relatively poor agreement with all of the other results, and gives a gas temperature

at the wall between the translational and rotational temperatures found using the other methods. A no-slip adiabatic boundary condition is used for the wall in the NS calculation, so some temperature discontinuity at the wall is expected.

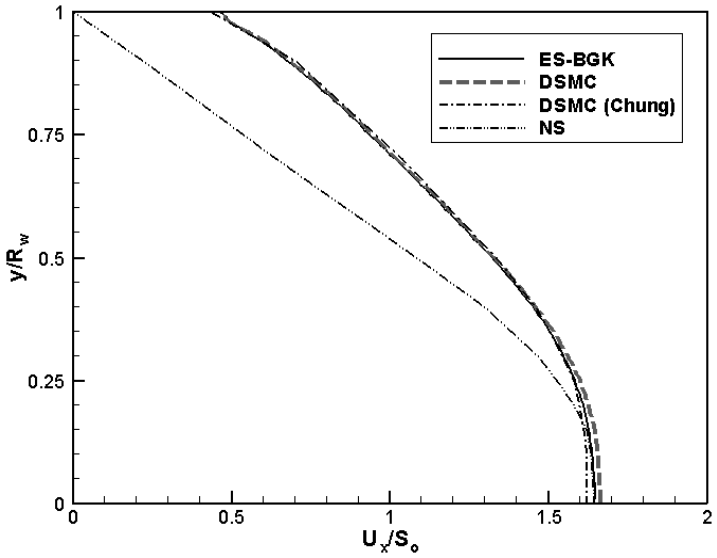

Figure 5.9. Axial velocity profiles at x/R_t=18.7.

Profiles of bulk axial velocity are shown in Fig. (5.9), again at the radial plane near the nozzle exit defined by x/R_t = 18.7. Velocities here are normalized by the most probable thermal speed at the stagnation temperature $S_o = (2RT_o)^{1/2}$ = 422 m/s. Nearly identical profiles are found for the ES-BGK and the two DSMC simulations, with a deviation between the three results of less than 5% at all points on the plot. The NS velocity profile shows excellent agreement with the other results at the centerline, but diverges significantly within a short distance from the axis. While the ES-BGK and DSMC simulations give a wall slip velocity equal to about 28% of the centerline velocity, the NS no-slip boundary condition results in a velocity of zero at the wall. If a Maxwell-type slip model (based on the velocity gradient at the wall) had been employed in the NS

simulation, we expect that better agreement would be found between the NS velocity profile and those for the other methods. A slip model would however affect density and temperature profiles as well, so it is not clear that its inclusion would lead to a net gain in overall accuracy for the NS simulation of this flow.

5.4.5 Evaluation of continuum breakdown

Figure (5.10) displays the variation along the centerline of continuum breakdown parameters, based on the DSMC simulation performed for this study. As defined by *Boyd, Chen and Candler* (1995), the local degree of thermal nonequilibrium may be roughly characterized by the maximum value of a gradient length local Knudsen number $\mathrm{Kn}_{\mathrm{GLL}}(\mathrm{Q})$, where

$$\mathrm{Kn}_{\mathrm{GLL}}(\mathrm{Q}) = \frac{\lambda}{\mathrm{Q}}\left|\frac{\partial \mathrm{Q}}{\partial \mathrm{s}}\right| \tag{5.37}$$

and Q is set to either the density, translational temperature or bulk speed of the gas. The symbol λ here denotes the mean free path, and $\partial \mathrm{Q}/\partial \mathrm{s}$ is the partial derivative of Q in the direction of maximum gradient. As radial derivatives of macroscopic flow quantities are by definition zero along the centerline, ∂s here is in the axial direction. Significant scatter is observed among data points in the figure, as a result of both statistical noise and subtractive cancellation error in the evaluation of the derivatives. Tenth order polynomial trend lines, based on a least-squares fit, are therefore used to more clearly show the general trends among the three different parameters.

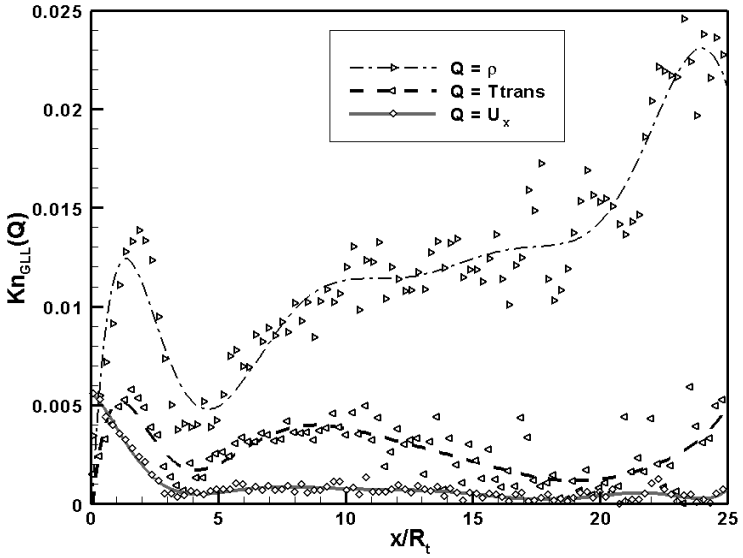

Figure 5.10. Continuum breakdown parameters along the nozzle centerline.

As is generally expected for a near-adiabatic expansion flow, the parameter based on density $Kn_{GLL}(\rho)$ gives the largest value through nearly the entire range considered. Based on this parameter, a local maximum in the degree of nonequilibrium is found a short distance downstream of the throat. This maximum can be attributed to the large curvature of streamlines around the throat, and the associated weak compression wave mentioned in the discussion of Figs. (5.3) and (5.4). The flow then equilibrates somewhat before rarefaction effects again become more prominent further downstream. A maximum $Kn_{GLL}(\rho)$ value of slightly less than 0.025 is ultimately reached in the nearfield plume region just upstream of the outflow boundary. Trends in this parameter are found to correlate well with the general level of agreement between ES-BGK and DSMC results as shown in Figs. (5.3) through (5.6). As the value of $Kn_{GLL}(\rho)$ increases with downstream distance along the centerline, translational and rotational temperatures are

increasingly overpredicted by the ES-BGK method, while density and Mach number are underpredicted.

5.4.6 Considerations of computational expense

It should be noted that the comparison of ES-BGK simulation results with DSMC, NS and experimental data is intended to assess the validity of the assumptions and approximations behind the method itself, and not to evaluate the tradeoff between efficiency and accuracy at larger time steps where advantages of the ES-BGK method over DSMC become apparent. However, if computational expense is measured as the mean calculation time per particle per time step at steady state, the ES-BGK simulation presented here is about 9% less expensive than the DSMC simulation. While this figure may seem discouraging, the ES-BGK calculations are not performed under conditions for which this method is intended in a practical engineering application, but instead under conditions where traditional DSMC techniques are more appropriate due to the relatively large Knudsen number regimes encountered here.

Throughout the computational domain, the time step used in both ES-BGK and DSMC simulations is no greater than the local mean collision time, as is standard practice in DSMC. (Through much of the flowfield, the time step is in fact several times smaller than the mean collision time.) The use of such a small time step contributes to a high degree of confidence in the overall accuracy of the DSMC simulation, and allows the ES-BGK simulation to be performed under conditions where several assumptions behind this method are known to be valid. In particular, the temporal decoupling of particle advection and collision processes in both ES-BGK and DSMC is strictly valid only when

this decoupling occurs over time scales smaller than the mean collision time. The above comparison should therefore be viewed as an evaluation of the ES-BGK method under ideal conditions where the accuracy of this method in a rarefied expansion flow can be properly assessed.

As discussed in Section 5.1, the proposed scheme is not intended as an alternative to DSMC as a general simulation method for nonequilibrium gas flows, but instead is meant for implementation in a hybrid code to simulate flows involving a wide range of Knudsen number regimes. In the intended application of this code, standard DSMC techniques are used in regions of highly nonequilibrium flow where DSMC is most appropriate, and ES-BGK calculations are performed only in higher density transition regime and continuum flow regions where DSMC may be prohibitively expensive. The boundary between DSMC and ES-BGK domains is determined according to standard continuum breakdown parameters such as Eq. (5.37). With the exception of areas close to this boundary, the ES-BGK procedures will be applied primarily to regions where, for computational efficiency, the time step and cell size are significantly larger than the mean collision time and mean free path respectively.

As the time step and cell size increase, some additional loss of accuracy is expected in the ES-BGK results, due to an error associated with the temporal and spatial decoupling of collision and advection processes in the gas, as well as a nonphysical equilibration of flow properties in each cell and an increase in numerical diffusion effects. [*Breuer et al*. (1995)] At the same time, the computational expense of collision procedures will approach an asymptotic limit where all particle velocity and rotational energy values are reassigned during each time step. In contrast, DSMC collision procedures either give

roughly linear scaling of computational expense with time step size (as in the no time counter scheme of *Bird* (1994)) or permit the occurrence of nonphysical collisions for which the collision probability is greater than one when the time step is sufficiently large (as in the scheme of *Baganoff and McDonald* (1990)).

While the simulations presented here have not been performed under conditions where the time step is much greater than the mean collision time, we can assume with confidence that the overall accuracy of the ES-BGK method under these conditions is comparable to that of a number of existing particle methods for the simulation of near-equilibrium flows. In particular, for a simple monatomic gas, the method presented here should give identical results to particle methods of *Pullin* (1980) and *Macrossan et al*. (2005) at the limit where the ratio of the time step to the local mean collision time approaches infinity. At this limit, all particle velocities are effectively resampled from a Maxwellian distribution, as is done in these other particle schemes. For ease of discussion, methods such as those of *Pullin* and *Macrossan et al*. which involve the reassignment of particle velocities from equilibrium distributions are referred to here collectively as direct resampling methods.

The velocity equilibration process in direct resampling methods can instead be accomplished in DSMC through the use of collision limiters, where every particle collides no more than a set number of times during each time step. [*Bartel et al.* (1994)] While the application of collision limiters in near-equilibrium regions provides a relatively simple approach to simulating flows which involve a wide range of Knudsen number regimes, a number of collisions are typically required for each particle in order to approximate a Maxwellian distribution. As a result, direct resampling methods – where

particle velocities are modified only once per time step – tend to require significantly fewer operations, so allow for a potentially large increase in overall efficiency.

As in direct resampling methods, the proposed ES-BGK method requires that particle velocities be reassigned no more than once per time step, so that the new method retains this efficiency advantage over collision limiter schemes for the simulation of near-equilibrium flows. However, unlike direct resampling methods, the ES-BGK method can account for nonequilibrium phenomena when the time step and cell dimensions are sufficiently small. For integration with DSMC in a hybrid simulation, these latter requirements are typically met in regions near the boundary between DSMC and ES-BGK domains. Thus, the use of this method in a hybrid scheme with DSMC should enable simulation results to be relatively insensitive to the location of the DSMC/ES-BGK domain boundary, while preserving the efficiency advantages of direct resampling methods in near-equilibrium regions.

Chapter VI

A Monte Carlo Model for Particle Radiation

6.1 Introduction

Much of the current and historical interest in flowfield simulation for high altitude SRM plumes is a result of the need for accurate prediction of plume radiation signatures. As outlined in Chapter 1, plume radiation analysis is required in the development of missile defense technologies, and radiative heating of rocket or spacecraft components is often a major concern during the vehicle design process. Radiative heating is a particularly important issue in SRM exhaust flows, as continuum radiation fluxes from liquid and solid Al_2O_3 may be orders of magnitude greater than gas phase emission through much of the plume. Particle radiation tends to dominate emissive properties of high altitude SRM plumes over a wide range of wavelengths, and gas contributions to plume spectral radiance profiles are typically limited to a few narrow spikes associated with gas species absorption and emission lines. [*Vitkin et al.* (1997), *Reed and Calia* (1993), *Duval, Soufiani and Taine* (2004), *McGregor et al.* (1992), *Plastinin et al.* (2001)] As a result, most previous efforts at radiation analysis for the plume flows of interest have focused on particle radiation, and the gas has commonly been assumed to be optically transparent. [*Rattenni* (2000), *Candler et al.* (1992)]

One characteristic of these flows which has not received much attention is the potential for strong two-way coupling between particle radiation and flowfield properties. The total intensity and spectral dependence of Al_2O_3 particle radiation are strong functions of particle temperature and phase composition, which in turn both depend on the heat transfer history of particles within the plume. Radiative emission and absorption may have a significant effect on particle temperatures, and to a lesser extent on gas temperatures and related flowfield properties. As the particle temperature appears in expressions for interphase momentum transfer given in Chapters 2 and 3, radiative heat transfer may influence particle and gas bulk velocities as well.

Most previous studies of rocket exhaust plume radiation – particularly those which have considered spectrally resolved emission, absorption and scattering properties of condensed phase particles – have used a post-processing approach to radiation analysis. [*Reardon* (1993), *Garrison, Ozawa and Levin* (2005)] In this approach, a detailed numerical simulation is first performed for the plume flow of interest. Radiation terms in the gas or particle energy balance are either neglected entirely or introduced in greatly simplified form, where absorption and scattering properties are ignored and particles are modeled as gray-body emitters. Simulation results are then used as input values for a separate code used to compute plume radiation signatures.

While this uncoupled approach allows for relatively inexpensive calculations and likely produces very accurate results for a wide range of flows, it leaves the potential impact of strong two-way coupling between flowfield and radiation properties an open question. As described above, a lack of consideration for this effect in an SRM exhaust

plume simulation may produce large errors in both calculated radiation and flowfield characteristics.

To demonstrate the potential impact of radiation-flowfield coupling on plume characteristics, consider a greatly simplified example which is roughly based on the simulations in Chapter 4. In this example, 1 μm diameter Al_2O_3 particles are expelled from a small-scale SRM into a vacuum, and we want to find the effect of radiative heat loss on particle temperatures and emissive power 100 m downstream of the nozzle exit. We assume that particle properties are affected by the surrounding gas only within a very small nearfield plume region, and that at the outer edge of this region all particles have a speed c_p = 3000 m/s and a temperature $T_{p,init}$ = 2000 K. Particles are modeled as gray-body emitters of emissivity ε = 0.01, and radiative absorption is neglected. Outside of the nearfield plume region, the particle energy balance can be written as

$$m_p c_s c_p \frac{dT_p}{dx} = -4\pi R_p^2 \sigma \varepsilon T_p^4 \tag{6.1}$$

where c_s = 1225 J/kg K is the specific heat of the particle material, R_p is the particle radius, and σ is the Stefan-Boltzmann constant. Equation (6.1) may be rearranged and integrated to find the temperature $T_{p,final}$ at a distance Δx = 100 m downstream:

$$T_{p,final} = \left[T_{p,init}^{-3} + \frac{12\pi R_p^2 \sigma \varepsilon \Delta x}{m_p c_s c_p} \right]^{-1/3} \tag{6.2}$$

Equation (6.2) is used to calculate a final temperature of 1654.6 K, so that particles are found in this example to cool by nearly 350 K due to radiative heat loss. As gray-body radiation intensity scales with the fourth power of temperature, this reduction in T_p corresponds to a particle emissive power which decreases to a fraction $(T_{p,final}/T_{p,init})^4$ = 0.4684 of the initial value. Thus, radiation-flowfield coupling is shown here to account

for a reduction in farfield emissive power of over 50%. It can be inferred from this simple calculation that radiative heat transfer plays a potentially important role in a range of flow characteristics for the SRM exhaust plumes of interest. The traditional approach to plume radiation modeling, where radiation calculations are performed for a predetermined flowfield, may therefore introduce a significant error into the calculated results. To avoid this error source, a new procedure is proposed for the coupled DSMC simulation and radiation analysis of high altitude SRM plume flows.

In the following sections, a particle radiation model is presented for use with procedures described in Chapters 2 through 5 for the simulation of a high altitude SRM plume flow. First, a detailed description of the method is given, including a discussion of procedures related to emission, absorption, scattering and two-way coupling between radiation and flowfield characteristics. Techniques are then outlined for consideration of nozzle searchlight emission and the calculation of spectral radiance. Finally, the method is extended for use with flows involving soot particles, so that the effect of soot on SRM plume radiation can be evaluated. The inclusion of soot particles also allows the procedures in this chapter to be used in the simulation of high altitude exhaust plumes from liquid propellant rockets. All models described here are applied to a detailed SRM plume flow simulation in Chapter 7, where the relative contributions of a number of particle radiation properties and input parameters are assessed.

6.2 Radiation modeling procedures

The proposed particle radiation model uses a Monte Carlo ray trace (MCRT) approach, where a Lagrangian representation is used to track large groups of photons

through the computational grid. [*Farmer and Howell* (1994), *Mahan* (2002)] As a first step, the portion of the spectrum of interest for radiative heat transfer – wavelengths of roughly 0.5 to 5 μm – is divided into a series of spectral bands. Following a standard convention, these bands are termed wave number bins and are assigned according to the wave numbers η at their centers. (The wave number is the inverse of the wavelength.) Given N_η different bins, each of width $\Delta\eta_i$ and centered at a wave number η_i, a large number N_b of representative "energy bundles" are generated once every few time steps at randomly selected source particles throughout the grid. An equal number of energy bundles is assigned to each of the N_η bins.

As in any MCRT scheme, each energy bundle represents some quantity of radiative power over a finite wave number range $\Delta\eta_i$. A newly generated bundle is given a direction of propagation according to a randomly generated unit vector **u**. The bundle is also given some initial power P_b, based on the assigned wave number bin and the properties of the source particle.

6.2.1 Determination of initial power for an energy bundle

Following a correlation of *Reed and Calia* (1993) based on Mie theory calculations of *Plass* (1965), the band-averaged spectral emissivity of the source particle at bin i may be approximated as

$$\varepsilon_i = 4k(T_p, \eta_i)R_p\eta_i \tag{6.3}$$

where T_p and R_p are the temperature and radius of the particle respectively, and k is a value for the absorption index of Al_2O_3 at temperature T_p and wave number η_i. Due to both a lack of experimental data and an extreme sensitivity of k for solid particles on

lattice defects and impurities, any dependence of k on the particle phase composition is neglected here. [*Reed and Calia* (1993)] By applying Eq. (6.3) to Planck's function for the spectral distribution of emissive power [*Siegel and Howell* (1981)], we can compute the source particle emissive power $P_{p,i}$ within the wave number range to which the bundle is assigned:

$$P_{p,i} = 32\pi^2 c_0^2 h R_p^3 \Omega_i(T_p) \tag{6.4}$$

where

$$\Omega_i(T) = \int_{\Delta\eta_i} \frac{k(T,\eta_i)\eta^4 d\eta}{\exp(hc_0\eta / k_B T) - 1} \tag{6.5}$$

In Eqs. (6.4) and (6.5) the symbol c_o is the speed of light through a vacuum, h is Planck's constant, and k_B is Boltzmann's constant.

Once $P_{p,i}$ is known, the initial power of the bundle P_b may be determined as

$$P_b = \frac{N_\eta N_p}{N_b} W_p P_{p,i} \tag{6.6}$$

where N_p is the total number of representative particles in the grid and W_p is the numerical weight of the source particle. Values of $\Omega_i(T)$ are calculated at simulation startup for each wave number bin, at temperatures T for which experimentally determined $k(T,\eta_i)$ values are available. The evaluation of $\Omega_i(T_p)$ in Eq. (6.4) is then performed through linear interpolation to the particle temperature T_p.

(Note in Eq. (6.4) that particles are modeled here as volumetric emitters, as emissive power is assumed to scale with R_p^3. [*Reed and Calia* (1993)] With some limitations, radiation calculations may therefore be extended to the nonspherical particles considered in Chapter 2 if R_p is taken as the radius for a sphere of equal volume.)

6.2.2 Procedures for absorption and scattering

Once created, each energy bundle is tracked through the grid during the current time step until it exits through an inflow, outflow, or absorbing wall boundary. As an energy bundle passes through a cell in which particles are located (or have been located during previous time steps) a fraction of the assigned power will be absorbed, and there is some probability that the bundle will be scattered. Absorption and scattering properties in the cell for a given wave number bin are determined, respectively, by the band-averaged spectral absorptance α_i and scattering coefficient σ_i. The spectral absorptance α_i is defined so that, over a differential distance *ds* through a homogeneous absorbing medium, the change in radiation intensity I_i within the wave number range $\Delta\eta_i$ will be $dI_i = -\alpha_i I_i \, ds$ assuming that both emission and scattering within the medium are negligible. Likewise, the scattering coefficient may be defined by $dI_i = -\sigma_i I_i \, ds$ if both emission and absorption are neglected.

Consider a simulation involving N_{spec} different particle species j, where species are designated according to the particle radius R_j. In the cell of interest, each species has an average temperature T_j and a number density n_j, where averaging is performed over a large number of time steps for both T_j and n_j. By applying Eq. (6.3) and Kirchkoff's law [*Siegel and Howell* (1981)] to the definition of spectral absorptance, we can compute α_i as the product of the band-averaged absorption cross section $\pi R_j^2 \varepsilon_i$ and number density n_j, summed over all particle species.

$$\alpha_i = 4\pi\eta_i \sum_{j=1}^{N_{spec}} k(T_j, \eta_i) R_j^3 \, n_j \tag{6.7}$$

The value of $k(T_j,\eta_i)$ for each species is found by interpolating tabulated k values to the temperature T_j. The corresponding scattering coefficient σ_i is also given as a summation over all particle species:

$$\sigma_i = \pi \sum_{j=1}^{N_{spec}} \Theta_{i,j} R_j^2 n_j \tag{6.8}$$

The symbol $\Theta_{i,j}$ in Eq. (6.8) is the scattering efficiency factor for wave number bin i and particle species j. Values of $\Theta_{i,j}$ are calculated at simulation startup, using a first-order Mie theory approximation of *Siegel and Howell* (1981). Assuming that $n_i >> k$, where n_i is the real part of the index of refraction for the particle material at wave number η_i, $\Theta_{i,j}$ may be given as a function of the nondimensional parameter $x_{i,j}=2\pi\eta_i R_j$.

$$\Theta_{i,j} = \frac{8}{3} x_{i,j}^4 \left[\frac{n_i^2 - 1}{n_i^2 + 2} \left(1 + \frac{3}{5} \left(\frac{n_i^2 - 2}{n_i^2 + 2} \right) x_{i,j}^2 \right) \right]^2 \tag{6.9}$$

While Eq. (6.9) can be assumed accurate for Al_2O_3 when $x_{i,j} << 1$, it greatly overpredicts $\Theta_{i,j}$ for larger values of $x_{i,j}$. To allow for use with a wider range of $x_{i,j}$ values, we impose a limiting condition $\Theta_{i,j} \leq 2$. This gives relatively good agreement with Mie theory calculations of *Plass* (1965), and avoids the detailed calculations required to find an exact Mie theory solution. Note that we neglect here any dependence of n_i on the particle temperature, following observations that n_i values for Al_2O_3 are nearly constant over a wide range of temperatures. [*Plass* (1965)] While experiments have shown some increase in n_i with particle size [*Laredo and Netzer* (1993)], we neglect this dependence as well due to a lack of available experimental data.

When an energy bundle enters a given cell, the total distance D_e to exit the cell along the initial trajectory is determined along with α_i and σ_i values corresponding to the

assigned wave number bin. The distance D_s to a scattering event is then determined by evaluating the probability P_{ns} that the bundle will not have been scattered after it has traveled a distance D_s, where

$$\frac{dP_{ns}}{dD_s} = -\sigma_i P_{ns} . \tag{6.10}$$

Solving for D_s and setting P_{ns} equal to a random number $R \in (0,1]$, we find

$$D_s = -\frac{1}{\sigma_i} \ln R . \tag{6.11}$$

If $D_s > D_e$ then the particle will exit the cell along its initial trajectory. Otherwise the bundle will be scattered. If scattered, the bundle is moved a distance D_s along the trajectory, after which its direction is reassigned and the procedure is repeated.

The anisotropic nature of the scattering process is approximated through the use of the Henyey Greenstein scattering phase function. [*Everson and Nelson* (1993)]

$$\Phi(\theta) = \frac{1-g^2}{4\pi\left(1+g^2-2g\cos\theta\right)^{3/2}} \tag{6.12}$$

The free parameter g in Eq. (6.12) is the average cosine of the scattering angle θ. We can recover the corresponding distribution function $f(\theta) = 2\pi\Phi(\theta)\sin\theta$ if we set

$$R = 2\pi\int_0^{\theta}\Phi(\theta')\sin\theta'\,d\theta' \tag{6.13}$$

for a random number R between 0 and 1. Following Eqs. (6.12) and (6.13), we determine θ through the formula

$$\cos\theta = \frac{1}{2g}\left[g^2+1-\left(\frac{1-g^2}{2gR-g-1}\right)^2\right]. \tag{6.14}$$

The unit vector $\mathbf{u}^*$ in the final direction of propagation is then calculated as

$$\mathbf{u}^* = \mathbf{u}\cos\theta + \mathbf{t}_1 \sin\theta\cos\phi + \mathbf{t}_2 \sin\theta\sin\phi \tag{6.15}$$

where the azimuthal angle ϕ is assigned a random value in $[0,2\pi]$, $\mathbf{u}$ is the initial direction, and the unit vectors $\mathbf{t}_1$ and $\mathbf{t}_2$ are given by

$$\mathbf{t}_1 = \frac{\mathbf{u}\times\hat{\mathbf{i}}}{\left|\mathbf{u}\times\hat{\mathbf{i}}\right|} \quad \text{and} \quad \mathbf{t}_2 = \mathbf{t}_1 \times \mathbf{u}\,. \tag{6.16}$$

For convenience, $\hat{\mathbf{i}}$ is defined here as the unit vector along the x-coordinate axis.

The procedure involving the evaluation of Eqs. (6.11), (6.14) and (6.15) is repeated until the bundle exits the cell. Given a total distance D_t which the bundle has traveled through the cell, the assigned power P_b is then reduced by a fraction $1–\exp(–\alpha_i D_t)$ to account for the effect of particle phase absorption on the transmitted radiation intensity. [*Farmer and Howell* (1994)]

6.2.3 Contribution to the particle energy balance

As the energy bundle passes through a cell, the power ΔQ_{abs} absorbed by an individual particle within the cell may be given as the product of the total absorbed power $P_b[1–\exp(–\alpha_i D_t)]$ and the fraction of this absorbed power attributed to the particle. From the derivation of Eq. (6.7), ΔQ_{abs} can be expressed as

$$\Delta Q_{abs} = \frac{\pi R_p^2 \varepsilon_i}{\alpha_i V_c} P_b \left[1 - \exp\left(-\alpha_i D_t\right)\right] \tag{6.17}$$

where R_p is the particle radius, V_c is the cell volume and P_b is the initial power assigned to the bundle on entering the cell. As the contribution of the bundle to the direction-averaged radiative energy flux Δq_i for the corresponding wave number bin is the ratio of ΔQ_{abs} to the absorption cross section $\pi R_j^2 \varepsilon_i$, it follows that

$$\Delta q_i = \frac{P_b}{\alpha_i V_c}\left[1 - \exp\left(-\alpha_i D_t\right)\right]. \tag{6.18}$$

In an optically thin cell where $\alpha_i D_t << 1$ the evaluation of Eq. (6.18) may result in a large subtractive cancellation error. To correct for this error, when $\alpha_i D_t < 10^{-5}$ we calculate Δq_i using a linearized form of Eq. (6.18)

$$\Delta q_i = \frac{P_b D_t}{V_c} \tag{6.19}$$

based on a Taylor expansion of the exponential term. Note that Eq. (6.19) gives an exact solution for Δq_i in regions outside the particle domain where α_i is zero.

During each time step for which energy bundles are tracked through the grid, energy flux values in every cell are determined by summing contributions Δq_i from all bundles which pass through the cell, using Eqs. (6.18) and (6.19). The resulting values are then averaged over a large number of time steps to reduce statistical scatter. Once the flowfield has reached steady state conditions, averaging may be performed over all subsequent time steps during which radiation calculations are made. Otherwise a subrelaxation technique of *Sun and Boyd* (2005) is used for the time-averaging procedure, so that increased weighting may be applied to more recent time steps.

As discussed in Section 6.1, strong two-way coupling may exist between flowfield characteristics and plume radiation. Radiative heat transfer can significantly affect particle temperatures, and may indirectly influence other properties such as the particle phase composition, material density, and the rates of momentum and energy transfer between the particles and gas. To account for the effect of radiative emission and absorption on particle temperatures, the temperature T_p of every representative particle is modified during each time step by

$$\Delta T_p = \frac{\Delta t}{m_p c_s} \dot{Q}_{rad} \tag{6.20}$$

where Δt is the time step interval, m_p is the particle mass, c_s is the specific heat of the particle material, and $\dot{Q}_{rad}$ is the net rate of radiative heat transfer to the particle. Note that the particle temperature is assumed spatially uniform, based on a low Biot number approximation which follows from the small particle size and relatively high thermal conductivity of Al_2O_3. [*Incropera and DeWitt* (1996)]

The radiative heat transfer rate $\dot{Q}_{rad}$ in Eq. (6.20) is calculated for each particle as

$$\dot{Q}_{rad} = 4\pi R_p^3 \sum_{i=1}^{N_\eta} \left[\eta_i k(T_p, \eta_i) q_i - 8\pi c_0^2 h \Omega_i(T_p) \right] \tag{6.21}$$

following Kirchkoff's law [*Siegel and Howell* (1981)] and Eqs. (6.3) and (6.4). The above symbol q_i is the time-averaged and direction-averaged energy flux within a wave number bin i, for the cell in which the particle is located. This value is found, as described above, by summing flux contributions Δq_i from energy bundles that pass through the cell then averaging over a large number of time steps.

6.2.4 Nozzle searchlight emission

In the plume flows of interest, radiative emission from within the nozzle has been found to significantly increase radiation intensity near the exit plane. [*Reed et al.* (1992)] This emission is generated primarily by the high-temperature interior walls in the divergent section of the nozzle, and is generally termed "searchlight emission" under past assumptions that its dominant source is upstream of the throat. Depending on the optical thickness of the exhaust flow, emission from particles within the nozzle may also contribute significantly. As searchlight emission is expected to influence the temperature

and phase composition of particles in the plume, a coupled approach to radiation and flowfield simulation should include consideration of this effect. We account for searchlight emission here through the generation of additional energy bundles along inflow boundaries at the nozzle exit.

Each inflow boundary on the exit plane is represented as a blackbody wall at some characteristic temperature T_w. Along every cell face located on an inflow boundary, a number N_f of new bundles are generated during each time step for which radiation calculations are performed. Each bundle is randomly assigned to a wave number bin i, and is given an initial direction **u** such that

$$\mathbf{u} \cdot \mathbf{n}_f = \cos\theta = R^{1/2} \tag{6.22}$$

where $\mathbf{n}_f$ is the inward normal unit vector at the cell face, θ is the zenithal angle of **u** relative to the face, and *R* is a random number between 0 and 1.

Equation (6.22) is derived in a similar manner to Eq. (3.4), and the derivation may be summarized as follows: For a flat diffusely emitting surface of area ∂A, the probability that a photon will be emitted within the differential solid angle $\sin\theta d\theta d\phi$ centered at an angle θ to the surface normal is proportional to the projected surface area $\partial A\cos\theta$ in this direction. The distribution function for θ is therefore proportional to the product $\sin\theta\cos\theta$, and is in fact identical to Eq. (2.3). Applying the inverse cumulative distribution function method [*Bird* (1994)] to this distribution function, we find $R = \sin^2\theta = 1-\cos^2\theta$. As *R* and 1–*R* are equivalent in a statistical sense, the quantity $\cos^2\theta$ may be set to a random number *R* as in Eq. (6.22).

Once θ is known, the unit vector **u** is determined through a procedure similar to that described in Section 6.2.2 for finding the directional vector $\mathbf{u}^*$ for a newly scattered

energy bundle. The initial power P_b is then computed using Eq. (6.23) as the product of the face area A_f, a weighting factor N_η/N_f, and the integral of Planck's function over the interval $\Delta\eta_i$ for the corresponding wave number bin. [*Siegel and Howell* (1981)]

$$P_b = 2\pi c_0^2 \, h \, A_f \frac{N_\eta}{N_f} \int_{\Delta\eta_i} \frac{\eta^3 d\eta}{\exp(hc_0\eta / k_B T_w) - 1} \tag{6.23}$$

6.2.5 Plume radiance calculations

One primary output value of interest in the radiation analysis of SRM plume flows is the spectral radiance. This measure of plume radiative emission is important for a variety of missile defense applications, and can be used for comparison between numerical results and experimental measurements to assess the accuracy of simulation techniques. (Such a comparison is performed in Chapter 7.) For a participating medium, the spectral radiance may be defined as the incident monochromatic radiative energy flux within a differential solid angle, on a flat surface oriented normal to the flux direction, per unit solid angle and per unit wavelength. [*Siegel and Howell* (1981)]

For calculations of plume radiance in the scheme presented here, one or more simulated sensors are positioned either within or outside the grid domain. Consider a sensor located outside the grid which has a surface area A_s, outward normal unit vector $\mathbf{n}_s$, and angular resolution defined by the zenithal angle ω. When each energy bundle exits the grid, we determine whether it will intersect the sensor surface along a trajectory given by the unit vector $\mathbf{u}$ for the bundle direction. If an intersection occurs and the condition

$$-\mathbf{u} \cdot \mathbf{n}_s \geq \cos\omega \tag{6.24}$$

is met, then the power P_b assigned to the bundle is added to the total absorbed power ΣP_i for the corresponding wave number bin during the current time step. An instantaneous value of the band-averaged spectral radiance I_i may then be calculated as the ratio of ΣP_i to the product of the sensor area, solid angle for absorbed radiation, and wavelength range of the bin. We find

$$I_i = \frac{\Sigma P_i}{2\pi(1-\cos\omega)A_s\,\Delta\lambda_i} \tag{6.25}$$

where

$$\Delta\lambda_i = \frac{\Delta\eta_i}{\eta_i^2 - \frac{1}{4}(\Delta\eta_i)^2}\,.$$

A similar procedure is used to calculate I_i values for a sensor located within the grid domain. In this case, any energy bundle which passes through a predetermined region surrounding the sensor is considered during each position reassignment for absorption on the sensor surface. If a bundle is within this region, then the distance D_p to the sensor surface along the direction of propagation $\mathbf{u}$ is computed. If this distance is smaller than the distance to the next cell face or scattering event, then the bundle is moved by the distance D_p along its trajectory. The resulting bundle position is then compared to the position of the sensor center to determine whether the bundle will be absorbed on the sensor surface.

For a circular sensor of radius R_s centered at the point $\mathbf{x}_s$, the distance D_p from the initial bundle location $\mathbf{x}_b$ to the plane of the sensor can be calculated as the ratio of the vector projection $(\mathbf{x}_b–\mathbf{x}_s)\cdot\mathbf{n}_s$ to the cosine of the angle between the unit vectors $\mathbf{n}_s$ and $\mathbf{u}$:

$$D_p = \frac{(\mathbf{x}_s - \mathbf{x}_b)\cdot\mathbf{n}_s}{\mathbf{u}\cdot\mathbf{n}_s} \tag{6.26}$$

If D_p is smaller than the distance to the nearest face or scattering event, and if

$$\left|\mathbf{x}_b + D_p\mathbf{u} - \mathbf{x}_s\right| \le R_s \tag{6.27}$$

and the condition of Eq. (6.24) is satisfied, then the power P_b assigned to the bundle is added to the summation ΣP_i used in Eq. (6.25) to find the radiance I_i for the corresponding wave number bin. Note that Eqs. (6.26) and (6.27) are not valid for an axisymmetric simulation, where to preserve the required symmetry, the sensor surface must be modeled as a surface of revolution around the central axis. In this case a more complicated system of equations must be used to determine the point of intersection between the bundle trajectory and the curved sensor surface.

Once values of I_i for each bin have been calculated as described above, these values are averaged over a large number of time steps to reduce scatter. Sampling is begun here only after the flowfield has reached steady state conditions, so the averaging procedure should be performed over all time steps since steady state is first achieved for which energy bundles are generated and moved through the grid. As energy bundles are randomly assigned with equal probability to any of the wave number bins used in the simulation, the rate of statistical convergence in the resulting radiance values will be roughly equal for every bin. While a much faster convergence rate is possible if we apply a reverse Monte Carlo method involving the generation of additional energy bundles at the sensor [*Everson and Nelson* (1993)], the procedure proposed here allows for relatively fast convergence without adding much to the complexity of the radiation model implementation.

6.3 Extension to soot particles

In addition to condensed phase particles of Al_2O_3, an SRM exhaust plume at high altitude may contain a significant concentration of soot particles. Soot is produced during the combustion process in a wide range of chemical-propellant rocket propulsion systems, and is thought to appear primarily as a result of local chemical nonequilibrium within reacting flow regions. [*Simmons* (2000)] Due to the complex nature of soot formation, and a general lack of understanding for the relevant physical processes, much uncertainty exists in the characterization of soot as part of the flowfield simulation and radiation analysis of SRM plume flows. However, experimental measurements in a high altitude test chamber have shown a relatively high soot content in off-axis regions of a SRM exhaust plume. [*Girata and McGregor* (1983)] Soot has been incorporated into detailed models for the simulation of low altitude SRM plume flows [*Plastinin et al.* (2001)] but an extensive literature search revealed no efforts at the simulation of high altitude SRM plumes which include consideration of soot radiation.

A simple model is proposed here so that soot may be included in coupled flowfield and radiation calculations for the high altitude plume flows of interest. Soot is included as an additional condensed phase particle species, with a Lagrangian tracking scheme similar to that outlined in Chapters 2 and 3. Due to the small mass and heat capacity of soot particles relative to Al_2O_3 particles, procedures described in Chapter 2 for updating particle velocity and temperature must be modified for application to soot. Instead of calculating the net force and heat transfer rates then updating the particle velocity and temperature once per time step, the time step is divided into smaller equally spaced intervals, and velocity and temperature updates are performed sequentially for each of

these intervals. This use of "substeps" is required to reduce errors associated with the temporal discretization of particle force and energy balance equations, as these errors are particularly prominent for the smaller soot particles. (As given by *Simmons* (2000), the most probable diameter of soot particles is in the range of 0.04 μm, whereas Al_2O_3 particles in the flows of interest are concentrated toward the 1 μm range.) Note the similarity of this substep procedure to that described in Section 4.3 for Al_2O_3 particle phase change calculations.

For inclusion of soot in the radiation model, all procedures are nearly identical to those used for Al_2O_3 particles as described in Section 6.2. The only exception is in the calculation of spectral emissivity; Eq. (6.3) is not valid for use with soot, so an alternate expression must be found for use in determining soot particle emission and absorption properties. As a starting point, Mie theory gives the following expression for the spectral absorptance α_λ at a wavelength λ for particles of radius $R_p<\lambda/2\pi$:

$$\alpha_\lambda = \frac{36\times10^{-4}\pi nk}{\left(n^2-k^2+2\right)^2+4n^2k^2}\cdot\frac{f_v}{\lambda} \tag{6.28}$$

Here k is the particle absorption index, n is the refractive index (n+ki make up the complex index of refraction at the wavelength λ) and f_v is the particle volume fraction, defined as the product of the particle number density n_p and the volume per particle $4/3\pi R_p^3$. Note that Eq. (6.28) differs from the formula provided by *Plastinin et al.* (2002) and *Simmons* (2000) in the inclusion of the factor 10^{-4}. This factor is required so that $\alpha_\lambda\cdot\lambda$ will be a nondimensional quantity. (In both of the references mentioned, α_λ is given in cm^{-1} while λ has units of μm.)

As in Eq. (6.7), the spectral absorptance may also be given as the product of the particle absorption cross section and number density.

$$\alpha_\lambda = \pi R_p^2 \varepsilon_\lambda n_p \tag{6.29}$$

By setting the right-hand sides of Eqs. (6.28) and (6.29) equal, we can express the spectral emissivity ε_λ as a function of the nondimensional ratio R_p/λ:

$$\varepsilon_\lambda = \frac{48 \times 10^{-4} \pi nk}{\left(n^2 - k^2 + 2\right)^2 + 4n^2k^2} \cdot \frac{R_p}{\lambda} \tag{6.30}$$

In Section 6.2, the spectral emissivity of Al_2O_3 is approximated as a function of R_p/λ using a correlation of *Reed and Calia* (1993) included here as Eq. (6.3). By substituting an effective absorption index k_{eff} for the actual absorption index k, we can modify this correlation for use with soot or other particles for which Eq. (6.28) is valid. In this case Eq. (6.3) is rewritten as

$$\varepsilon_\lambda = 4k_{eff} \frac{R_p}{\lambda} \tag{6.31}$$

so that, by comparison with Eq. (6.30), we find:

$$k_{eff} = \frac{12 \times 10^{-4} \pi nk}{\left(n^2 - k^2 + 2\right)^2 + 4n^2k^2} \tag{6.32}$$

In the proposed implementation, k_{eff} is evaluated for the wave number η_i at the center of each bin, at a number of different temperatures for which experimental values of n and k are available. Soot is then included as an additional particle species, and k values in Eqs. (6.5), (6.7) and (6.21) are replaced with k_{eff} values interpolated, where appropriate, to either the source particle temperature or the average temperature among all soot particles in the cell. Note in Eq. (6.32) that k_{eff} is independent of the soot particle radius R_p. From Eq. (6.31), the spectral emissivity therefore scales with R_p, so that – as with

Al_2O_3 particles – soot is modeled here as a volumetric emitter. [*Reed and Calia* (1993)] Also note that no consideration is made for the presence of larger soot agglomerates. While agglomerate particles are expected in the plume flows of interest, they are ignored here due to the inherent complexity of any modeling procedures for particle-gas interaction and radiative energy transfer involving particles of such highly nonspherical shapes. [*Simmons* (2000)]

Chapter VII

Simulation of a Representative Plume Flow

7.1 Background and simulation setup

Several of the simulation procedures and physical models developed in previous chapters have been evaluated through application to small-scale flows and comparison with experimental measurements or theoretical results. These evaluations do not, however, lead to confidence in the overall accuracy of the proposed simulation method for the high altitude SRM plume flows of interest. To characterize the general utility of the numerical scheme described in Chapters 2 through 6, simulation results based on this scheme should ideally be compared to available experimental data for a high altitude SRM exhaust plume. Such an approach is presented in the following sections.

First, a comparison is made between calculated UV radiation characteristics and corresponding experimental measurements for a representative SRM plume flow. Additional simulations are performed for which individual models are disabled or input parameters are varied, in an effort to determine the importance of several physical processes and numerical approximations on flowfield and radiation properties. Results are presented with the general goal of quantifying the influence and interaction of various

phenomena, so that less uncertainty over the importance of these phenomena may exist in future simulation efforts for similar flows.

7.1.1 Application to the BSUV-2 plume flow

For ease of comparison and to limit the required computer resources, experimental measurements are desired for a plume flow which can be modeled through an axisymmetric simulation. The exhaust flow should therefore be expelled through a single nozzle, and the rocket should be oriented at a relatively small inclination to its direction of motion. As found from an extensive literature search, the only experimental measurements for a single-nozzle high altitude SRM plume flow in the open literature are those of *Erdman et al.* (1992) described in Chapter 1. In a flight experiment termed "Bow Shock Ultraviolet 2" (BSUV-2), onboard sensors were used to measure spectral radiance in the near-UV range (wavelengths of 0.2 to 0.4 μm) from upper stage SRM exhaust plumes at altitudes between roughly 100 and 120 km. The plume from the third stage Star-27 SRM at an altitude of 114 km is used as a test case here, and while no experimental data is available for flowfield properties, we can to a limited extent infer overall simulation accuracy from a comparison of radiation characteristics between numerical and experimental results.

Following previous simulations of *Candler et al.* (1992) for the same flow at 114 km, we perform a series of axisymmetric simulations on a rectangular grid which extends from 10 m upstream to 75 m downstream of the nozzle exit plane, and 30 m radially outward from the nozzle centerline. The nozzle exit diameter is 0.78 m, and the rocket

surface geometry is approximated as a blunted cone-cylinder shape of length 3.1 m. The grid geometry is shown in Fig. (7.1).

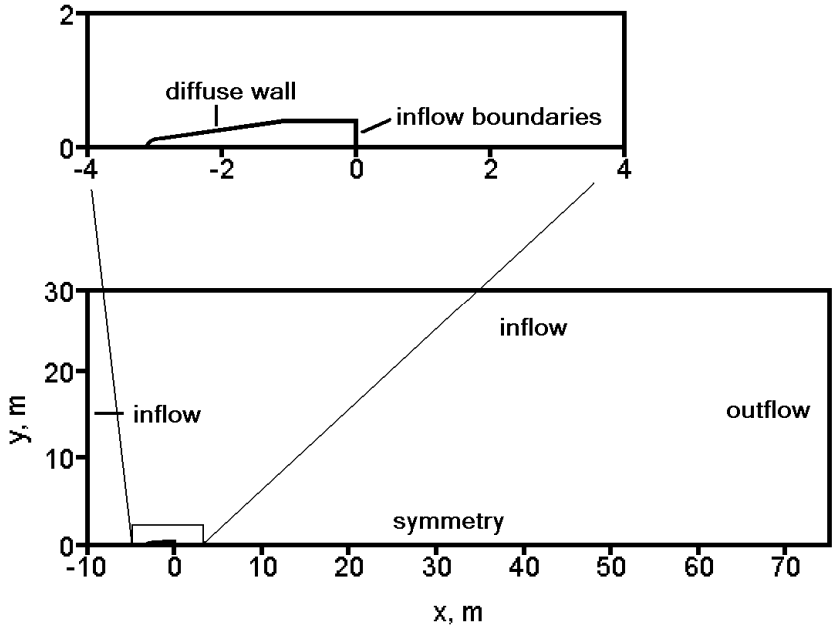

Figure 7.1. Grid geometry for simulations of the BSUV-2 flow.

7.1.2 Gas phase calculations

To account for the high degree of gas thermal nonequilibrium expected through much of the grid domain, the direct simulation Monte Carlo (DSMC) method is used to calculate gas properties in regions of relatively low density flow. The variable hard sphere (VHS) collision model is employed to approximate the variation in transport properties with temperature, and the Larsen-Borgnakke model [*Bird* (1994)] is used together with a total collision energy model for the probability of inelastic collisions [*Boyd* (1990)] to determine energy exchange between translational and rotational modes.

As discussed in Chapter 5, the gas density in plume core regions downstream of the nozzle may be far too high to meet standard DSMC cell size requirements, so an alternate approach for gas phase simulation must be used in these regions. The traditional collision-limiter approach [*Bartel et al.* (1994)] provides a simple solution, but is considerably less efficient and arguably less accurate than alternate methods which involve resampling some fraction of gas particle velocities during each time step from predetermined distribution functions. Both types of approaches can produce large artificial diffusion errors, and tend to enforce a near-equilibrium gas velocity distribution that may not be physically justified when cell dimensions are much greater than a mean free path. [Breuer et al. (1995)] However, these approaches are generally far simpler to implement than alternate methods, such as hybrid CFD/DSMC codes, for simulating flowfields that include both continuum regions and nonequilibrium regions in which a DSMC calculation is desired. This is particularly true for simulations involving a large number of additional physical models, as is the case here, or those for which strong two-way coupling may exist between continuum and nonequilibrium regions.

For simulation of the BSUV-2 flow, gas properties in the high density, near-equilibrium plume core region are calculated using the ES-BGK particle method presented in Chapter 5. The location of the boundary between DSMC and ES-BGK domains is determined using a standard cutoff value (0.05) of the maximum gradient-length local Knudsen number Kn_{GLL} given by Eq. (5.37). [*Boyd, Chen and Candler* (1995)] This parameter is calculated throughout the grid for an initial simulation where the ES-BGK scheme is applied to regions of both high and low gas density, and the ES-BGK method is subsequently used only in regions where the condition

$\max\{Kn_{GLL}\}<0.05$ is satisfied in the initial simulation. Domains for ES-BGK and DSMC methods are shown in Fig. (7.2). Note that nearly the entire plume region downstream of the nozzle exit is contained within the ES-BGK domain. We expect, however, that a larger portion of the plume would be within the DSMC domain if the grid extended further downstream where, as described in Chapter 1, the reduced gas density should make nonequilibrium effects more prominent.

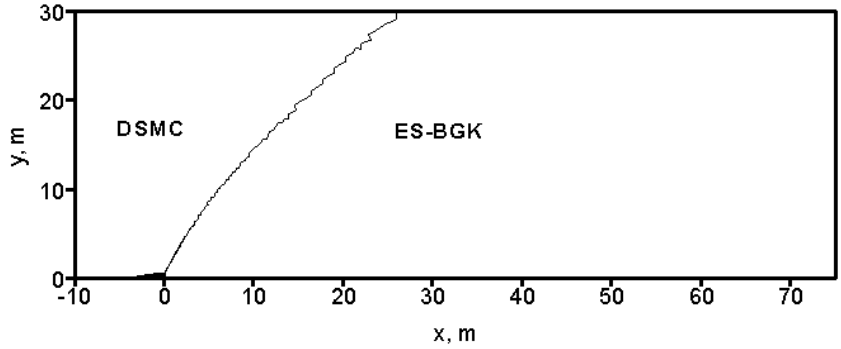

Figure 7.2. Domains for DSMC and ES-BGK simulation methods.

7.1.3 Boundary conditions

Following simulations of *Anfimov et al.* (1993) for the same BSUV-2 flow, the Al_2O_3 particle phase is assumed to account for 30% of the mass flow rate at the nozzle exit, and is made up of seven discrete particle sizes ranging from 0.3 to 6 μm in diameter. Properties for each particle size are independently specified along inflow boundaries at the nozzle exit plane. These inflow properties, as well as those of the gas, are taken from a nozzle flow simulation by the same authors, and are identical to those used in the

subscale plume simulations of Chapter 4. Particle phase inflow properties are provided in Table (4.1).

As in Chapter 4, the exhaust gas species are limited to H_2, N_2 and CO, with initial mole fractions of 0.38, 0.31 and 0.31 respectively. At atmospheric inflow boundaries shown in Fig. (7.1), the gas has mole fractions of 0.78 for N_2 and 0.22 for O_2, with a temperature of 288 K, a density of 5.79×10^{-8} kg/m^3, and a freestream Mach number of 13.5. Following the simulations of Chapter 4, a thermal accommodation coefficient of 0.9 is used for collisions between gas molecules and condensed phase particles, while the outer surfaces of the rocket are modeled as diffusely reflecting walls at 300 K with full thermal accommodation.

7.1.4 Plume radiation properties

In the particle radiation model presented in Chapter 6, values of the absorption index k are calculated as a function of temperature and wavelength. Within the IR range where most radiative energy transfer through the plume is concentrated, absorption index values are taken from experimental measurements of *Konopka, Reed and Calia* (1983). Based on this data, we use 10 wave number bins within the IR range corresponding to wavelengths of 1.0 to 4.5 μm. Of the two SRM exhaust flows from which particles were collected and investigated by these authors, the second (rocket 2) was found to give k values more in line with other experimental data and correlations in the literature. [*Duval, Soufiani and Taine* (2004)] Values calculated from scanning electron microscope (SEM) measurements for the second flow are therefore used here.

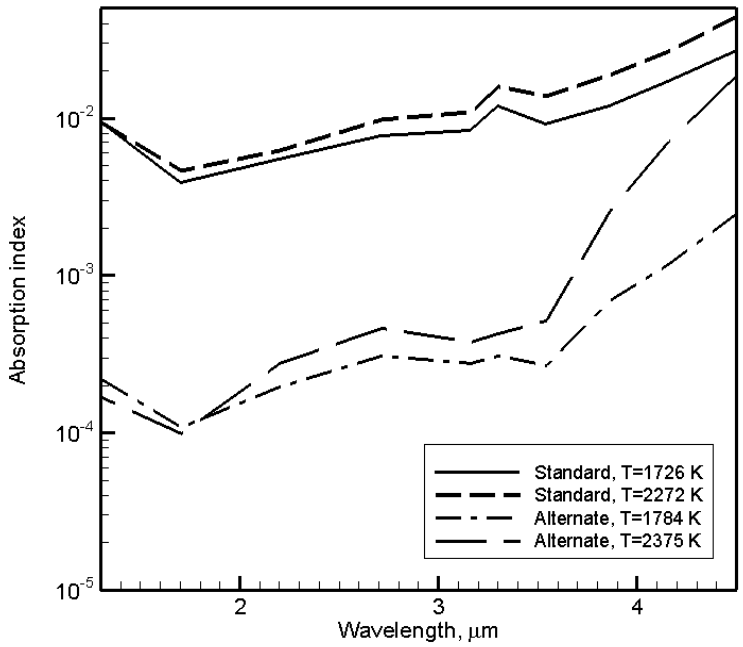

Figure 7.3. Measured IR absorption index values for Al_2O_3.

To demonstrate the degree of variation in k with both wavelength and temperature, measured k values of *Konopka, Reed and Calia* (1983) are plotted in Fig. (7.3) as a function of wavelength for two different particle temperatures. Lines in the figure labeled as "standard" denote data for the second rocket, while lines labeled "alternate" give k values measured for the first. Note that, through much of the wavelength range considered, the two sets of data points differ by roughly an order of magnitude. As discussed by these authors and by *Reed and Calia* (1993), this difference may be attributed primarily to the large influence of lattice defects and impurities on the radiative properties of solid Al_2O_3, which tend to produce a significant and unavoidable uncertainty in results from SRM plume radiation calculations.

For comparison with the experimental plume radiance measurements of *Erdman et al.* (1992), radiation calculations must include UV-range wavelengths between 0.2 and 0.4

μm. While very few data sets exist for Al_2O_3 absorption index values in this range, the correlations employed in plume calculations of *Anfimov et al.* (1993) are stated as valid over the UV wavelengths of interest. These correlations involve a summation over four different intrinsic emission/absorption mechanisms, and as in the data of *Konopka, Reed and Calia* (1983), k values here depend on both wavelength and temperature but are independent of the particle phase composition. Plots of the UV absorption index as a function of wavelength are shown in Fig. (7.4) for three different particle temperatures, based on these correlations. (The two additional lines in the figure – those for constant emissivity and constant absorption index – will be discussed in Section 7.2.)

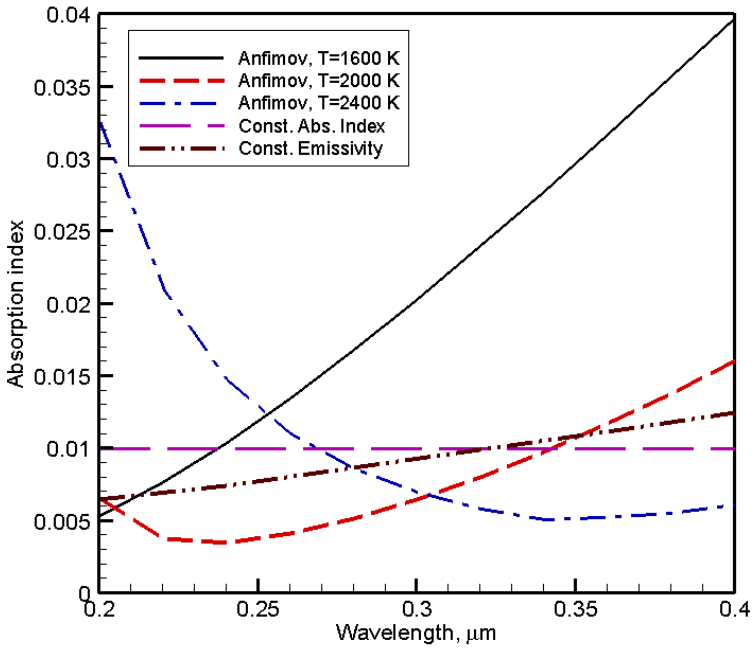

Figure 7.4. UV absorption index values for Al_2O_3.

To incorporate UV radiation calculations into the plume simulation, an additional eight wave number bins are added to cover the wavelength range between 0.2 and 1.0 μm, with most of these bins concentrated toward smaller wavelengths (0.2 to 0.4 μm) for

which experimental plume radiance values are available. Absorption index values over this entire range are taken from the correlations of *Anfimov et al.* (1993).

For all 18 wave number bins over the wavelength range between 0.2 and 4.5 μm, the real part n of the particle index of refraction is computed as a function of the wave number η_i at the center of each bin through a correlation given by *Duval, Soufiani and Taine* (2004)

$$n = \left(0.9904 + 2.02\times10^{-5}T_p\right)\left[1 + \frac{1.024}{1-0.00376\eta_i^2} + \frac{1.058}{1-0.01225\eta_i^2} + \frac{5.281}{1-321.4\eta_i^2}\right]^{1/2} \qquad (7.1)$$

where the weak temperature dependence in Eq. (7.1) is neglected by assuming a particle temperature T_p of 2000 K. Following Reed et al. (1992), the average cosine of the scattering angle in the Henyey Greenstein scattering phase function [*Everson and Nelson* (1993)] is set to g = 0.5, and an effective temperature of T_w = 1300 K is used for searchlight emission at the nozzle exit.

7.1.5 Additional simulation parameters

Spectral radiance calculations are made for two different simulated sensors. The first of these is positioned near the rocket surface, with its center 2 m upstream of the nozzle exit plane and 0.6 m from the central axis. The conical viewing region has a maximum zenithal angle of ω = 2°, and is centered along a line oriented at a 4° inclination to the axis. The sensor position and direction are set here for comparison between calculated radiance values and measurements taken through a periscope-mounted onboard radiometer in the BSUV-2 flight experiment.

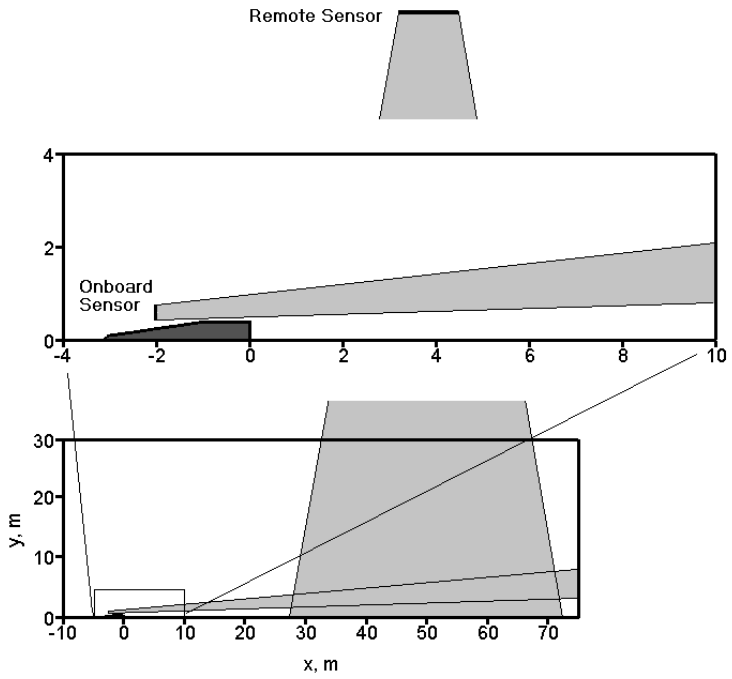

Figure 7.5. Sensor viewing regions for plume radiance calculations.

An additional simulated sensor is positioned outside the grid domain, and is used to characterize plume emission as would be measured from ground or air-based remote sensors. (No such measurements were made for the BSUV-2 flight.) This second sensor is centered at a point 50 m downstream of the nozzle exit and 100 m radially outward from the axis, with a conical viewing region oriented normal to the axis and bounded by the zenithal angle $\omega = 10°$. Locations and viewing regions for both sensors are shown in Fig. (7.5). Note that, while axial symmetry must be preserved in the shape of the sensor surfaces (both sensors are modeled as curved surfaces of revolution around the central axis) the conical shape of the sensor viewing regions implies a lack of symmetry. The non-axisymmetric nature of the sensor geometry is taken into account through Eq. (6.22), by finding the cosine in three-dimensional space between the direction vector **u** for an

incoming energy bundle and an outward normal unit vector $\mathbf{n}_s$ within the grid plane at the sensor surface.

Calculations are run for approximately 60 hours on eight 1.4 GHz AMD Athlon processors. Domain decomposition is used to roughly evenly divide the computational load among all processors, and cell size, time step and numerical weights are carefully varied throughout the grid to balance overall simulation accuracy with computational efficiency. The unstructured grid is divided into about 87,000 triangular cells, through which around 7.5 million DSMC gas particles and 160,000 representative Al_2O_3 particles are tracked at steady state.

7.1.6 Test for grid convergence

To assure grid convergence, a second simulation is run for which all cell dimensions are halved, and a variety of flow property values are compared between the two sets of simulation results. The most sensitive of the properties considered – the gas translational temperature T_t – is found to vary by no more than a few percent between simulations using the original and refined grids. Values of T_t for both simulations are plotted in Fig. (7.6) along a straight extraction line which runs from the midpoint along the nozzle exit radius to a point 75 m downstream and 25 m radially outward. This extraction line runs roughly along the gas streamline which passes half way between the nozzle lip and central axis, and is used in subsequent sections as a convenient measure for the variation of gas and particle properties through the plume. The location of this line is shown in Fig. (7.7).

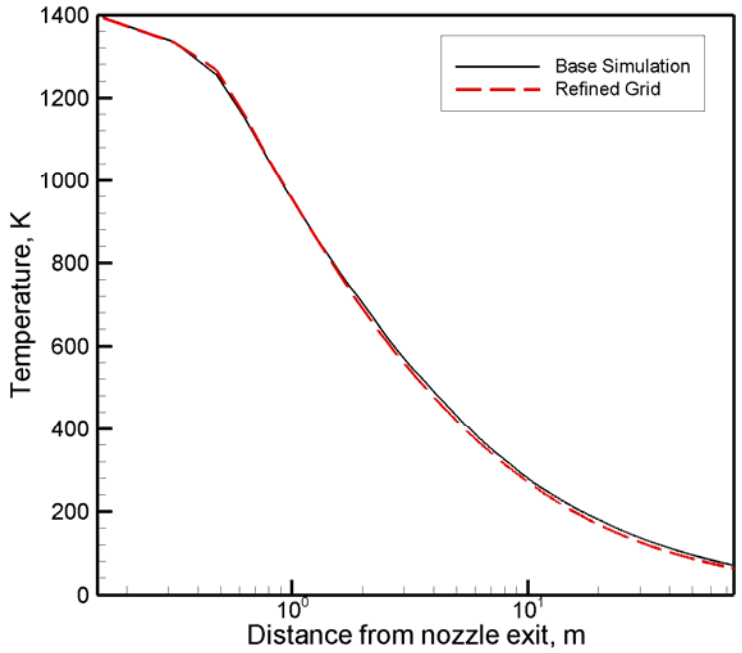

Figure 7.6. Gas translational temperature along the extraction line.

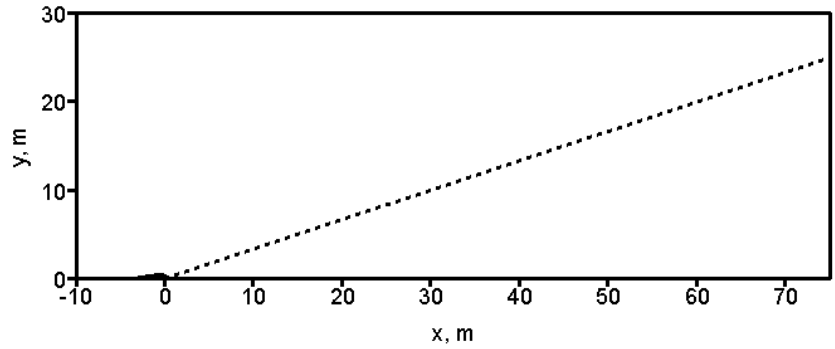

Figure 7.7. Location of the extraction line.

7.2 Simulation results

In this section, selected results from the BSUV-2 flow simulation are presented, and a comparison is made between calculated radiance values and experimental measurements. This comparison can, to a limited extent, be used to evaluate the overall accuracy of the

simulation procedures. However, the inherent uncertainty in inflow conditions and input parameters for the radiation model, as well as a complete lack of experimental data on flowfield properties, lead to some doubt in the adequacy of this evaluation method. As no other experimental results are available for a similar plume flow, the comparison of UV spectral radiance profiles presented here seems to be a reasonable, if not completely sufficient, method by which to assess the overall accuracy of the simulation scheme.

7.2.1 Gas bulk velocity

Some general characteristics of the simulated flowfield are displayed in Fig. (7.8), which gives a close-up view of gas bulk velocity contours and streamlines in a 10 m long region surrounding the rocket. The figure shows a highly diffuse bow shock, with a large boundary layer along the front portion of the rocket surface. Further downstream, a thick mixing layer forms along the region of plume-atmosphere interaction, and a small plume backflow region is found just upstream of the nozzle exit and within a few meters of the rocket. Within the plume, streamlines and velocity contours show the characteristics of a near-free expansion flow – including a complete absence of shocks – as expected for a highly underexpanded plume at very high altitude. [*Simmons* (2000)] Note the well resolved boundary between the plume and atmospheric flow regions.

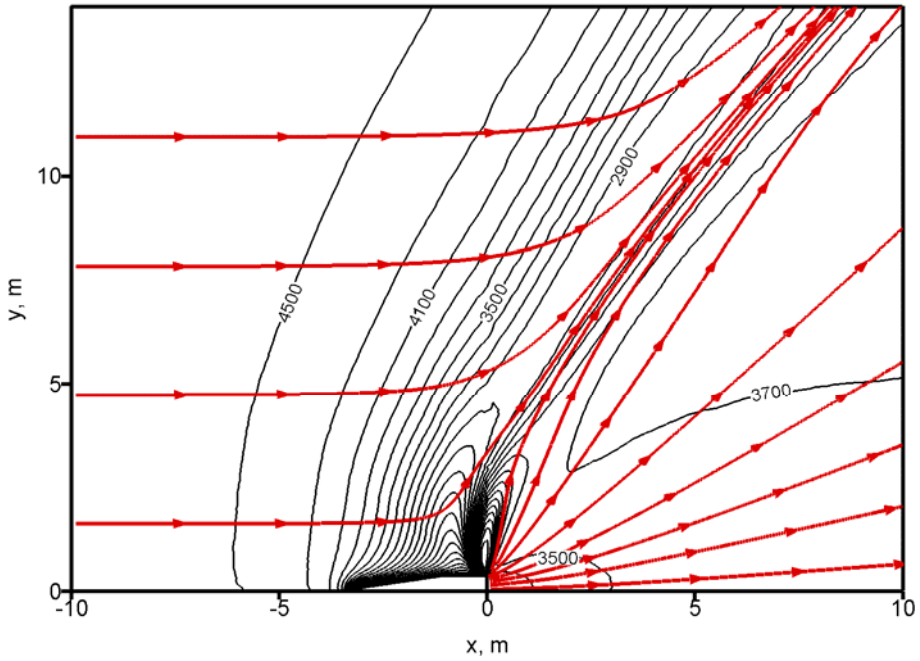

Figure 7.8. Gas streamlines and contours of bulk velocity magnitude. Contour line values are given in m/s.

7.2.2 Gas and particle mass density

Contours of mass density throughout the grid are shown in Fig. (7.9). Particle phase mass density is displayed on the top half of the figure, while the lower half gives contours of gas density. Note first that particles are only found in roughly half of the simulation domain, as the maximum divergence angle for the particle phase is restricted by particle mass. Within much of the region where particles are found, the particle mass density is shown to continuously increase with distance from the axis. This trend can be explained as follows: As described in Section 4.4, all particles are given initial trajectories between 0° and 17.2° off the centerline along inflow boundaries at the nozzle exit, where the angle

for each initial particle trajectory scales linearly with distance from the axis. In the plume nearfield region just beyond the nozzle exit, particles are forced outward from the centerline by the expanding gas. As the drag force on a particle scales with the square of the particle diameter D_p and the particle mass is proportional to D_p^3, the radial acceleration of an individual particle in this region will vary as roughly $1/ D_p$. Thus, in a given radial plane, smaller particles will be found over a range which extends further from the axis. As shown in the top half of Fig. (7.9), this results in a gradual decrease in particle mass density with distance from the axis, due to the presence of a range of particle sizes.

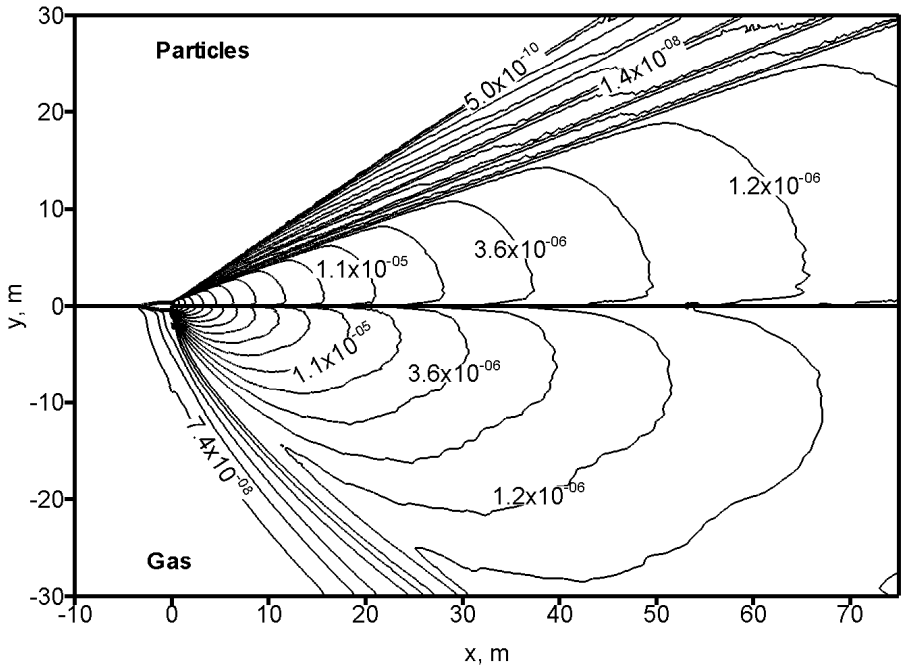

Figure 7.9. Contours of mass density for particle and gas. Values are shown in kg/m^3.

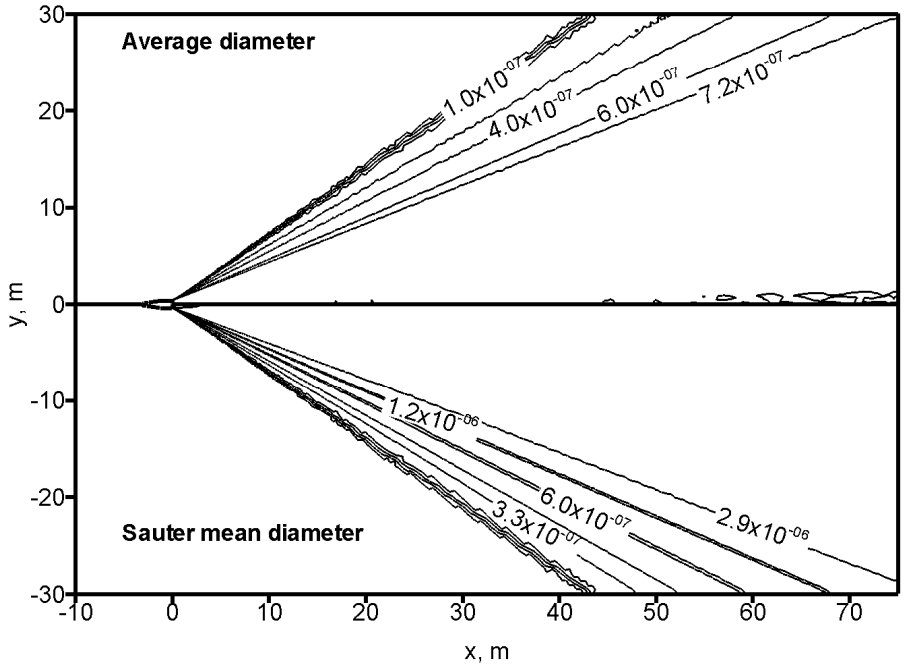

Figure 7.10. Contours of average particle diameter and Sauter mean diameter.

The variation in maximum divergence angle with particle size is further shown in Fig. (7.10), which displays the spatial variation in characteristic particle dimensions throughout the grid. The upper half of the figure shows contours of the average particle diameter, while the lower half gives contours of the Sauter mean diameter. (The latter quantity is defined as the diameter of a particle with a volume-to-surface area ratio equal to the ratio of total volume to total surface area among all particles in a differential control volume.) Although both the upper and lower portions of Fig. (7.10) show a continual decrease in the characteristic particle size with distance from the axis through

much of the grid, the slope of this decrease is not constant due to the use of a discrete particle size distribution.

As the dimensions of the simulation domain are about two orders of magnitude greater than the nozzle exit radius, particle characteristics observed in both Figs. (7.9) and (7.10) primarily reflect trends in the farfield region where interphase momentum transfer can be assumed negligible. The particles move along nearly straight trajectories far from the nozzle, so the contour lines shown projecting from the nozzle exit can be assumed straight if we neglect effects of statistical scatter and interpolation between cell centers.

The continuous reduction in particle mass density with downstream distance found in Fig. (7.9) is due to the divergence of particle trajectories, and the restricted maximum divergence angle is shown in the figure to result in centerline values of the particle phase mass fraction (the ratio of particle mass density to total mass density for both particles and gas) which increase with distance from the nozzle. In comparing the upper and lower halves of Fig. (7.9), we observe a monotonic increase in the particle mass fraction along the central axis, with a final value 75 m downstream of the nozzle exit which is about 2.1 times greater than the initial value of 0.3.

The gas density is shown in the lower half of Fig. (7.9) to decrease continuously with downstream distance through much of the simulation domain, as is expected for any highly underexpanded plume flow. A sharp upward spike in gas density is observed in the plume-atmosphere interaction region, where a diffuse shock forms as a result of both the presence of a solid body and the convergence of streamlines between areas of atmospheric and exhaust flows. The reduction in gas density found near the central axis is a non-physical characteristic of axisymmetric simulations using particle methods; to

populate cells near the axis with a sufficient number of gas particles, the numerical weight of particles in these regions will often need to be reduced. This in turn leads to random walk errors, which tend to decrease the accuracy of simulation results at points near the axis.

7.2.3 Particle temperatures

Contours of average particle temperature are shown in Fig. (7.11) for two different sizes of Al_2O_3 particles. The upper half of the figure gives temperatures for 0.4 μm diameter particles, which are toward the lower end of the particle size distribution, while temperature contours in the lower half of the figure are for much larger particles of 4 μm diameter. Note first the difference in the regions occupied by particles of the two different sizes. As discussed above, smaller particles experience a greater radial acceleration in the plume nearfield region just beyond the nozzle exit, so the maximum divergence angle is greater for the smaller particle size. Also note that the temperature of the smaller 0.4 μm particles is uniformly shown to be about 1200 K lower than that of the 4 μm particles. This follows primarily from the relation between particle heat capacity, which scales as D_p^3, and the convective heat transfer rate, which is proportional to D_p^2. It can be shown from these scaling relations that the rate of change in particle temperature tends to vary as $1/D_p$, so that smaller particles will be more rapidly cooled by the surrounding gas in the plume nearfield region where convective heat transfer is significant.

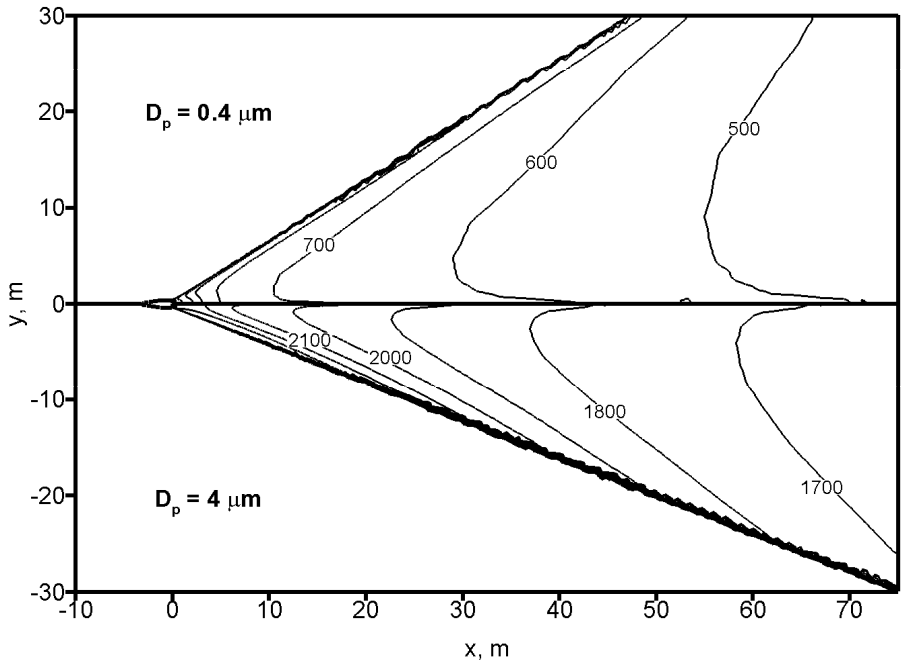

Figure 7.11. Average temperature contours for 0.4 and 4 μm diameter particles. Values are in K.

For both particle sizes in Fig. (7.11), the average temperature is generally found to increase with distance from the central axis. This is due to the fact that, on the scale of the simulation domain, most trends in particle temperature are dominated by the influence of convective heat transfer. As the convective heat transfer rate is proportional to the local gas density, we expect that particles which pass through the lower-density portions of the plume nearfield region further from the axis will experience less heat loss to the cooler surrounding gas. Particles further from the axis will therefore retain higher temperatures far downstream, as is shown in the figure. The increase in particle temperatures at points very close to the axis is also related to the radial variation in gas density within the plume

nearfield region. As explained in the above discussion of Fig. (7.9), random walk errors in cells near the axis produce an artificially low gas density, which in turn reduces convective heat transfer rates for particles which pass through these cells.

Most of the streamwise reduction in temperature shown for both particle sizes in Fig. (7.11) is a result of radiative heat loss. Due to the large scale of the simulation domain in relation to the size of the rocket, the regions where convective heat transfer and phase change make significant contributions to the particle energy balance are restricted to a small area within a few meters of the nozzle exit. A close-up view of average particle temperatures in this area, again for particles of diameter 0.4 and 4 μm, is shown in Fig. (7.12).

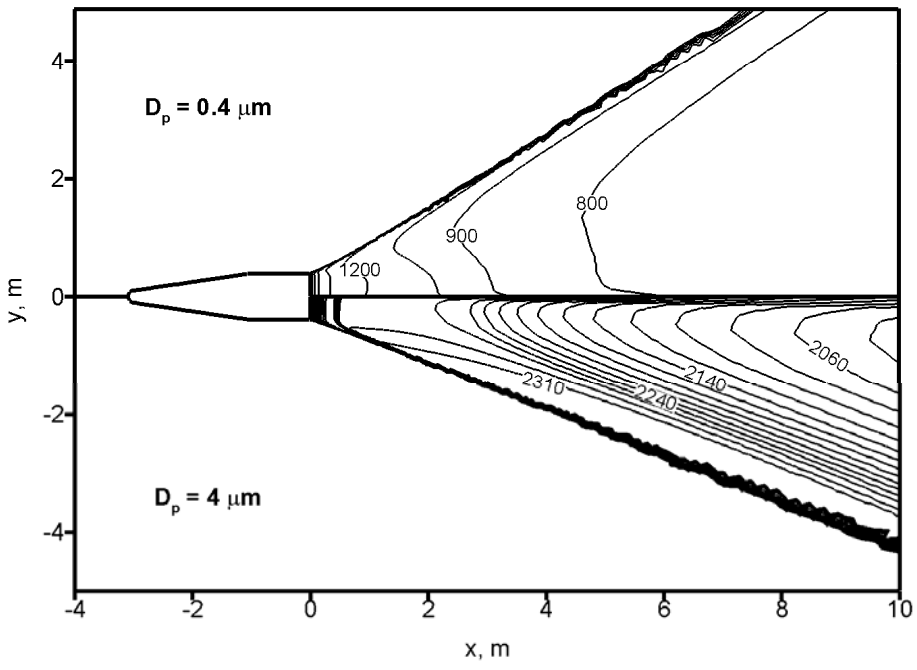

Figure 7.12. Close-up view of particle temperature contours. Values are given in K.

Note the contrast between Figs. (7.11) and (7.12) in the magnitude of observed temperature variation with downstream distance for both particle sizes. Particle temperatures are found to vary far more rapidly in the plume nearfield region displayed in Fig. (7.12) than in regions further downstream, shown in Fig. (7.11), which make up most of the simulation domain. This difference in temperature gradients is due primarily to the rapid reduction in gas density with downstream distance. As shown in Fig. (7.9), the gas density is far higher in the nearfield plume region just downstream of the nozzle than elsewhere in the plume, so convective heat transfer rates will be far higher as well near the nozzle exit.

7.2.4 Particle phase change

A close observation of 4 μm particle temperature contours in Fig. (7.12) reveals a rapid temperature jump about 0.4 m downstream of the nozzle exit. This jump is associated with the initiation of the phase change process, and results from the release of the latent heat of fusion for liquid Al_2O_3. As described in Chapter 4, 4 μm particles are assumed to be in a completely liquid state at inflow boundaries along the nozzle exit, and are rapidly cooled by the surrounding gas until they reach the nucleation temperature (T_f = 1930 K) for homogeneous crystallization. Once this temperature is reached, a radially symmetric crystallization front progresses from the surface of a particle toward its center. The heat release associated with the phase change process causes a sudden increase in particle temperature, and this temperature increase in turn slows the progress of the crystallization front. For some time a quasi-equilibrium state may be reached, where the heat release during crystallization is balanced by convective and radiative heat loss, and

the particle maintains a nearly uniform temperature. Further downstream, as the liquid mass fraction approaches zero and the rate of heat release is reduced, the particle temperature again begins to decrease as observed in Fig. (7.12).

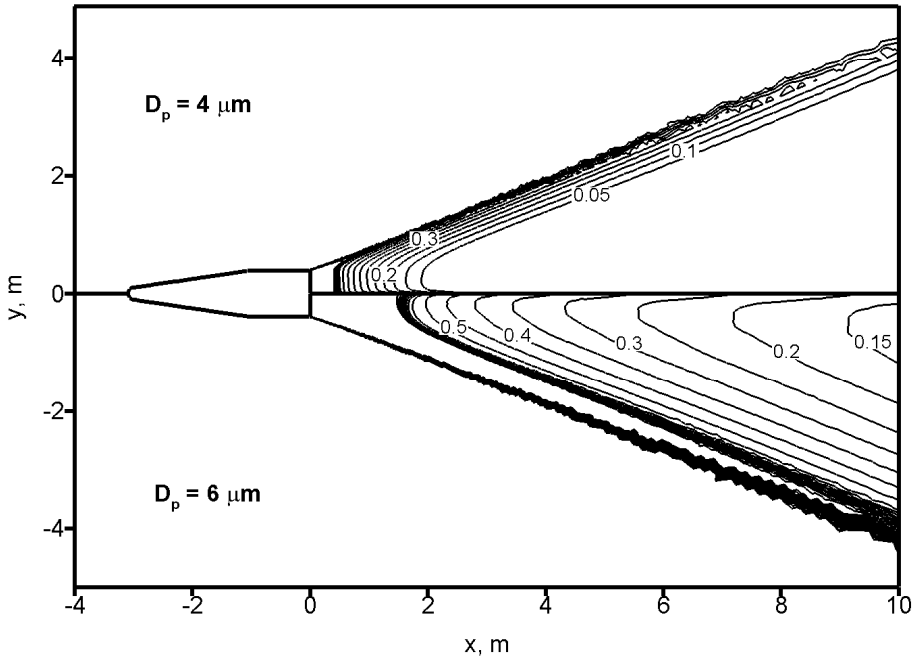

Figure 7.13. Contours of liquid mass fraction for 4 and 6 μm diameter particles.

To demonstrate the correlation between phase change and the variation in particle temperatures, a contour plot of the liquid mass fraction is included here as Fig. (7.13). The top half of the figure shows cell-averaged liquid mass fractions for 4 μm particles, while the lower half gives contours for even larger particles of 6 μm diameter. (As given in Table (4.1), most particles of smaller sizes are assumed to be in a completely solid state at the nozzle exit, so crystallization processes occur within the plume only for the larger particles.) A comparison of characteristics for 4 μm particles between Figs. (7.13)

and (7.12) shows that, as described above, the particle temperature jump about 0.4 m downstream of the nozzle exit is accompanied by the initiation of phase change and a rapid reduction in the liquid mass fraction. Particle temperatures level off further downstream, as the gradient in the liquid mass fraction decreases, and the particles ultimately approach a completely solid state.

In comparing liquid mass fraction contours for the two different particle sizes shown in Fig. (7.13), we find that phase change begins significantly further downstream for the larger 6 μm particles. As explained above, the rate of temperature decrease due to convective heat transfer tends to vary as roughly the inverse of the particle diameter, so that larger particles will experience a longer residence time in a completely liquid state before reaching the nucleation temperature T_f at which crystallization may begin.

For both 4 and 6 μm particles, the onset of crystallization is shown in Fig. (7.13) to occur progressively downstream for particles which move along trajectories further from the axis. As with the radial variation in particle temperatures, this trend is a result of the decrease in gas density with distance from the axis. Particles which pass through regions of lower gas density will cool more slowly through convective heat transfer, so these particles tend to reach the nucleation temperature T_f at points further downstream.

7.2.5 Convective and radiative heat transfer rates

Figure (7.14) shows the variation with downstream distance in the magnitude of mean convective and radiative heat transfer rates, as calculated per particle and averaged over all particle sizes. Values are extracted along a line which runs very close to the central axis, but is sufficiently far from the axis to be relatively unaffected by random walk

errors associated with the variation in numerical weights. Both heat transfer rates in the figure are negative through the entire simulation domain, as particles throughout the plume are losing energy to their surroundings through both convective and radiative heat transfer.

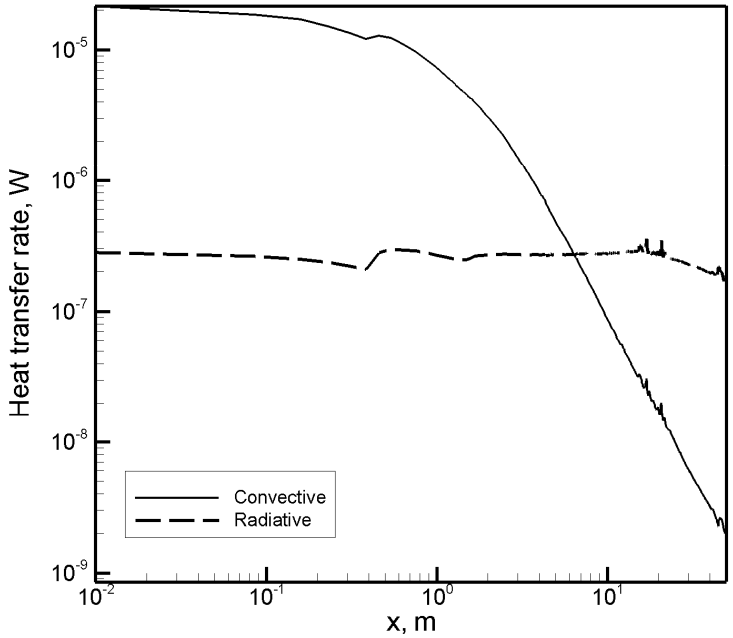

Figure 7.14. Magnitude of average convective and radiative heat transfer rates per particle along the centerline.

The radiative heat transfer rate is shown to be relatively constant with downstream distance, due to an overall gradual variation in particle temperatures and the fact that radiative absorption is found to have a comparatively small effect. Much of the variation in radiative transfer observed on the plot is a consequence of statistical scatter, as results from the small number of representative particles which pass through cells bordering the axis. However, a significant increase in the radiative transfer rate is found about 0.4 m downstream of the nozzle exit. This may be attributed to the temperature jump associated

with the onset of phase change in 4 μm particles, which account for roughly 60% of the total Al_2O_3 mass within the plume.

The slow reduction in radiative heat transfer observed to begin about 10 m downstream of the nozzle is also the result of a variation in particle temperature. As particle temperatures decrease due to radiative heat loss in the farfield plume region, the magnitude of the radiative energy transfer rate will decrease as well due to the strong temperature dependence of particle emissive power.

In contrast to the relatively uniform rate of radiative heat transfer, the mean convective heat transfer rate is shown in Fig. (7.14) to decrease rapidly with downstream distance. The spatial variation in convective heat transfer occurs mainly as a result of the downstream decrease in gas density. As the gas approaches a free molecular state far from the nozzle, the gas density will decrease along the centerline as the inverse square of the distance from the nozzle exit. The farfield convective heat transfer rate will therefore have the same inverse square variation, as is shown in the figure.

A convenient definition of the plume nearfield region in a freely expanding SRM plume flow is the range beyond the nozzle exit where the particle energy balance is dominated by convective heat transfer to the gas. By this definition, the nearfield region extends along the centerline about 6 m (or 8 nozzle exit diameters) downstream of the nozzle exit, beyond which radiative emission becomes the dominant mechanism for energy transfer between a particle and its surroundings.

7.2.6 Radiative energy flux

In Fig. (7.15), contours are shown for the direction-averaged spectral radiative energy flux E_λ at wavelengths of 2.2 μm and 0.24 μm. This flux is defined as the rate per unit wavelength at which photons within a narrow wavelength range impinge on a spherical surface, divided by the cross sectional area of the sphere. Following the procedures described in Chapter 6, E_λ may be calculated as the ratio of the energy flux q_i to the wavelength range $\Delta\lambda_i$ for a given wave number bin i.

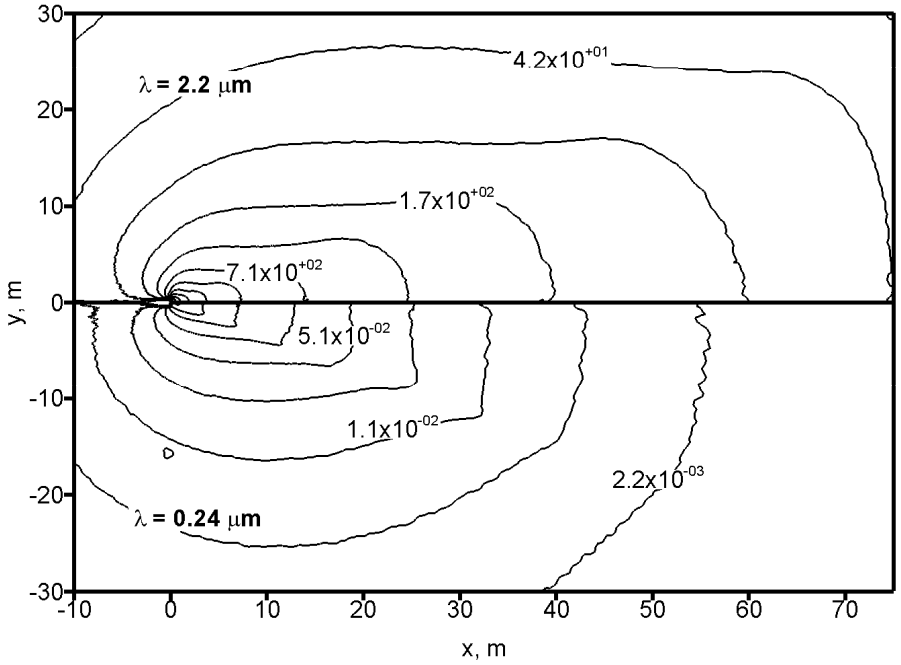

Figure 7.15. Contours of the direction-averaged spectral energy flux at wavelengths of 2.2 μm and 0.24 μm. Values are in W/m^{2}μm.

Note that the wavelength λ corresponding to each calculated value of E_λ is equidistant from the wavelengths which bound the wave number bin, so λ will not exactly equal the

inverse of the wave number η_i at the center of this bin. In general, λ may be related to η_i by

$$\lambda = \frac{\eta_i}{\eta_i^2 - \frac{1}{4}(\Delta\eta_i)^2} \tag{7.2}$$

where $\Delta\eta_i$ is the wave number range for the given bin.

While E_λ values have little physical significance outside of the radiation model presented in Chapter 6, contours of E_λ provide a convenient means of quantifying the variation in spectrally resolved radiation intensity throughout the simulated flowfield. The upper half of Fig. (7.15) can therefore be viewed as a measure of IR radiation intensity through the grid, while the lower half shows the intensity at a representative wavelength in the UV range. In comparing E_λ contours for the two different wavelengths, we find that the IR radiation intensity is consistently about four orders of magnitude greater than the UV intensity, as follows from the fact that thermal radiative emission at the particle temperatures shown in Figs. (7.11) and (7.12) is typically concentrated in the IR range. [*Reed and Calia* (1993)]

A significant difference is also found in the shape of contour lines between the two wavelengths shown in Fig. (7.15). This difference may be attributed to the variation with wavelength in the temperature dependence for thermal emission. At smaller wavelengths the spectral emissive power for a blackbody tends to depend far more strongly on the temperature of the body. [*Siegel and Howell* (1981)] This characteristic is preserved in Eqs. (6.4) and (6.5), which give the emissive power output of a source particle used in the radiation model. As shown in Fig. (7.11), particles further from the axis tend to have higher temperatures, so experience a greater rate of radiative heat loss. This temperature

difference has a stronger correlation to emissive power in the UV range than in the IR range, so a more pronounced ridge is shown in the UV energy flux contours near the location of higher temperature particles.

As shown in Fig. (7.15), the energy flux for both wavelengths is greatest at the nozzle exit, due primarily to the corresponding maximum in particle mass density and a reduction in the intensity of searchlight emission with distance from the nozzle. Particles are modeled through Eq. (6.3) as volumetric emitters [*Reed and Calia* (1993)], so the magnitude of radiative energy flux should scale roughly with the local particle mass density. As this density decreases with downstream distance due to the divergence of particle trajectories through the plume, a continuous reduction in radiative energy flux is found in the axial direction.

A reduction in energy flux is also observed in the radial direction, particularly outside the region where particles are found. This follows from the fact that, in an axisymmetric simulation, the ratio of cell volume to the projected area on the grid will scale with distance from the axis. The average number of energy bundles which pass through a cell is proportional to the projected area of that cell, and the contribution of each bundle to the energy flux is proportional to the inverse of the cell volume. We therefore expect the net energy flux through cells outside the particle domain to scale approximately with the inverse of the distance from the axis, as is shown in both the upper and lower halves of Fig. (7.15).

7.2.7 Plume spectral radiance

In Fig. (7.16) values are presented for the plume spectral radiance I_i as observed at the onboard and remote simulated sensors shown in Fig. (7.5). Values in the figure are averaged over results from eight different simulations. In each of these simulations the random number generator is initialized at a different point, but all are otherwise identical. The error bars for the onboard sensor values give 95% confidence intervals based on a wavelength-averaged standard deviation $\sigma_{avg,i}$ from the eight simulations, and show that the stochastic nature of the radiation model produces significant scatter in these values. Error bars for radiance values from the remote sensor are too small to include in the figure. (The variation in scatter between the two sets of values is mainly the result of differences in sensor surface area, viewing angle and angular resolution as shown in Fig. (7.5).)

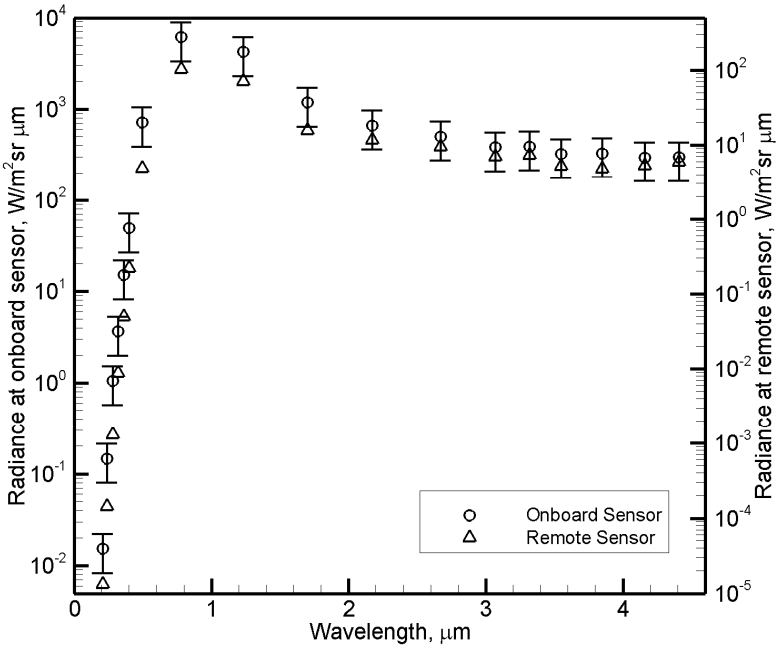

Figure 7.16. Spectral radiance at onboard and remote sensors.

To determine the height of the error bars shown in Fig. (7.16), we assume a Gaussian distribution of radiance values among the eight simulations for each wave number bin i, and we further assume that the ratio of the standard deviation σ_i to the mean radiance I_i from the eight simulations is independent of wavelength. It follows from these assumptions that error bars for a 95% confidence interval should be spaced a distance of about $1.96\sigma_{avg,i}$ from the corresponding mean value I_i [*Hogg and Tanis* (1997)], where $\sigma_{avg,i} = I_i\langle\sigma_j/I_j\rangle$ and the averaging operation $\langle\rangle$ is taken over all wave number bins.

Both data sets plotted in Fig. (7.16) display a relatively small wavelength dependence through much of the IR range, and a sharp drop-off in the visible and UV regions. These trends, as well as the general shape of the radiance profiles, are consistent with Planck's solution for the spectral distribution of blackbody emissive power. It can further be shown through Wien's displacement law that the wavelength of maximum radiance for both sensors, around 0.8 μm, corresponds to a blackbody temperature of roughly 3600 K. [*Siegel and Howell* (1981)] While no particles in the simulation actually reach that temperature, we expect that, if a greater spectral resolution is used in radiation calculations and if the wavelength dependence in particle emissivity is disabled, the corresponding blackbody temperature would be significantly lower.

As described in Section 7.1.5, the location and orientation of the simulated onboard sensor corresponds to that of a periscope-mounted radiometer used to measure UV spectral radiance during the BSUV-2 flight experiment. These measured values are presented in Fig. (7.17) along with corresponding simulation results in the wavelength range between 0.2 and 0.4 μm. Published numerical results of *Candler et al.* (1992) and *Anfimov et al*. (1993) are also included for comparison. Both of these previous

simulations employ continuum CFD methods which for this flow may be less appropriate than the kinetic approach used here, particularly in the highly rarefied regions within the DSMC domain shown in Fig. (7.2). Still, somewhat better agreement is found with experiment for these results than for those from the present simulations, particularly at wavelengths below around 0.25 μm. Note however that in the simulations of *Candler et al.*, particle phase enthalpies at the nozzle exit were selected for best agreement between calculated and experimental radiance values at the 0.23 μm wavelength. This procedure effectively rescales the UV radiance profile to match experimental results, and makes any quantitative comparison with experiment of questionable value.

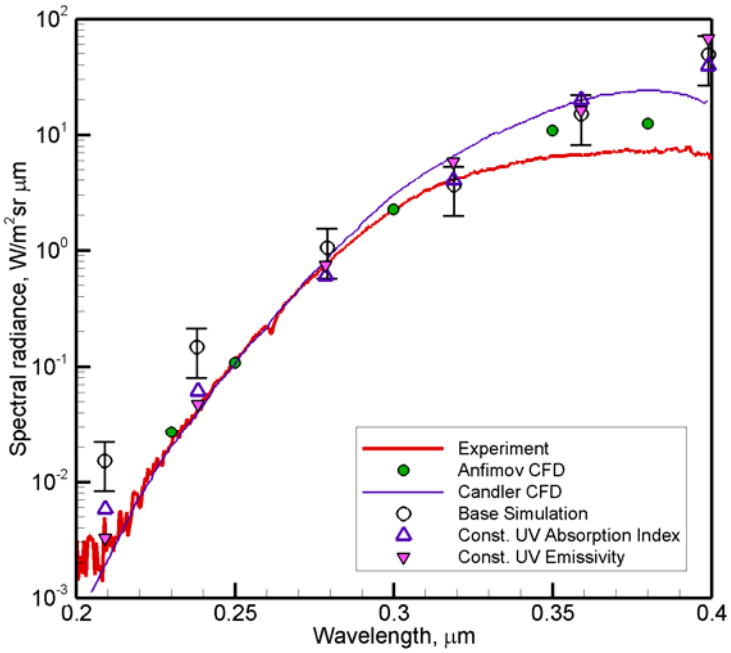

Figure 7.17. UV spectral radiance measured at the onboard sensor.

In comparing the level of agreement between the different sets of results, also note that radiance values determined by *Anfimov et al.* (1993) are subject to uncertainty associated with correlations for the particle absorption index introduced by these same

authors. The correlations exhibit a strong temperature and wavelength dependence that has not been verified elsewhere in the literature, and they do not account for extrinsic properties (such as impurity concentrations and lattice defects) that have been found to dominate radiation characteristics of solid phase particles. [*Reed and Calia* (1993)] As the same correlations are employed for the simulations presented here, the resulting uncertainty in radiance values for both the new simulations and those of *Anfimov et al.* leads to some doubt regarding the validity of using these values to assess overall simulation accuracy.

To determine the effect of the UV absorption index correlations on radiance values, two additional simulations are performed. In the first simulation, the absorption index is given a constant value of 0.01 through the UV range. As shown in Fig. (7.4), this value roughly characterizes an average of values taken from the correlations of *Anfimov et al.* (1993) over a range of temperatures and wavelengths. In the second simulation the UV absorption index is set so that, for a given particle size, the spectral emissivity ε_λ in the UV range is constant. It follows from Eq. (6.3) that, for a constant emissivity, the absorption index k in this range must be proportional to the wavelength λ. For a given particle radius R_p, we can relate k to λ by

$$k = \frac{\varepsilon_\lambda \cdot \lambda}{4R_p}. \tag{7.3}$$

Particles are modeled through Eq. (6.3) as volumetric emitters, so that in an isothermal enclosure containing particles with a range of sizes, the emissive heat flux per unit volume will scale with the mean-cubed particle radius. As this flux should also scale with the average over all particle sizes of the quantity $\varepsilon_\lambda R_p^2$, an effective emissivity

which is independent of the particle radius must be proportional to the ratio of the mean-cubed radius to the mean-squared radius. This ratio is equal to one-half the Sauter mean diameter, which may be substituted for R_p in Eq. (7.3) for use with an effective emissivity which is independent of particle size.

Thus, to allow for values of the UV absorption index which give a uniform effective emissivity, we assume a characteristic Sauter mean diameter of 3.2 μm (as is found through much of the plume region occupied by particles) and use an emissivity of 0.2. From Eq. (7.3), this corresponds to the relation $k = 0.031\lambda$. As shown in Fig. (7.4) the resulting k values for this "constant emissivity" case are generally of the same order as those found through the correlations of *Anfimov et al.* (1993), and are very much in line with values used in the simulation involving a constant absorption index.

Radiance values from both additional simulations are shown in Fig. (7.17), and exhibit significantly better agreement with experiment than do base simulation results. (The term "base simulation" refers here to simulations performed using the input parameters described in Section 7.1, including the absorption index correlations of *Anfimov et al.*) In particular, the constant emissivity simulation gives excellent agreement with the experimental data at smaller wavelengths where the correlations of *Anfimov et al.* produce the greatest disagreement. While the choice of constant emissivity or absorption index values is to some extent arbitrary, the resulting consistency with experiment gives us some confidence in the overall accuracy of the simulations.

In drawing conclusions from the results shown in Fig. (7.17), it should be emphasized that this comparison is in no way sufficient to validate the physical models and numerical procedures introduced here. Although the relatively good agreement observed between

calculated results and experimental data is an encouraging indication of simulation accuracy, there is too little data to assess the accuracy of individual models, or to judge with reasonable certainty whether bulk flowfield properties are accurately determined.

As mentioned in Section 7.1.1, the BSUV-2 plume flow is chosen as test case only because no other suitable experimental data sets can be found in the open literature. Had more extensive measurements been available, a rigorous validation or more comprehensive evaluation of the proposed simulation techniques may have been possible. In particular, any experiments suitable for code validation would have to include detailed measurements of both flowfield and radiation properties. These experiments would ideally involve multiple rocket firings under a range of conditions (different particle mass loadings, motor sizes, altitudes, etc.) so that simulation accuracy could be assessed for a number of different plume flows. The use of multiple test cases would add confidence in any conclusions drawn from the comparison between simulation and experimental data, and would indicate a range of flow conditions for which the simulation methods may be accurately applied. See Section 8.2 for additional discussion of the need for future experiments.

7.3 Parametric study for gas/particle interaction

The simulations presented here involve a large number of modeling procedures, covering a range of physical phenomena, for which the sensitivity of input parameters to simulation results may not be known. The importance of coupling between the various models is also generally uncertain, and assumptions underlying several of these models may not always be valid under relevant flowfield conditions. As the choice of input

parameters and modeling approximations is of great importance in assessing the overall accuracy of the simulation approach, we desire to evaluate the relative contributions and interactions among a number of the modeling procedures discussed in previous chapters. For this evaluation, results from the base simulation described above are compared with those from a series of simulations for which individual models are turned off or input parameters are varied. The first category of physical models and numerical approximations to be assessed are those involved in momentum and energy exchange between the particles and gas.

7.3.1 Additional simulations for comparison

First, the influence of momentum and energy coupling from particles to the surrounding gas is considered by deactivating the two-way coupling model, then performing a simulation for which gas properties are not affected by the presence of the particle phase. The effects of particle rotation are considered next, through the activation of models presented in Chapter 2 for the exchange of angular momentum, linear momentum and energy between a rotating sphere and a locally free molecular nonequilibrium gas.

Following *Vasenin et al.* (1995), we assume that coalescing collisions between liquid droplets within the nozzle are the dominant contributors to particle rotation. The maximum allowable particle angular velocity magnitude is then determined by a criterion for the centrifugal breakup of liquid droplets. A normalized angular velocity

$$\Omega = \frac{4}{5}\,\omega_p \sqrt{\frac{\pi}{3}\frac{m_p}{\sigma_{liq}}} \tag{7.4}$$

is set to equal some critical value Ω_{crit} for all particles at the nozzle exit, where m_p is the particle mass, σ_{liq} is the liquid surface tension, and ω_p is the magnitude of the particle angular velocity $\boldsymbol{\omega}_p$. While ω_p values will be equal for all particles of a given diameter at the nozzle exit, the initial direction of $\boldsymbol{\omega}_p$ for each particle is randomly selected on a plane normal to the central axis. *Salita* (1991) uses momentum and energy conservation arguments to show that the collision-induced rotation rate of spherical liquid agglomerates should be limited by Ω_{crit}=3.31. Following these arguments, we perform a simulation for which initial particle angular velocities correspond to Ω=3.31 in order to evaluate potential upper bounds for the influence of particle rotation on various flow characteristics.

Another property considered here is the influence of particle shape. While Al_2O_3 particles extracted from SRM exhaust flows have been found to be roughly spherical, some authors have discussed an expected deviation of particle shapes from a perfect sphere due to surface forces on a solidifying droplet, or due to gas release during crystallization. [*Reed and Calia* (1993), *Gosse et al.* (2003)] To quantitatively evaluate effects of particle shape, a simulation is performed for which particles are assumed to have the same surface area-to-volume ratio as a cube. Following the analysis in Chapter 2 of momentum and energy transfer rates between a rotating nonspherical particle and a locally free-molecular gas, the effective particle radius and material density are modified in order to approximate the influence of a cube-shaped surface. While this represents a deviation from spherical shape well out of the expected range, a comparison with base simulation results can be used to establish upper bounds for the influence of particle shape on plume radiation and flowfield properties.

A final characteristic of gas-particle interaction considered here is the effect of the thermal accommodation coefficient (TAC) at the particle surface. For all simulations described above, the TAC value is set for all particles to 0.9, so that 90% of interphase collisions involve diffuse reflection with full accommodation to the particle temperature, and the remaining 10% involve specular reflection. While this TAC value is within the general range observed experimentally [*Epstein* (1924)], the phenomenological nature of the collision model and a potentially strong dependence on surface and gas properties lead to some uncertainty over what value would be most appropriate. To assess the influence of the TAC value on flowfield properties, an additional simulation is performed for which the TAC is set to 0.45, so that interphase collisions are half as likely to involve diffuse reflection as in the base simulation.

Results from these simulations are compared by evaluating flowfield properties along the extraction line shown in Fig. (7.6). As discussed in Section 7.1.6, the extraction line roughly follows a gas streamline originating midway between the nozzle lip and the intersection of the central axis with the nozzle exit plane. This line is chosen to give a general sense of the downstream variation in gas and particle properties through the plume, while avoiding regions near the central axis which are particularly prone to effects of random walk error and statistical scatter.

7.3.2 Gas translational temperature

In Fig. (7.18), the gas translational temperature for each of the simulations described above is plotted as a function of distance from the nozzle exit along the extraction line. The temperature variation with downstream distance for the base simulation shows

generally expected trends for a plume flow expanding into a near-vacuum: The largest temperature gradients occur in the nearfield region just downstream of the nozzle exit, following a rapid conversion of thermal energy into bulk kinetic energy within this region. The rate of change decreases with downstream distance as collisional processes become progressively less significant, and the translational temperature asymptotically approaches a farfield value near 0 K. Note that effects of rotational freezing allow for a potentially much higher asymptotic rotational temperature.

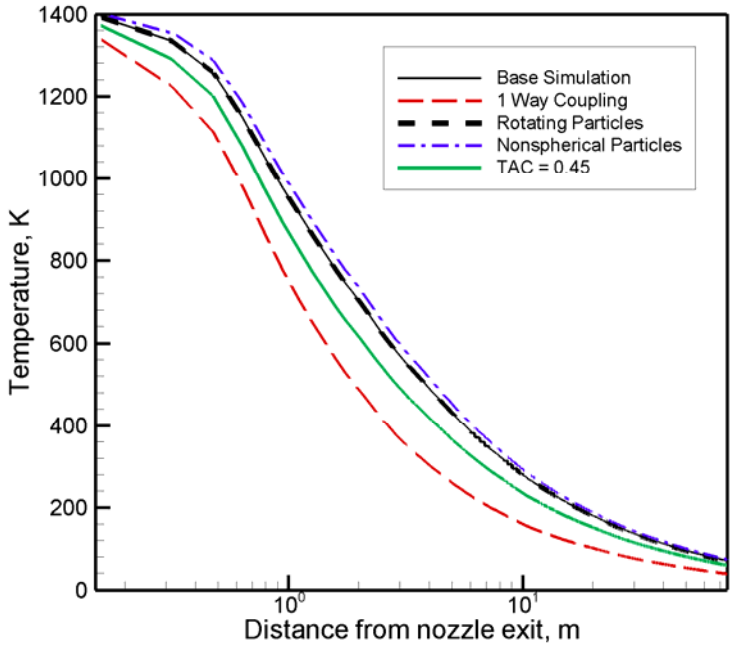

Figure 7.18. Gas translational temperature along the extraction line.

In comparing results with those from the base simulation, the one-way coupling case is found to give significantly lower gas translational temperatures, particularly within the nearfield plume region close to the nozzle exit. When the heat transfer from Al_2O_3 particles to the cooler surrounding gas is neglected, gas temperatures may be reduced by well over 100 K. In contrast, the effect of particle rotation is found here to be negligible,

as the gas temperature is shown to be nearly identical between the base simulation and the simulation for which particles leave the nozzle with maximum possible angular velocities.

Particle shape is shown in Fig. (7.18) to have a potentially noticeable, although small, influence on gas temperatures through much of the plume. When particles of fixed mass are given greater surface area, the interphase collision frequency will increase, and higher gas temperatures will result from a corresponding rise in convective heat transfer rates between the particles and gas. The simulation for which the particle TAC is set to 0.45 also gives translational temperature values noticeably different from those of the base simulation. When the probability that an interphase collision involves diffuse reflection is halved, the heat transfer rate between the particles and gas will be reduced by roughly 50%, and particles will be considerably less effective in heating the surrounding gas. As a result, the gas translational temperature is found to decrease by up to approximately 50 K when the TAC is varied from 0.9 to 0.45.

7.3.3 Temperature of small particles

Average temperatures along the extraction line for 0.4 μm diameter particles are shown in Fig. (7.19). As described in Section 7.2, the downstream reduction in particle temperatures occurs primarily as a result of convective heat transfer in the nearfield plume region close to the nozzle, while radiative heat transfer dominates further downstream. In comparing results between the base simulation and the one-way coupling simulation, for which effects on the gas of interphase momentum and energy exchange are neglected, we find trends similar to those described above for the gas temperature. As

the gas temperature is uniformly lower when one-way coupling is assumed and particles are unable to heat the surrounding gas, the local temperature difference between particles and gas will increase. A larger temperature difference corresponds to a greater convective heat transfer rate, so that particles will cool more rapidly and maintain lower temperatures, as is shown in the figure.

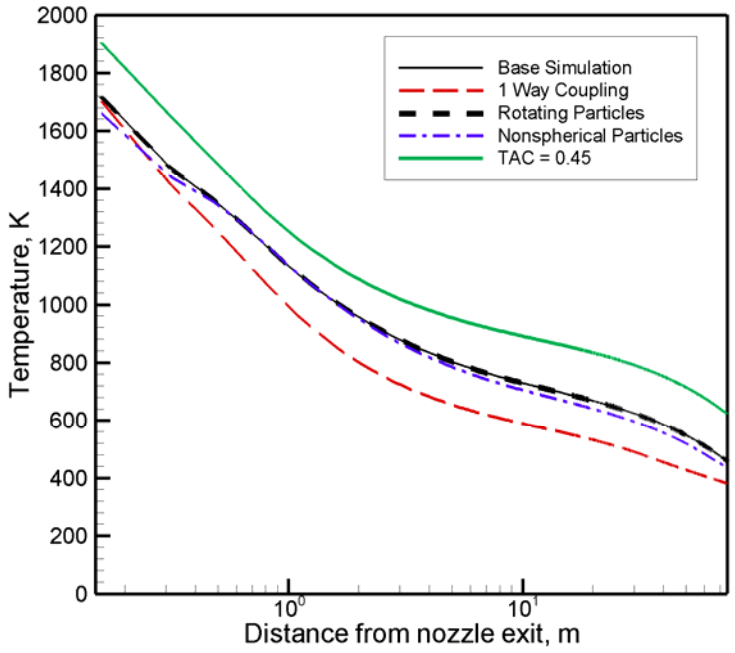

Figure 7.19. Temperature variation along the extraction line for 0.4 μm particles.

As with gas temperatures, the temperature of 0.4 μm particles is found to be almost completely unaffected by particle rotation. Particle temperatures are however shown to decrease slightly when given a nonspherical shape. Nonspherical particles will have a larger average collision cross section than spherical particles of equal mass, so will cool more rapidly as a result of convective heat transfer. Note that, as stated in Chapter 6, particles are modeled as volumetric emitters, so particle shape will have no effect on radiative heat transfer rates other than that associated with the difference in temperatures

shown in Fig (7.19). From the temperature plot for the simulation where TAC = 0.45, we find that the TAC value significantly influences 0.4 μm particle temperatures throughout the plume. As convective heat transfer rates are roughly 50% lower in this simulation, the temperature of 0.4 μm particles is found to be uniformly about 100 K higher than in the base simulation.

7.3.4 Temperature of large particles

Figure (7.20) shows the variation along the extraction line in average temperature for 4 μm diameter particles. The non-monotonicity of all results in the figure is a consequence of the nonequilibrium crystallization process described in Section 7.2.4, and the general trends observed here can be explained as follows: Particles of this size are assumed to exit the nozzle as liquid droplets. Through convective and radiative cooling, the temperature of a droplet is ultimately reduced to a temperature (1930 K) at which homogeneous crystallization may occur over its surface. Heterogeneous crystallization then begins, as a crystallization front progresses toward the particle center and the particle temperature rapidly increases due to heat release during the phase change process. This temperature increase results in a drop in the crystallization rate, and for some time the particle maintains a nearly constant temperature while the heat released through crystallization is balanced by convective and radiative energy transfer. Finally, as the liquid mass fraction approaches zero, the particle temperature again begins to decrease due primarily to radiative heat loss.

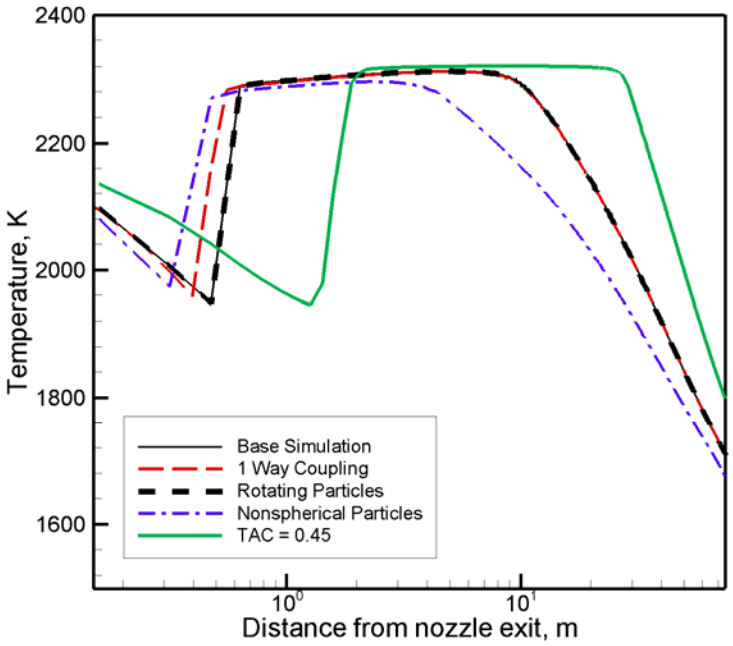

Figure 7.20. Temperature variation along the extraction line for 4 μm particles.

A comparison between the base simulation results in Fig. (7.20) and those from the other simulations shows some surprising characteristics. When the TAC is reduced, convective heat transfer rates decrease and the location at which phase change begins is moved further downstream. While this results in higher particle temperatures in the farfield plume region, the delay in phase change initiation leads to significantly lower particle temperatures in a small region upstream of the temperature spike. This region, where a lower TAC corresponds to reduced particle temperatures, is shown in the figure at locations between 0.5 and 1.1 m from the nozzle exit. Likewise, the increase in convective heat transfer rates associated with both nonspherical particles and an assumption of one-way coupling tends to force the phase change initiation point upstream. Note however that the one-way coupling simulation gives farfield particle

temperatures nearly identical to those from the base simulation, while particle shape effects are found to be potentially significant throughout the plume.

As in Figs. (7.18) and (7.19), particle rotation is shown to have no noticeable effect here. This is in fact true of all flowfield characteristics considered, so we can conclude that, for this flow, particle rotation has a negligible influence on all simulation results of interest. This conclusion is however subject to assumptions regarding the mechanisms by which particles develop angular momentum. If collisions involving partially or fully solidified particles are considered, the appropriate value of the maximum normalized angular velocity Ω_{crit} may be far higher. Higher Ω_{crit} values may also result from consideration of the interaction between solid particles and either nozzle walls or large-scale turbulent structures within the nozzle.

7.3.5 Radiative energy flux

Figure (7.21) shows the variation in net direction-averaged radiative energy flux along the extraction line. This flux is defined as the integral of the spectral radiative energy flux, shown in the contour plots of Fig. (7.15), over the entire wavelength range (0.2 to 4.5 μm) considered in the radiation model. As described in the discussion of Fig. (7.15), the radiative energy flux is found to decrease continuously with downstream distance through the plume, primarily as a result of the divergence of particle trajectories. The greatest variation from base simulation results is observed for the simulation with TAC = 0.45, for which the energy flux through much of the farfield plume region is significantly higher. Much of this increase can be attributed to the difference in temperatures for 4 μm particles between the two simulations. These particles are shown

in Fig. (7.20) to experience the greatest temperature difference about 25 m downstream of the nozzle exit. This location corresponds nearly exactly to the point in Fig. (7.21) where the maximum difference in energy flux is observed. As 4 μm particles make up roughly 60% of the total Al_2O_3 mass in the plume, and as the net emissive heat transfer rate increases with particle temperature, this correlation between trends shown in Figs. (7.20) and (7.21) is both logical and expected.

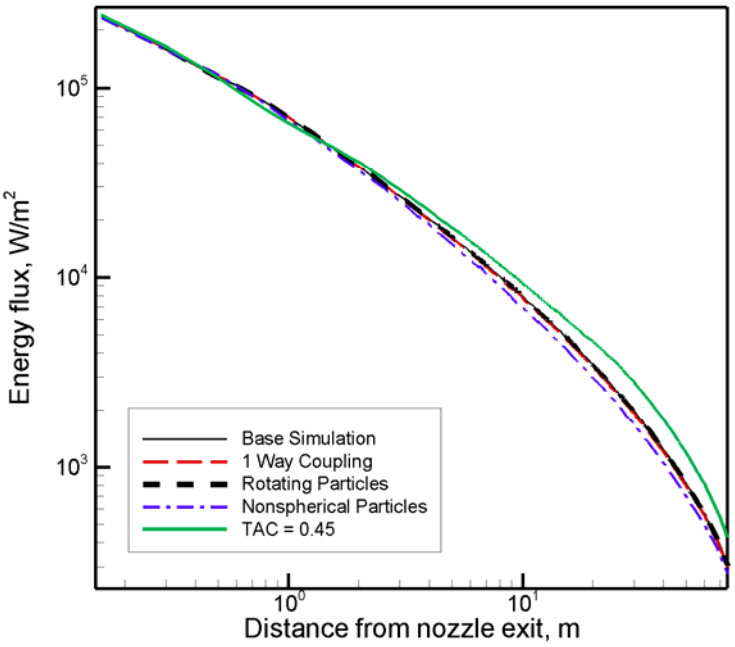

Figure 7.21. Net direction-averaged radiative energy flux along the extraction line.

A similar correlation between the two figures is observed in comparing results for the base simulation and the simulation involving nonspherical particles. Spherical particles of 4 μm diameter are found in Fig. (7.20) to maintain significantly higher temperatures through much of the plume than nonspherical particles of equal mass. This temperature difference corresponds to a noticeable reduction in the radiative energy flux when nonspherical particles are used. In contrast, simulations involving one-way interphase

coupling and rotating particles are both shown in Fig. (7.21) to give energy flux values which are, within the scale of the figure, identical to those taken from base simulation results.

Note in Fig. (7.20) that the variation in TAC has a significant effect on 4 μm particle temperatures in the nearfield plume region within a few meters of the nozzle exit, although no similar effect is found on energy flux values in this region. Nearfield differences in the temperature of 4 μm particles when two-way coupling is disabled, or when nonspherical particles are employed, are also not reflected in Fig. (7.21). The lack of a correlation here between particle temperatures and energy flux is likely due to some combination of factors: First, smaller particles cool more quickly than larger 4 μm particles, so the relative effect of smaller particles on radiative energy flux will be greater at locations further upstream. Second, the net radiative energy flux at any point in the flowfield is a function of particle temperatures throughout the plume, so that contributions to the energy flux associated with large temperature variations in the nearfield plume region will to some extent be "smoothed out" over the length of this region. Finally, nozzle searchlight emission is expected to have a significant influence on the energy flux near the nozzle exit, so that Al_2O_3 particle emission will have a comparatively smaller effect on flux values here than at locations further downstream.

7.3.6 UV spectral radiance

In Fig. (7.22) UV spectral radiance values at the onboard sensor are shown for the base simulation and for all other simulations described in Section 7.3.1, and the measured UV radiance profile from the BSUV-2 flight experiment is included here for reference.

Ideally a comparison of radiance values from these simulations would give us some insight as to which numerical approximations and assumptions contribute most significantly to the discrepancy between simulation and experimental results. However, no clear trends are observed among the calculated radiance values, and through most of the UV range shown here, the variation between results from the different simulations is within the level of statistical uncertainty given by the error bars. We can at least conclude from this comparison that none of the modeling assumptions evaluated in this section are alone responsible for the discrepancy between experimental and calculated UV radiance profiles.

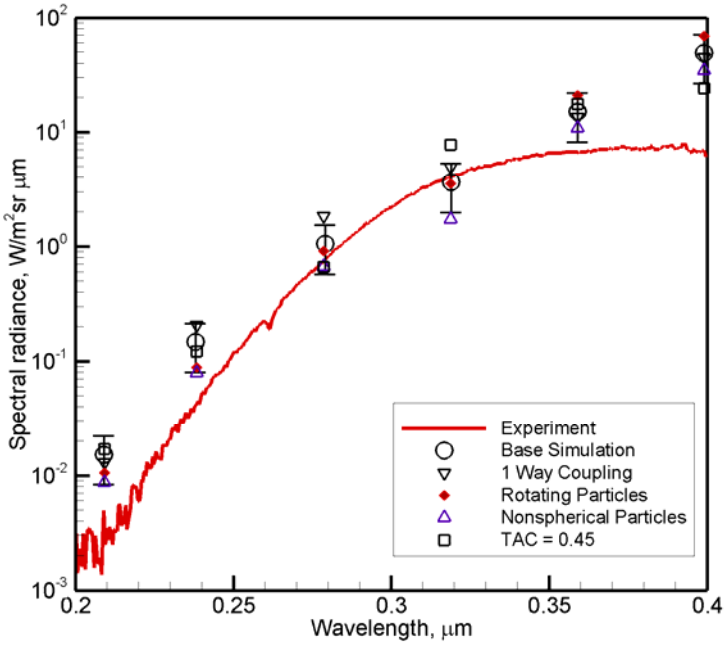

Figure 7.22. UV spectral radiance at the onboard sensor.

7.4 Parametric study for particle radiation

In addition to numerical approximations and assumptions used for gas/particle interaction, the overall accuracy of simulation results is subject to a number of

approximations in procedures for particle radiation modeling. To assess the influence of the radiation model on output properties of interest, further simulations are performed for which elements of flowfield-radiation coupling are disabled or input parameters for the radiation model are modified.

7.4.1 Additional simulations

First, the influence of radiative absorption is neglected by modifying the code so that MCRT energy bundles have no influence on the temperature of particles assigned to cells through which the energy bundles pass. (As described in Chapter 6, each energy bundle represents a large collection of photons over some finite wavelength range.) This in effect decouples radiative absorption calculations from the flowfield simulation. Next, another simulation is run using the traditional post-processing approach to plume radiation analysis, where all radiative terms are neglected in the particle energy balance. Here both absorption and emission are effectively decoupled from the calculation of flowfield properties.

Results from additional simulations are used for comparison to determine the influence of particle absorption index values on flowfield and radiation characteristics. In one simulation, the alternate set of IR absorption index values from measurements of *Konopka et al.* (1983) are used. As shown in Fig. (7.3), these values are generally about one order of magnitude lower than those used in the base simulation, although the ratio of corresponding values between the two data sets of *Konopka et al.* is a strong function of both wavelength and particle temperature. The inclusion of both data sets should allow us to evaluate the sensitivity of simulation results to the large inherent uncertainty in Al_2O_3

IR absorption index values. Results are also considered from the two simulations discussed in Section 7.2.7 for which either UV absorption index or spectral emissivity values are assumed independent of both temperature and wavelength.

Two additional simulations are included here for comparison. In the first of these, the anisotropic scattering model employed in all other cases is disabled, and isotropic scattering is instead assumed. (See Section 6.2.2 for a detailed description of the scattering model.) In the second simulation, the effect of searchlight emission (i.e. continuum radiation from the interior of the nozzle) is neglected, so that all energy bundles used in the radiation calculations originate at source particles within the interior of the grid.

7.4.2 Effect of particle radiation on the gas

In comparing results between all simulations for which parameters of the radiation model are varied, we find no significant differences in gas flow properties. This is not surprising, as the gas is assumed here to be optically transparent and may therefore be influenced by plume radiation only indirectly through momentum and energy exchange between the particles and gas. Radiative heat transfer is shown in Section 7.2 to significantly affect particle properties only in the farfield plume region where interphase momentum and energy exchange become negligible, so that plume radiation is expected to have little if any influence on gas flow characteristics throughout the simulation domain.

7.4.3 Particle temperatures

In Fig. (7.23), temperatures for 0.4 μm diameter particles along the extraction line are compared among all simulations described in Section 7.4.1. The corresponding temperature variation for 4 μm particles is shown in Fig. (7.24). Note that every modification to the radiation model considered in Section 7.4.1 has virtually no effect on particle temperatures in the plume nearfield region within a few meters of the nozzle exit. Here radiative heat transfer has a negligible contribution to the particle energy balance, and particle residence time in this region is too small for the emissive heat loss to have any significant cumulative effect. Any changes to radiation input parameters or modeling approximations should therefore have no impact on particle temperatures in this region, as is observed in Figs. (7.23) and (7.24).

In comparing temperatures of both 0.4 μm and 4 μm particles between the base simulation and those for which elements of flowfield-radiation coupling are disabled, we find that radiative absorption has no significant effect on particle temperatures even in the farfield plume region toward the downstream edge of the simulation domain. In contrast, particle temperatures in this region may increase considerably when the contribution of emissive heat transfer is neglected.

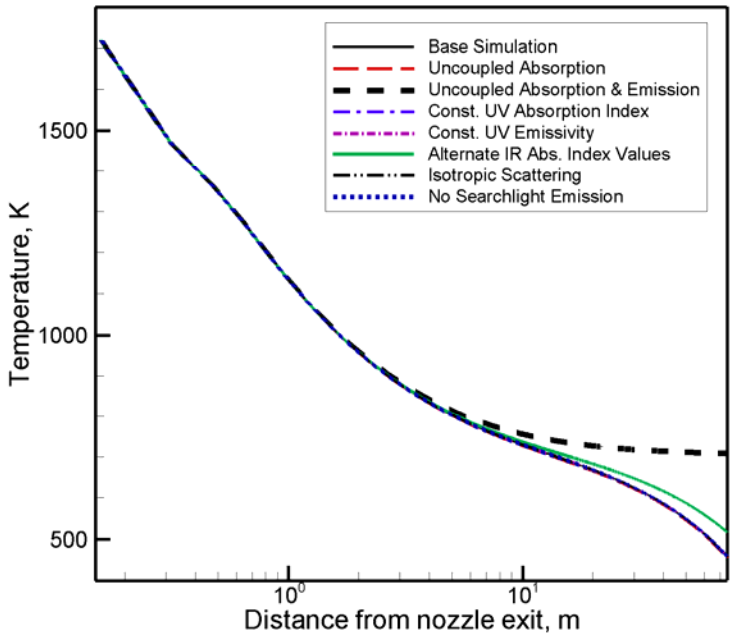

Figure 7.23. Temperature of 0.4 μm particles along the extraction line.

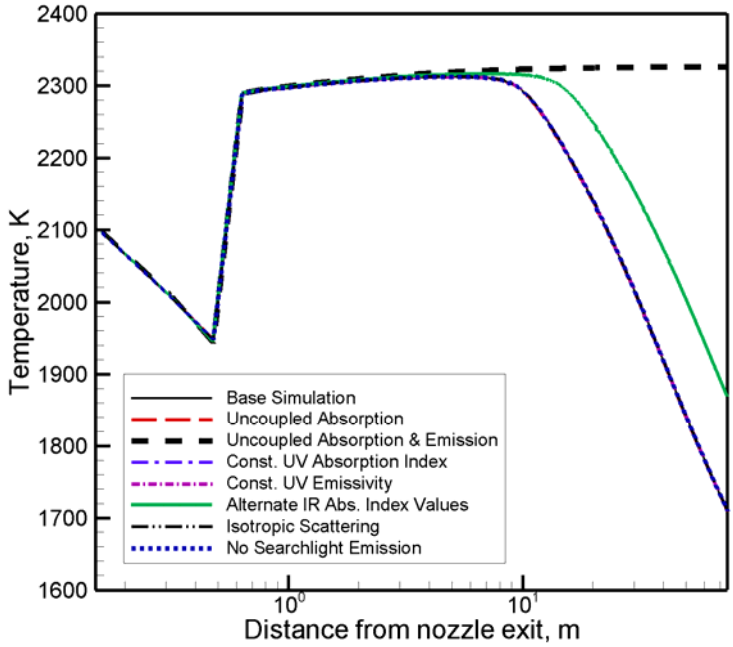

Figure 7.24. Temperature of 4 μm particles along the extraction line.

When full radiation-flowfield coupling is included and IR absorption index values are reduced by roughly an order of magnitude to the "alternate" values of *Konopka et al.* (1983), the farfield temperature for both small and large particles is shown in Figs. (7.23) and (7.24) to increase significantly. Based on findings of *Konopka et al.* that the difference between standard and alternate values plotted in Fig. (7.3) represents the typical uncertainty in the IR absorption index range for Al_2O_3 particles in a SRM plume flow, we can assume that the difference between temperature curves for the base simulation and the simulation with alternate IR absorption index values corresponds to an unavoidable error margin in the results.

In contrast, the use of alternate absorption index values in the UV range produces no significant change in particle temperatures, due to the relatively small contribution of UV emission to the total radiative heat transfer rate. Results from the simulations where anisotropic scattering or searchlight emission are neglected also appear nearly identical to those from the base simulation. Both searchlight emission and the angular dependence of scattering probabilities are therefore found to have no significant influence on the temperature of 0.4 μm or 4 μm diameter particles throughout the plume.

7.4.4 Radiative energy flux

Values of the net direction-averaged radiative energy flux are shown in Fig. (7.25) for all simulations involving modifications to the radiation model. Note first that no difference is observed between results from the base simulation and those from the simulation where the influence of radiative absorption on flowfield properties is neglected. However, a lack of radiation-flowfield coupling for both absorption and

emission is found to significantly increase energy flux values far downstream of the nozzle, as results from the corresponding increase in particle temperatures shown in Figs. (7.23) and (7.24).

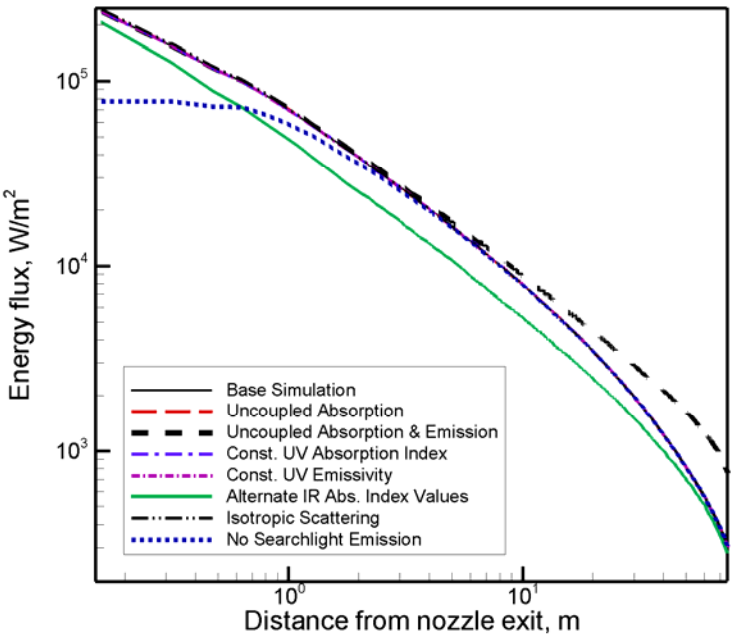

Figure 7.25. Variation along the extraction line in the net direction-averaged radiative energy flux.

The choice of values for the IR particle absorption index is found to significantly influence energy flux values through the entire plume. When the lower "alternate" values are used, the net energy flux is considerably reduced in both nearfield and farfield plume regions. This is due to the fact that thermal radiative emission in the relevant temperature range for Al_2O_3 particles occurs primarily at IR wavelengths. As spectral emissivity is assumed in the radiation model to scale linearly with the absorption index, any large change to IR absorption index values will result in a comparable change to values of the net radiative energy flux.

We find no significant difference in the net energy flux when UV absorption index values are varied, as a relatively small fraction of emissive heat loss occurs in the UV range. A similar lack of influence on the energy flux is found in the scattering model; results shown in Fig. (7.25) for the simulation with isotropic scattering are virtually identical to those for the base simulation.

Nozzle searchlight emission is observed in the figure to account for over 50% of the net radiative energy flux around the nozzle exit, while providing a negligible contribution to flux values at distances greater than a few meters from the nozzle. Much of the downstream reduction in the radiative energy flux within the plume nearfield region can be attributed to the corresponding decrease in the intensity of radiation emitted inside the nozzle. When nozzle searchlight emission is disabled, a far more gradual downstream reduction in energy flux is found in this region.

7.4.5 UV spectral radiance

Figure (7.26) shows values of UV spectral radiance at the onboard sensor for all simulations described in Section 7.4, and data points from the BSUV-2 flight experiment are plotted for comparison. As mentioned in the discussion of Fig. (7.17), when either the UV absorption index or emissivity is assumed to be independent of wavelength, significantly better agreement is found with experimental radiance values in the 0.2 to 0.25 μm range where a particularly large discrepancy is observed between experimental values and those from the base simulation. The simulation for which both emission and absorption are uncoupled from flowfield calculations shows consistently higher radiance

values than most other simulations, as results from the corresponding increase in particle temperatures.

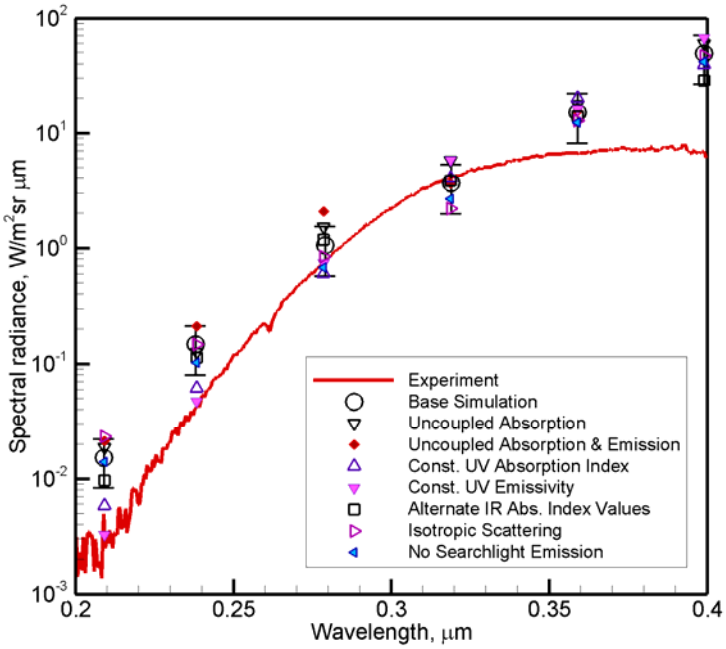

Figure 7.26. Dependence of UV spectral radiance on radiation model parameters.

The level of statistical scatter in Fig. (7.26) is great enough that few definite conclusions can be drawn from any trends observed in the figure. We do find, however, that of all the modifications to the radiation model considered here, only adjustments to the UV absorption index produce a statistically significant effect on calculated UV radiance values. It follows from this comparison that most other modifications to the radiation model cannot be assumed to measurably improve overall simulation accuracy, to the extent that simulation accuracy is established by the level of agreement between experiment and simulation results. Note that no broad conclusions can be drawn here for the general application of the radiation model to high altitude SRM plume flows. If, for example, a much larger scale plume of greater optical thickness had been considered, we

expect that modifications to the scattering model would have a far more significant effect on the calculated radiance. The influence of both the scattering model and searchlight emission would also likely be much greater if the sensor field of view were aligned more closely to the nozzle exit plane. [*Reed et al.* (1992)]

7.5 Potential influence of soot on plume radiation

As discussed in Section 6.3, soot production takes place in a wide range of chemical propulsion systems involving a hydrocarbon propellant, and is thought to occur primarily as a result of local chemical nonequilibrium during the combustion process. While few papers in the open literature include measurements of soot concentrations in an SRM exhaust flow, soot has been found experimentally as an exhaust product during SRM firings in a low density test chamber [*Girata and McGregor* (1983)]. In both experimental and numerical radiation studies for liquid-propellant rocket plumes, soot is often cited as a major contributor to plume emission characteristics. [*Wright et al.* (1998), *Simmons* (2000), *Garrison et al.* (2005)]

As much uncertainty exists in the potential contribution of soot to radiation properties for the high altitude SRM plume flows of interest, additional simulations are run for the BSUV-2 flow in which soot is included as an additional particle species. In particular, we hope to determine the effect of soot on calculated UV radiance values at the onboard sensor, so that the influence of soot particles on the discrepancy between experimental and numerical results may be quantitatively evaluated.

7.5.1 Soot concentration and input parameters

Based on previous simulations [*Wright et al.* (1998)] and experimental measurements of soot concentrations in exhaust flows from liquid-propellant rocket engines [*Simmons* (2000)], we assume a 2% mass loading of soot at the nozzle exit. Although no corresponding data can be found for an SRM exhaust flow, the 2% value represents a reasonable – although very rough – estimate of the expected soot concentration in the simulated flowfield. We assume for simplicity that the soot concentration is uniform over the nozzle exit plane, and soot particles are given initial temperatures and velocities which are identical to those used for the gas. While noticeable soot velocity and temperature lags may exist inside the nozzle, the very small mass and heat capacity of soot particles allow these particles to rapidly equilibrate to local gas properties within the plume nearfield region. The approximation of full equilibration at the nozzle exit should therefore have little or no impact on most flowfield properties of interest.

Following the expected soot particle size distribution given by *Simmons* (2000), all soot particles are given a diameter of 0.04 μm. Input parameters for the radiation model include wavelength and temperature-dependent values of both the refractive and absorption indices, based on an analysis of experimental data also compiled by *Simmons* (2000).

Two additional simulations are performed to assess the potential influence of soot in the BSUV-2 flow. The first simulation includes soot among the exhaust products as described above, and is in all other ways identical to the base simulation. In the second simulation, Al_2O_3 particles are entirely removed, so that the contribution of soot to plume radiation characteristics may be independently evaluated. Note however that the second

simulation neglects any effects of soot absorption and scattering on radiation emitted by Al_2O_3 particles, so the removal of Al_2O_3 particles allows for only an approximate assessment of the influence of soot.

7.5.2 Soot density and temperature

Figure (7.27) shows contours of soot mass density and temperature throughout the grid domain, for the simulation where both soot and Al_2O_3 particles are included. In comparing soot density contours (in the upper half of the figure) to the density contours for Al_2O_3 particles in Fig. (7.9), we find a significantly larger maximum divergence angle for soot, so that soot particles are found over a larger portion of the simulated flowfield. As explained in Section 7.2.2, smaller particles experience a greater radial acceleration due to interphase momentum exchange in the plume nearfield region. Soot particles are far smaller than any Al_2O_3 particles in the simulation, so will be deflected at potentially much larger angles to the central axis by the rapidly expanding gas. As the gas density through most of the plume is too low for soot particles to be noticeably accelerated far downstream of the nozzle, these particles move along nearly ballistic trajectories through much of the grid domain. We therefore expect a roughly inverse-square variation in soot density with downstream distance, as is observed in Fig. (7.27). Note the similar trend in Al_2O_3 particle density contours shown in Fig. (7.9).

Contours of average soot temperature are displayed in the lower half of Fig. (7.27). First note that these temperatures are uniformly several hundred degrees lower than Al_2O_3 particle temperatures shown in Fig. (7.11), as follows from the far smaller heat capacity of soot particles and the relation between particle heat capacity and the rate of

convective heat transfer. (A detailed explanation of the expected temperature variation with particle size is provided in Section 7.2.3.) As in Fig. (7.11), soot particles which move along trajectories at large angles to the central axis are shown in Fig. (7.27) to experience higher temperatures than particles closer to the axis, due to the reduction in convective heat loss which results from a decrease in gas density with radial distance. Higher temperatures are also observed for particles very close to the axis. This trend is found in Fig. (7.11) as well, and is likely an unphysical result of inaccurate gas property calculations near the axis. (See Sections 7.2.2 and 7.2.3 for further discussion of this problem.)

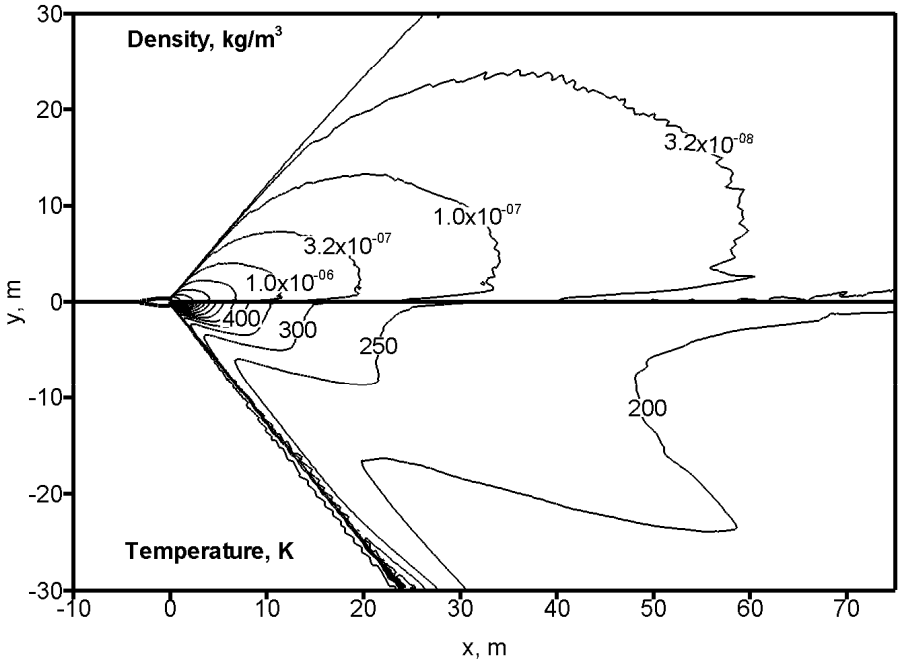

Figure 7.27. Contours of soot mass and average temperature.

Note the spike in farfield soot temperature contours for particles with trajectories inclined about 20° to the central axis; particles within a relatively narrow region seem to

cool significantly more slowly than particles with either larger or smaller divergence angles. This difference can be attributed in part to the influence of radiative absorption. As shown in Fig. (7.15) the magnitude of the radiative energy flux tends to be somewhat larger near regions populated by higher temperature Al_2O_3 particles. This creates an elevated level of incident radiation for soot particles which pass through regions shown in Fig. (7.11) near the maximum divergence angle for 4 μm Al_2O_3 particles, and allows these soot particles to experience an increased rate of radiative absorption. This trend can be more clearly observed in Fig. (7.28), in which soot temperature contours are compared between the simulation where both soot and Al_2O_3 particles are included, and the simulation which includes only soot.

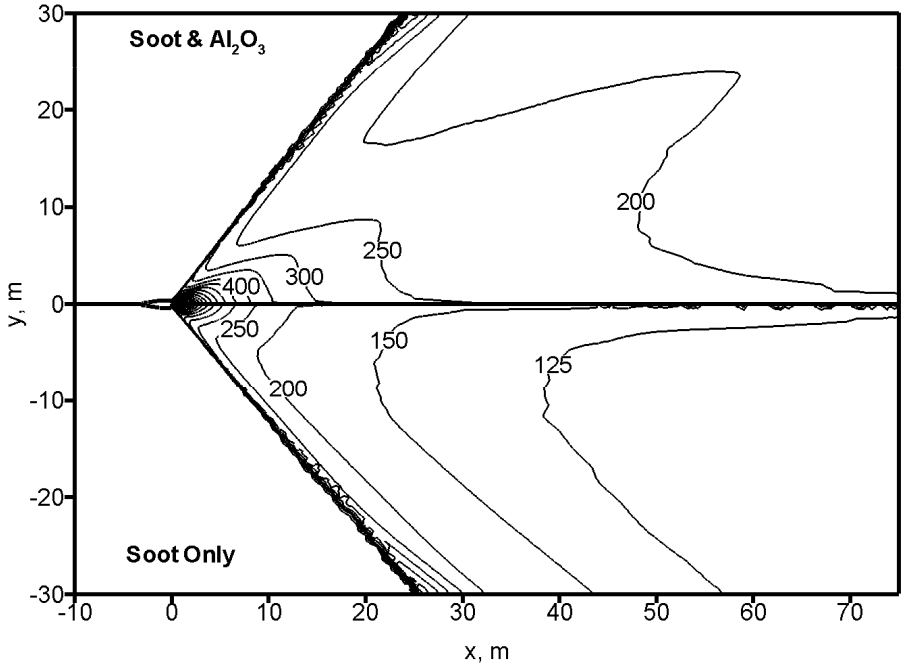

Figure 7.28. Contours of soot temperature for simulations with and without Al_2O_3 particles. Temperatures are given in K.

Note that the spike in farfield temperature for particles with a roughly 20° divergence angle is completely absent in the lower half of Fig. (7.28), which shows results from the simulation where Al_2O_3 particles are excluded. Soot temperatures are found to be uniformly about 100 K lower in this second simulation, due in part to the decrease in radiative absorption associated with the greatly reduced incident intensity when Al_2O_3 particles are left out of the simulation. Much of the difference in temperatures observed between the upper and lower halves of Fig. (7.28) may also be caused by the influence of Al_2O_3 particles on gas temperatures in the nearfield plume region, where significant convective heat transfer occurs between soot particles and the gas.

7.5.3 Radiative energy flux

The variation in net radiative energy flux along the extraction line is shown in Fig. (7.29). Results are presented here for the base simulation, the simulation involving both soot and Al_2O_3 particles, and the simulation where only soot particles are included. In comparing results between the first two simulations, we find that soot has a very small effect on the net energy flux over the entire length of the extraction line. When soot particles are considered independently, the total radiation intensity is found to be about 35% lower around the nozzle exit, and over two orders of magnitude lower at a distance of about 75 m downstream.

The divergence in simulation results with downstream distance can be traced in part to the large difference in temperature gradients between soot and Al_2O_3 particles, due to convective heat transfer in the nearfield plume region. As discussed in Section 7.5.2, soot particles will cool far more rapidly than the much larger Al_2O_3 particles through energy

exchange with the surrounding gas. Thermal radiation intensity scales with roughly the fourth power of the source temperature, so the downstream increase in the average temperature difference between soot and Al_2O_3 particles corresponds to a far larger difference in radiation intensity contributions from the two types of particles.

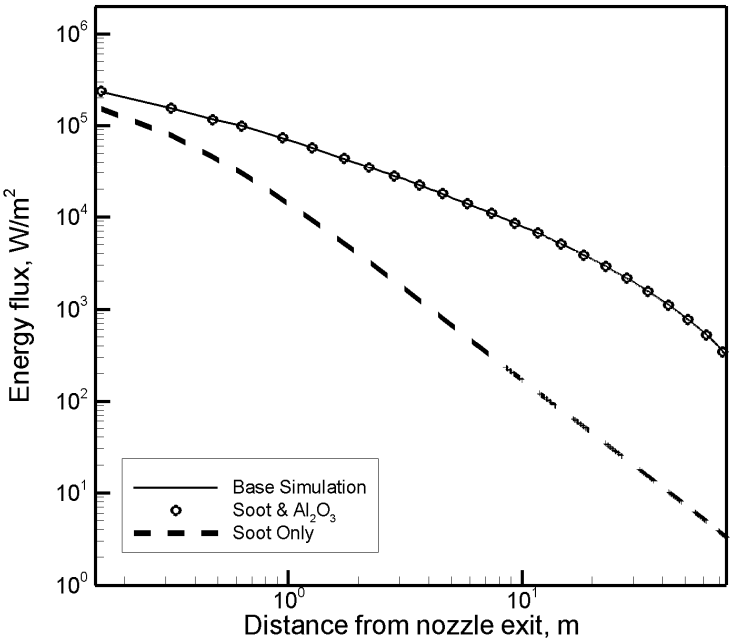

Figure 7.29. Effect of soot on the net radiative energy flux along the extraction line.

Another factor in the downstream increase in differences between simulation results shown in Fig. (7.29) is the influence of nozzle searchlight emission. As discussed in Section 7.4.4, the contribution of searchlight emission to the radiative energy flux decreases continuously with distance from the nozzle exit, so that particle emission, absorption and scattering play a comparatively larger role with increasing downstream distance. The intensity of searchlight emission is equal for all three simulations considered here, so we expect that differences among these simulations in particle

radiation characteristics will result in a downstream increase in the variation between calculated energy flux values.

7.5.4 UV spectral radiance

Figure (7.30) shows profiles of the plume UV spectral radiance, as measured at the onboard sensor for the base simulation and the two simulations which include soot. By comparing results from these simulations to the experimental values also shown in the figure, we can roughly assess the expected contribution of soot to the discrepancy between experiment and simulation results. An examination of Fig. (7.30) reveals that, for this particular flow and for the estimated soot concentration used here, soot has no significant influence on the calculated UV radiance values. All differences between radiance values for the base simulation and those for the simulation involving both soot and Al_2O_3 particles are within the error bars for statistical scatter, and values for the simulation which includes only soot are uniformly over four orders of magnitude lower.

The fact that soot has such a small effect on plume UV radiance can be attributed to the very small soot mass loading used in the simulations (less than 7% that of Al_2O_3 particles), and particularly to the large difference between soot and Al_2O_3 particle temperatures throughout the plume. Note that thermal radiation intensity in the UV range is particularly sensitive to source particle temperatures, while most of the radiative energy flux throughout the simulated flowfield is concentrated at IR wavelengths where particle radiative emission is a weaker function of temperature. The relative contribution of soot is therefore found to be far smaller in Fig. (7.30) than in the net radiative energy flux values displayed in Fig. (7.29).

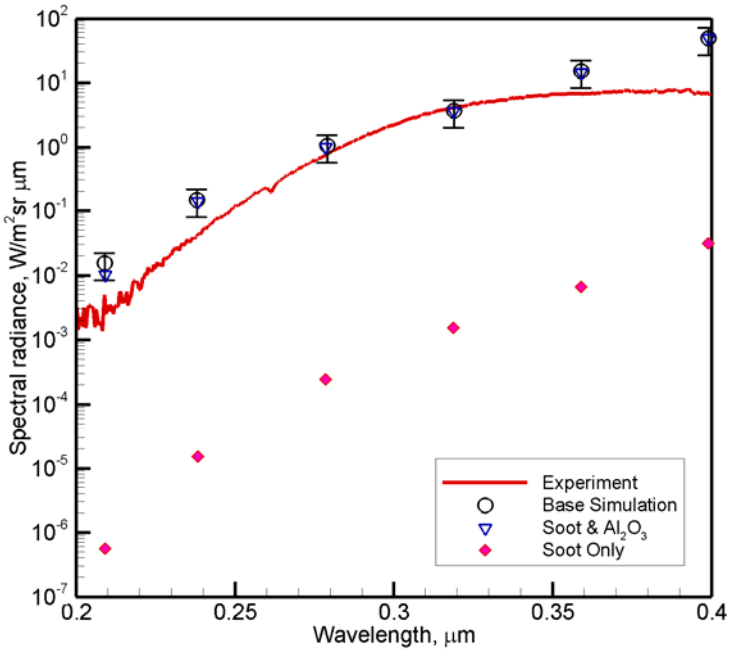

Figure 7.30. Effect of soot on UV radiance at the onboard sensor.

Chapter VIII

Summary and Future Work

8.1 Summary

The simulation of high altitude exhaust plumes from solid propellant rockets presents a number of modeling difficulties, and involves consideration of several complex physical processes which are not entirely understood. The work presented in this thesis has been performed with the goal of advancing the current state of modeling capabilities for these flows, and assessing the relative influence and interaction between potentially important phenomena. While the current effort does not resolve many of the known sources of inaccuracy in the simulation of high altitude SRM plume flows, it does address several flow physical processes that have received little previous attention in the literature, and allows these processes to be considered together within a unified numerical scheme.

Using the well-established DSMC method as a basis, procedures are developed here for the integration of condensed-phase particles into the simulation of a rarefied gas flow. We begin with the method of *Gallis et al.* (2001) for the determination of interphase momentum and energy exchange rates between a locally free molecular monatomic gas and a solid sphere. The method is extended for use with nonspherical particles or rotating

particles, and a further proposed modification allows for consideration of rotational energy exchange in a diatomic gas.

Next, a series of procedures is developed for the simulation of two phase rarefied flows involving two-way coupled momentum and energy transfer between the particles and gas. The influence of particles on the surrounding gas is considered through Monte Carlo procedures which involve the probabilistic modeling of individual interphase collisions, and an alternate scheme is included for application to two-way coupled flows involving rotating particles. A sample calculation is used to demonstrate momentum and energy conservation in a time-averaged sense.

Following the introduction of Monte Carlo schemes for two phase flow simulation, a set of nondimensional coupling parameters is developed for use in quantifying the effect of interphase momentum and energy exchange. When evaluated periodically throughout the grid, these parameters may be used to determine when a number of numerical procedures for interphase coupling can be neglected without significantly influencing simulation results. A model for nonequilibrium crystallization of liquid Al_2O_3 droplets is presented, and is used in simulations of a subscale SRM plume flow to demonstrate the potential efficiency benefits of simulation procedures which utilize the coupling parameters.

One major difficulty in simulating the plume flows of interest is the enormous cost associated with the DSMC simulation of near-equilibrium, high density regions within the plume. We attempt to address this problem through the introduction of a new gas simulation scheme for near-equilibrium flowfield regions. This is shown to be well suited for integration in a DSMC code and for simulation of two phase flows using the models

described above. Using as a basis previous Monte Carlo methods for the ES-BGK model of the Boltzmann equation, we develop a series of procedures which enforces momentum and energy conservation and allows for rotational-translational energy exchange in a diatomic gas. Homogeneous relaxation simulations are used to demonstrate that rotational relaxation occurs at the correct rate, and the overall accuracy of the method is assessed through simulations of a rarefied nozzle flow.

As a final addition to the proposed simulation method, a MCRT model is presented for plume radiation analysis and for integration of radiative heat transfer effects into the particle energy balance. Condensed phase emission, absorption and anisotropic scattering are considered, and a model for nozzle searchlight emission is included as well. No assumptions are made regarding plume optical thickness, although all gas species are assumed to be optically transparent. The radiation model is fully integrated with flowfield simulation procedures, to account for potentially significant two-way coupling between radiation and flowfield properties. Additional procedures are described for the integration of soot or other very small particles into the simulation.

In an effort to evaluate the overall accuracy of the proposed scheme, a series of simulations is performed for a representative SRM plume flow. A number of simulation results are presented, and various flowfield characteristics are discussed. Limited comparisons are made between calculated UV radiance values and measured values from a flight experiment. While no definite conclusions can be drawn from these comparisons, relatively good agreement is observed between simulation and experimental results. Note that a rigorous assessment of simulation accuracy is not possible due a lack of more

detailed experimental data, although the level of agreement observed here is an encouraging indication of overall accuracy.

A series of parametric studies involving simulations of the same SRM plume flow is used to evaluate the influence of several physical processes and input parameters. The first of these studies considers models for gas-particle interaction. Here we find that particle and gas temperatures through much of the plume may be significantly affected by two-way interphase momentum and energy exchange. Values of the particle thermal accommodation coefficient are found to greatly influence flowfield properties as well as radiation intensity in the farfield plume region, while effects of particle rotation are shown to be negligible.

Another parametric study examines models and parameters related to plume radiation. In this study, we find that only the choice of particle UV absorption index values can account for the discrepancy observed between simulation and experimental values of plume spectral radiance in the 0.2 to 0.25 μm wavelength range. Most of the disagreement with the experimental data can therefore be traced to a large inherent uncertainty in the determination of absorption index values. Within the IR range, these values are also found to strongly influence particle temperatures and net radiation intensity through much of the plume. Nozzle searchlight emission is shown to significantly contribute to net radiation intensity in the nearfield plume region, while particle radiative emission – but not absorption – has a considerable effect on particle temperatures further downstream.

In a third parametric study, we consider the potential influence of soot on plume radiation properties. Soot is found to have a very small effect on net radiation intensity

throughout the plume, with a contribution relative to that of Al_2O_3 particles which decreases continuously with downstream distance. As measured from a simulated onboard sensor, UV spectral radiance values associated with soot are roughly four orders of magnitude smaller than base simulation values, so that the presence of soot may be safely ruled out as a significant contributor to the differences observed between simulation results and experimental data.

8.2 Modeling difficulties and proposed future work

While it is hoped that the work introduced here represents significant progress in the development of capabilities for high altitude SRM plume simulation, the inherent complexity and challenges associated with these simulations leave extensive room for future progress. A number of research areas exist for the improvement of simulation accuracy or computational efficiency, while a sufficient evaluation of simulation techniques likely requires that additional flight experiments be performed.

8.2.1 Unified nozzle/plume flow simulations

One important area of future work is in the development of codes and numerical methods for the unified simulation of SRM exhaust flows, where multiphase flow processes within the propellant grain, nozzle and plume are considered together within a single numerical framework. As internal and external rocket exhaust flows typically require different simulation capabilities and present different challenges, the integration of simulation techniques valid for all flowfield regimes in high altitude SRM exhaust flows may be a very demanding task. However, such an integrated simulation scheme

would allow for far more rapid, and potentially more accurate, characterization of flowfield and radiation properties of interest. More detailed and spatially nonuniform flow property information could be easily obtained in the region around the nozzle exit, and two-way coupling effects between the nozzle and plume flow regions could more simply and accurately be addressed. These coupling effects may be particularly important for consideration of radiative heat transfer, and for accurate characterization of the subsonic boundary layer and sonic point around the nozzle lip.

8.2.2 Monte Carlo methods for near-equilibrium flows

As discussed in Chapter 5, the wide range of the Knudsen number regimes encountered in the flowfields of interest – from continuum to near free-molecular – presents a particularly difficult problem in the development of a unified numerical framework. While the DSMC method may be required to accurately simulate portions of the plume and atmospheric flow regions, DSMC is very inefficient when applied to higher density plume regions and is completely inappropriate for the simulation of internal SRM exhaust flows. The use of hybrid CFD-DSMC schemes, as has been employed in past simulation efforts for these flows [*Hueser et al.* (1984)], may require the development and application of a number of compatible modeling procedures for physical processes occurring in both continuum and rarefied flow regions. For example, the use of separate models for radiative heat transfer and particle-gas interaction may be needed for regions within the CFD and DSMC calculation domains.

One potentially simpler alternative to this approach is the use of alternate Monte Carlo methods for gas phase simulation in near-equilibrium regions, as is proposed in

Chapter 5. The gas simulation scheme introduced here is one of a number of relatively new particle methods for the simulation of continuum to moderately rarefied flows, which can be easily integrated with standard DSMC to avoid many of the problems associated with the hybrid CFD-DSMC approach. Although this and similar schemes have been successfully applied to flowfield regimes relevant to the current effort, a few potentially important error sources make these schemes generally unsuitable for widespread use.

As shown by *Breuer et al.* (1995) for simulations employing a DSMC collision limiter procedure, errors associated with artificial thermal equilibration tend to occur when the cell size greatly exceeds the local mean free path. The gas thermal energy may be partitioned nearly equally among the various translational and internal degrees of freedom, even when this equilibration does not take place in the flow being simulated. Given the inherent limitations of available computational resources, it is often unfeasible to use cell dimensions on the order of a mean free path, and this artificial equilibration effect may be unavoidable.

While the artificial equilibration error may be considerable in a moderately rarefied flow, it does become insignificant for very low Knudsen number flows where the high collision frequency promotes near-complete thermal equilibration. However, another error source remains important even at the continuum flow limit. *Breuer et al.* (1995) describe the numerical viscosity error which develops as a result of thermal velocity fluctuations when cell dimensions are much larger than a mean free path. For gas simulation techniques where particle advection and collision processes are decoupled during each time step, and where collisional processes are not influenced by the relative

position of particles within a cell, it can be shown that the numerical viscosity, thermal conductivity and mass diffusion coefficients will all scale linearly with the characteristic cell size. As the corresponding physical transport coefficients tend to scale with the mean free path, the ratio of numerical to physical coefficients will increase as the ratio of the cell size to the mean free path. This may lead to large artificial diffusion errors in the simulation of low Knudsen number flows, and tends to make these techniques generally less accurate and practical for the characterization of high density SRM exhaust flow regions than continuum CFD methods.

To improve overall accuracy and applicability of Monte Carlo gas simulation techniques for continuum to moderately rarefied flows, these error sources should be addressed. In order to reduce errors associated with artificial equilibration and numerical diffusion, one likely direction for future work may involve the use of Brownian motion theory to simultaneously move particles through the grid and resample particle velocities. This avoids the approximation of temporal decoupling between advection and collision procedures, and may reduce the dependence of various transport properties on cell size and time step.

8.2.3 Gas radiation modeling

Other proposed areas of future work include the extension of the radiation model presented in Chapter 6 to gas phase emission, absorption, and scattering. While the expected contribution of gas species to radiation characteristics of most SRM plume flows is relatively small, the inclusion of gas radiation may considerably increase the precision and spectral resolution of plume radiance calculations. Few efforts at

noncontinuum gas radiation analysis through MCRT models can be found in the literature, although procedures described by *Modest* (1992) seem well suited for integration into the condensed phase radiation model presented here.

8.2.4 Radiation modeling for Al_2O_3 particles

Although the inclusion of gas radiation effects should improve simulation capabilities and marginally increase the overall accuracy of radiation calculations, the uncertainty in Al_2O_3 radiation characteristics far outweighs the influence of the gas. As discussed in Chapter 7, radiative properties of Al_2O_3 particles are extremely complex and difficult to model. In particular, calculations requiring spectrally resolved Al_2O_3 absorption and emission characteristics are subject to significant uncertainty, due to the large number of flowfield and material properties which must be considered for reasonably accurate results. The spectral emissivity and absorption index of these particles has been observed to vary as a strong function of particle size, phase composition, temperature, impurity concentrations and the prevalence of lattice defects. [*Reed and Calia* (1993)]

While previous simulation efforts for similar flows have used detailed Al_2O_3 radiation models which incorporate parameters not considered here [*Plastinin et al.* (2001)], the inherent uncertainty in input values makes the utility of including additional parameters seem questionable. For example, impurity concentrations may vary widely between different SRM exhaust flows, and between different regions of the same flow. [*Konopka, Reed and Calia* (1983)] Even when the strong dependence of emissive characteristics on impurities is incorporated into the radiation model, the inherent lack of accurate input values may lead to a large margin of error in simulation results. While no solutions to this

problem seem apparent, the issue is sufficiently important for the analysis of SRM plume radiation that much further study is warranted.

8.2.5 The need for future experiments

One final proposed area of future work is the detailed experimental measurement of both flowfield and radiation properties for a representative high altitude SRM exhaust plume. As no such combined measurements appear to exist in the open literature, the unavailability of experimental data makes the assessment of simulation techniques and analysis tools extremely difficult. Although it is useful, the limited comparison with experiment included in Chapter 7 is inadequate to sufficiently evaluate the overall accuracy of simulation procedures presented here. A proper evaluation of these procedures would require a more detailed comparison of simulation results with measured flowfield and radiation characteristics. To allow for this type of comparison in the future, additional data will be needed from either flight experiments or SRM firings in a vacuum chamber. (Such data is in fact believed to exist in the classified literature, based on tests conducted at the Arnold Engineering Development Center in Tennessee. A more feasible alternative to costly experiments may therefore be a limited declassification for some of this data.)

Appendices

Appendix A

Nomenclature

Abbreviations

BSUV-2	bow shock ultraviolet 2 flight experiment
CFD	computational fluid dynamics
DSMC	direct simulation Monte Carlo
ES-BGK	ellipsoidal statistical Bhatnagar-Gross-Krook equation
MCRT	Monte Carlo ray trace radiation model
MOC	method of characteristics
NS	Navier Stokes equations
NTC	no time counter collision selection scheme
SRM	solid rocket motor
TAC	thermal accommodation coefficient
VHS	variable hard sphere collision model

Symbols

A	coefficient for radial distance in a least-squares fit of the particle number flux profile

A_c	crystallization rate coefficient
A_f	area of a cell face
A_s	particle surface area; surface area of a radiation sensor
c_{g1}	gas bulk speed
c_{g2}	root-mean-squared gas molecule speed
c_{nr}^*	magnitude of non-rotational component of post-collision relative velocity
c_p	particle speed
c_r	gas molecule relative speed
c_r^*	post-collision relative speed
$(c_r)_{max}$	maximum pre-collision relative speed
c_{r1}	magnitude of the difference between $\mathbf{u}_p$ and $\mathbf{u}_g$
c_{r2}	average gas molecule speed relative to $\mathbf{u}_p$
c_{r3}	root-mean-squared gas molecule speed relative to $\mathbf{u}_p$
c_s	particle specific heat
C_1	cutoff value for gas-to-particle coupling
C_2	cutoff value for particle-to-gas coupling
d_{ref}	molecular collision diameter at the reference temperature
D_e	distance required for an energy bundle to exit the currently assigned cell
D_p	average particle diameter; distance to the surface of a radiation sensor along the direction of propagation for an energy bundle
D_s	distance along energy bundle trajectory to a scattering event
D_t	total distance that an energy bundle has traveled through the currently assigned cell
e_{int}	total internal energy per molecule

e^{*}_{kin}	post-collision gas kinetic energy
e_r	mean rotational energy per gas molecule
$\dot{E}$	interphase energy transfer rate per unit volume
E_r	DSMC gas particle rotational energy
E_λ	direction-averaged spectral radiative energy flux
f	gas velocity distribution function
f_e	equilibrium (Maxwellian) velocity distribution function
f_G	anisotropic Gaussian velocity distribution function
f_p	average interphase collision frequency per particle
f_v	particle phase volume fraction
F_{coll}	gas collision frequency
F_i	net body force per unit mass
$\mathbf{F}_p$	force on a solid particle; particle force Green's function
$\mathbf{F}_{p,net}$	net particle force based on Green's function integration
$\mathbf{F}_{rot}$	force Green's function associated with particle rotation
g	average cosine of the scattering angle
h_f	particle latent heat of fusion
I_i	band-averaged spectral radiance for wave number bin i
k	particle absorption index
k_{eff}	effective absorption index value for soot
Kn_{GLL}	gradient length local Knudsen number
L	global characteristic length scale
m	mass per gas molecule

m_p	particle mass
$\dot{m}_p$	particle mass flux
M_p	particle Mach number
$\mathbf{M}_p$	Green's function for the moment on a rotating particle
$\mathbf{M}_{p,net}$	net moment on a rotating particle
n	particle index of refraction
n_c	crystallization rate exponent
$\mathbf{n}_c$	outward normal vector at the collision point
$\mathbf{n}_f$	inward normal unit vector at a cell face
n_g	gas number density
n_j	time-averaged number density for particle species j
$\mathbf{n}_s$	outward unit normal vector for a radiation sensor surface
N_b	number of energy bundles created per time step
N_f	number of energy bundles generated per cell face along inflow boundaries
N_g	number of DSMC gas molecules in a cell
N_r	number of particles selected for reassignment of rotational energy
N_s	number of DSMC gas molecules selected for potential collisions; number of substeps for phase change calculations
N_{spec}	number of different gas or particle species
N_v	number of particles selected for velocity reassignment
N_η	number of wave number bins
p	scalar pressure
p_o	source pressure
P_b	power assigned to an energy bundle

P_{coll}	collision probability
$P_{p,i}$	source particle emissive power for wave number bin i
Pr	Prandtl number
P_{1e}	gas-to-particle energy coupling parameter
P_{1m}	gas-to-particle momentum coupling parameter
P_{2e}	particle-to-gas energy coupling parameter
P_{2m}	particle-to-gas momentum coupling parameter
q_i	direction-averaged radiative energy flux for wave number bin i
$\dot{Q}_p$	particle heat transfer rate; heat transfer Green's function
$\dot{Q}_{p,net}$	net particle heat transfer rate based on Green's function integration
$\dot{Q}_{rad}$	net rate of radiative heat transfer to a particle
r_l	ratio of the crystallization front radius to the particle radius
R	random number between 0 and 1
R_j	radius for particle species j
R_p	particle radius
R_s	radius of the radiation sensor surface
R_t	nozzle throat radius
R_w	nozzle inner radius at a given axial location
S_{ij}	anisotropic Gaussian transformation matrix
S_o	most probable gas thermal speed at the stagnation temperature
$T_a^{(2)}$	temperature equivalent to $T^{(2)}$ based on cell-averaged quantities
T_{eq}	equilibrium gas temperature based on translational and rotational temperatures

T_f	nucleation temperature for homogeneous crystallization
T_g	gas total temperature
T_j	cell-averaged temperature of particle species j
T_m	equilibrium melting temperature
T_p	particle temperature
T_r	gas rotational temperature
T_{ref}	reference temperature
T_t	cell-averaged gas translational temperature
T_o	gas stagnation temperature
$T^{(2)}$	gas temperature based on resampled velocities and rotational energies
$\mathbf{u}$	unit vector in the final direction of propagation for an energy bundle
u_i	point in velocity space
$\mathbf{u}_g$	gas bulk velocity
$\mathbf{u}_m$	absolute velocity of a gas molecule
$\mathbf{u}_m^*$	post-collision absolute gas molecule velocity
$\mathbf{u}_{nr}^*$	non-rotational component of post-collision relative velocity
$\mathbf{u}_p$	particle velocity, average velocity of particles in a cell
$\mathbf{u}_r$	gas molecule relative velocity
$\mathbf{u}_r^*$	post-collision relative velocity
$\mathbf{u}_{rot}^*$	rotational component of post-collision relative velocity
$\mathbf{u}_t$	tangential velocity on the particle surface
$\mathbf{u}^{(0)}$	initial gas particle velocity before resampling procedures
$\mathbf{u}^{(1)}$	resampled gas particle velocity

$\mathbf{u}^{(2)}$	gas particle velocity following renormalization for momentum and energy conservation
V_c	cell volume
W_g	gas relative weight
W_p	particle relative weight
$\mathbf{x}_b$	location of an energy bundle
$\mathbf{x}_s$	location of the center of a radiation sensor surface
Z_r	rotational collision number
α_i	band-averaged spectral absorptance for wave number bin i
α_λ	particle spectral absorptance
β	inverse of gas thermal speed scale
β	correction factor for the rotational relaxation rate
δ	solid angle for a particle beam; collision deflection angle
ε	total emissivity
ε_i	band-averaged particle spectral emissivity for wave number bin i
ε_λ	particle spectral emissivity
ζ_r	number of gas rotational degrees of freedom
$\zeta_{t,eff}$	effective translational degrees of freedom
η	wave number
η_i	wave number at center of bin i
θ	interphase collision angle; scattering angle
θ_v	characteristic temperature of vibration
λ	gas mean free path; wavelength

μ	ratio of particle moment of inertia to that of a uniform density sphere
μ	gas dynamic viscosity
μ_{ref}	viscosity at reference temperature
ν	characteristic translational relaxation rate
ν_r	rotational relaxation rate
ρ_g	mass density of the gas
ρ_p	particle material density
ρ_o	gas stagnation density
σ	logical variable for a diatomic gas; interphase collision cross section
$\sigma_{avg,i}$	wavelength-averaged standard deviation of calculated spectral radiance
σ_i	scattering coefficient for wave number bin i; standard deviation of spectral radiance
σ_{liq}	liquid surface tension
τ	particle thermal accommodation coefficient
τ_{coll}	characteristic mean collision time
ϕ	angle between angular velocity and relative velocity vectors
ϕ	azimuthal angle corresponding to θ
φ	angle between surface normal vector and $\mathbf{u}_r^*$
χ	azimuthal angle corresponding to φ
ψ	particle shape factor
ω	maximum absorption angle for a radiation sensor
ω	VHS temperature exponent
$\boldsymbol{\omega}_p$	particle angular velocity

ω_p	angular velocity magnitude
Δq_i	contribution from an energy bundle to the direction-averaged radiative energy flux for wave number bin i
ΔQ_{abs}	net rate of radiative energy absorption for an individual particle
Δt	local DSMC time step
$\Delta \eta_i$	wave number interval for bin i
$\Delta \lambda_i$	wavelength interval for wave number bin i
$\Theta_{i,j}$	band-averaged scattering efficiency factor
ΣP_i	total absorbed power on a sensor surface for wave number bin i
Φ	scattering phase function
Φ_g	gas streamwise energy flux
Ψ_1	logical variable for gas-to-particle coupling
Ψ_2	logical variable for particle-to-gas coupling
Ω_{crit}	critical value for the normalized angular velocity
Ω_i	function of temperature used to compute particle emissive power

Constants

c_o	speed of light through a vacuum (2.99792458×10^{8} m/s)
h	Planck's constant (6.626068×10^{-34} kg m^2/s)
k_B	Boltzmann's constant (1.3806503×10^{-23} m^2 kg s^{-2} K^{-1})
σ	Stefan-Boltzmann constant (5.670×10^{-8} W m^{-2}K^{-4})

Numerical operators

floor	nearest smaller integer
$\langle\ \rangle_a$	average over all DSMC gas particles in a cell
$\langle\ \rangle_{\mathrm{r}}$	average over gas particles used for rotational energy resampling
$\langle\ \rangle_{\mathrm{v}}$	average over gas particles used for velocity resampling

Appendix B

Derivation of a Formula for the Deflection Angle

A derivation is provided here for the relation between the angles θ, ϕ, χ, and δ given as Eq. (3.3), based on the geometry shown in Fig. (3.1). This relation allows the deflection angle δ in a diffusely refleccting interphase collision to be calculated as a function of parameters which may be efficiently sampled from known distributions. First, we define a unit vector **n** in the direction of the post-collision relative velocity vector $\mathbf{u}_r^*$, with components (n_x, n_y, n_z) and ($n_{x'}$,$n_{y'}$,$n_{z'}$) in the (x,y,z) and (x',y',z') coordinate systems respectively. Two additional angles must also be defined: Denote as ξ the angle between $\mathbf{u}_r^*$ and the projection of $\mathbf{u}_r^*$ onto the x'-y' plane, and let ω be the angle between this projection and the y'-axis.

The following expressions can be found for ω, χ, and φ in terms of the components of the unit vector **n**:

$$\tan\omega = n_{x'}/n_{y'} \qquad \tan\varphi = \sqrt{n_{x'}^2+n_{z'}^2}\Big/n_{y'} \qquad \cos\chi = n_{x'}\Big/\sqrt{n_{x'}^2+n_{z'}^2}$$

Substitution then gives

$$\tan\omega = \tan\varphi\cos\chi \tag{B.1}$$

Similarly, the relations

$$\sin\xi = n_{z'} \qquad \sin\varphi = \sqrt{n_{x'}^2 + n_{z'}^2} \qquad \sin\chi = n_{z'} \Big/ \sqrt{n_{x'}^2 + n_{z'}^2}$$

are used to find an expression for ξ in terms of φ and χ:

$$\sin\xi = \sin\varphi \sin\chi \tag{B.2}$$

Next, δ can be related to θ, ω, and ξ by recognizing that

$$\cos\delta = n_y \qquad \cos(\theta+\omega) = n_y \Big/ \sqrt{n_x^2 + n_y^2} \qquad \cos\xi = \sqrt{n_x^2 + n_y^2}$$

Then by substitution and a trigonometry identity:

$$\cos\delta = \cos\xi \cos(\theta+\omega) = \cos\xi (\cos\theta \cos\omega - \sin\theta \sin\omega) \tag{B.3}$$

Note that both ξ and ω are confined to the range $[-\pi/2, \pi/2]$, hence $\cos\xi = \sqrt{1-\sin^2\xi}$, $\cos\omega = \left(1+\tan^2\omega\right)^{-1/2}$, and $\sin\omega = \tan\omega\left(1+\tan^2\omega\right)^{-1/2}$. Using these relations, Eqs. (B.1) and (B.2) are substituted into Eq. (B.3) to give an expression for δ in terms of θ, χ, and φ. After some algebraic simplification, this expression can be written as

$$\cos\delta = (\cos\theta - \sin\theta \tan\varphi \cos\chi)\left[\frac{1-(\sin\varphi\sin\chi)^2}{1+(\tan\varphi\cos\chi)^2}\right]^{1/2}. \tag{B.4}$$

Bibliography

Bibliography

P. Andries, J. Bourgat, P. Le Tallec, and B. Perthame. Numerical Comparison Between the Boltzmann and ES-BGK Models for Rarefied Gases. *Institut National de Recherche en Informatique et en Automatique*, Report No. 3872, 2000.

P. Andries and B. Perthame. The ES-BGK Model Equation with Correct Prandtl Number. *Proceedings of the 22nd International Symposium on Rarefied Gas Dynamics*, *AIP Conference Proceedings*, 426-433, 2001.

N. A. Anfimov, G. F. Karabadjak, B. A. Khmelinin, Y. A. Plastinin, and A. V. Rodionov. Analysis of Mechanisms and Nature of Radiation from Aluminum Oxide in Different Phase States in Solid Rocket Exhaust Plumes. AIAA Paper 93-2818, 1993.

D. Baganoff and J. D. McDonald. A Collision-Section Rule for a Particle Simulation Method Suited to Vector Computers. Physics of Fluids A, 2(7):1248-1259, 1990.

W. S. Bailey, E. N. Nilson, R. A. Serra, and T. F. Zupnik. Gas Particle Flow in an Axisymmetric Nozzle. *ARS Journal*, 793-798, June 1961.

T. J. Bartel, T. M. Sterk, J. L. Payne, and P. Preppernau. DSMC Simulation of Nozzle Expansion Flow Fields. AIAA Paper 94-2047, 1994.

P. L. Bhatnagar, E. O. Gross, and M. Krook. Model for Collision Processes in Gases, I. *Physical Review E*, 94:511, 1954.

G. A. Bird. *Molecular Gas Dynamics and the Direct Simulation of Gas Flows*. Clarendon Press, 1994.

I. D. Boyd. Analysis of Rotational Noequilibrium in Standing Shock Waves of Nitrogen. *AIAA Journal*, 28(11):1997-1999, 1990.

I. D. Boyd. Predicting Breakdown of the Continuum Equations Under Rarefied Flow Conditions. *Proceedings of the 23nd International Symposium on Rarefied Gas Dynamics*, *AIP Conference Proceedings*, 663(1):899-906, 2003.

I. D. Boyd, G. Chen, and G. V. Candler. Predicting Failure of the Continuum Fluid Equations in Transitional Hypersonic Flows. *Physics of Fluids*, 7(1):210-219, 1995.

I. D. Boyd, P. F. Penko, D. L. Meissner, and K. J. DeWitt. Experimental and Numerical Investigations of Low-Density Nozzle and Plume Flows of Nitrogen. *AIAA Journal*, 30(10):2453-2461, 1992.

K. S. Breuer, E. S. Piekos, and D. A. Gonzales. DSMC Simulations of Continuum Flows. AIAA Paper 95-2088, 1995.

D. Bruno, M. Capitelli, and S. Longo. A BGK/MC Method for the Simulation of Shock Waves in Binary Mixtures. AIAA Paper 2002-2895, 2002.

D. Bruno and S. Longo. Monte Carlo Simulation of Nearly Kinematic Shock Fronts in Rarefied Gases. *European Physical Journal*, *Applied Physics*, 17:233-241, 2002.

G. V. Candler, D. A. Levin, J. Brandenburg, R. Collins, P. Erdman, E. Zipf, C. Howlett. Comparison of Theory with Plume Radiance Measurements from the Bow Shock Ultraviolet 2 Rocket Flight. AIAA Paper 92-0125, 1992.

C. Cercignani. *The Boltzmann Equation and its Applications*. Applied Mathematical Sciences, Springer Verlag, 1988.

I. Chang. One and Two-Phase Nozzle Flows. AIAA Paper 80-0272, 1980.

C. Chung, S. C. Kim, R. M. Stubbs, and K. J. De Witt. Low Density Nozzle Flow by the Direct Simulation Monte Carlo and Continuum Methods. *Journal of Propulsion and Power*, 11(1):64-70, 1995.

M. S. Clark, S. C. Fisher, and E. P. French. The Flow of Very Small Alumina Particles in a Solid Rocket Plume. AIAA Paper 81-1384, 1981.

C. Crowe, M. Sommerfeld, and Y. Tsuji. *Multiphase Flows with Droplets and Particles*. CRC Press, 1998.

S. M. Dash, D. E. Wolf, R. A. Beddini, and H. S. Pergament. Analysis of Two-Phase Flow Processes in Rocket Exhaust Plumes. *Journal of Spacecraft*, 22(3):367-380, 1985.

S. Dietrich and I. D. Boyd. Scalar and Parallel Optimized Implementation of the Direct Simulation Monte Carlo Method. *Journal of Computational Physics*, 126:328-342, 1996.

J. Dupays. Two-phase Unsteady Flow in Solid Rocket Motors. *Aerospace Science and Technology*, 6(6):413-422, 2002.

R. Duval, A. Soufiani, and J. Taine. Coupled Radiation and Turbulent Multiphase Flow in an Aluminised Solid Propellant Rocket Engine. *Journal of Quantitative Spectroscopy and Radiative Transfer*, 84(4):513-526, 2004.

P. S. Epstein. On the Resistance Experienced by Spheres in their Motion through Gases. *Physical Review*, 24:710-733, 1924.

P. W. Erdman, E. Zipf, P. Espy, C. Howlett, D. A. Levin, and G. V. Candler. In-Situ Measurements of UV and VUV Radiation from a Rocket Plume and Re-entry Bow Shock. AIAA Paper 92-0124, 1992.

J. Everson and H. F. Nelson. Development and Application of a Reverse Monte Carlo Radiative Transfer Code for Rocket Plume Base Heating. AIAA Paper 93-0138, 1993.

J. T. Farmer and J. R. Howell. Monte Carlo Prediction of Radiative Heat Transfer in Inhomogeneous, Anisotropic, Nongray Media. *Journal of Thermophysics and Heat Transfer*, 8(1):133-139, 1994.

H. L. Fein. A Theoretical Model for Predicting Aluminum Oxide Particle Size Distributions in Rocket Exhausts. *AIAA Journal*, 4(1):92-98, 1966.

M. A. Gallis and J. R. Torczynski. The Application of the BGK Model in Particle Simulations. AIAA Paper 2000-2360, 2000.

M. A. Gallis, J. R. Torczynski, and D. J. Rader. An Approach for Simulating the Transport of Spherical Particles in a Rarefied Gas Flow via the Direct Simulation Monte Carlo Method. *Physics of Fluids*, 13(11):3482-3492, 2001.

M. Garrison, T. Ozawa and D. Levin. An Improved CO_2, H_20 and Soot Infrared Radiation Models for High Temperature Flows. AIAA Paper 2005-4777, 2005.

R. L. Geisler. A Global View of the Use of Aluminum Fuel in Solid Rocket Motors. AIAA Paper 2002-3748, 2002.

P. T. Girata and W. K. McGregor. Particle Sampling of Solid Rocket Motor (SRM) Exhausts in High Altitude Test Cells. AIAA Paper 83-245, 1983.

S. Gosse, V. Sarou-Kanian, E. Veron, F. Millot, J. C. Rifflet, and P. Simon. Characterization and Morphology of Alumina Particles in Solid Propellant Subscale Rocket Motor Plumes. AIAA Paper 2003-3649, 2003.

C. B. Henderson. Effect of Crystallization Kinetics on Rocket Performance. *AIAA Journal*, 15(4):600-602, 1977.

R. W. Hermsen. Aluminum Oxide Particle Size for Solid Rocket Motor Performance Prediction. AIAA Paper 81-0035, 1981.

R. V. Hogg and E. A. Tanis. *Probability and Statistical Inference*. Prentice Hall, 1997.

R. F. Hoglund. Recent Advances in Gas-Particle Nozzle Flows. *ARS Journal*, 662-671, May 1962.

L. H. Holway. Kinetic Theory of Shock Structure Using an Ellipsoidal Distribution Function. *Proceedings of the Fourth International Symposium on Rarefied Gas Dynamics*, *AIP Conference Proceedings*, 193-215, 1966.

J. E. Hueser, L. T. Melfi, G. A. Bird, and F. J. Brock. Analysis of Large Solid Propellant Rocket Exhaust Plumes Using the Direct Simulation Monte Carlo Method. AIAA Paper 84-0496, 1984.

S. C. Hunter, S. S. Cherry, J. R. Kliegel, and C. H. Waldman. Gas-Particle Nozzle Flows with Reaction and Particle Size Change. AIAA Paper 81-0037, 1981.

C. J. Hwang and G. C. Chang. Numerical Study of Gas-Particle Flow in a Solid Rocket Nozzle. *AIAA Journal*, 682-689, June 1988.

T. Hyakutake and Kyoji Yamamoto. Numerical Simulation of Rarefied Plume Flow Exhausting from a Small Nozzle. *AIP Conference Proceedings*, 663(1):604-611, 2003.

F. P. Incropera and D. P. DeWitt. *Fundamentals of Heat and Mass Transfer*. John Wiley and Sons, 1996.

G. Israel and K. Friedlander. High-Speed Beams of Small Particles. *Journal of Colloid and Interface Science*, 24:330-337, 1967.

S. G. Ivanov and A. M. Yanshin. Forces and Moments Acting on Bodies Rotating About a Symmetry Axis in a Free Molecular Flow. Fluid Dynamics, 15(3):449-453, 1980.

J. H. Jeans. *The Dynamical Theory of Gases*. Cambridge University Press, 1916.

R. M. Jenkins and R. F. Hoglund. A Unified Theory of Particle Growth in Rocket Chambers and Nozzles. AIAA Paper 69-541, 1969.

T. T. Kassal. Scattering Properties of Ice Particles Formed by Release of H_2O in Vacuum. *Journal of Spacecraft*, Vol.11(1):54-56, 1974.

J. R. Kliegel and G. R. Nickerson. Flow of Gas-Particle Mixtures in Axially Symmetric Nozzles. *ARS Preprint*, 1715-1761, April 1961.

W. L. Konopka, R. A. Reed, and V. S. Calia. Measurements of Infrared Optical Properties of Al2O3 Rocket Particles. AIAA Paper 83-1568, 1983.

O. B. Kovalev. Motor and Plume Particle Size Prediction in Solid Rocket Motors. *Journal of Propulsion and Power*, 18(6):1199-1210, 2002.

D. Laredo and D. W. Netzer. The Dominant Effect of Alumina on Nearfield Plume Radiation. *Journal of Quantitative Spectroscopy and Radiative Transfer*, 50(5):511-530, 1993.

M. N. Macrossan. A Particle Simulation Method for the BGK Equation. *Proceedings of the 22nd International Symposium on Rarefied Gas Dynamics , AIP Conference proceedings*, 426-433, 2001.

M. N. Macrossan, M. V. Metchnik, and P. A. Pinto. Hypersonic Flow over a Wedge with a Particle Flux Method. *Proceedings of the 24nd International Symposium on Rarefied Gas Dynamics , AIP Conference proceedings*, 650-655, 2005.

J. R. Mahan. *Radiation Heat Transfer: a Statistical Approach*. John Wiley and Sons, 2002.

W. K. McGregor, J. A. Drakes, K. S. Beale, and F. G. Sherrell. The AlCl Absorption Feature in Solid Rocket Plume Radiation. AIAA Paper 92-2917, 1992.

L. Miessens and H. Struchtrup. Numerical Comparison of Bhatnagar-Gross-Krook Models with Proper Prandtl Number. *Physics of Fluids*, 16(8):2797-2813, 2004.

M. F. Modest. The Monte Carlo Method Applied to Gases with Spectral Line Structure. *Developments in Radiative Heat Transfer*, ASME HTD 203:79-84, 1992.

J. M. Montanero, A. Santos, J. W. Duffy, and J. F. Lutsko. Stability of Uniform Shear Flow. *Physical Review E*, 57(1):546-556, 1998.

F. M. Najjar, A. Haselbacher, J. P. Ferry, B. Wasistho, S. Balachandar, and R. D. Moser. Large-Scale Multiphase Large-Eddy Simulation of Flows in Solid-Rocket Motors. AIAA Paper 2003-3700, 2003.

J. G. Parker. Rotational and Vibrational Relaxation in Diatomic Gases. *Physics of Fluids*, 2:449-462, 1959.

G. N. Plass. Temperature Dependence of the Mie Scattering and Absorption Cross Sections for Aluminum Oxide. *Applied Optics*, 4(12):1616-1619, 1965.

Y. A. Plastinin, N. A. Anfimov, G. G. Baula, G. F. Karabadzhak, B. A. Khmelinin, and A. V. Rodionov. Modeling of Aluminum Oxide Particle Radiation in a Solid Propellant Motor Exhaust. AIAA Paper 96-1879, 1996.

Y. A. Plastinin, G. Karabadzhak, and B. Khmelinin. Ultraviolet, Visible and Infrared Spectra Modeling for Solid and Liquid-Fuel Rocket Exhausts. AIAA Paper 2001-660, 2001.

Y. A. Plastinin, H. P. Sipatchev, G. F. Karabadzhak, B. A. Knmelinin, E. Y. Szhenov, A. G. Khlebnikov, and Y. N. Shishkin. Experimental Investigation of Alumina Particles' Phase Transition and Radiation. AIAA Paper 98-0862, 1998.

D. I. Pullin. Direct Simulation Methods for Compressible Inviscid Ideal-Gas Flow. *Journal of Computational Physics*, 34:231-244, 1980.

L. Rattenni. Solid Motor Plume Analysis for the STAR-1 Spacecraft. AIAA Paper 2000-3190, 2000.

J. Reardon. Rocket Plume Base Heat Transfer Methodology. AIAA Paper 93-2823, 1993.

R. A. Reed, K. S. Beale, D. W. Neese, F. G. Sherrell, D. W. Roberds, and S. M. Oliver. The Effect of Seachlight Emission on Radiation from Solid Rocket Plumes. AIAA Paper 92-2918, 1992.

R. A. Reed and V. S. Calia. Review of Aluminum Oxide Rocket Exhaust Particles. AIAA Paper 93-2819, 1993.

A. V. Rodionov, Y. A. Plastinin, J. A. Drakes, M. A. Simmons, and R. S. Hiers. Modeling of Multiphase Alumina-Loaded Jet Flow Fields. AIAA Paper 98-3462, 1998.

D. E. Rothe. Electron-Beam Studies of Viscous Flow in Supersonic Nozzles. *AIAA Journal*, 9(5):804-811, 1971.

M. J. Salita. Use of Water and Mercury Droplets to Simulate Al_2O_3 Collision/Coalescence in Rocket Motors. *Journal of Propulsion and Power*, 7(4):505-512, 1991.

R. Siegel and J. R. Howell. *Thermal Radiation Heat Transfer*. McGraw-Hill, 1981.

F. S. Simmons. *Rocket Exhaust Plume Phenomenology*. Aerospace Press, 2000.

Q. Sun and I. D. Boyd. Evaluation of Macroscopic Properties in the Direct Simulation Monte Carlo Method. *Journal of Thermophysics and Heat Transfer*, 19(3):329-335, 2005.

I. M. Vasenin, R. K. Narimanov, A. A. Glazunov, N. E. Kuvshinov, and V. A. Ivanov. Two-Phase Flows in the Nozzles of Solid Rocket Motors. *Journal of Propulsion and Power*, 11(4):583-592, 1995.

W. G. Vincenti and C. H. Kruger. *Introduction to Physical Gas Dynamics*. Krieger Publishing, 1986.

E. I. Vitkin, V. G. Karelin, A. A. Kirillov, A. S. Suprun, and J. V. Knadyka. A Physico-Mathematical Model of Rocket Exhaust Plumes. *International Journal of Heat and Mass Transfer*, 40(5):1227-1241, 1997.

C. Wang. Free Molecular Flow Over a Rotating Sphere. *AIAA Journal*, 10(5):713-714, 1972.

M. J. Wright, R. M. Rao, G. V. Candler, J. S. Hong, T. A. Schilling, D. A. Levin. Modeling Issues in the Computation of Plume Radiation Signatures. AIAA Paper 98-3622, 1998.

B. J. York, R. A. Lee, N. Sinha, and S. M. Dash. Progress in the Simulation of Particulate Interactions in Solid Propellant Rocket Exhausts. AIAA Paper 2001-3590, 2001.